UNIVERSITY OF DURHAM

DOCTORAL THESIS

Analogue and numerical models of earthquake rupture

Author:
Simon GUERIN-MARTHE

Supervisors:
Dr. Stefan NIELSEN
Dr. Stefano GIANI
Dr. Simon MATHIAS

External examiner:
Dr. David MARSAN

Internal examiner:
Dr. Richard WALTERS

A thesis submitted in fulfilment of the requirements for the degree of Doctor of Philosophy in Geophysics

in the

Rock Mechanics Laboratory
Department of Earth Sciences

UNIVERSITY OF DURHAM

Abstract

University of Durham
Department of Earth Sciences

Doctor of Philosophy

Analogue and numerical models of earthquake rupture

by Simon GUERIN-MARTHE

Earthquakes represent one of the most important natural risks facing human populations in urban areas. Understanding the processes at the origin of these destructive events requires seismological observations, but also the use of laboratory analogues and numerical models for earthquake rupture. They allow for controlled conditions under which we can investigate the relative importance of different physical quantities involved in the system. The main points investigated in this thesis are the influence of loading rate on the nucleation of earthquakes, and the evolution of friction during dynamic ruptures. I conduct photoelastic experiments using polycarbonate plates, but also direct-shear experiments of precut granite blocks in a pressure vessel. I use finite-difference numerical models to reproduce and understand the dynamic laboratory ruptures, and I developed static finite element codes in order to reproduce the loading conditions induced by the experimental setup. The main results are that under certain conditions, increasing the loading rate makes the nucleation length shrink, and affects the nucleation position, which in this case is consistently situated on high coulomb stress areas. This is not necessarily the case for low loading rates. The shrinking of nucleation length may explain partly why some asperities in subduction zones can behave seismically or aseismically depending on the local tectonic loading velocity. Finally, I propose a method to estimate the dependence of friction on slip and slip velocity from strain gauge data during friction experiments. When conducted under realistic pressure conditions, this can provide useful constitutive laws to implement in numerical models simulating earthquakes. Eventually, the results presented in this thesis can be used in order to improve rupture scenarios, and short-term earthquake forecast.

Contents

List of Tables

List of Figures

List of Abbreviations

DG Discontinuous Galerkin. 75, 107, 111, 112, 114, 115

DIC Digital Image Correlation. 168, 173, 176

dof degrees of freedom. 71, 73, 75, 111, 112, 153

ETS Episodic Tremor and Slip. 16, 17

FEM Finite Element Method. 63, 66, 71, 75, 77, 107, 111, 115, 123, 152, 154–156, 162, 164, 167, 173, 174

fps frames per seconds. 46, 161, 176

GPS Global Positioning System. 16, 82, 83, 104

LEFM Linear Elastic Fracture Mechanics. 20, 23, 66, 108

LFE Low Frequency Earthquake. 16

LVDT Linear Variable Differential Transformer. 50, 138, 139

SSE Slow Slip Event. 16, 17

VLF Very Low Frequency. 16, 17

List of Symbols

A_r	real contact area	m^2
a and b	rate and state parameters	
c	stress optic coefficient	m^2/N
$\overline{D}$	average slip	m
D_c	slip weakening distance	m
d_c	characteristic sliding distance	m
$\underline{D}$	stress-strain matrix	
E	young's modulus	Pa
E^*	effective young's modulus	Pa
E_s	radiated energy	J
f_σ	fringe value	$N\,m^{-1}$/fringe
$\vec{f}$	force vector	
G	shear modulus	Pa
G^*	effective shear modulus	Pa
Gc	critical energy release rate	$J\,m^{-2}$
G_f	gauge factor	
G_I, G_{II} an G_{III}	energy release rates	$J\,m^{-2}$
$\underline{J}$	jacobian matrix	
K_I, K_{II} an k_{III}	stress intensity factors	$Pa\,m^{0.5}$
k	spring stiffness	Pa
k_f	fault stiffness	Pa
$\underline{K}$	finite element stiffness matrix	
L_c	general critical nucleation length notation	m
L_{sc}	critical nucleation length as defined by ohnaka	m
L_b	lower critical nucleation length bound	m
L_∞	upper critical nucleation length bound	m
L_{b-a}	critical nucleation length as defined by rubin	m
M_0	seismic moment	N m
M_w	earthquake moment magnitude	
N	fringe order	
$N1$ to $N4$	shape functions	
P_{conf}	confining pressure	Pa
P_{eff}	effective pressure	Pa
Q	activation energy	$J\,mol^{-1}$
S	prestress ratio	
$\vec{u}$	displacement vector	
U_e	elastic energy	J
U_f	frictional work	J
U_k	kinematic energy	J

U_s	fracture energy	J
V_{in}	input voltage	V
V_{out}	output voltage	V
V_p	p-wave velocity	$\mathrm{m\,s^{-1}}$
V_r	rupture velocity	$\mathrm{m\,s^{-1}}$
V_{ray}	Rayleigh wave velocity	$\mathrm{m\,s^{-1}}$
V_s	s-wave velocity	$\mathrm{m\,s^{-1}}$
W	work by external forces	J
X_e	breakdown zone length	m
$\Delta\tau$	stress drop	Pa
$\Delta\epsilon$	strain drop	
Δ	relative retardation	
η_{ef}	seismic efficiency	
$\underline{\epsilon}$	strain tensor	
ϵ	strain	
ϵ_d	strain measured at 45° to the fault plane	
$\dot{\epsilon}$	strain rate	$\mathrm{s^{-1}}$
γ	specific surface energy	$\mathrm{J\,m^{-2}}$
γ_{xy}	shear strain (engineering convention)	
λ	Lamé parameter	Pa
λ_w	wavelength	m
μ_0	initial friction	
μ_p	peak friction	
μ_r	residual friction	
ν	Poisson's ratio	
∇	Del operator	
ω_c	corner frequency	Hz
ρ	density	$\mathrm{Kg\,m^{-3}}$
$\underline{\sigma}$	stress tensor	
σ_n	normal stress	Pa
σ_{diff}	differential stress	Pa
σ_∞	remote stress	Pa
τ	shear stress	Pa
$\dot{\tau}$	shear stress rate	$\mathrm{Pa\,s^{-1}}$
τ_{max}	maximum shear stress	Pa
τ_0	initial stress	Pa
τ_p	peak stress	Pa
τ_r	residual stress	Pa
θ	state variable	s
ζ and η	finite element local coordinates	

Acknowledgements

I met a lot of people during the PhD time a Durham, many of which contributed to make good memories, and eventually to hand in this thesis. I am very grateful to all of them, including the ones I might forget in the following lines.

A special thanks goes to my supervisor Stefan Nielsen who has been of great help, for the theoretical parts, numerical techniques (we could share our love for python), in the laboratory... On a personal note he is also a great person, and it was a pleasure to work, or even go surfing (on a Friday morning) and play trumpet with him. I thank my co-supervisors: Simon Mathias who speaks Matlab better than I speak English, and Stefano Giani who was always in a good mood and available when I struggled with Finite Element models. A big thanks to Rob for helping me with this too and spending so much time discussing and trying to make me understand the mathematics behind the methods while you were very busy on your side. I thank all the people from the lab: Chris for being of great company while "playing" with the strain gauges, Giacomo which I always appreciate much (maybe except after few hours of conversation about microstructures), and for the nice diners, Fadul for all the help in the lab and for making me run even more during the football games, Telemaco for your enthusiasm when breaking rocks, Nic for being almost like a supervisor, and always helpful in the lab.

I also want to thank all the good friends that I made during my time here, as I might forget the time spent in front of a computer, but not the good moments spent with those people: Nico for being a great flatmate, for the nice demonstrating sessions, the trips, drinks shared, I'm sure we'll have a few more of these in the future, Ilaria for cheering everyone up in spite of being 'so tired', Alex for the nice Saturday morning coffees and walks, and for teaching me unicycling, a skill I didn't imagine I would get in Durham, Kate for always being of great company for any outdoor activity. In these Brexit days I also want to thank groups of people by nationalities: the Greeks, Dimitrios for your jokes, Nikos for the guitar sessions and basketball games, Pavlos for sharing the suspense when waiting for the reviews, Dimitris who was missed in the Department, and 'speaking of which' I still have to go and visit in London. I thank all the annoying French people of course: not only we could win a volleyball tournament together but we also shared a lot of laughter. In details there is Matthieu, a really nice and funny guy, and the only one I know who hurt himself with a potato, Guillaume always complaining but yet of great and funny company, Thomas for sharing the nostalgia of Grenoble, Eloïse for having survived in a castle without insulation in the North of England. I will also remember all my Chilean and Mexican friends who kept me practising Spanish: Fifi for your cool surfing attitude, Emmanuel for almost getting us in a fight during a third farewell party, Javiera Consuelo and Nico for the nice barbecues with Pisco. I also thank my bay colleagues who were in the same writing situation during the last months: Olly, Sean, Liz, Chris... Ayo as well for the time we spent together struggling with formulas and coding, Helena for helping me demonstrating mathematics, and Jack for the great time we had in MEP, and during the memorable week in New-Orleans. I hope to see you all again at some point (including the people I got to know toward the end like CJ, Marie-Anne, Stella and others)!

I also owe a bit this thesis to my parents, for their support from the start of my studies. It was perfect to have them at a reasonable flying distance to spend occasional holidays in France and for them to come and do some hiking together (and practice some English basics). I enjoyed much my sisters' visits too and wish we can have more precious family time together in the next years.

I thank you Mara for the love and the support you gave me since I know you. From the time I was writing my master's thesis in Auckland, and during the months together in Durham town, whatever happened at work didn't matter as long as I was with you in the evenings. Although I wish we had more of these moments I am very grateful for the beautiful time we had. A little word too for my good friend Nico Torino who somehow ended up in the North before I arrived there myself and with whom we could share our occasional bad mood, but also many fun moments at Ustinov or in Glasgow.

A last thought goes to Ludmila Adam and Francois Renard who wrote the cover letters and made this experience possible, and to Richard Walters and David Marsan who read thoroughly this manuscript, and created a very nice discussion during the viva, which was a perfect conclusion for these three years. In spite of complaining a lot about the UK and the PhD I really enjoyed it overall, learned a lot, and I would do it again.

"The universe is not required to be in perfect harmony with human ambition."

Carl Sagan

Overview of the thesis

Understanding the origin of earthquakes is a major challenge in a context of growing urban areas. Energy generated by plate tectonics may be released slowly along faults by creeping-like phenomena, or more suddenly, generating strong and sometimes very destructive ground motion. While seismology provides vital observations which can be used to infer the physical processes leading to a large rupture in a very complex natural system, controlled laboratory experiments and numerical models are needed in order to better understand the relative importance of different physical quantities in simplified earthquake models.

The simplified fault model used in laboratory experiments often consists of a planar contact interface, separating rectangular blocks composed of elastic materials. By applying forces at the blocks' edges, we are able to store elastic energy in the system, similarly to what happens during tectonic loading. Under applied normal load, the contact interface resists shear stress by friction, until the so-called fault strength is reached. At this point, some relative slip occurs between the two blocks. At the nucleation stage, the slip is generally confined to a small patch which is often referred to as a crack. Inside the crack, frictional resistance decreases with slip and slip velocity, therefore driving its growth. Although the crack growth is initially slow and controlled by the applied forces, it may accelerate and become unstable if the energy released at its tips is sufficient. The size of the crack before acceleration is called the critical nucleation length L_c. It is crucial to understand which system variables control L_c as this is directly linked to the stability of a fault. Understanding the stability of faults, aseismic versus seismic behaviour, and in particular the critical nucleation length dependence on the applied shear loading rate is the main focus in this thesis.

In chapter 1, a general introduction on natural earthquakes is given in order to highlight the complexity of such events. This is needed in order to understand

how meaningful laboratory, numerical and theoretical studies described later are with regard to natural systems. I also give some background necessary in order to understand fracture mechanics, wave propagation, friction laws, and the relation with natural faults. The basic equations of stress and strain are given so that the reader can familiarise themselves with the symbology used in the manuscript. This theory underpins the wave equation and the 2-Dimensional approximation used in numerical models (chapter 4), the static crack stress field equations used to benchmark static numerical models, and the dynamic crack equations used to invert photoelastic fringes in appendix A. The goal of the chapter is also to give an overview of previous laboratory and numerical nucleation studies, and to introduce the concept of nucleation length L_c. I finally discuss briefly the types of friction laws used in numerical models and in stability analysis theory, in order to explain how L_c may be estimated.

The numerical methods, laboratory setups and materials used are presented in chapter 2. Even though parts of this chapter are repeated in other result chapters, this is all gathered here for clarity. I first introduce the different deformation apparatuses used: a biaxial press with polycarbonate plates, and a triaxial pressure vessel adapted to study rock friction under high confining pressure conditions. I show how a rupture propagation can be tracked and quantified using photoelaticity with a high-speed camera, and/or using strain gauges with a high frequency acquisition system. A large part of this chapter is also dedicated to introduce numerical models, and in particular explaining the Finite Element method in detail. Although most of the information contained in this section can already be found in the literature, this is not always very clear for non-mathematicians. Therefore, a lot of details have been written in order for a new PhD student to use it for building a simple elastic model from scratch for instance. Moreover, it should make it easier for someone who would like to keep working on the static and dynamic finite element python codes developed in this thesis, which can be found on Github (see appendix C).

The results from chapter 3 constitute the most significant piece of work of the thesis. The experiments presented in this chapter aim at tracking directly the rupture front of several shear ruptures under varying applied shear loading rates,

thanks to photoelasticity combined with a high-speed camera. As suggested by previous studies on laboratory earthquake nucleation, the loading rate often neglected in theoretical studies influences the size L_c. This study, published in the Journal of Geophysical Research: Solid Earth (Guerin-Marthe et al., 2018), evidences that indeed L_c decreases at higher loading rates, but also that it affects the nucleation position of the localized slipping patch. Under a slow applied loading rate, the nucleation position initiates more or less randomly along the interface, while it localizes consistently on the same spots at higher rates. I discuss these results using rate-and-state friction laws, and show their implications for natural earthquakes and for the seismicity of subduction zones.

In chapter 4, following the observations of localized nucleations at high loading rates, I build a static finite element model of 2D elasticity in order to infer the initial stress distribution in the biaxial experiments. Using different loading configurations in the model by changing the boundary conditions, I am able to simulate the photoelastic fringes it would generate, and match the simulated fringe pattern with the observed pattern in the experiments. This evidences two areas of high coulomb stress where the rupture initiates, and is published as an appendix in Guerin-Marthe et al., 2018. A finite difference code based on Virieux and Madariaga, 1982 is also written in order to model the dynamic propagation. Some features observed in the strain gauge signals are well explained by the numerical models, such as the shear stress evolution during supershear ruptures. I also use it to validate and discuss the method used in chapter 3 to estimate the friction dependence on slip and slip velocity.

After having explored the nucleation of shear ruptures along simulated faults under relatively low normal stress, using polycarbonate plates, and having simulated the experiments with numerical models, chapter 5 aims at exploring more realistic nucleation conditions. I use Westerly Granite blocks under a direct shear configuration, applying confining pressures up to 100 MPa in a pressure vessel, corresponding to the Earth's upper crust. A previously built setup has been successfully adapted in order to enable up to 6 strain gauges to be fixed along a 4 cm long simulated interface. I show that for long healing times, increasing the loading rate tends to promote instability, while instability is inhibited for shorter

healing times. The results are interpreted using rate-and-state laws, complementing the discussion of chapter 3.

In chapter 6, the static finite element model is used, as in chapter 4, in order to understand the loading conditions of the triaxial experiments in chapter 5 and to discuss their effect on the low apparent friction measured, and the difference with strain gauge signals in the experiments of chapter 5. The second part of the chapter uses the finite difference code and is used to verify how accurately one can determine friction laws of granite under upper-crustal pressure conditions, given the loading configuration used in chapter 5.

Chapter 7 summarizes the work done during the PhD, and the main results presented. It also gives an overview of the additional methods tested in the appendices, and suggests new research ideas following the thesis.

Chapter 1

Introduction

1.1 Rupture at the scale of tectonic plates

1.1.1 Global seismicity

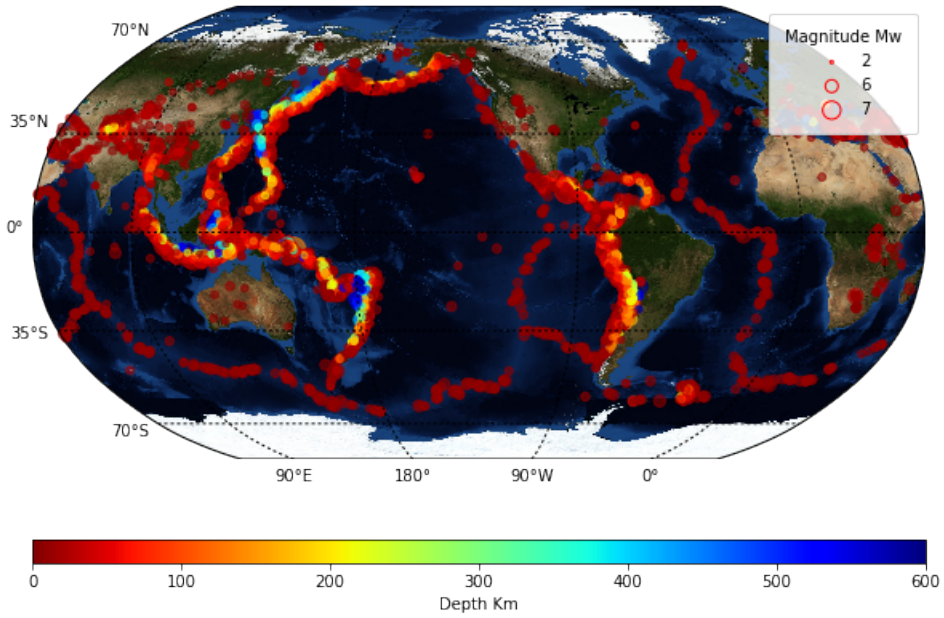

FIGURE 1.1: Global seismicity map presenting the 10000 biggest events of the year 2017, up to 600 km depth (data taken from the iris website, and plotted with the script given in appendix C)

.

Earthquakes represent the most disastrous natural hazard in term of economic damage and death toll, at least from 2000 until now (www.statista.com). They have fascinated, confused and scared people for centuries and still today. Once believed to be caused by explosions or exhalations of gases trapped underground at the Greek time with Aristotle, fourth century BC (Udías et al., 2014), there were significant advances toward a better understanding of the source of earthquakes during the last century.

By looking at the global seismicity pattern (fig. 1.1), we observe that most earthquakes occur along well-defined segments that highlight the tectonic plate boundaries (Kanamori and Brodsky, 2004), in which case they are refered to as interplate earthquakes, as opposed to intraplate earthquakes. By looking at the depth distribution of events along the so-called Pacific ring of fire, one can also notice the Benioff–Wadati plane evidencing the presence of subduction zones along which the biggest earthquakes occur, including tsunamigenic ones.

There are fewer large earthquakes compared to small ones; the number of events $N(M_w)$ of magnitude $\geq M_w$ follows the Gutenberg-Richter law:

$$\log N(M_w) = a - bM_w \tag{1.1}$$

Where a is linked to the seismicity rate, and the b value corresponds to the ratio between large and small events. It has been shown that in some cases b decreased prior to large earthquakes, meaning an relative increase of larger earthquakes during the precursory phase (Imoto, 1991). The Gutenberg-Richter law also holds for small earthquakes even though they are not necessarily all detected below the magnitude of completeness $M_w \approx 5$. For large ones (around $M_w = 8$, see fig 1.2), there is a statistical bias if the period considered is too short (it is also possible that the occurrence probability of large earthquakes does not fit this law).

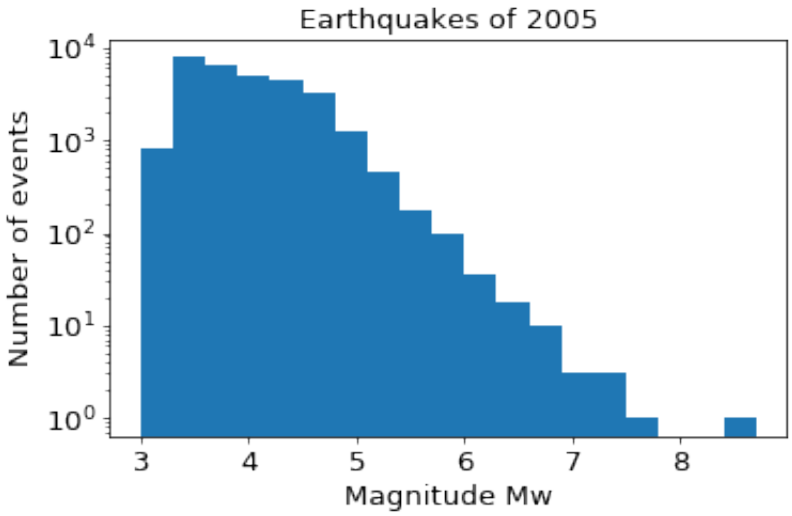

FIGURE 1.2: Example of Gutenberg-Richter relationship for the $M_w > 3$ of 2005 using the data from the iris earthquake catalogue

1.1.2 Architecture of a fault

The faults along which ruptures propagate exhibit a complex geometry: exposed fault traces and geological observations show that they are irregular structures comprising bends and jogs, and have a self-affine nature (Candela et al., 2012). Ruptures are also affected by a complex surrounding medium composed of different materials (Chester et al., 1993), partially altered by previous events (Bhat et al., 2007; Biegel et al., 2008) (see figure 1.3). In order to simplify those geometrical complexities, the concept of a fault plane is used, based on the fact that cumulative slip tends to flatten the surface of mature faults. The area of rupture increases with magnitude. The shape of the fault can be characterized by the aspect ratio L/W (length over width) (Udías et al., 2014). For small earthquakes ($L < 20$ km) the shape can be approximated by a circle or a square, with $L/W \approx 1$. Brittle fracture extent is limited by the brittle-ductile transition in the crust, situated around 15 to 20 km in depth. For large strike-slip earthquakes, the shape becomes rectangular or elliptical, with an aspect ratio that can be greater than 10, with the exception of large earthquakes in subduction zones, where L can be longer than 400 km, and W around 100 km (Udías et al., 2014).

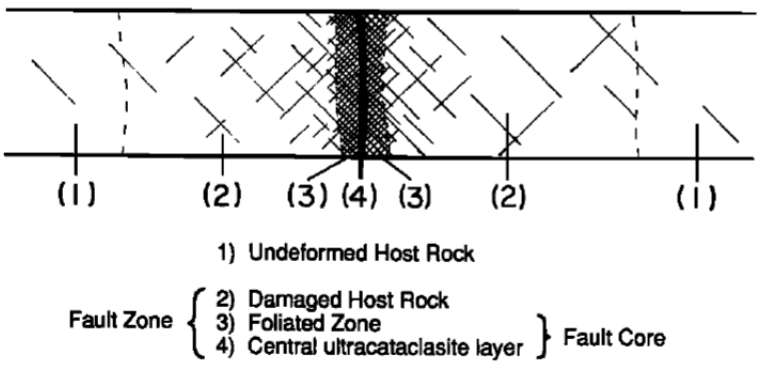

FIGURE 1.3: Fault architecture after Chester et al., 1993. (1) Intact host rock (2) Damage zone, fractured, 10 m to 100 m wide (3) Gouge, 1 m to 10s m wide (4) Ultracataclasite shear zone, usually clay rich, 10s mm to 100s mm wide (5) Principal slip surface (within (4)) that can be < 1 mm.

1.1.3 Rheology of the crust

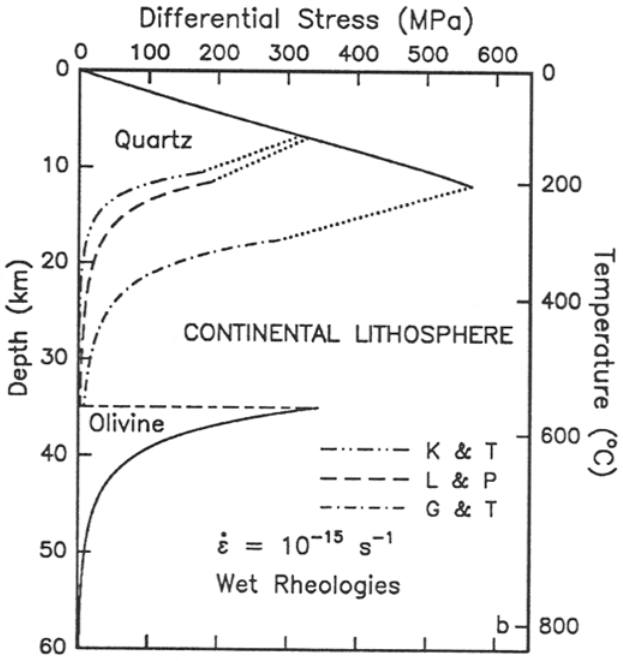

FIGURE 1.4: Lithosphere rheology (Kohlstedt et al., 1995)

On top of the geometrical complexities, the rheology of the rocks on the fault plane is also heterogeneous but in the general case follows some trend with depth due to the layered structure of the Earth (Kohlstedt et al., 1995). The upper crust

strength follows Byerlee's friction law, shown in more details later in fig. 1.23 (Byerlee, 1978), up to a depth around 10 to 15 km where a temperature threshold is reached, corresponding to the onset of Quartz plasticity ($\approx 300°C$), followed by the onset of Feldspar plasticity ($\approx 450°C$). At this point, the strength gradually decreases following a plastic flow law, depending on the thermal gradient and the strain rate $\dot{\epsilon}$. It becomes stronger again where the upper mantle is reached, in which stronger mineral such as olivine are found (see fig. 1.4).

1.1.4 Earthquake cycle

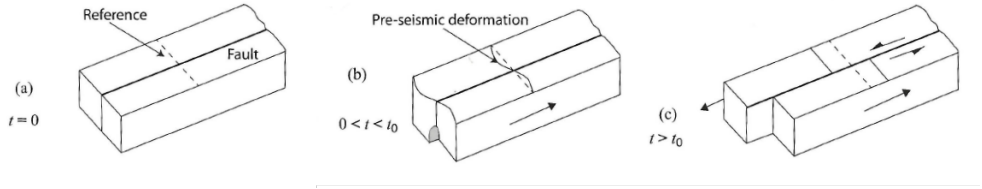

FIGURE 1.5: Illustration of elastic rebound theory of Reid, 1911, after Udías et al., 2014. a) Two reference fault segments during the interseismic period. b) Deformation due to tectonic loading. c) Final deformation after strain release by the rupture

.

A widely accepted model of earthquakes has been proposed by Reid (1911). In this model, plate motion produces deformation that localizes around the fault during the interseismic period (fig. 1.5.a-b). The local deformation leads to stress accumulation. When the stress accumulated becomes higher than the fault plane strength, the strain energy is rapidly released, producing a slip called elastic rebound during the coseismic period (fig. 1.5.c). In reality, some strain can be released before and after an earthquake triggering foreshocks and aftershocks respectively. The strain can also be released via aseismic creep or during recently discovered slow-slip events (Peng and Gomberg, 2010).

A typical timescale with depth and slip magnitude is illustrated in figure 1.6. However the amount of slip and the recurrence time (hence the length of interseismic, nucleation and postseismic periods) are variable and scale dependant (linked to the rupture asperity size). This gives rise to a strong variability of the

earthquake cycles to be expected depending on the fault considered. The scaling laws will be discussed later in section 1.1.6.

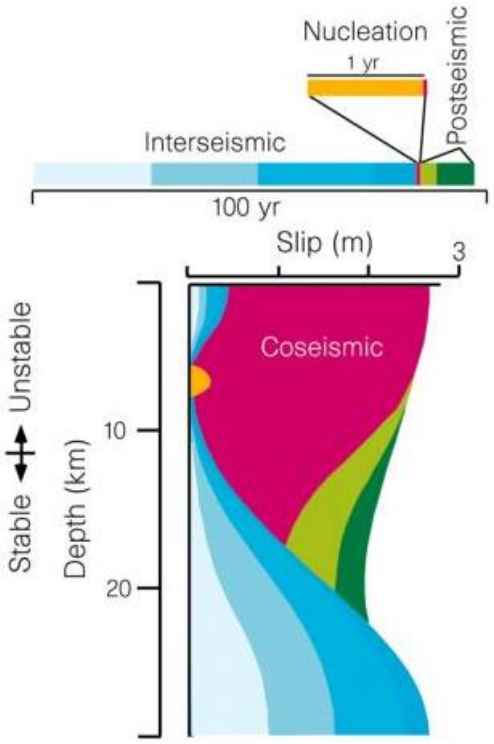

FIGURE 1.6: Illustration of a typical earthquake cycle, after Scholz, 2002

1.1.5 Point approximation of earthquake source: double-couple and beach-ball diagrams

During the coseismic period, the sudden dislocation produced by a remote earthquake source can be approximated by a point source from where a double couple generates displacements in the surrounding medium. The far-field displacements (u_r, u_θ and u_ϕ) for a point source (as illustrated fig. 1.7.a) in an homogeneous

medium can be written using polar coordinates in the form (Kanamori and Brodsky, 2004):

$$\begin{Bmatrix} u_r \\ u_\theta \\ u_\phi \end{Bmatrix} = \frac{1}{4\pi\rho r V_p^3} M_0'(t - \frac{r}{V_p}) \begin{Bmatrix} R_r(\theta,\phi) \\ 0 \\ 0 \end{Bmatrix} + \frac{1}{4\pi\rho r V_s^3} M_0'(t - \frac{r}{V_s}) \begin{Bmatrix} 0 \\ R_\theta(\theta,\phi) \\ R_\phi(\theta,\phi) \end{Bmatrix} \tag{1.2}$$

Where ρ is the density, V_p is the compressionnal wave speed, M_0 is the seismic moment, r is the radius, and t is the time. $R_r(\theta,\phi)$ (associated with the P-waves), $R_\theta(\theta,\phi)$ and $R_\phi(\theta,\phi)$ (associated with the S-waves) are radiation patterns which depend on the source geometry and the observation point (Kanamori and Brodsky, 2004). They can be written $R_r(\theta,\phi) = \sin(2\theta)\cos(\phi)\hat{r}$, $R_\theta(\theta,\phi) = \cos(2\theta)\cos(\phi)\hat{\theta}$ and $R_\phi(\theta,\phi) = -\cos(\theta)\sin(\phi)\hat{\phi}$, after Shearer, 2009.

The pressures associated with this dislocation can be visualized in the form of focal mechanism 'beach balls' with compressional and dilatational quadrants (see fig. 1.7.b). The first motion of particles in the compressional quadrant are outwards, and inwards in the dilatational quadrant. By convention, only the lower hemisphere of the focal mechanism sphere is represented on maps, from a top view, as the fastest way for the seismic waves to propagate up to a remote station is toward the interior of the Earth first before coming back up at the surface.

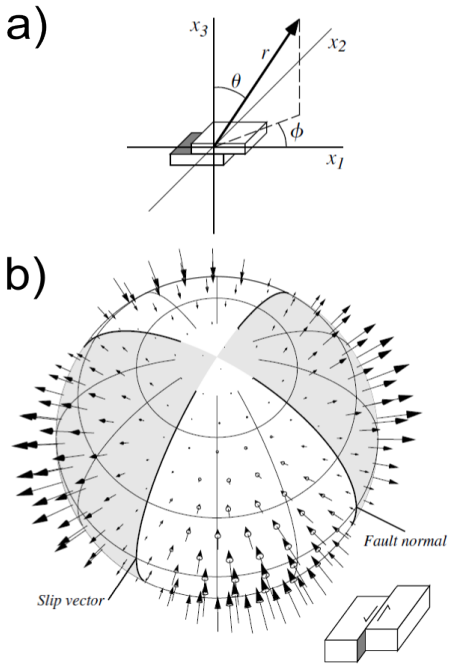

FIGURE 1.7: a) Double couple source approximation. b) Focal mechanism of earthquakes where the arrows represent the particles first motion. The compressional quadrant is shaded while the dilatational one is white. The black thick lines are the primary and auxiliary planes. They correspond to the fault plane and the plane perpendicular to it, repsectively. Figure from Shearer, 2009

1.1.6 Magnitude of earthquakes and scaling laws

Earthquake magnitude

The radiated seismic waves that propagate within the earth, and along its surface are recorded at seismic stations and used to estimate the magnitude of earthquakes. The high frequency P-waves arrive first with a low amplitude, and then come the S-waves with a higher amplitude, and lower frequency. After those body waves arrivals, very high amplitude surfaces waves are recorded: Love and then Rayleigh waves. Surface waves are dispersive which means the wave speed is frequency-dependant; the larger wavelengths are propagating faster in this case. The Rayleigh waves result from the interaction of P and S waves propagating along a surface, they have a velocity $V_{ray} \approx 0.92V_s$, where V_s is the S-wave speed. Their dispersion comes from the fact that larger wavelengths penetrate deeper in the earth and are thus sensitive to faster media. On the other hand the

Love waves are a constructive interferences of SH waves (horizontally polarized S-waves) guided in a low velocity layer (compared to the one below).

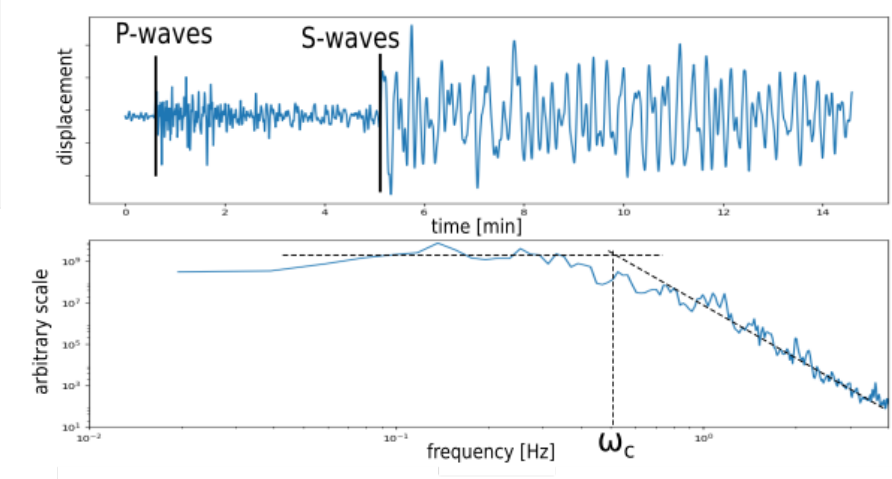

FIGURE 1.8: a) Seismic waves recorded at IU-SLBS station (Mexico) for a M_w6.2 (22-08-2018), with an epicenter off the coast of Oregon, US. b) Power spectrum of P-waves and corner frequency around 0.5 Hz. Data has been dowloaded from Iris and then processed to produced the power spectrum

The magnitude can be estimated using the body wave spectrum, up to $M_w \approx 6$, and using the surface waves amplitude for larger events. An example of waves recorded at IU-SLBS station (Mexico) for a M_w6.2 that happened on the 22^{nd} of August 2018, off the coast of Oregon, US is shown fig. 1.8.a. Plotting the amplitude spectrum in a log-log diagram, we can measure the so-called corner frequency ω_c of the P-waves. The smaller the corner frequency the larger the event. Indeed, the duration of the slip pulse generated during an earthquake is linked to the size of the rupture $L \approx T_r V_r$, where T_r is the rupture duration and V_r is the rupture velocity ($\approx$ constant). Therefore, because L is larger for big earthquakes, the duration of the slip pulse is also larger, radiating larger wavelengths, and thus lower frequencies. The scaling between ω_c and M_0 is illustrated in fig. 1.9. Using this scaling relationship and estimating ω_c thus enables to estimate M_w (fig. 1.8.b)

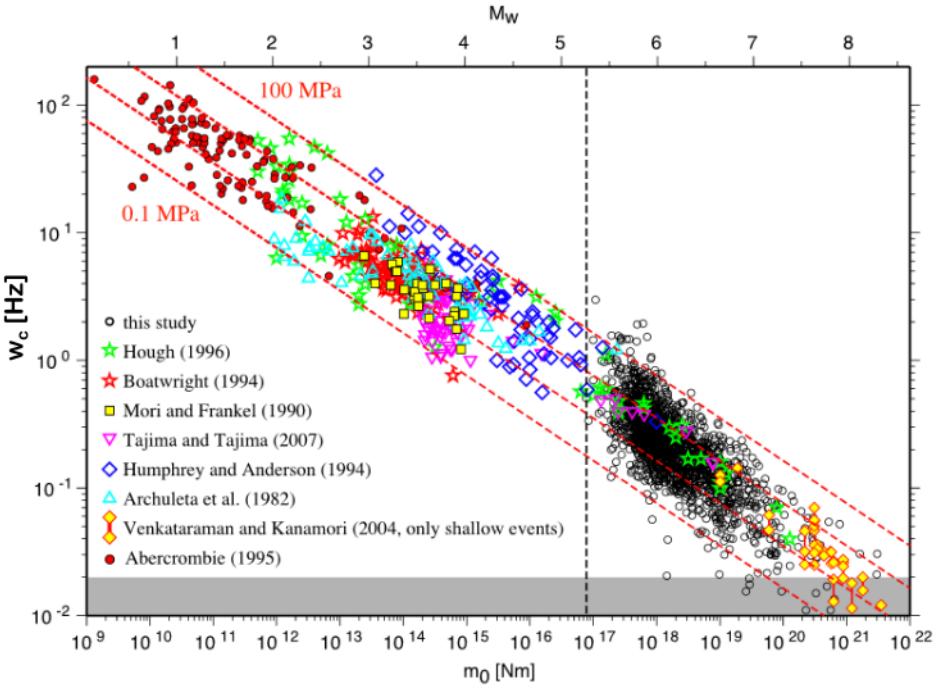

FIGURE 1.9: Relation between the corner frequency ω_c and magnitude M_w after Allmann and Shearer, 2009

Although seismic waves can provide a fast estimate of the magnitude M_w, useful for early-warning systems for instance, M_w is more accurately calculated based on the properties of the earthquake source: the shear modulus G and the average slip $\overline{D}$ over the slip area S. It uses the seismic moment $M_0 = G\overline{D}S$ in [N.m]. The moment magnitude is then calculated using:

$$M_w = \frac{2}{3}(\log_{10}(M_0) - 9.1) \tag{1.3}$$

Relations between seismic moment, slip surface and stress drop of earthquakes

The stress drop Δ_τ during an earthquake is almost always between 10^5 and 10^8 Pa, regardless of M_w (fig.1.9). It is linked to the strain drop Δ_ϵ and the shear modulus G by $\Delta_\tau = G\Delta_\epsilon \approx CG\frac{\overline{D}}{\tilde{L}}$, where $\tilde{L} \equiv \sqrt{S}$ is a characteristic length of the fault, and C is a geometrical constant. $C = 7\pi/16$ for a circular crack, and $C = 2\pi$ in the case of a fault length L to fault width W ratio $L/W \gg 1$. This implies that $M_0 \propto S^{3/2}$ as $\Delta_\tau \approx CM_0/S^{3/2}$ and is confirmed by the data in fig. 1.10.

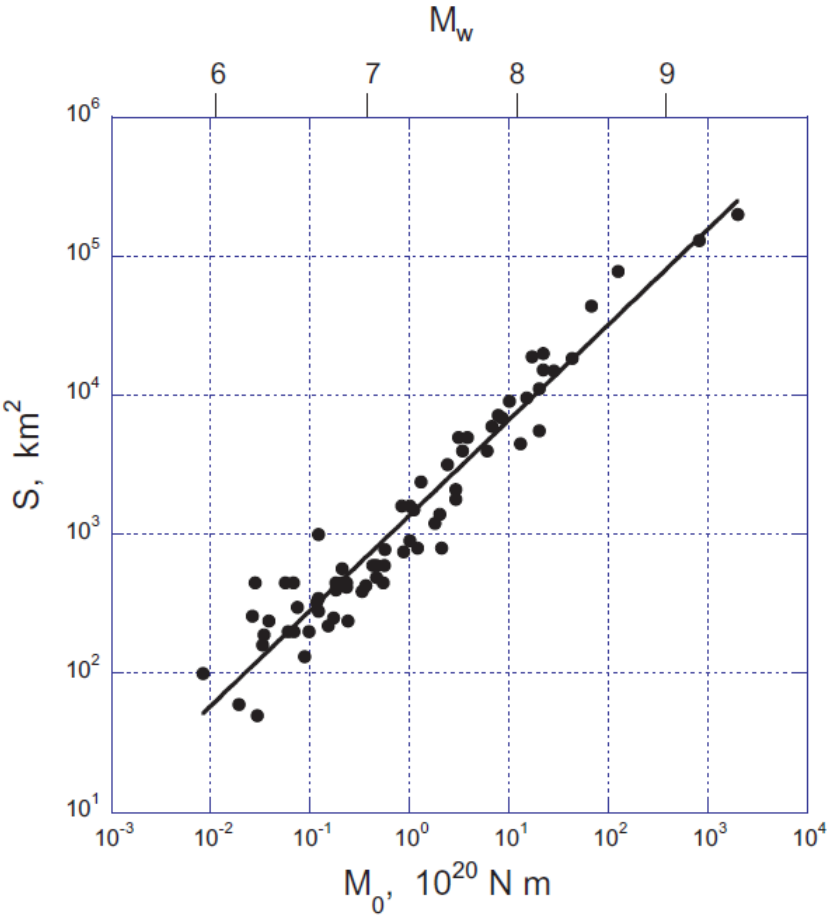

FIGURE 1.10: Scaling between the seismic moment M_0 and the slip surface S showing $M_0 \propto S^{3/2}$, after Kanamori and Brodsky, 2004

1.1.7 Nucleation models and seismicity patterns in subduction zones

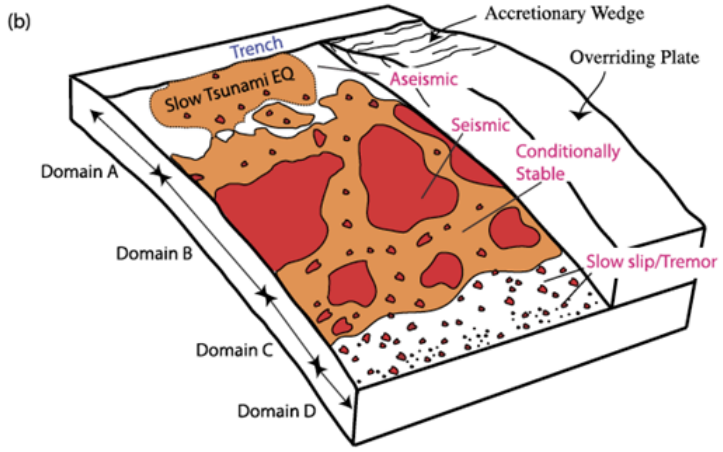

FIGURE 1.11: Seismicity of subduction zones (Lay et al., 2012)

Understanding the seismicity of subduction zones is of crucial importance as these complex physical systems host the largest megathrust earthquakes. Recently, significant advance in technology enabled the detection of a whole range of seismic signals, with the deployment of instruments such as strainmeters, tiltmeters, high-sensitivity seismometers, accelerometers, and Global Positioning System (GPS) stations. Those signals with characteristics that may differ from classical radiations emitted during earthquakes are referred to as Episodic Tremor and Slip (ETS) and include Low Frequency Earthquake (LFE), Very Low Frequency (VLF) earthquakes and Slow Slip Events (SSEs). The characteristic period of those events is shown in figure 1.12. It ranges from 0.1 s for LFEs to several months for SSEs.

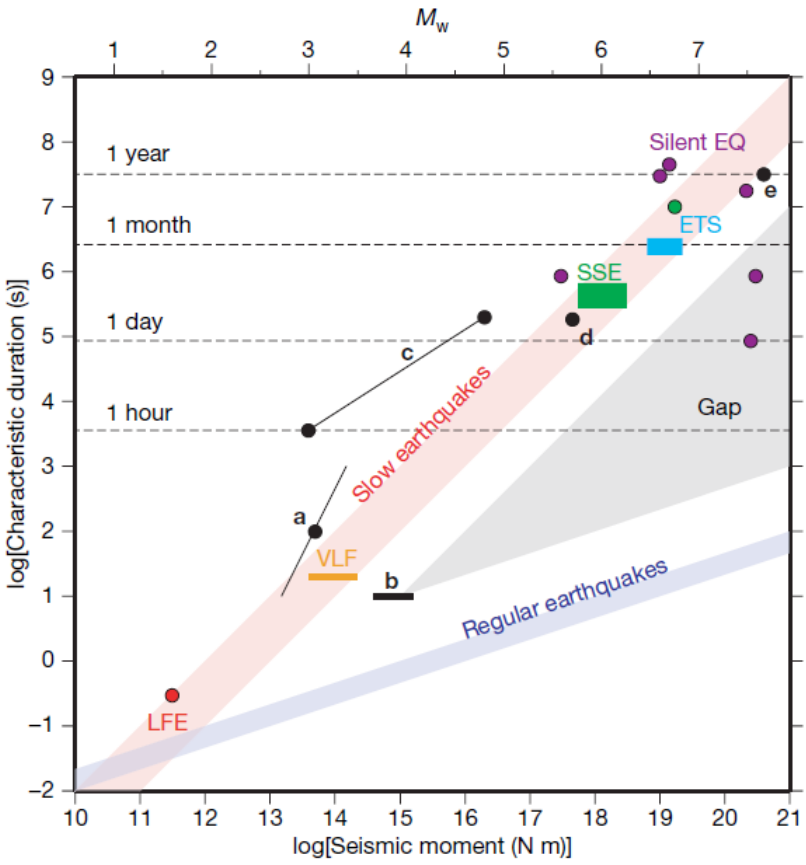

FIGURE 1.12: Timescale of low-frequency events after Ide et al., 2007. The ETS events plotted are recorded in the Cascadia subduction zone.

Taking the example of Japan (although the picture is complicated), it seems that the subduction zone can be divided into four main domains (fig.1.11; Ide et al., 2007, Lay et al., 2012). The domain B where the megathrust earthquakes occur is limited at the top by a domain A, mainly characterized by stable sliding but where tsunamigenic rupture can propagate and where shallow VLF and tremors can be found at the transition between domains A and B. Below, there is a conditionally stable portion (domain C) where long term SSEs occur. And the deeper part, domain D, is characterised by deep tremor activity, VLF and short term SSEs. All those events are inter-related in a non-trivial way, for example it seems that the continuous tremor activity of domain D is triggered by the propagation of SSEs (Frank et al., 2016).

This kind of signals are also observable in other places such as Chile (Ruiz

et al., 2014; Ruiz et al., 2017), Mexico (Radiguet et al., 2016) or Cascadia (see science of slow earthquakes website). But although the general pattern for most of the subduction zones is similar, and includes the seismogenic zone, surrounded by conditionally stable areas from where slow slip is likely to occur at the rheological transitions, there are few differences depending on the place considered (Schwartz and Rokosky, 2007). Not all of these signals are observed everywhere, and it might be due to the fact that the instrumentation is not as developed everywhere as in Japan, but also that the seismicity itself is not necessarily the same. For instance, while slow slip is observed almost everywhere along the Pacific ring of fire, tremors are mainly observed in Japan, Cascadia, and Costa Rica, and are well correlated to slow slip only in Cascadia and in the South of Japan (Schwartz and Rokosky, 2007). Slow slip can also be observed in continental settings such as the San Andreas fault (Rousset et al., 2019), or the North Anatolian fault (Rousset et al., 2016). In San Andreas, a correlation between slow slip and tremors is also observed (Schwartz and Rokosky, 2007).

In order for a large earthquake to propagate, an initial patch of domain B needs to reach instability (see fig. 1.11). This will happen when the tectonic loading brings the asperity close to its strength. The loading process can be accentuated by surrounding stress perturbations, including foreshocks and pre-slip around the asperity during the precursory phase few days to few months before the main rupture (see nucleation model of Socquet et al., 2017 for the M_w8.2 Iquique earthquake in 2014). Once the initial patch breaks, in order to propagate and become a megathrust earthquake, the stress drop inside the nucleation zone needs to be large enough so that the energy that is released is sufficient to break the surrounding asperities, and propagate through stable areas that act as energy sinks. The available energy depends on the strength of the interface that is encountered, which can be unusually weak for certain rock types like serpentinite or clays. Weakening mechanisms such as thermal pressurisation or flash heating can also significantly lower the friction during dynamic rupture propagation (Rice, 2006).

Weather or not an asperity of radius r will initially break and radiate seismic waves is linked to the questions of whether there is a critical nucleation length L_c

for the asperity, what controls it, and under what conditions $L_c < r$, in which case an instability is possible. The question of will it propagate and when will it stop are linked to the dynamic frictional evolution of the interface; at which point the energy released is not sufficient anymore for the rupture to overcome the friction and propagate further.

What controls the nucleation length size L_c and how dynamic friction evolves during rupture are the main motivations for this study, and are tackled by using laboratory analogues for earthquake rupture, and numerical models. In order to understand the small scale physics and the equations behind the models, I introduce in the next few sections the main equations used later in the thesis.

1.2 Mathematical treatment of earthquake source

Large scale wave propagation in the Earth is not investigated in this thesis. I look at a smaller scale, at the source mechanisms of earthquakes, and dynamic rupture propagation. In this section the concept of linear elasticity which constitutes a basis for Linear Elastic Fracture Mechanics (LEFM) is introduced, giving the theoretical stress field around a crack tip, and an energy based criterion for fracture propagation. Linear elasticity is also used to derive the wave equation, an essential ingredient of numerical models and theoretical studies in order to explain rupture dynamics.

1.2.1 Hooke's law: stress and strain relationships

We start by giving the relations between displacements, deformations and stresses in an elastic medium.

In a 3D elastic medium, the stress and strain tensors $\underline{\sigma}$ and $\underline{\epsilon}$ are symmetric ($\epsilon_{ij} = \epsilon_{ji}$ and $\sigma_{ij} = \sigma_{ji}$), and defined with their 9 components each by:

$$\underline{\sigma} = \begin{bmatrix} \sigma_{xx} & \tau_{xy} & \tau_{xz} \\ \tau_{yx} & \sigma_{yy} & \tau_{yz} \\ \tau_{zx} & \tau_{zy} & \sigma_{zz} \end{bmatrix} = \begin{bmatrix} \sigma_{11} & \sigma_{12} & \sigma_{13} \\ \sigma_{21} & \sigma_{22} & \sigma_{23} \\ \sigma_{31} & \sigma_{32} & \sigma_{33} \end{bmatrix} \qquad \underline{\epsilon} = \begin{bmatrix} \epsilon_{xx} & \epsilon_{xy} & \epsilon_{xz} \\ \epsilon_{yx} & \epsilon_{yy} & \epsilon_{yz} \\ \epsilon_{zx} & \epsilon_{zy} & \epsilon_{zz} \end{bmatrix}$$

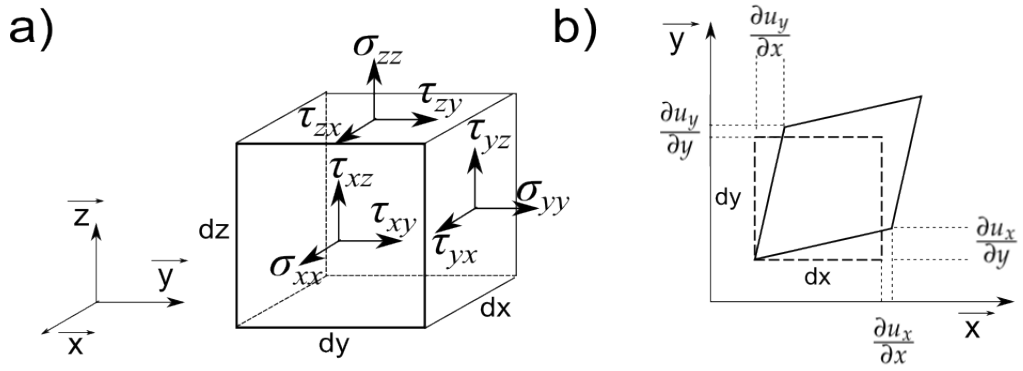

FIGURE 1.13: a) The stress tensor components. b) Infinitesimal deformations in 2D

.

The strains are linked to the spatial derivatives of the displacement field $\vec{u} = \begin{Bmatrix} u_x & u_y & u_z \end{Bmatrix}^T$ (see fig 1.13.b for an illustration in 2D):

$$\begin{aligned} \underline{\epsilon} &= \frac{1}{2}\left[\nabla\vec{u} + (\nabla\vec{u})^T\right] \\ &= \begin{bmatrix} \frac{\partial u_x}{\partial x} & \frac{1}{2}(\frac{\partial u_x}{\partial y} + \frac{\partial u_y}{\partial x}) & \frac{1}{2}(\frac{\partial u_x}{\partial z} + \frac{\partial u_z}{\partial x}) \\ \frac{1}{2}(\frac{\partial u_x}{\partial y} + \frac{\partial u_y}{\partial x}) & \frac{\partial u_y}{\partial y} & \frac{1}{2}(\frac{\partial u_y}{\partial z} + \frac{\partial u_z}{\partial y}) \\ \frac{1}{2}(\frac{\partial u_x}{\partial z} + \frac{\partial u_z}{\partial x}) & \frac{1}{2}(\frac{\partial u_y}{\partial z} + \frac{\partial u_z}{\partial y}) & \frac{\partial u_z}{\partial z} \end{bmatrix} \end{aligned} \tag{1.4}$$

In the general case, the stress tensor can be expressed as a function of the displacements as:

$$\sigma_{ij} = C_{ijkl} u_{k,l} \qquad where \qquad u_{k,l} \equiv \frac{\partial u_k}{\partial l} \tag{1.5}$$

However, in the case of an isotropic elastic medium, the 81 components of the tensor of elastic coefficients C_{ijkl} can be simplified to two independent components G and λ, the Lamé parameters. The stress tensor is then found using Hooke's law:

$$\begin{aligned} \underline{\sigma} &= \lambda \mathrm{tr}(\underline{\epsilon}) I + 2G\underline{\epsilon} \\ &= \lambda \begin{bmatrix} \frac{\partial u_x}{\partial x} + \frac{\partial u_y}{\partial y} + \frac{\partial u_z}{\partial z} & 0 & 0 \\ 0 & \frac{\partial u_x}{\partial x} + \frac{\partial u_y}{\partial y} + \frac{\partial u_z}{\partial z} & 0 \\ 0 & 0 & \frac{\partial u_x}{\partial x} + \frac{\partial u_y}{\partial y} + \frac{\partial u_z}{\partial z} \end{bmatrix} \\ &+ G \begin{bmatrix} 2\frac{\partial u_x}{\partial x} & (\frac{\partial u_x}{\partial y} + \frac{\partial u_y}{\partial x}) & (\frac{\partial u_x}{\partial z} + \frac{\partial u_z}{\partial x}) \\ (\frac{\partial u_x}{\partial y} + \frac{\partial u_y}{\partial x}) & 2\frac{\partial u_y}{\partial y} & (\frac{\partial u_y}{\partial z} + \frac{\partial u_z}{\partial y}) \\ (\frac{\partial u_x}{\partial z} + \frac{\partial u_z}{\partial x}) & (\frac{\partial u_y}{\partial z} + \frac{\partial u_z}{\partial y}) & 2\frac{\partial u_z}{\partial z} \end{bmatrix} \end{aligned} \tag{1.6}$$

Where the shear modulus G and the Lamé parameter λ can be expressed as a function of the Young's modulus E and the Poisson ratio ν using:

$$\lambda = \frac{E\nu}{(1+\nu)(1-2\nu)} \qquad \text{and} \qquad G = \frac{E}{2(1+\nu)} \tag{1.7}$$

Under a pressure parallel to an axis $\vec{x}$, E quantifies how much a solid can deform along $\vec{x}$. ν quantifies the ratio of deformations perpendicular and parallel to $\vec{x}$ (see fig. 1.14.a). G quantifies how much a solid deforms under an given applied shear stress (see fig. 1.14.b).

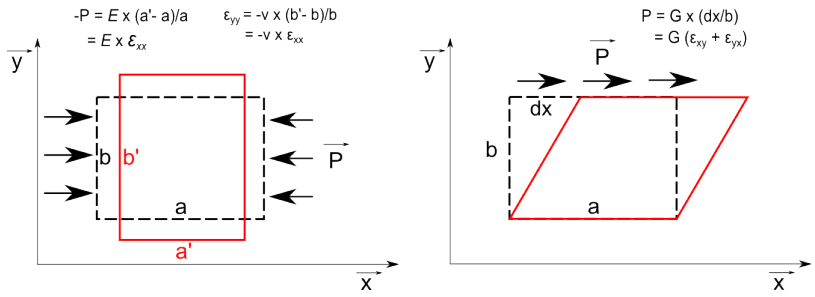

FIGURE 1.14: Elastic modulus illustration under simple deformation modes

.

As it is often useful to reduce 3D problems to 2 dimensions, especially when considering the time cost of numerical models, I present two particular cases of 2D elasticity called plane-stress and plane-strain. In the plane-strain problem, an elastic solid is considered having one dimension much longer than the two others, along $\vec{z}$ for instance. In this case $\epsilon_{zz} = \epsilon_{xz} = \epsilon_{yz} = \tau_{xz} = \tau_{yz} = 0$. In the plane-stress problem, one dimension is much shorter than the two others, and $\epsilon_{xz} = \epsilon_{yz} = \sigma_{zz} = \tau_{xz} = \tau_{yz} = 0$. The other components can have non-zero values. In both cases the simplified relation between stress and strain can be written as:

$$\begin{Bmatrix} \sigma_{xx} \\ \sigma_{yy} \\ \tau_{xy} \end{Bmatrix} = \underline{D} \begin{Bmatrix} \epsilon_{xx} \\ \epsilon_{yy} \\ 2\epsilon_{xy} \end{Bmatrix} \tag{1.8a}$$

Where for the plane-strain case,

$$\underline{D} = \underline{D_\epsilon} = \frac{E}{(1+\nu)(1-2\nu)} \times \begin{bmatrix} 1-\nu & \nu & 0 \\ \nu & 1-\nu & 0 \\ 0 & 0 & \frac{1-2\nu}{2} \end{bmatrix} \tag{1.8b}$$

and for the plane-stress case,

$$\underline{D} = \underline{D}_\sigma = \frac{E}{1-\nu^2} \times \begin{bmatrix} 1 & \nu & 0 \\ \nu & 1 & 0 \\ 0 & 0 & \frac{1-\nu}{2} \end{bmatrix} \tag{1.8c}$$

1.2.2 Fracture mechanics: static crack

In the case of fractures, treating the problem with linear elasticity means that there would exist a singularity at the crack tips, with infinite stress values. LEFM bypasses this issue by defining stress intensity factors which characterize the stress field shape in the vicinity of the crack tips. It can also be used in order to obtain an energy based criterion for rupture propagation.

Crack propagation modes and stress intensity factor

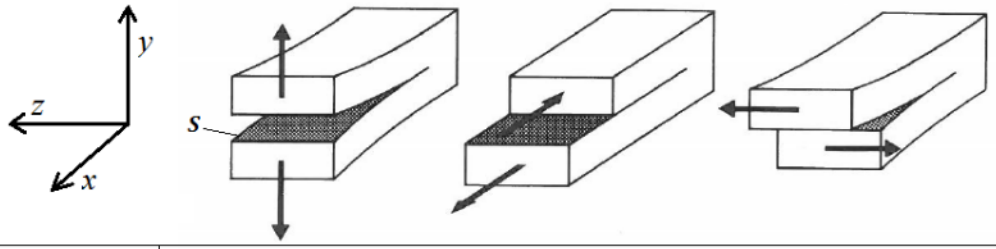

fracture modes	I tensile-opening	II in-plane shear	III anti-plane shear
stresses acting on the surface S	$\sigma_{yy} = 0$ $\tau_{yx} = 0$ $\tau_{yz} = 0$	$\tau_{yx} = \mu\sigma_{yy}$ $\tau_{yz} = 0$	$\tau_{yx} = 0$ $\tau_{yz} = \mu\sigma_{yy}$

FIGURE 1.15: Propagation modes for a crack extenting along x, and stresses σ_{yi} acting on the crack surface S. Modified after Scholz, 1998.

There are three possible opening modes for a crack or fracture, as shown in figure 1.15. Mode I crack opening, or tensile-opening corresponds to a pure traction applied in the direction perpendicular to the crack surface S. Because S is a free surface in this mode, there are no forces acting on it. Mode II or in-plane shear

corresponds to a relative slip on S parallel to the propagation direction. The traction on S is proportional to the friction coefficient μ (more details will be given about friction in section 1.4), and to the normal force σ_{yy} : $\tau_{yx} = \mu\sigma_{yy}$. Mode III or anti-plane shear (also referred as out-of-plane shear) corresponds to a relative slip on S perpendicular to the propagation direction, and $\tau_{yz} = \mu\sigma_{yy}$.

For modes I, II and III, stress intensity factors K_I, K_{II} and K_{III} are defined as:

$$K_I = \lim_{r\to 0} \sqrt{2\pi r}\sigma_{yy} \tag{1.9a}$$

$$K_{II} = \lim_{r\to 0} \sqrt{2\pi r}\tau_{xy} \tag{1.9b}$$

$$K_{III} = \lim_{r\to 0} \sqrt{2\pi r}\tau_{yz} \tag{1.9c}$$

And the energy release rates G_I, G_{II} and G_{III} are:

$$G_I = K_I^2/E^* \tag{1.10a}$$

$$G_{II} = K_{II}^2/E^* \tag{1.10b}$$

$$G_{III} = K_{III}^2(1+\nu)/E \tag{1.10c}$$

$E^* = E$ for plane stress, and $E^* = E/(1-\nu^2)$ for plane strain, and r is the distance to the crack tip. These definitions are commonly used in fracture mechanics and are a useful way to describe the stress field around crack tips and to derive failure criterion for elastic solids.

Griffith's fracture model

Griffith's model (Griffith, 1921) is an example of how a failure criterion can be derived, and consists of a simple elliptical crack of length $2a$ embedded in an elastic medium, under a uniform remote stress σ_∞. In this case the stress intensity factors are in the form $K_i = \sigma_\infty\sqrt{\pi a}$.

His study shows that under quasi-static driving stress, a crack in tensile-opening mode will grow satisfying the following energy balance:

$$\delta W - \delta U_E - 2\gamma\delta S = 0 \tag{1.11}$$

where δW is the work done by the external forces, δU_E is the change in strain energy due to the crack opening displacement, and $2\gamma\delta S = U_s$ is the fracture energy, the energy required to extend the two fracture surfaces by an element δS, given a specific surface energy γ (material property). Using equation 1.11, Griffith's study evidenced that in order for a crack to propagate, it must reach a critical energy release rate $G_c = 2\gamma$.

In the case of a shear crack, the situation is more complex (figure 1.16). The crack opens in mode III on the edge parallel to the slip direction, and in mode II on the edge perpendicular (Fialko, 2007; Kanamori and Brodsky, 2004). In a purely elastic crack model, the stress field also has a singularity at the tips. Because an infinite stress is not physically realistic, the concept of a breakdown zone at the crack edges is needed (Livne et al., 2008; Dally and Riley, 1965). This zone accounts for the fact that there must be some kind of plastic deformation in the vicinity of the crack tip, where the stress degrades gradually.

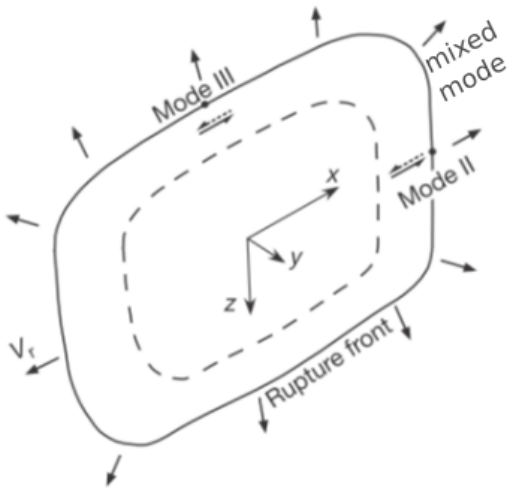

FIGURE 1.16: Sketch of a shear crack expanding, after Fialko, 2007. For a pulse-like rupture, the slipping area is confined between the solid and the dashed lines.

Stress field around a static crack tip

I give here the equations of the stress field around a crack tip as I use them later in order to attempt to invert photoelastic fringe patterns in appendix A. For a mixed-mode I and II static crack, the stresses are witten in polar coordinates (r,θ) by Freund, 1998 in the form:

$$\sigma_{ij} = \frac{K_I(t)}{\sqrt{2\pi r}}\Sigma_{ij}^{I} + \frac{K_{II}(t)}{\sqrt{2\pi r}}\Sigma_{ij}^{II} \tag{1.12}$$

except:

$$\sigma_{11} = \frac{K_I(t)}{\sqrt{2\pi r}}\Sigma_{11}^{I} + \frac{K_{II}(t)}{\sqrt{2\pi r}}\Sigma_{11}^{II} + \sigma_{0x}$$

where

$$\sigma_{0x} = \sigma_{22}^{\infty} - \sigma_{11}^{\infty}$$

which represents the difference of remote stresses (Dally and Riley, 1965).

The form of the $\Sigma_{ij}s$ for a static crack are given by equations 1.13a to 1.13f (Dally and Riley, 1965, p525):

$$\Sigma_{11}^{I} = \cos(\theta/2)(1 - \sin(\theta/2)\sin(3\theta/2)) \tag{1.13a}$$
$$\Sigma_{12}^{I} = \sin(\theta/2)\cos(\theta/2)\cos(3\theta/2) \tag{1.13b}$$
$$\Sigma_{22}^{I} = \cos(\theta/2)(1 + \sin(\theta/2)\sin(3\theta/2)) \tag{1.13c}$$
$$\Sigma_{11}^{II} = -\sin(\theta/2)(2 + \cos(\theta/2)\cos(3\theta/2)) \tag{1.13d}$$
$$\Sigma_{12}^{II} = \cos(\theta/2)(1 - \sin(\theta/2)\sin(3\theta/2)) \tag{1.13e}$$
$$\Sigma_{22}^{II} = \sin(\theta/2)\cos(\theta/2)\cos(3\theta/2) \tag{1.13f}$$

After Dally and Riley, 1965 the maximum shear stress τ_{max} can be obtained using:

$$\begin{aligned}(2\tau_{max})^2 &= (\sigma_{11}-\sigma_{22})^2 + 4\sigma_{12}^2 \\ &= \frac{1}{2\pi r}[(K_I \sin\theta + 2K_{II}\cos\theta)^2 + (K_{II}\sin\theta)^2] \\ &+ \frac{2\sigma_{0x}}{\sqrt{2\pi r}}\sin(\theta/2)[K_I \sin\theta(1+2\cos\theta) \\ &+ K_{II}(1+2\cos^2\theta+\cos\theta)] + \sigma_{0x}^2\end{aligned} \tag{1.14}$$

This expression can be used almost directly to invert the photoelastic fringes, which can be visualized as contour lines of the maximum shear stress (more details about the photoelastic method are given in section 2.2.1). I also used eq. 1.14 to verify that the equations of a dynamic crack propagating at a velocity V_r presented in the next section and the ones of a static crack are comparable when V_r tends toward 0.

1.2.3 Fracture mechanics: dynamic crack

Stress field around a propagating mixed-mode crack

For a dynamic crack, the stresses have the same general form as given in eq. 1.12. The $\Sigma_{ij}s$ are given by Freund, 1998 (p163):

$$\Sigma_{11}^{I} = \frac{1}{D}[(1+\alpha_s^2)(1+2\alpha_p^2-\alpha_s^2)\frac{\cos(\theta_p/2)}{\sqrt{\gamma_p}} - 4\alpha_s\alpha_p\frac{\cos(\theta_s/2)}{\sqrt{\gamma_s}}] \tag{1.15a}$$

$$\Sigma_{12}^{I} = \frac{2\alpha_p(1+\alpha_s^2)}{D}[\frac{\sin(\theta_p/2)}{\sqrt{\gamma_p}} - \frac{\sin(\theta_s/2)}{\sqrt{\gamma_s}}] \tag{1.15b}$$

$$\Sigma_{22}^{I} = -\frac{1}{D}[(1+\alpha_s^2)^2\frac{\cos(\theta_p/2)}{\sqrt{\gamma_p}} - 4\alpha_s\alpha_p\frac{\cos(\theta_s/2)}{\sqrt{\gamma_s}}] \tag{1.15c}$$

$$\Sigma_{11}^{II} = -\frac{2\alpha_s}{D}[(1+2\alpha_p^2-\alpha_s^2)\frac{\sin(\theta_p/2)}{\sqrt{\gamma_p}} - (1+\alpha_s^2)\frac{\sin(\theta_s/2)}{\sqrt{\gamma_s}}] \tag{1.15d}$$

$$\Sigma_{12}^{II} = \frac{1}{D}[4\alpha_s\alpha_p\frac{\cos(\theta_p/2)}{\sqrt{\gamma_p}} - (1+\alpha_s^2)^2\frac{\sin(\theta_s/2)}{\sqrt{\gamma_s}}] \tag{1.15e}$$

$$\Sigma_{22}^{II} = \frac{2\alpha_s(1+\alpha_s^2)}{D}[\frac{\sin(\theta_p/2)}{\sqrt{\gamma_p}} - \frac{\sin(\theta_s/2)}{\sqrt{\gamma_s}}] \tag{1.15f}$$

Where

$$D = 4\alpha_s\alpha_p - (1+\alpha_s^2)^2; \quad \gamma_p = \sqrt{1-\left(\frac{V_r\sin\theta}{V_p}\right)^2}; \quad \gamma_s = \sqrt{1-\left(\frac{V_r\sin\theta}{V_s}\right)^2}$$

θ and r are the angle and radius for polar coordinates. I also define the distorted angles and radius (θ_p, r_p) and (θ_s, r_s), needed when taking into account the Lorentz contractions for rupture fronts approaching P-wave and S-wave speed respectively:

$$\theta_s = \tan^{-1}(y\alpha_s/x) \qquad \theta_p = \tan^{-1}(y\alpha_p/x) \qquad \theta = \tan^{-1}(y/x)$$

$$r_s = \sqrt{x^2+(y\alpha_s)^2} \qquad r_p = \sqrt{x^2+(y\alpha_p)^2} \qquad r = \sqrt{x^2+y^2}$$

Where x and y are the Cartesian coordinates, $\alpha_p = \sqrt{1-(V_r/V_p)^2}$, and $\alpha_s = \sqrt{1-(V_r/V_s)^2}$.

Equations 1.15a-1.15f are valid for subshear ruptures at constant velocities, and are used for inversion of photoelastic fringes in Appendix A. For rupture velocities approaching 0 m/s, equations 1.13a-1.13f and 1.15a-1.15f are equivalent.

Energy balance of earthquakes

In the case of a dynamic rupture, the energy balance is more complex than equation 1.11 and includes other terms such as the frictional work U_f and the radiated energy $E_s = \delta U_k$, δU_k being the variation of kinetic energy. Although off-fault damage may not be negligible in the energy budget, it is often neglected and a simplified form of the energy balance can be written:

$$E_s = \delta U_e - U_f - U_s + \delta W \tag{1.16}$$

In eq. 1.16 the work done by the external forces δW is generally small relatively to the other terms. The latter terms can be visualized on a friction versus slip plot such as the one shown in fig. 1.17. δU_e is the change of strain energy and corresponds to the area under the green curve in fig. 1.17

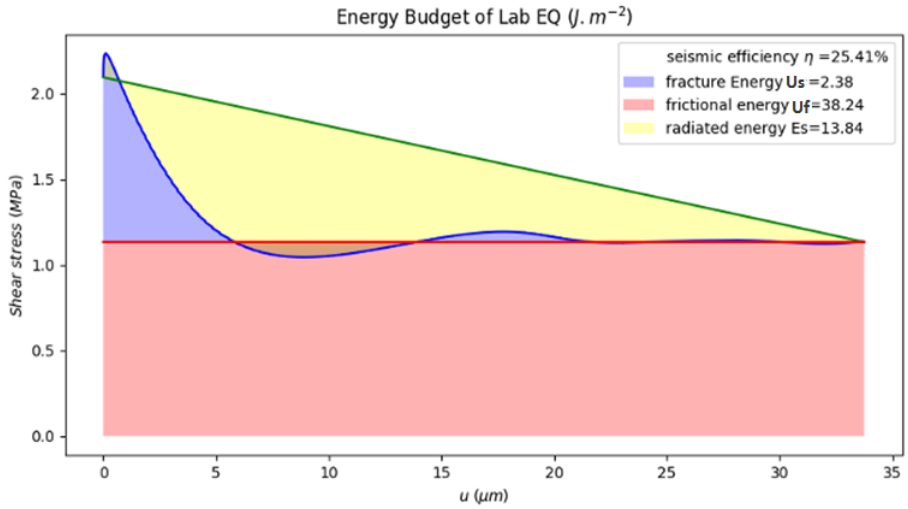

FIGURE 1.17: Friction law of laboratory earthquake (measured experimentally for polycarbonate), and energy partitioning

The amount of radiated energy can also be quantified using the seismic efficiency $\eta_{ef} = E_s/\delta U_e$. E_s is the area under the green curve (δU_e) minus the area

under the blue curve $\tau_{xy}(u)$ where u is in this case the relative displacement between the two sliding surfaces.

1.2.4 The wave equation

To understand the ground motion generated by earthquakes, and how a rupture propagates dynamically, the basic equations of particle motion in a continuous medium have to be defined.

The momentum equation is derived from Newton's second law, equating the net sum of forces ΣF acting on a system of mass m, to its acceleration a: $\Sigma F = ma$. Let's consider an infinitesimal cube of volume $dx \times dy \times dz$ as illustrated in figure 1.13.a, of density ρ. Here, ΣF is the sum of the forces $\frac{\partial \sigma_{ij}}{\partial x_j}$, acting on the surfaces, and of the internal forces F_i. If assuming ρ constant, $ma = \rho \frac{\partial^2 u_i}{\partial t^2}$. For $dx \to 0$, the momentum equation for an infinite medium becomes:

$$\rho \frac{\partial^2 u_i}{\partial t^2} = \frac{\partial \sigma_{ij}}{\partial x_j} + F_i \tag{1.17}$$

Using Hooke's law and assuming an isotropic homogeneous material (λ and G constant), 1.17 can be rewritten as (Udías et al., 2014):

$$\rho \frac{\partial^2 \vec{u}}{\partial t^2} = (\lambda + G)\nabla(\nabla.\vec{u}) + G\nabla^2\vec{u} + \vec{F} \tag{1.18}$$

Equation 1.18 is one form of the seismic wave equation. It can be rearranged to evidence the compressional (P-waves) and rotational/transverse (S-waves) components of the particle motion. Denoting the P-wave velocity $V_p = \sqrt{(\lambda + 2G)/\rho}$, the S-wave velocity $V_s = \sqrt{G/\rho}$ and using vector identities such as $\nabla \times \nabla \times \vec{u} = \nabla(\nabla.\vec{u}) - \nabla^2\vec{u}$, or $\nabla.(\nabla \times \vec{u}) = \nabla \times (\nabla\vec{u}) = 0$, equation 1.18 can be modified to:

$$\frac{\partial^2 \vec{u}}{\partial t^2} = V_p^2 \nabla(\nabla.\vec{u}) - V_s^2 \nabla \times (\nabla \times \vec{u}) + \frac{\vec{F}}{\rho} \tag{1.19}$$

From which it can be seen that the P-waves are related to the divergence of the displacements $\nabla.\vec{u}$ and the S-waves to the curl of the displacements $\nabla \times \vec{u}$.

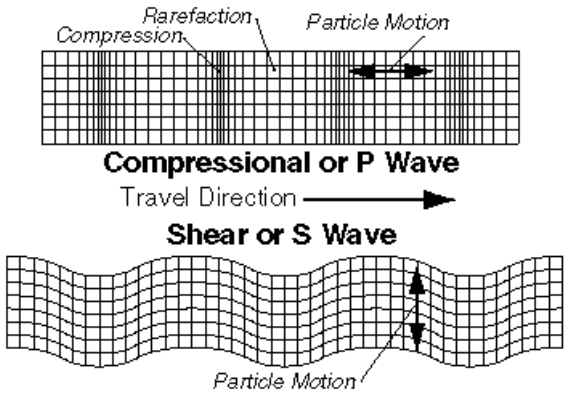

FIGURE 1.18: Particle motion associated to P and S waves (source: www.colorado.edu)

.

1.3 Laboratory studies of dynamic crack propagation

During the preparatory phase preceding earthquakes (which can last several days to several months), preslip can sometimes be observed (Ruiz et al., 2014). Laboratory models are very useful to understand the prevalence of preslip during the nucleation stage and what controls it. They can also be used to investigate how further complexities such as fault geometry or fault material properties can affect the nucleation process and the following dynamic rupture. In this section, I give an overview on the characteristics of laboratory earthquakes, and present a few results from previous studies.

1.3.1 The nucleation stage, concept of a nucleation length

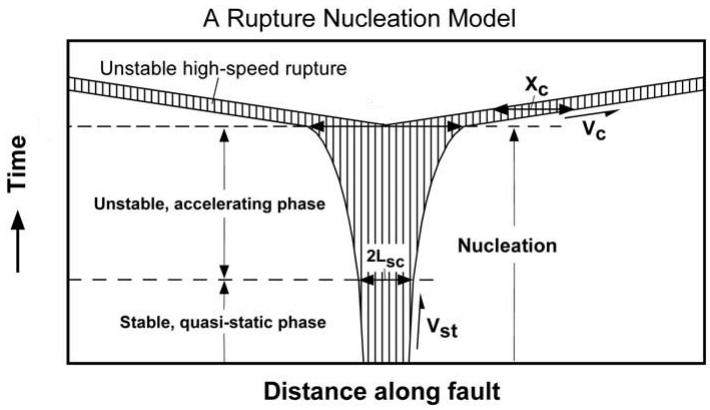

FIGURE 1.19: Nucleation model for a self-similar crack, after Ohnaka, 2003

.

Laboratory models of earthquakes show the presence of 3 main stages during the nucleation phase (see model of Ohnaka (2013), fig. 1.19).

During phase I, the rupture is stable, quasi-static, and some slow slip takes place in a localized nucleation area, which expands at a velocity controlled by the applied load (Ohnaka, 2013). This phase has been measured to last around 200 µs during the laboratory experiments of Nielsen et al., 2010 using PMMA (PolyMethyl Methacrylate) plates, and the rupture velocity was around 30 to 60 $m.s^{-1}$. Other experiments imaging the contact between PMMA plates observe a similar phase, also lasting around 200 µs (Ben-David et al., 2010). In their case, it has been interpreted to be a series of arrested rupture fronts that renew a part of the contact population.

The second phase is an acceleration of the rupture growth, controlled by inertia (the crack propagation does not depend anymore on the applied loading rate), after a critical length L_{sc} is reached (Ben-David et al., 2010). This length L_{sc} depends on the applied loading rate, and on the roughness of the surface (Ohnaka, 2003).

Phase III is the dynamic rupture where the rupture front tends to its limiting velocity, quasi-stable, sub-Rayleigh ($V_r < V_{ray} \approx 0.92V_s$, where V_{ray} is the Rayleigh wave speed), or possibly switches to supershear ($V_r > V_s$), depending on the loading conditions.

Understanding the scaling of the nucleation length (generally called L_c) of a slipping patch is critical as the observed pre-slip in nature is a possible precursory signal of real earthquakes (Tape et al., 2018). Using an energy criterion similar to the one of Griffith, 1921, Andrews, 1976 has shown that L_c can be estimated as:

$$L_c = \frac{2G^*}{\pi} \frac{(\tau_p - \tau_r)D_c}{(\tau_0 - \tau_r)^2} \tag{1.20}$$

where $G^* = G/(1-\nu)$ is the effective shear modulus, ν is the Poisson's coefficient, and τ_0, τ_p and τ_r are the initial, peak and residual stresses, respectively (see figure 1.25).

Controls on rupture velocity

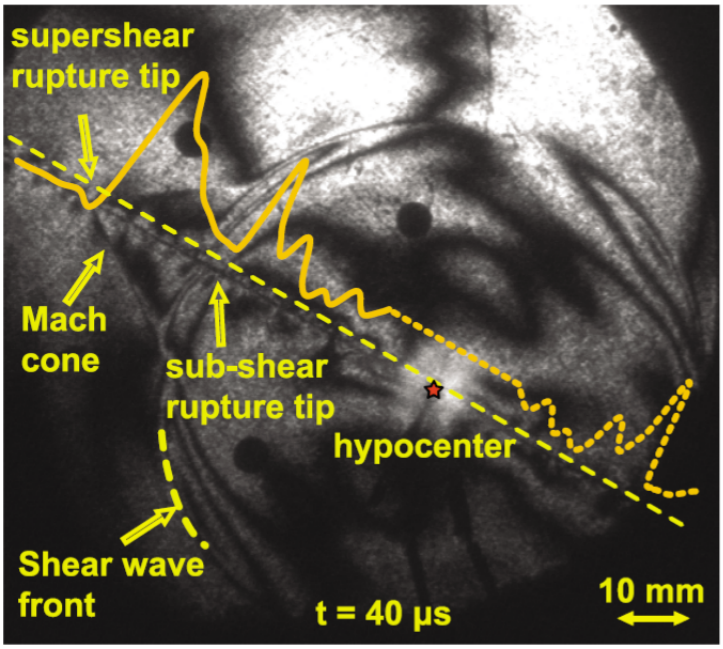

FIGURE 1.20: Mach cone visualised using photoelasticity, associated with a supershear rupture (Lu et al., 2010b). The particles velocity is superimposed in yellow.

Once the instability is triggered, the rupture asymsoptically tends to a limiting velocity V_r which is generally around V_{ray} for mode II and around V_s for mode III, until it switches to intersonic velocity in some cases ($V_s < V_r < V_p$) as observed in recent laboratory studies (Dunham et al., 2003; Lu et al., 2010b; Schubnel et al., 2011; Passelègue et al., 2013). Observations of rupture velocities higher than the

shear wave velocity V_s have also been reported in nature (example of Kokoxili 2001 event in Tibet, Bhat et al., 2007). $V_r \approx \sqrt{2}V_s$ is an energetically favorable intersonic rupture velocity. This type of rupture is observed when the prestress is sufficiently high, and can be triggered from strong asperities that concentrate energy (Dunham et al., 2003). Andrews (1976) showed that for 2D studies, the seismic ratio defined as $S = (\tau_p - \tau_0)/(\tau_0 - \tau_r)$ controls the ratio L/L_c, where L is the distance at which the rupture switches from sub-Rayleigh to supershear. If L is longer than the sample size in the laboratory experiment, a supershear rupture might not be observed despite a high prestress ratio (Passelègue et al., 2013). The latter experiments, performed on crustal rocks (Westerly granite) showed that supershear took place when $\tau_0/\sigma_n > 0.7$.

The bimaterial contrast (two different materials in contact) also strongly influences the rupture velocity. When a rupture propagates in the positive direction (direction of motion of the most compliant side), V_{r+} is similar to the compliant material shear wave velocity $V_{s\ cpt}$, accompanied by a large normal stress reduction near the crack tip (Shlomai and Fineberg, 2016). In the negative direction (direction of motion of the stiffer side), the rupture never propagates at V_s, but is more likely to be sub-Rayleigh or supershear (Shlomai and Fineberg, 2016).

Supershear ruptures, often recognizable in photoelastic experiments with their highly energetic mach cone with a low geometrical attenuation (see figure 1.20) are likely to create off-fault damage in the surrounding materials (Bhat et al., 2007; Biegel et al., 2008). Ground motion simulations also show that these conic waves amplify ground shaking on fault analogues hanging wall and footwall (Gabuchian et al., 2014).

Rupture modes, crack-like versus pulse-like

As observed in the field with seismic data (Heaton, 1990), a crack can propagate as a crack-like rupture, through the entire interface, or as pulse-like rupture, and be localized between a portion ahead of the crack tip that has not slipped yet, and a restrengthening portion behind, as illustrated in figure 1.21.

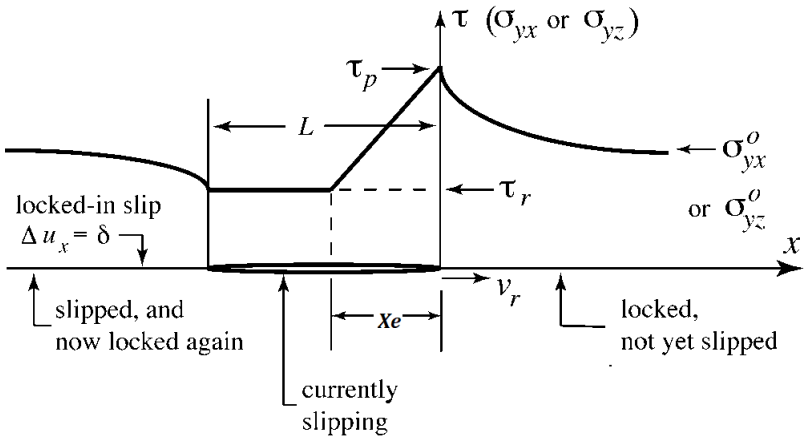

FIGURE 1.21: Pulse-like crack model with a linear variation of shear stress in the slip weakening-zone, after Rice et al., 2005.

Experimental and numerical studies on the rise time (local duration of relative slip between two surfaces) support the field observations, and show that this rise time can be much shorter than the overall rupture duration, by an order of magnitude (Lu et al., 2010b; Lu et al., 2007; Ben-Zion, 2001; Rice et al., 2005; Nielsen and Madariaga, 2003). Those rupture modes are important to understand as they influence the constitutive and scaling laws, the energy partition, the heat generation, and the spatio-temporal complexity of the slip on the fault fault plane (Lu et al., 2010b). Although it is not clear which processes influencing the rupture mode are dominant in nature, several mechanisms have been proposed to explain similar observations in the laboratory (Lu et al., 2010b). In homogeneous models with simple geometries, it is found that a transition to pulse-like mode occurs when reducing the prestress ratio τ_0/σ_0, and more generally, when decreasing the absolute values of τ_0 and σ_0 (Lu et al., 2010b; Lu et al., 2007). Another explanation supported by numerical models (Nielsen and Madariaga, 2003; Cochard and Madariaga, 1994) is an interface with strong velocity-weakening friction. In nature, a possible velocity-weakening mechanism can be the local increase of pore pressure due to frictional heating (Lu et al., 2010b). The increased pore pressure can be only localized just behind the crack tip, leading to the rapid restrengthening of the contacts further away from it. Such variations of normal stress have a strong influence on the rupture mode and on the healing of a fault (Richardson and Marone, 1999). In a real fault, waves that are reflected back from barriers

can have the effect of accelerating healing (Lu et al., 2007). The geometric barriers are also found to influence the rupture mode and are a natural explanation for the field observations of pulse-like ruptures (Ben-Zion, 2001). The barrier model to explain pulses consists of several crack-like ruptures delimited by geometric irregularities that locally stop the motion (Lu et al., 2007). Finally, the rupture mode is also affected by bimaterial interfaces (Ben-Zion, 2001; Shlomai and Fineberg, 2016): when propagating in the positive direction, the rupture is likely to be pulse-like, associated with a large normal stress drop at the crack tip, and propagating at the shear wave speed of the softer material. In the negative direction, the bimaterial coupling favours crack-like rupture (Shlomai and Fineberg, 2016).

1.4 The friction laws

During a rupture, when relative slip occurs at a contact interface, the concept of friction is extensively used to simplify complex interactions between asperities in contact (Ohnaka, 2013; Marone, 1998a; Scholz, 1998).

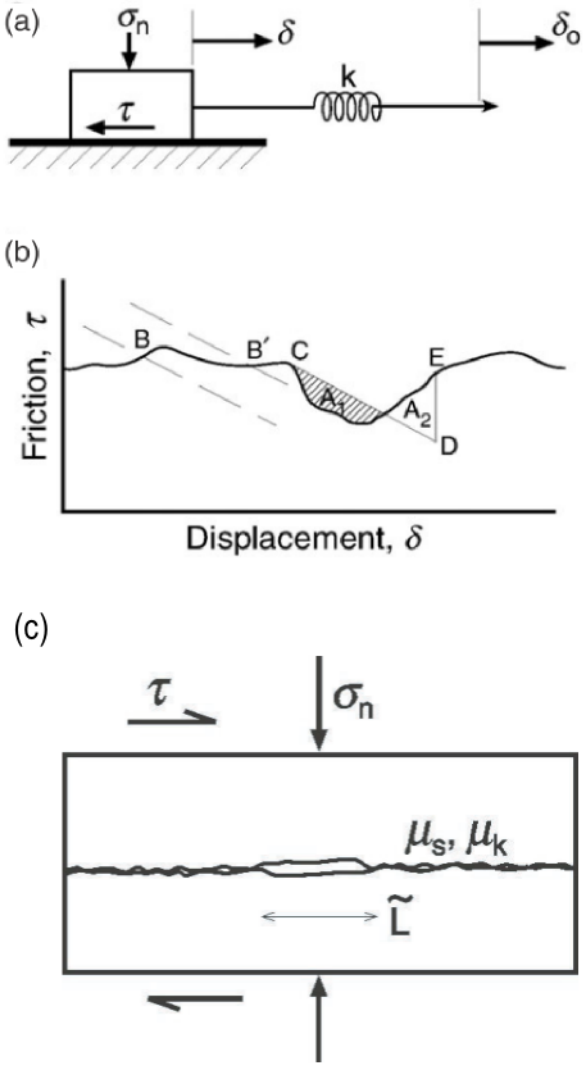

FIGURE 1.22: a) Simple spring slider model where the friction coefficient μ links the shear resistance τ and the normal stress σ_n. b) Schematic evolution of friction as a function of the slider displacement where an instability starts at point C. c) Critical crack size $\tilde{L}$ at the interface between two blocks in contact over an nominal area A, and a real contact area A_r. Figure from Kanamori and Brodsky, 2004

To quantify the friction, the Coulomb coefficient of friction μ is used, and represents the ratio of shear strength τ_{max} to normal stress σ_n, applied on a surface (fig. 1.22.a). τ_{max} is the maximum value of shear stress that can be applied on

a contact surface before it slides. The static coefficients of friction for different rocks and with different roughnesses have been measured experimentally by Byerlee, 1978. His study shows that μ_s systematically varies between 0.6 and 0.8, except for a number of clay minerals (see fig. 1.23). However, when it comes to studying this coefficient is not constant during a dynamic event, and friction laws are needed in order to describe its evolution with time. The friction laws are generally divided into two categories. The first ones are the rate-and-state laws which consider the dependence of the friction coefficient on slip velocity. The other category are the slip weakening laws which consider the friction coefficient as a function of the relative slip between two surfaces.

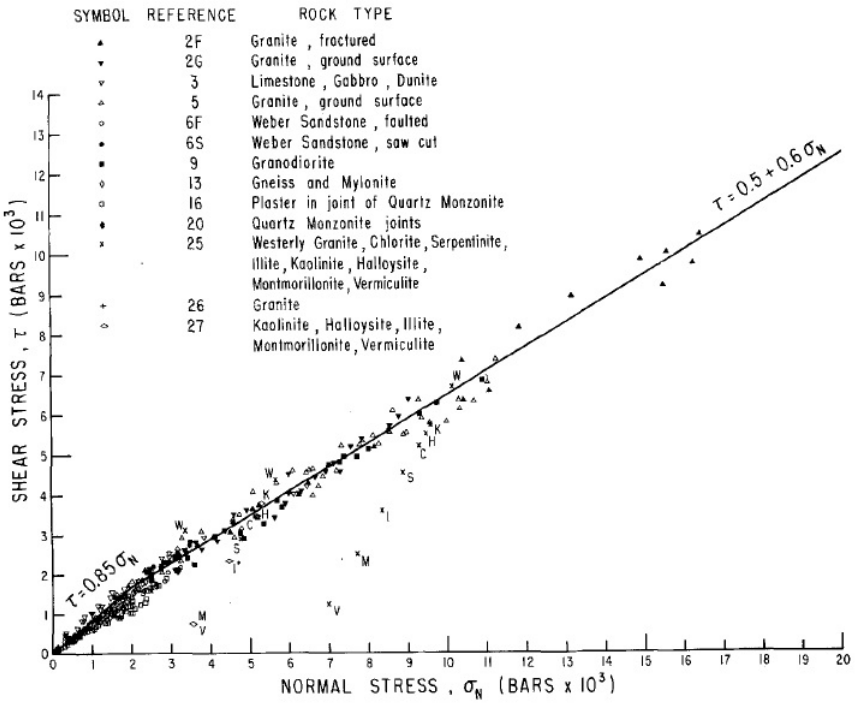

FIGURE 1.23: Friction of crustal rocks after Byerlee, 1978

1.4.1 Rate-and-State model

The rate-and-state laws express the coefficient of friction as a function of the slip velocity V and of the evolution of one or more state variables, as illustrated in figure 1.24. They are based on empirical fit of laboratory experiments.

Some physical interpretation lies in the fact that the shear resistance of an interface τ_p is proportional to the real area of contacts A_r (fig. 1.22.c) multiplied

by the strength of those contacts. The "rate" term accounts for the fact that there is a direct effect of slip rate, that tends to increase the friction in the case of creep behaviour, and which can be seen in flow laws (Scholz, 1998). The "state" term represents the change of fault properties with velocity and time. It captures the fact that A_r increases logarithmically with time in the form:

$$A_r(\theta) = A_0 \left[1 + b \ln \left(\frac{\theta V_0}{d_c} \right) \right]$$

where θ has the dimension of a time (Dieterich and Kilgore, 1994).

A common formulation for this type of law is the Dieterich-Ruina aging law (Scholz, 1998):

$$\mu = \mu_0 + a \ln \left(\frac{V}{V_0} \right) + b \ln \left(\frac{\theta V_0}{d_c} \right) \tag{1.21}$$

where

$$\dot{\theta} = 1 - \frac{\theta V}{d_c} \tag{1.22}$$

The constants a and b are non-dimensional parameters determined experimentally, V is the sliding velocity, V_0 is a reference velocity at which $\mu = \mu_0$, its steady-state value. θ is a state variable which depends on time, and contains the information on the state of a surface, which depends on its history. d_c is a characteristic sliding distance. It is interpreted to be the distance needed to renew the contacts population of the interface. If (a-b)<0, the interface is said to be rate-weakening, and can allow instabilities to be triggered. If (a-b)>0, the interface is rate-strengthening, the coefficient of friction increases with velocity, and thus rupture cannot propagate.

At steady-state ($\dot{\theta} = 0$ or $\theta / d_c = 1/V$) one can see the direct relationship between friction coefficient μ_{ss} and slip velocity V_{ss}:

$$\mu_{ss} = \mu_0 + (a - b) \ln \left(\frac{V_{ss}}{V_0} \right) \tag{1.23}$$

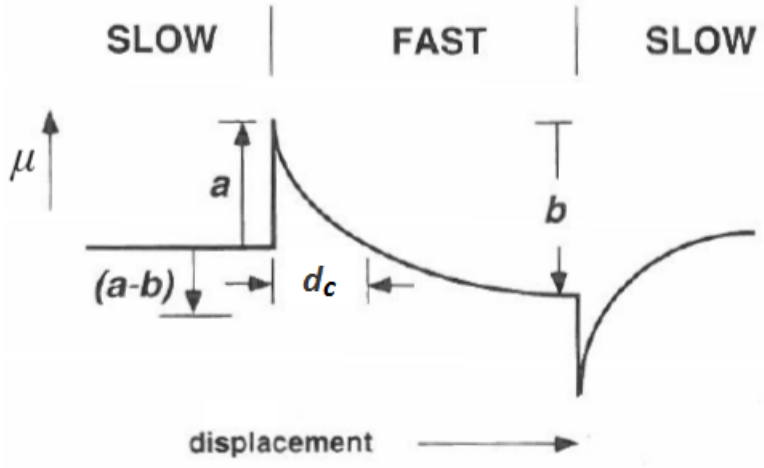

FIGURE 1.24: Rate-and-State law Scholz, 1998.

This formulation works well to explain a large range of observed phenomena in the laboratory and in nature (Scholz, 1998; Marone, 1998a).

It also enables the estimation of a scaling for the critical length of a crack $\tilde{L}$ at which an instability is to be expected. Indeed, considering again the spring slider model in fig. 1.22.a, the force balance yields $\tau = k(\delta_0 - \delta)$, and an instability will be triggered if $|\Delta\tau/\Delta\delta| > k$ (fig. 1.22.b). Assuming fault stiffness k_f in the form $E'/\tilde{L}$, E' being a relevant elastic modulus, the critical length $\tilde{L}$ will then be (Kanamori and Brodsky, 2004):

$$\tilde{L} \approx \frac{E' d_c}{\Delta\tau} = \frac{E' d_c}{\sigma_n(\mu_s - \mu_r)} \tag{1.24}$$

The corresponding Rate-and-State estimate L_{b-a} is derived by stability analysis and given in Rice, 1993 by:

$$L_{b-a} = \frac{G^* d_c}{\sigma_n(b-a)} \tag{1.25}$$

Where $G^* = G/(1-\nu)$ is the effective shear modulus.

An extensive discussion about the nucleation length estimates using rate-and-state friction laws can be found in Rubin and Ampuero, 2005 where the authors derive a lower bound L_b, and an upper bound L_∞ that corresponds roughly to the L_c derived by Andrews, 1976 (see next section). The different values of L_c can be due to different loading conditions and histories (Rubin and Ampuero, 2005), but

further complexity also arises from the heterogeneous nature of faults (Harbord et al., 2017). Further discussion on the nucleation length is given in chapter 3.

1.4.2 Slip-weakening model

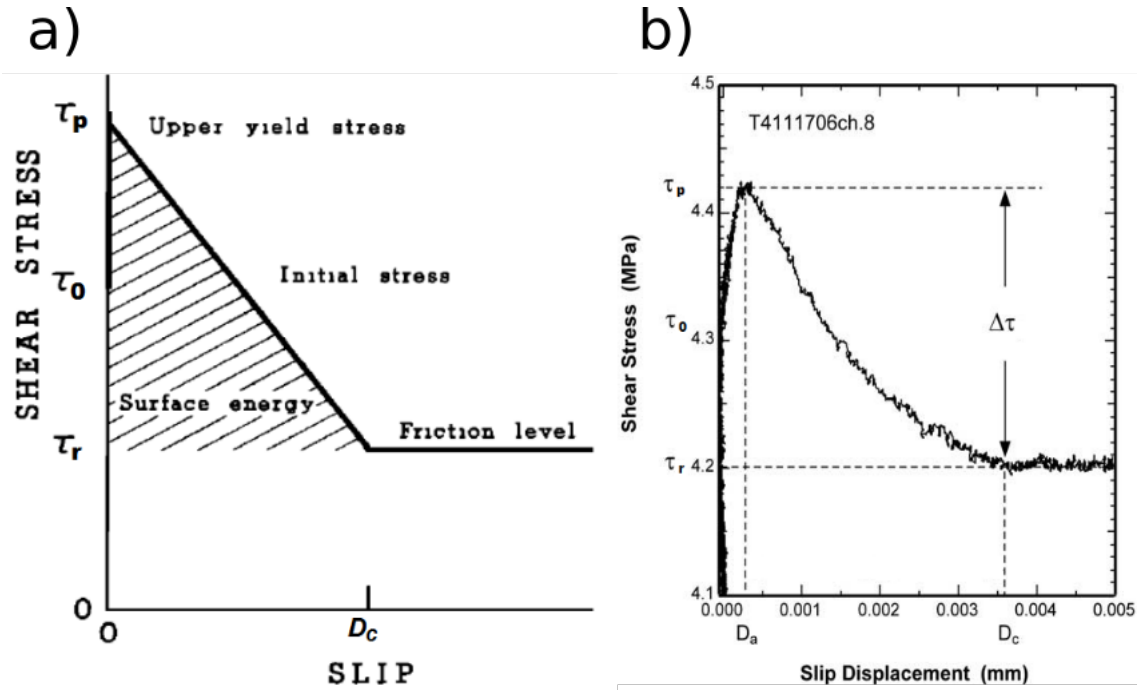

FIGURE 1.25: Slip weakening model, after Andrews, 1976 b) Typical observed slip-weakening law Ohnaka, 2013

.

One can also consider the variation of the friction coefficient with respect to relative slip. A simple model first proposed by Ida, 1973 and then Andrews, 1976, consists of a linear decrease of shear stress versus relative slip, from the peak value τ_p ahead of the crack, down to a dynamic value τ_r attained after a characteristic amount of relative slip D_c, called the slip-weakening distance (see figure 1.25.a). In this case, the estimate of the critical nucleation length is given by $L_{Andrews} = 2G^* D_c/\pi \times (\tau_p - \tau_f)/(\tau_0 - \tau_f)^2$, where τ_0 is the initial shear stress. In reality, as highlighted by several laboratory experiments (Ohnaka, 2013), the shear stress increases first from τ_0 to a peak value τ_p in a distance D_a, before decreasing exponentially after the critical slip D_c, to its dynamic value τ_r of residual friction, in the center of the crack, as shown in figure 1.25.b. An upper

bound for D_c in laboratory experiments on fault analogues has been found to be 500 µm (Nielsen et al., 2010), and typical values are around 1 µm to 10 µm.

1.5 Main focus of the PhD

In spite of decades of research, there are a lot of open questions that remain in earthquake science. How do earthquake start? Do small and large earthquakes start in a similar manner? If there exists a difference, can we measure it and use it for short-term forecasting? Can it also be used to predict the size of the events? What is the role of the recently discovered slow slip regarding these questions?

Advances in positioning systems have enables to sometimes detect slow slip during the nucleation phase of the earthquake cycle. When this pre-slip is detected, what we want to know is what controls its size and prevalence, and what does it tell about the subsequent rupture.

In this thesis, we propose to look at the pre-slip during the nucleation phase of controlled laboratory ruptures, in order to look specifically at how it is affected by the loading rate, and what are the implications for real earthquakes. A better understanding of this slow slip and more generally of the nucleation of earthquakes has got direct implications for probabilistic earthquake forecast and early-warning systems. It enables a better societal preparedness, and therefore to reduce the vulnerability to earthquake risk.

Chapter 2

Material and methods

This chapter presents the main methods used during this PhD. I used and developed laboratory experiments, as well as numerical codes in order to study the nucleation and dynamic propagation of ruptures. As a considerable amount of time has been spend developing those tools, this part aims at giving enough details for someone to reproduce or use them. I introduce the photoelasticity technique used in chapter 3 to visualize the crack tips of a rupture in the biaxial shear apparatus. I also give the main equations used to process the strain gauge signals, both in the biaxial, and in the triaxial shear apparatus. The second part is dedicated to the numerical techniques, mainly used in chapters 4 and 6. It includes the numerical model schemes: the finite difference method used to simulate dynamic ruptures, and the finite element method used to reproduce the loading conditions of the fault analogues in the laboratory. Finally, I give some details about the inversion procedure used in appendix A in order to attempt to invert photoelastic fringes.

2.1 Shear deformation apparatus

2.1.1 Biaxial experiments

Overview of the setup

The biaxial experiment illustrated in figures 2.1 and 2.2 is used to visualize a rupture propagating through a contact interface. Two thin plates (each 1 cm thick, 15 cm wide and 30 cm long) are initially pressed together and then sheared, making the asperities initially welded together progressively detach. Although the rupture process may last several seconds on real faults, at the laboratory scale it represents only a fraction of a millisecond. Stress changes propagating at speeds around hundreds of $m.s^{-1}$ along a 30 cm interface can only be captured using very high speed acquisition devices. One way of tracking a rupture propagation is by using strain gauges, another is to use the birefringent properties of transparent materials such as polycarbonate. This technique called photoelasticity uses the fact that the refraction indices of birefringent material change depending on stresses, creating extinction fringes visible when a polarized light passes through.

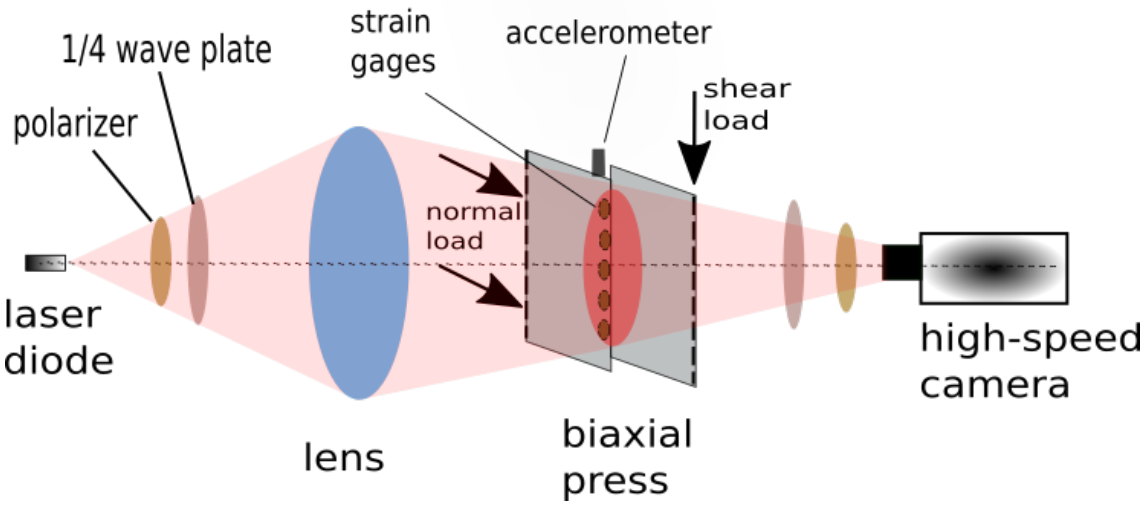

FIGURE 2.1: Biaxial experiments setup. A monochromatic light source (red: $\approx$ 635 nm) go through the optical elements in the following order: polarizer, 1/4 wave plate, lens, birefringent samples (polycarbonate), 1/4 wave plate, polariser, high-speed camera.

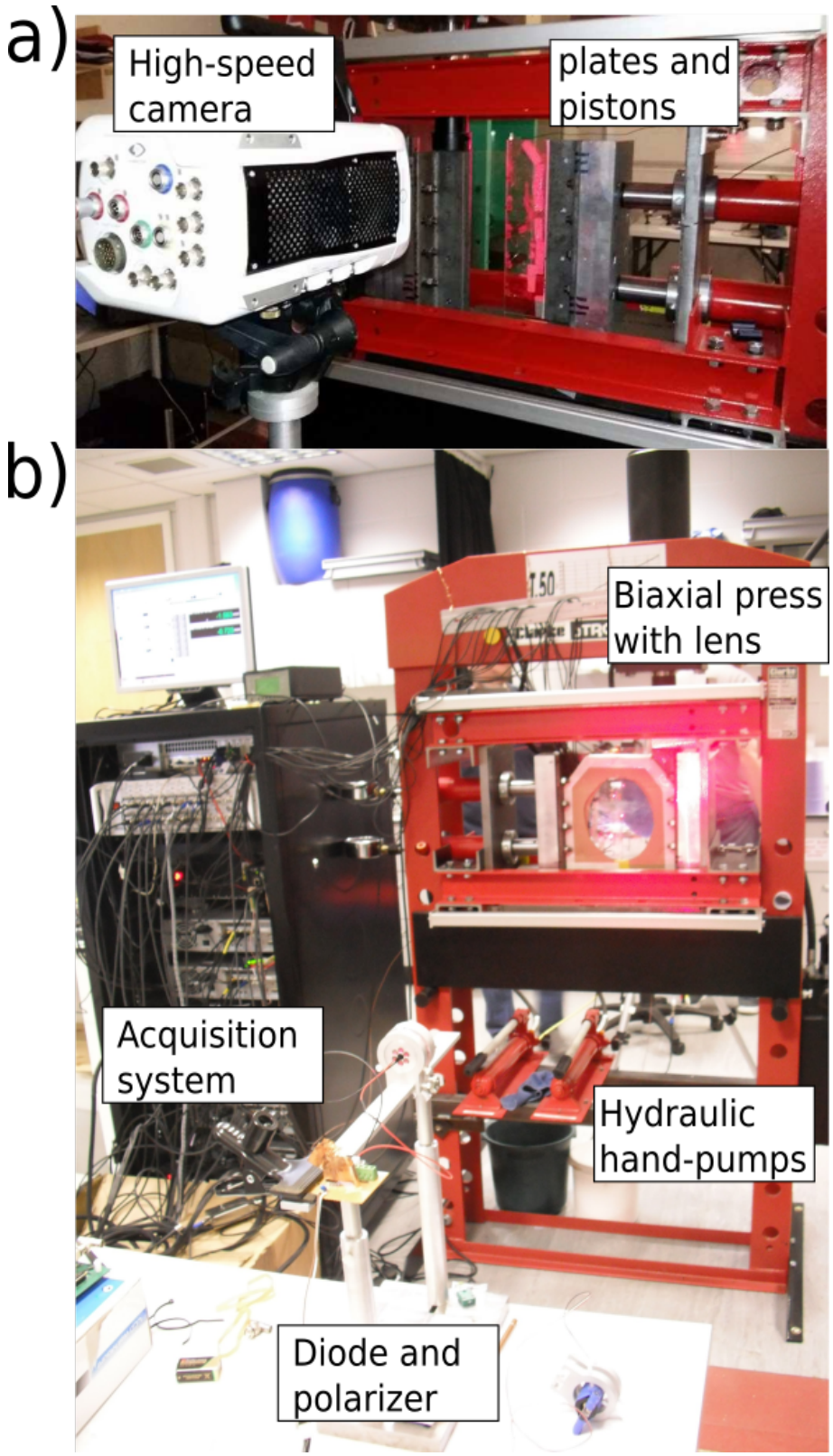

FIGURE 2.2: a) Photograph of the biaxial press used for the rupture experiments with the camera on one side. b) Picture of the other side where we can see the diode, the aquisition system on the left, the lens in front of the polycarbonate plates in the press, and the hydraulic hand-pumps below to control the pistons applying the forces.

In order to polarize the light, polarisers and quarter wave plates are used on both sides of the plates, and a powerful monochromatic light source (red diode with a wavelength $\lambda_w \approx 635$ nm) ensures that enough photons will be captured in a short exposure time by the Phantom® V642 camera used. I usually adopt a frame rate of up to 200000 frames per seconds (fps) with a resolution of 464 by 64 pixels, limited by the buffer memory.

The photoloelaticity technique detailed later used simultaneously with strain gauge signals, has enabled to investigate the slow propagation phase of ruptures, which is the object of chapter 3.

Loading geometry

Inside the biaxial press, two polycarbonate plates are clamped by metallic slabs, over a width of 7.5 cm. A normal load is then applied uniformly thanks to two pistons pushing horizontally on a metallic block (figure 2.3.a). This forces the two plates to be in contact along a 30 by 1 cm interface. The contact interface is then sheared by using a third piston pushing down vertically (simple shear configuration), and the rupture starts when the strength of the interface is reached.

Although the loading system seems relatively simple, as I will show chapter 4, depending on whether or not the plates are properly clamped so that they do not slide between the clamps when the pressure is applied, this setup can create different initial shear stress distributions prior to a rupture. I also had the problem that the pumps controlling the horizontal pistons could not hold a high pressure (5 MPa) for a long time. Therefore even though ideally the normal stresses would have been constant and uniform during the experiments, it could vary by $\pm$ 0.7 MPa from one experiment to another. Instead of changing the pumps and redoing the experiments which could have taken a lot of time, I chose to correct for this effect when investigating the nucleation length of ruptures in chapter 3.

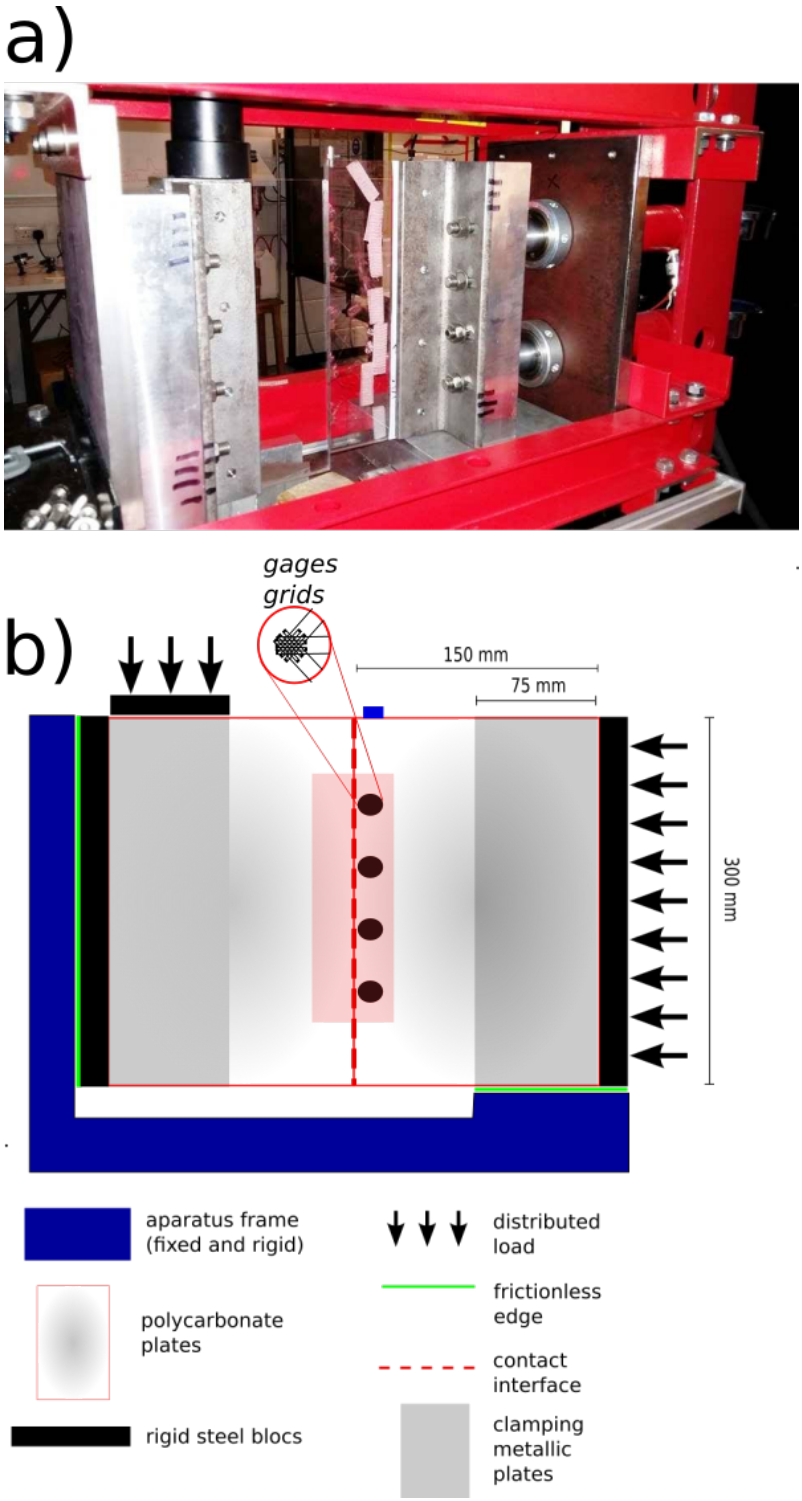

FIGURE 2.3: a) Photograph of the biaxial press loading configuration, showing the two pistons applying the normal stress, and the one for the shear stress. b) Sketch of the elements and the loading configuration in the biaxial press

Polycarbonate mechanical properties

The polycarbonate mechanical properties can be found in Latour et al., 2013 or Dally and Riley, 1965, and are summarized in table 2.1. From the experimental results, the polycarbonate used in our experiments has similar properties to the one used by Latour et al., 2013. I will therefore use the latter values in these studies. We can also mention here that the friction coefficient typically ranges from 0.3 to 0.4.

source:	Latour et al., 2013	Dally and Riley, 1965
E	2.59 [GPa]	2.48 [GPa]
ν	0.35	0.38
G	0.957 [GPa]	0.898 [GPa]
λ	2.24 [GPa]	2.81 [GPa]
V_p	1860 [m.s^{-1}]	1957 [m.s^{-1}]
V_s	893 [m.s^{-1}]	865 [m.s^{-1}]
V_{ray}	821 [m.s^{-1}]	796 [m.s^{-1}]
ρ	1200 [kg.m^{-3}]	1200 [kg.m^{-3}]

TABLE 2.1: Polycarbonate properties

2.1.2 Triaxial experiments

The study of rock friction under pressure, and in particular the effect of roughness in the triaxial vessel had been started in the Rock Mechanics Lab of Durham University, and a detailed description of the setup can be found in the PhD thesis of C. Harbord (Harbord, 2018). As I use the same setup except for few improvements (use of longer samples and feedthrough connectors enabling more strain gauge measurements along the interface), I present here a lighter description. In this thesis, the triaxial apparatus is used in order to understand the dynamic friction of rocks under crustal pressure conditions, and how it can be affected by the different loading conditions.

Overview of the setup

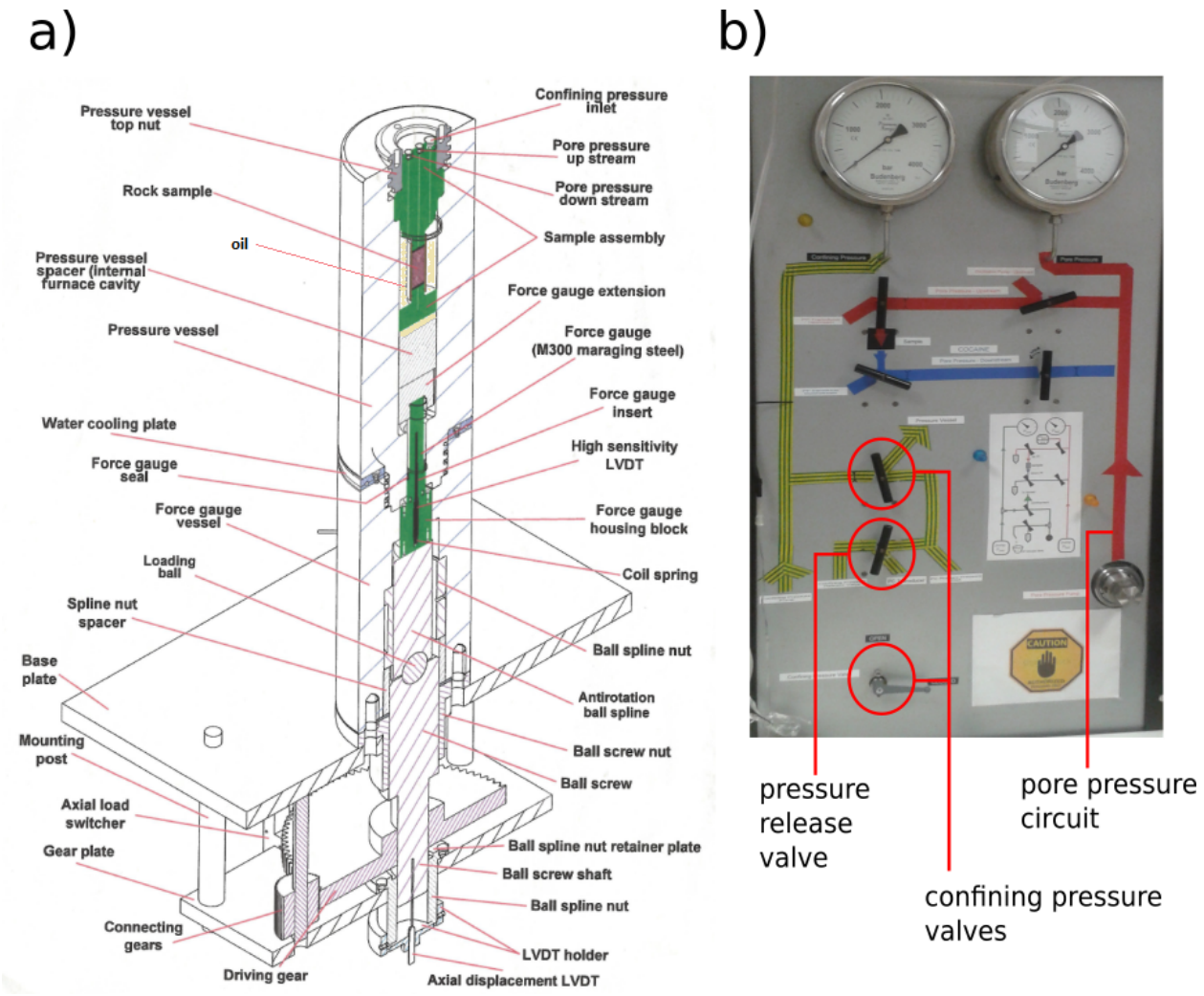

FIGURE 2.4: a) Description of the triaxial machine elements used to perform dynamic rupture experiments under pressure, from the technical notes. b) Picture of the outside of the machine from where the valves control the confining and pore pressures applied.

The experiments are performed in a deformation rig able to apply confining pressures up to 250 MPa, and a vertical axial force. It also has the possibility to apply upstream (from the top) and downstream (from the bottom) pore fluids pressures via a servo-controlled pump, and to go to temperatures up to 200°C (not used here). The pressure vessel at the top is where the sample assembly goes. It is closed by a threaded top nut, and sealed thanks to several o-rings. The pressure fluid is a low viscosity silicone oil (0.01 Pa.s), and is controlled by an air-driven hydraulic pump. Finer adjustments for the confining pressure can also be made

thanks to a Nova Swiss syringe pump. Concerning the axial force, it is measured by a Linear Variable Differential Transformer (LVDT) force gauge sitting on top of a loading column, and under the sample assembly. In order to apply the axial load on the sample, a motor at the bottom, which can be servo-controlled drives up the loading column that contains a THK ball spline in the middle to avoid rotations. The contact is made when the top of the force gauge LVDT touches the bottom of the sample assembly. The experiments can be run by controlling the displacement rates using the axial displacement LVDT at the bottom, and a servo-control system. In this case, due to the loading column compliance (even though it should be low compared to the sample compliance), the displacement measured at the bottom should be slightly more than at the top of the column, and therefore a correction should be applied. In general I fix the motor voltage (hence the displacement rate) rather than working in servo-control, and measure the stressing rate directly along the contact interface using strain gauges, or using the load cell data. I usually go up to 14 $\mu m.s^{-1}$. The experiment is controlled using Labview with a code written mainly by Dan Faulkner.

Loading geometry

The rock samples are prepared as illustrated in fig. 2.5, in a direct shear configuration: two slabs of rock are first fixed on stainless steel holders using cyanoacrylate, and polished using usually 400 grit diamond powder, and then 800 grit sandpaper. The two parts are then put in contact together, silicon spacers are placed to fill the voids, and everything is wrapped in Teflon sheets to avoid friction with the PVC jacket into which it is inserted. The strain gauge wires that were fixed on the samples are then pulled out of holes cut through the jacket, and later filled with soft Loctite® Hysol 9455 flexible epoxy. The gauge wires are connected to the outside of the vessel by soldering them on shielded cables (fig. 2.5.a) or anodised wires (fig. 2.5.b) that are passed through the sample assembly. The anodised wire are advantageous as up to 6 of them can be passed through feedthrough conical hollow screws. The sealing to resist pressure is achieved by filling the feedthrough with Permabound® ET5428 two-part epoxy (shear strength around

22 MPa for mild steel). The confining pressure applies the normal load at the interface between the two slabs, and the vertical axial load enables to increase the shear stress in a direct shear configuration.

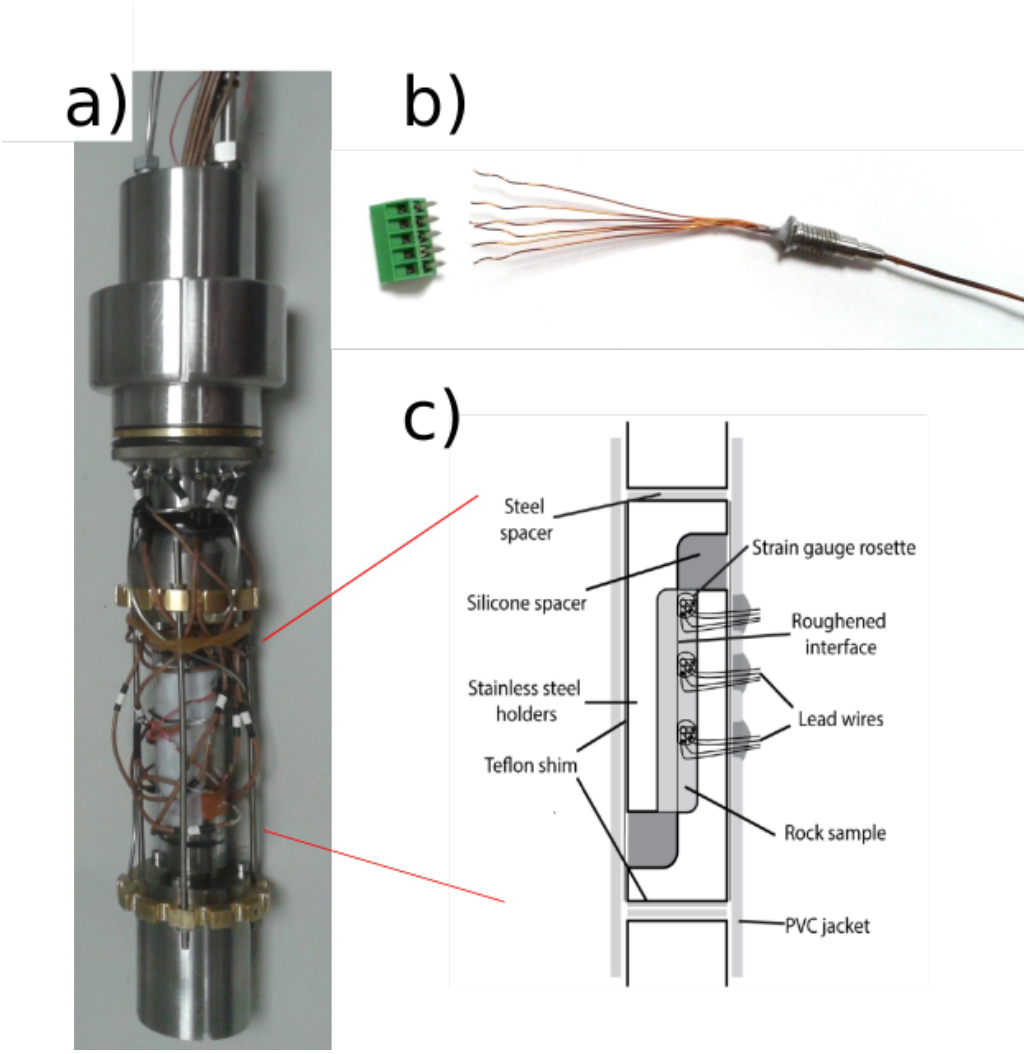

FIGURE 2.5: Photograph of the assembly designed to hold and load the sample (not visible on the picture as it is wrapped into teflon sheet). The brown coaxial wires around are designed to transmit the strain gauge signals fixed on the sample. b) Feedthrough cones designed to connect the strain gauges inside the pressure vessel to the amplifier outside, via anodized wires soldered on terminal blocks. c) Detail of the loading geometry reproduced after Harbord, 2018; two stainless steel holders inside a PVC jacket maintain the rock slabs together in a direct shear configuration. The strain gauges anodized wires are pulled through holes outside the jacket, which are later filled with soft epoxy.

Rock mechanical properties

The properties of the rock used are summarized in the table 2.2. They depend on the temperature, pressure conditions, and on the sample damage history. I present here some of the values found in literature at 0 MPa and 75 MPa of confining pressure, room temperature, and for intact samples. To account for the Young's modulus dependence on pressure, we can assume a linear relation between $E = 50$ GPa at $P_{eff} = 0$ MPa, and $E = 75$ GPa at $P_{eff} = 75$ MPa, for simplicity (in reality it is more a log type of relation).

P_{eff}	0 [MPa]	75 [MPa]	source
E	50 [GPa]	70 [GPa]	(Heap and Faulkner, 2008)
ν	0.25		(Bhat et al., 2011)
G	20 [GPa]	28 [GPa]	
λ	20 [GPa]	28 [GPa]	
V_p	5500 [m.s^{-1}]	6000 [m.s^{-1}]	(Nasseri et al., 2009)
V_s	2500 [m.s^{-1}]	3600 [m.s^{-1}]	(Nasseri et al., 2009)
V_{ray}	3036 [m.s^{-1}]	3312 [m.s^{-1}]	(taking $V_{ray} \approx 0.92 V_s$)
ρ	2700 [kg.m^{-3}]	2700 [kg.m^{-3}]	

TABLE 2.2: Westerly granite properties at room temperature, intact samples ($\approx 20°C$)

2.2 Quantification of rupture processes

2.2.1 Photoelasticity

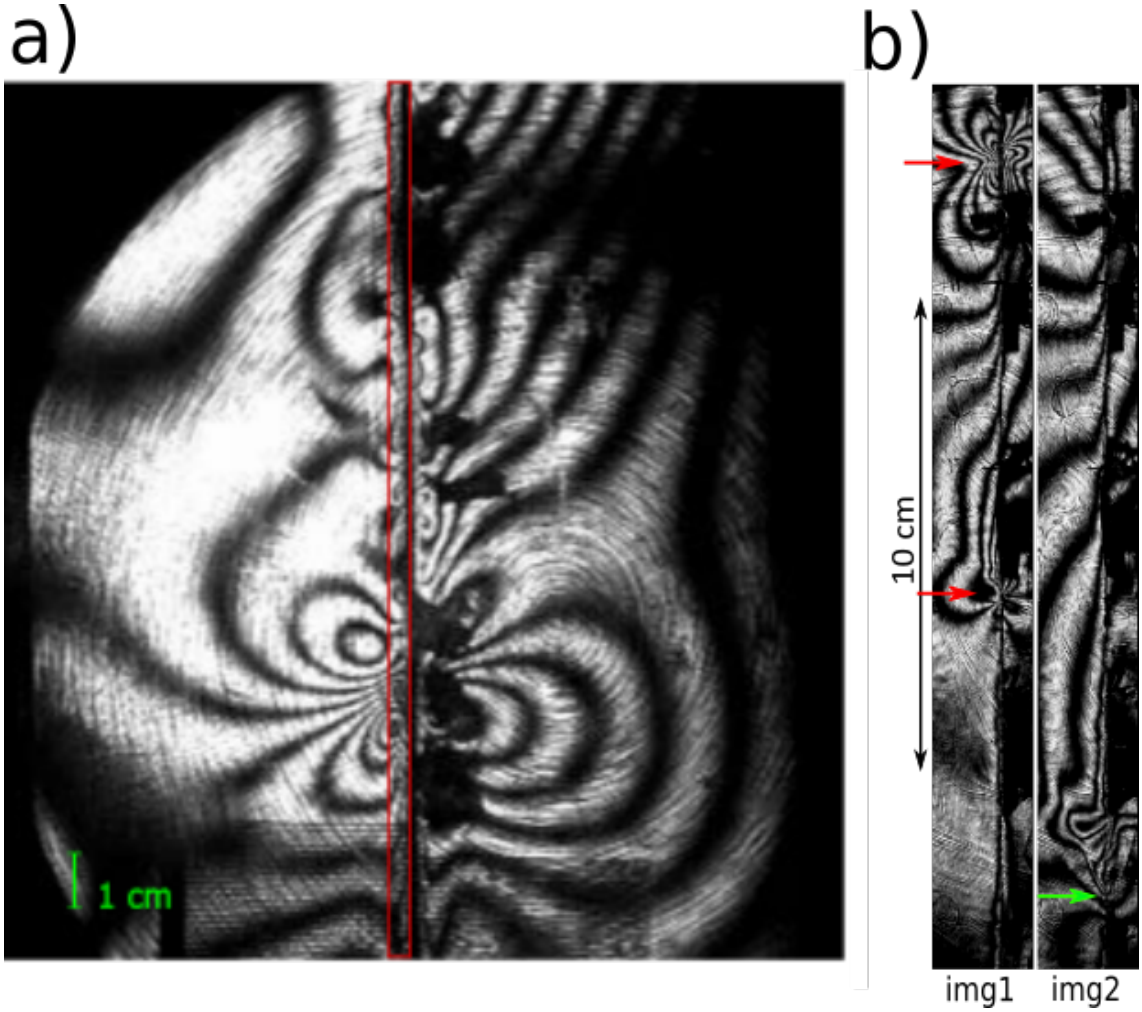

FIGURE 2.6: (a) Isochromatic fringes before a rupture propagation. b)Isochromatic fringe patterns recorded during a rupture propagation. The slipping zone of img1 is situated between the two red arrows that represent the crack tips or rupture fronts propagating. The green arrow on img2 points at the bottom tip that has transitioned to supershear while the top tip went out of the camera field.

Photoelasticity is a well-known technique used to image the stress in birefringent materials, which has been used in several studies on rupture propagation (Schubnel et al., 2011; Nielsen et al., 2010; Biegel et al., 2008; Lu et al., 2010b). When a polarized light passes through a medium and through an analyser on the opposite side, bright and dark fringes appear. Those fringes can be divided into two types. The first type of fringe are the isoclinics, and correspond to the alignment

of one of the principal stress direction with the polarity axis of light. Those fringes disappear when using a circular polariscope arrangement (see fig. 2.7). The other type are the isochromatics. The isochromatic fringes can be considered as contour lines of the maximum shear stress field (figure 2.6). This can be shown using the stress-optic law (Dally and Riley, 1965). It states that the variation of the indices of refractions are linearly proportional to the stresses in linearly elastic materials. The general form for the optical stress law for two-dimensional plane-stress birefringent material is expressed as follows:

$$\Delta = \frac{2\pi hc}{\lambda_w}(\sigma_1 - \sigma_2), \tag{2.1}$$

where Δ is the relative retardation that corresponds to the relative angular phase-shift, as the stressed material acts as a wave-plate, thus modifying the indices of refractions in the principal stress directions σ_1 and σ_2. λ_w is the wavelength, c is the stress-optic coefficient in $m^2.N^{-1}$, and h is the thickness of the material in m.

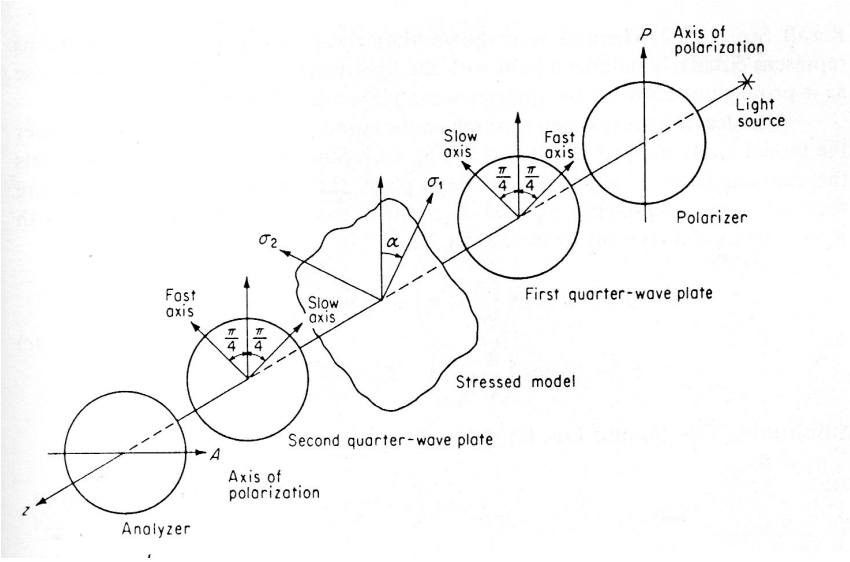

FIGURE 2.7: Circular polariscope arrangement from Dally and Riley, 1965

When working with monochromatic light, this form can be simplified to :

$$\frac{Nf_\sigma}{h} = \sigma_1 - \sigma_2 = 2\tau_{max} \tag{2.2}$$

where

$$N = \frac{\Delta}{2\pi} \qquad \text{and} \qquad f_\sigma = \frac{\lambda_w}{c} \tag{2.3}$$

The fringe order N corresponds to the number of retardation cycles, and the fringe value f_σ in $\mathrm{N.m^{-1}}$ (per fringe) is a material constant. After Dally and Riley, 1965, if using polycarbonate, f_σ = 7 $\mathrm{kN.m^{-1}}$ for green light (λ_w = 546 nm), which give $f_\sigma \approx$ 8.1 $\mathrm{kN.m^{-1}}$ for red light (λ_w = 635 nm). In chapter 4 however, we use a lower value f_σ = 4 $\mathrm{kN.m^{-1}}$ which works better in order to simulate numerically the fringe patterns observed. Ideally we would need to calibrate this value of f_σ. The theoretical light intensity is given by:

$I(x,y) = A\sin^2(\pi N(x,y)) + C(x,y)$

Where A is the amplitude of the light intensity, $C(x,y)$ is the background light.

2.2.2 Strain gauges

The acquisition system

The strain gauge signals are transmitted via shielded cables to an Elsys SGA_2 conditioning unit. The unit contains a total of 24 channels; wheastone bridges that can be powered by either 5V or 10V. The output voltages can then be amplified by a gain factor of 1, 10 or 100 ($\pm$0.1%). The amplifier acts as a low-pass filter with a cut-off frequency of 1.5 MHz for a gain of 1, down to 600 KHz for a gain of 100. The output signals have an impedance of 50 Ohms, matching the impedance of the analog-to-digital converter units called Richters, to which they are transmitted via shielded BNC to BNC cables. The 6 Richter units can digitize continuously the signal at a frequency of up to 10 MHz on the total of 24 channels available (16-bit resolution). One of the Richter units is the master (Richter M, fig 2.8), deciding on the aquisition parameters for the 5 others (Richters S1 to S5, fig 2.8). The units are controlled by a PC, with the Insite software from

ITASCA^{TM} for the continuous recording. There is also the possibility to use a Cecchi system which can record at 50 MHz, 80 V_{PP}, 12-bit resolution, but on trigger mode for short time windows. The continuous data acquired is saved in several large HDF5 files, and as a lot of time has been spent writing the python scripts in order to deal with those files in an efficient way, some of the scripts are given in appendix C.

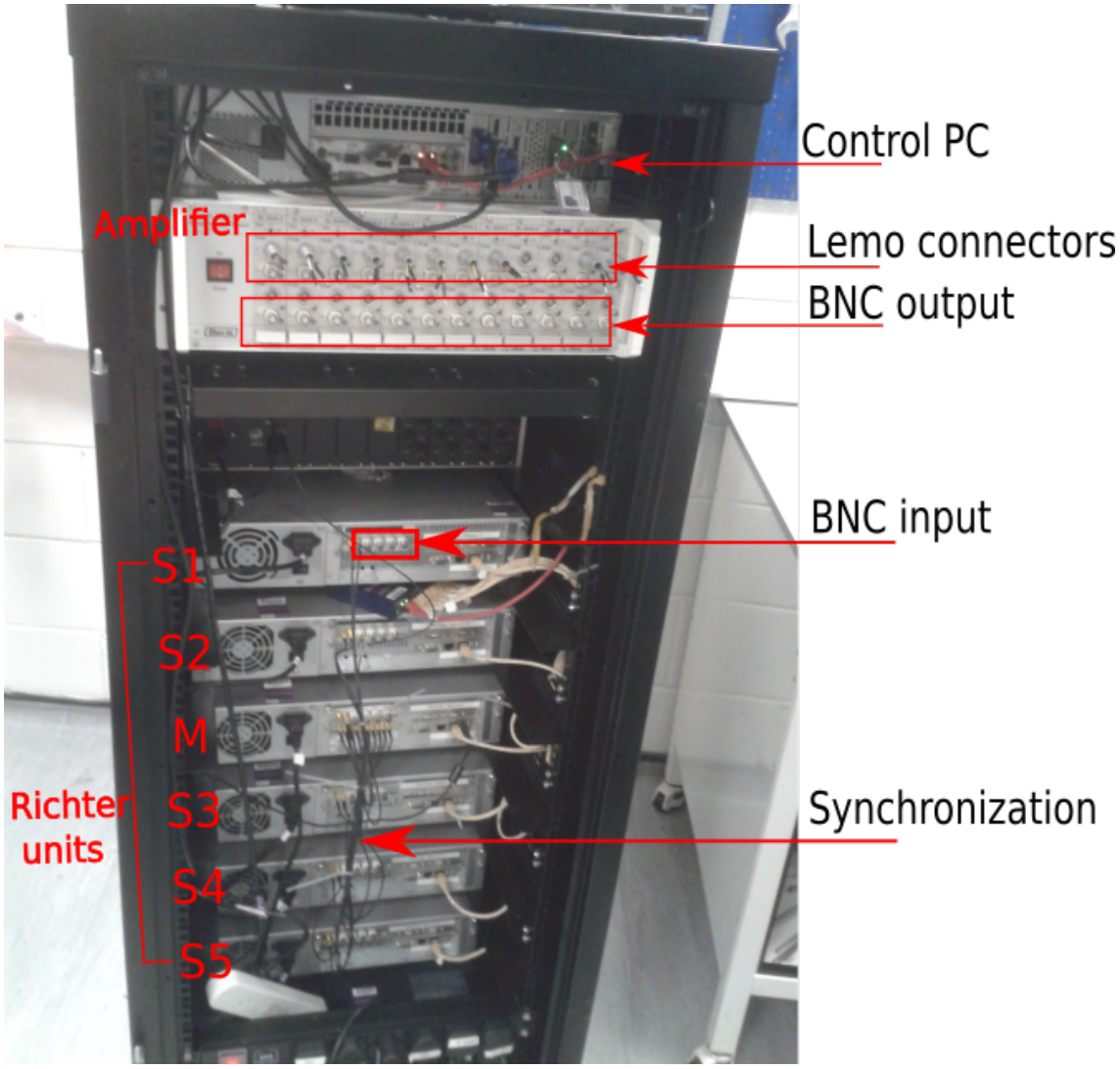

FIGURE 2.8: Photograph of the acquisition system. The strain gauges signals are transmitted by Lemo connectors to a conditioning unit which contains the Wheastone briges and amplifies the signals. The amplified signals are connected to synchronized analog-to-digital converter units called richters, via BNC cables. All the units are controlled by a PC, with Insite software from ITASCA^{TM}.

3-wire Wheatstone bridge configuration

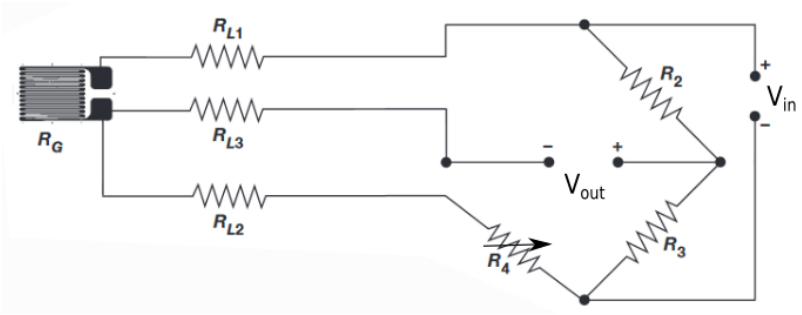

FIGURE 2.9: Three-wire quarter-bridge circuit from www.vishaypg.com

Strain gauges in a 3-wires quarter-bridge configuration are used, and the output voltage $V_{out}(t)$ is measured. Adjusting the output voltage $V_{out} = 0$ when $\epsilon = 0$ by changing the value of the resistor R4 (see fig. 2.9), then $\epsilon(t)$ can be obtained by the relation:

$$\epsilon(t) = \frac{-4V_{out}(t)}{G_f(V_{in} + 2V_{out}(t))} \tag{2.4}$$

Where V_{in} is the bridge excitation voltage, and G_f is the gauge factor (generally equal to 2).

Grid configurations for stress calculations

The rosette strain gauges enable me to measure the 2D strain tensor during our experiments. Here I present the different configurations used, and how to obtain the stresses from them. The gauges were fixed on polycarbonate surfaces (fig. 2.10.a) or on the rock samples (fig. 2.10.b), using Loctite® 424 adhesive (ethyl-based cyanoacrylate). When using polycarbonate, because of the low heat dissipation, I also placed a copper sheet (1 cm by 1 cm) on top of the gauges to avoid heating of the interface which could alter the stress measurements.

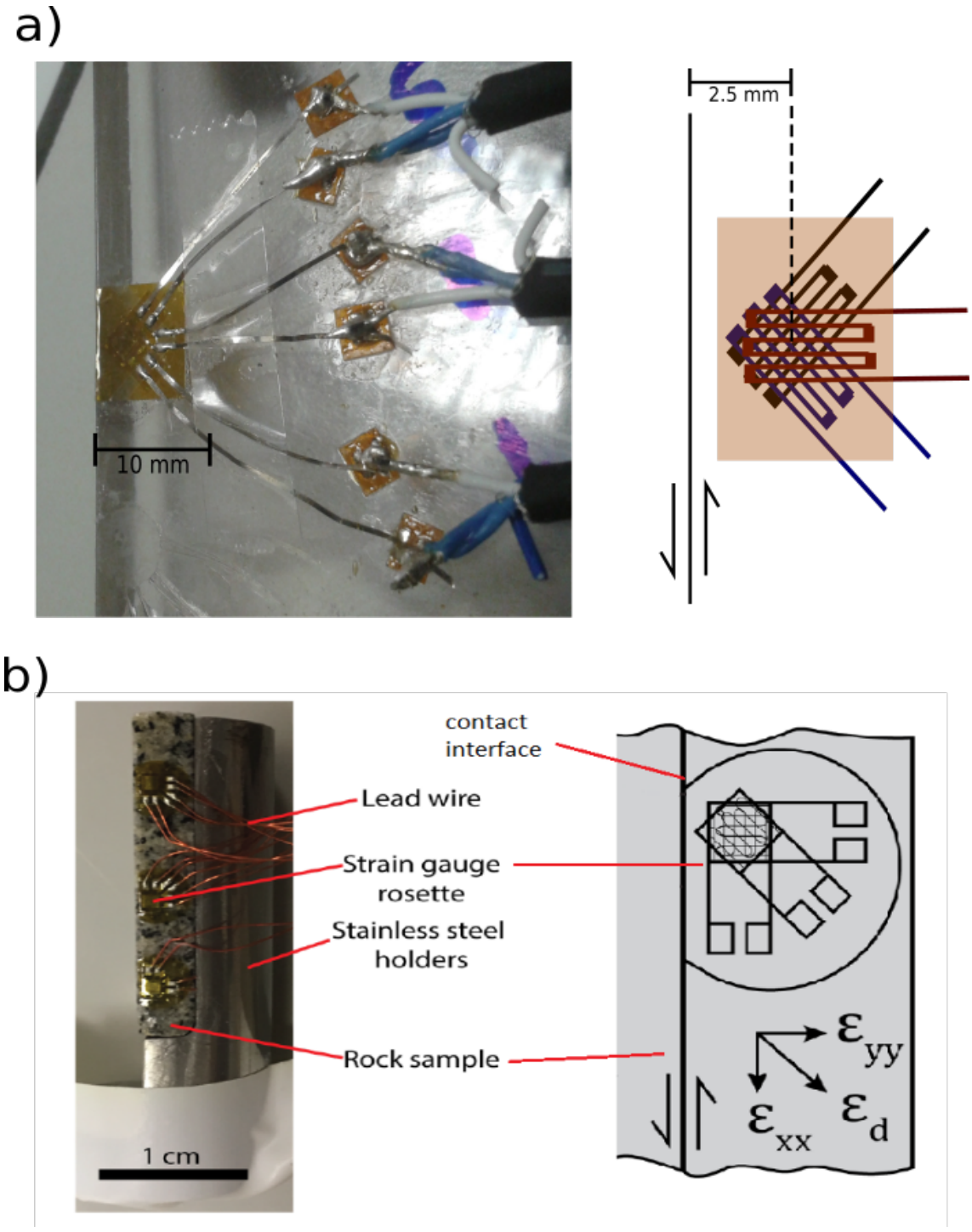

FIGURE 2.10: a) Example of 3-component rosette strain gauges used on polycarbonate. The three strain components oriented at 45°, 90° and 135° to the interface plane are used. b) a) Example of 3-component rosette strain gauges used on rocks (Micro Measurements G1350, 120 Ohms), photography and sketch from Harbord, 2018. In this case, only the components oriented at 0° (ϵ_{xx}) and 45° (ϵ_d) are usually used.

The 3 stacked gauge grids enable me to measure the strains ϵ_1, ϵ_2, ϵ_3 in 3 different orientations θ_1, θ_2, θ_3, along axes u_1, u_2 and u_3 respectively (fig. 2.11).

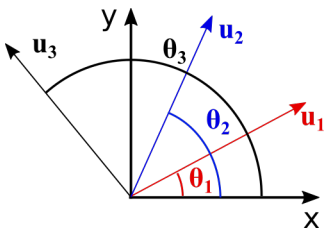

FIGURE 2.11: Rotation of strains

If x is the axis aligned with the interface, the parallel, perpendicular and shear components of strain ϵ_{xx}, ϵ_{yy} and γ_{xy} can be inverted using :

$$\epsilon_{i=1,2,3} = \epsilon_{xx}(\cos\theta_i)^2 + \epsilon_{yy}(\sin\theta_i)^2 + \gamma_{xy}\sin\theta_i\cos\theta_i \tag{2.5}$$

For the biaxial experiments (fig. 2.10.a), $\theta_1 = 45°$, $\theta_2 = 90°$, $\theta_3 = 135°$, which reduces to:

$$\begin{cases} \epsilon_{xx} = \epsilon_3 + \epsilon_1 - \epsilon_2 \\ \epsilon_{yy} = \epsilon_2 \\ \gamma_{xy} = \epsilon_1 - \epsilon_3 \end{cases} \tag{2.6}$$

The stresses can then be retrieved using Hooke's law:

$$\begin{cases} \sigma_{xx} = \frac{E}{1-\nu^2}(\epsilon_{xx} + \nu\epsilon_{yy}) \\ \sigma_{yy} = \frac{E}{1-\nu^2}(\epsilon_{yy} + \nu\epsilon_{xx}) \\ \sigma_{xy} = G\gamma_{xy} = \frac{E}{2(1+\nu)}\gamma_{xy} \end{cases} \tag{2.7}$$

In the triaxial vessel, I assume the normal stress σ_n to be roughly constant and equal to the confining pressure P_{conf} (it generally does not vary significantly during the passage of a rupture front, and it has been checked on polycarbonate, figure 2.12). In this case, by measuring the fault-parallel strain ϵ_{xx}, and the strain at 45° ϵ_d, the experiments and calculations can be simplified, as only two strain gauges are needed in this case.

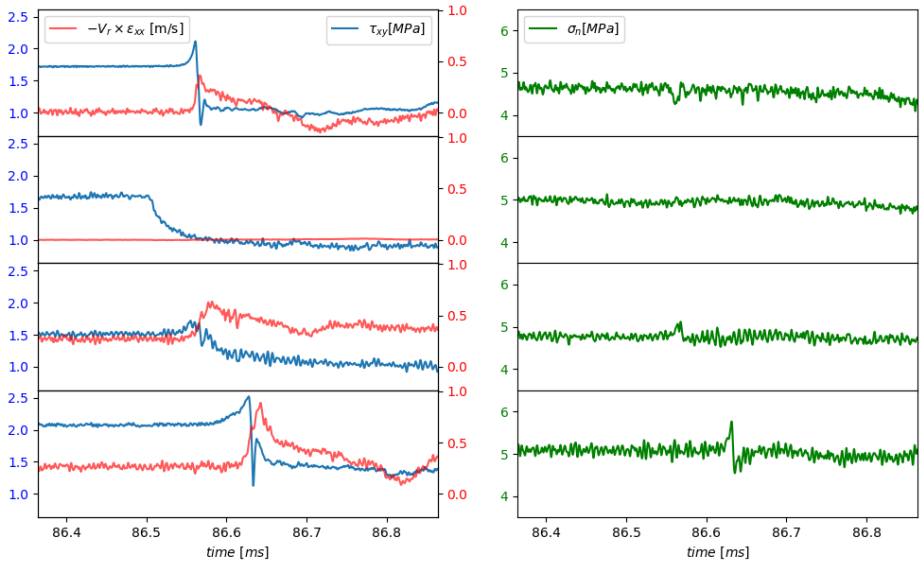

FIGURE 2.12: Example of strain gauge signals recorded during a rupture and filtered at 500 kHz a) Shear stresses τ_{xy} and fault parallel particle velocities $-V_r\epsilon_{xx}$ recorded at the 4 different locations 5 cm apart b) Normal stresses σ_n recorded at the same locations. The initial shear stresses τ_0, peak stresses τ_p and residual stresses τ_r can be distinguished in the shear stress record on the left. in general, the normal stresses measured σ_n do not vary significantly during ruptures .

From Hooke's law:

$$\sigma_n = \sigma_{yy} = \lambda(\epsilon_{xx} + \epsilon_{yy}) + 2G\epsilon_{yy} \tag{2.8}$$

Which gives:

$$\epsilon_{yy} = -\frac{\lambda}{\lambda + 2G}\epsilon_{xx} + \frac{\sigma_{yy}}{\lambda + 2G} \tag{2.9}$$

Then using eq. 2.5, with $\theta = \pi/4$ (meaning $\cos^2(\theta) = \sin^2(\theta) = \cos(\theta)\sin(\theta) = 1/2$), we obtain:

$$\epsilon_d = \frac{1}{2}(\epsilon_{xx} + \epsilon_{yy} + \gamma_{xy}) \tag{2.10}$$

and therefore:

$$\gamma_{xy}(=2\epsilon_{xy}) = 2\epsilon_d + \epsilon_{xx}(\frac{\lambda}{\lambda+2G} - 1) - \frac{\sigma_{yy}}{\lambda+2G} \tag{2.11}$$

The shear stress τ_{xy} is finally given by:

$$\tau_{xy} = G\gamma_{xy} = 2G\epsilon_d + G\epsilon_{xx}(\frac{\lambda}{\lambda+2G} - 1) - \frac{G\sigma_{yy}}{\lambda+2G} \tag{2.12}$$

which assuming a Poisson's ratio of 0.25 ($\lambda = G$) simplifies to :

$$\tau_{xy} = 2G(\epsilon_d - \frac{\epsilon_{xx}}{3}) - \frac{\sigma_{yy}}{3} \tag{2.13}$$

The strain gauges could also be used with orientations of 45° and 135°. In term of noise, it would mean that for $\gamma_{xy} = \epsilon_{45°} - \epsilon_{135°}$ (assuming $\nu = 0.25$), the electromagnetic noise sensed identically by the gauge grids ϵ_{err} would be suppressed ($\epsilon_{err}^{tot} = \epsilon_{err} - \epsilon_{err}$). However, as we might also be interested in calculating ϵ_{xx}, a quick calculation shows that in this case, assuming $\nu = 0.25$, $\epsilon_{err}^{tot} = 3\epsilon_{err}$. When ϵ_d at 45° and ϵ_{xx} are measured directly, $\epsilon_{err}^{tot} = \epsilon_{err}$ for ϵ_{xx}, and $\epsilon_{err}^{tot} = 2/3\epsilon_{err}$ for ϵ_d. When only two strain gauges are used, assuming σ_{yy} constant, I therefore prefer to use ϵ_d and ϵ_{xx} as a compromise for noise reduction.

In spite of this precaution, along with minimising the exposed parts of wires (not shielded), the noise is still significant on the amplified signals and I usually apply a low-pass filter with a cut-off frequency of 500 kHz to visualize the dynamic stress variations (see fig. 2.12).

Slip calculation for the friction law

In order to obtain the relative slip to plot the friction laws I use the same method presented in Svetlizky and Fineberg (2014). Assuming that the rupture front is at steady-state and propagating at constant velocity V_r (we can check using the high speed camera), the relative slip velocity $V(x,t)$ (twice the particle velocity on one side of the fault) can be obtained using the measurement of fault-parallel strain:

$$V(x,t) = 2\,\frac{\partial u(x,t)}{\partial t} = 2\,\frac{\partial u(x-V_r t)}{\partial t} = 2\,\frac{\partial u}{\partial x}\frac{\partial x}{\partial t} = -2\,V_r \epsilon_{xx}(x,t) \tag{2.14}$$

Where u is the particle displacement in the x direction (parallel to the fault). Now defining $t = t_0$ as the time just before a rupture front passes at the position of the strain gauge at x, and $\epsilon^0_{xx} = \epsilon_{xx}(t_0)$, the fault slip U is obtained using:

$$U(x,t) = \int_{t_0}^{t} 2\frac{\partial u(x,t')}{\partial t'}dt' = -2\,V_r \int_{t_0}^{t} \left(\epsilon_{xx}(x,t') - \epsilon^0_{xx}\right)dt' \tag{2.15}$$

This method is used in Chapter 3, which presents experimental results of strain gauge data during dynamic ruptures. It enables to obtain the friction coefficient dependence on slip and slip velocity. The method is also tested and validated using the numerical models presented in chapters 4 and 6.

2.3 Numerical methods

The numerical methods used in order to simulate the experiments are presented here. Two main modelling methods are used: the finite difference and the finite element methods. While the Finite Element Method (FEM) is an efficient way of modelling static deformations of elastic materials (see sections 4.1 and 6.1 of chapters 4 and 6 respectively), it is computationally expensive. When modelling dynamic ruptures in sections 4.2 and 6.2, we therefore prefer to use the finite difference method which is more efficient in the case of dynamic problems.

2.3.1 Finite differences

I present here a brief description of the finite difference scheme used for dynamic rupture simulations in chapters 4 and 6.

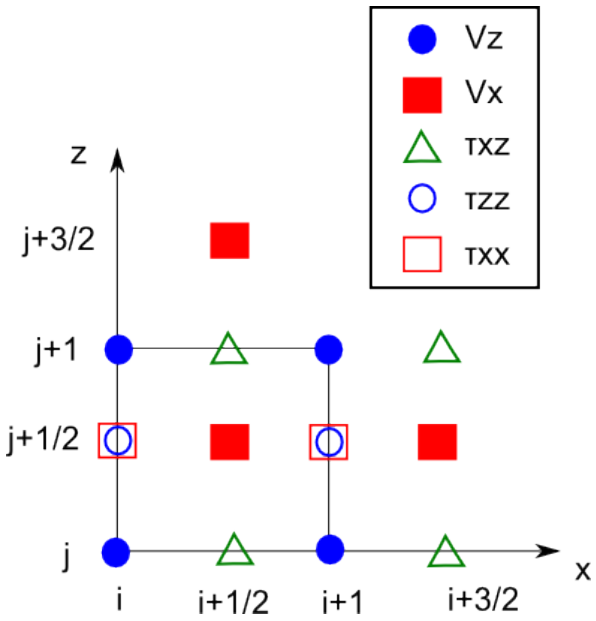

FIGURE 2.13: Finite-difference staggered grid for the 2D stress-velocity form of the wave equation after Virieux and Madariaga, 1982. Velocities are defined at time t, and stresses at time t+1/2

The finite-difference method consists of approximating the spatial and temporal derivatives of a problem, at specified grid points, using values at nearby grid points. A popular approach for rupture modelling is described by Virieux and Madariaga, 1982, and a similar method was also used by Andrews, 1976.

For the 2D stress-velocity form of the wave equation, I use a staggered grid (fig. 2.13) and the five discretized equations (eqs. 2.17) describing the evolution of particle velocities V_x and V_z in x and z directions, and of the stresses τ_{xx}, τ_{zz} and τ_{xz} (Virieux and Madariaga, 1982), obtained from equations 2.16.

$$\begin{aligned}
\frac{\partial v_x}{\partial t} &= \frac{1}{\rho}\left(\frac{\partial \tau_{xx}}{\partial x} + \frac{\partial \tau_{xz}}{\partial z}\right) \\
\frac{\partial v_z}{\partial t} &= \frac{1}{\rho}\left(\frac{\partial \tau_{xz}}{\partial x} + \frac{\partial \tau_{zz}}{\partial z}\right) \\
\frac{\partial \tau_{xx}}{\partial t} &= (\lambda + 2G)\frac{\partial v_x}{\partial x} + \lambda \frac{\partial v_z}{\partial z} \\
\frac{\partial \tau_{zz}}{\partial t} &= (\lambda + 2G)\frac{\partial v_z}{\partial z} + \lambda \frac{\partial v_x}{\partial x} \\
\frac{\tau_{xz}}{\partial t} &= G\left(\frac{\partial v_x}{\partial z} + \frac{\partial v_z}{\partial x}\right)
\end{aligned} \tag{2.16}$$

$$\begin{aligned}
V_x\Big|_{i+1/2,\,j+1/2}^{t+1} &= V_x\Big|_{i+1/2,\,j+1/2}^{t} + \frac{dt}{\rho}\left(\frac{\tau_{xx}\Big|_{i+1,\,j+1/2}^{t+1/2} - \tau_{xx}\Big|_{i,\,j+1/2}^{t+1/2}}{dx} + \frac{\tau_{xz}\Big|_{i+1/2,\,j+1}^{t+1/2} - \tau_{xz}\Big|_{i+1/2,\,j}^{t+1/2}}{dz}\right) \\
V_z\Big|_{i+1,\,j+1}^{t+1} &= V_z\Big|_{i+1,\,j+1}^{t} + \frac{dt}{\rho}\left(\frac{\tau_{xz}\Big|_{i+3/2,\,j+1}^{t+1/2} - \tau_{xz}\Big|_{i+1/2,\,j+1}^{t+1/2}}{dx} + \frac{\tau_{zz}\Big|_{i+1,\,j+3/2}^{t+1/2} - \tau_{zz}\Big|_{i+1,\,j+1/2}^{t+1/2}}{dz}\right) \\
\tau_{xx}\Big|_{i+1,\,j+1/2}^{t+3/2} &= \tau_{xx}\Big|_{i+1,\,j+1/2}^{t+1/2} + dt\left((\lambda + 2G)\frac{V_x\Big|_{i+3/2,\,j+1/2}^{t+1} - V_x\Big|_{i+1/2,\,j+1/2}^{t+1}}{dx} + \lambda\frac{V_z\Big|_{i+1,\,j+1}^{t+1} - V_z\Big|_{i+1,\,j}^{t+1}}{dz}\right) \\
\tau_{zz}\Big|_{i+1,\,j+1/2}^{t+3/2} &= \tau_{zz}\Big|_{i+1,\,j+1/2}^{t+1/2} + dt\left(\lambda\frac{V_x\Big|_{i+3/2,\,j+1/2}^{t+1} - V_x\Big|_{i+1/2,\,j+1/2}^{t+1}}{dx} + (\lambda + 2G)\frac{V_z\Big|_{i+1,\,j+1}^{t+1} - V_z\Big|_{i+1,\,j}^{t+1}}{dz}\right) \\
\tau_{xz}\Big|_{i+1/2,\,j+1}^{t+3/2} &= \tau_{xz}\Big|_{i+1/2,\,j+1}^{t+1/2} + Gdt\left(\frac{V_x\Big|_{i+1/2,\,j+3/2}^{t+1} - V_x\Big|_{i+1/2,\,j+1/2}^{t+1}}{dz} + \frac{V_z\Big|_{i+1,\,j+1}^{t+1} - V_z\Big|_{i,\,j+1}^{t+1}}{dx}\right)
\end{aligned} \tag{2.17}$$

The critical time-step is dt $\leq min(\Delta x, \Delta z)/V_p$ to ensure a stable solution.

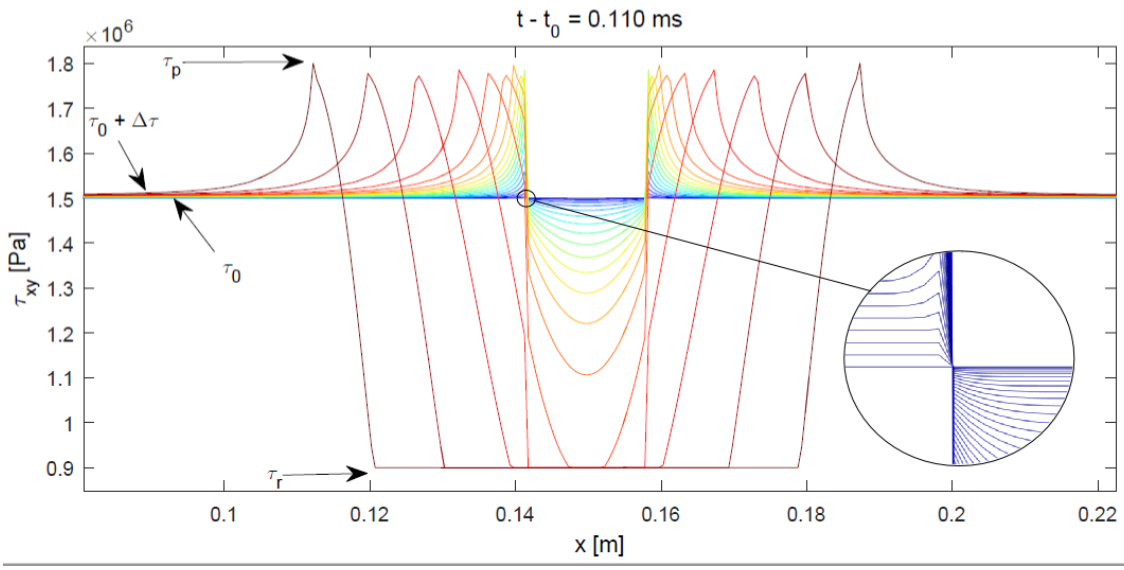

FIGURE 2.14: Example of stress drop along a defined interface, during a dynamic rupture numerical simulation, using finite-differences, and a linear slip-weakening friction law. On the figure, $\Delta\tau = \dot{\tau} \times (t - t_0)$, t_0 being the start of the simulation, at which I start forcing the stress to drop at a rate $\dot{\tau}$ inside the predefined patch between x = 0.14 m and x = 0.16 m.

In order to model a dynamic rupture, I force the shear stress to increase everywhere at a rate of $\dot{\tau}$ along a line which corresponds to the interface in the 2D model, except inside a pre-defined patch (from 0.14 to 0.16 m in fig. 2.14). The relative lower shear stress within this patch induces some increase of relative dispacement. As the relative displacement increases, the shear stress decreases further inside the patch, according to a prescribed slip-weakening friction law which gives the relation between shear stress and relative displacement, as implemented in Andrews (1976) (linear decrease from τ_p to τ_r after a relative slip amount equal to the critical slip-weakening distance D_c). While the stress drops inside the patch, it also increases outside of it, at the crack tips, therefore driving its growth. One remarkable result from Andrews (1976), using this relatively simple model, is the possibility for a transition from sub-shear to supershear rupture velocities.

2.3.2 Finite elements

Basic 1D spring model

The FEM consists in discretizing a domain into so-called elements, in order to solve the partial differential equations governing a physical problem. In this case, I apply the method to linear elasticity, and LEFM.

I present here the simplest model possible in order to understand the concept of the FEM, as described in Ottosen and Petersson, 1992. Consider a spring at equilibrium subjected to forces $-\overrightarrow{F}$ and $\overrightarrow{F}$ at the left and right nodes respectively, so that $\Sigma\overrightarrow{F} = \overrightarrow{0}$ (fig. 2.15.a). If the spring stiffness is noted k, then the nodal forces and displacements are linked by:

$$F = k(u2 - u1); \text{ considering the right node} \tag{2.18}$$

$$-F = k(u1 - u2); \text{ considering the left node} \tag{2.19}$$

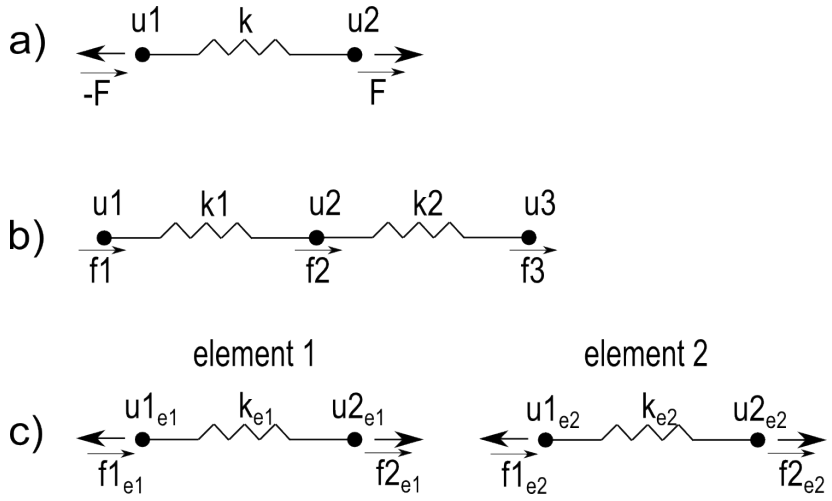

FIGURE 2.15: a) Spring subjected to simple traction. b) Two springs system subject to a simple traction with global forces and displacements. c) Two springs system decomposed into two elements with local forces and displacements

Now instead of a single spring, consider a system of two springs with two end nodes and a third one in the middle connecting them (fig. 2.15.b), where we would like to relate the global nodal displacements u1, u2 and u3 to the global nodal forces $\overrightarrow{f1}$, $\overrightarrow{f2}$ and $\overrightarrow{f3}$. In the FEM, we start by considering each spring

with its associated nodes individually as a so-called element (fig. 2.15.c). A single global node can belong to several elements; u2 belongs to element 1 and element 2 in this case, and depending if I refer to the node in element 1 or element 2, I will refer to it as $u2_{e1}$ or $u1_{e2}$, respectively. Now that the physical domain is divided into elements, the displacement-force relations (see eq. 2.19) can be written for each of the elements, in a matrix form $\underline{k_{ei}}\vec{u} = \vec{f}_{ei}$: For element 1:

$$\begin{bmatrix} k_{e1} & -k_{e1} \\ -k_{e1} & k_{e1} \end{bmatrix} \begin{Bmatrix} u1_{e1} \\ u2_{e1} \end{Bmatrix} = \begin{Bmatrix} f1_{e1} \\ f2_{e1} \end{Bmatrix} \tag{2.20a}$$

And for element 2:

$$\begin{bmatrix} k_{e2} & -k_{e2} \\ -k_{e2} & k_{e2} \end{bmatrix} \begin{Bmatrix} u1_{e2} \\ u2_{e2} \end{Bmatrix} = \begin{Bmatrix} f1_{e2} \\ f2_{e2} \end{Bmatrix} \tag{2.20b}$$

Which, written as a function of the global displacements $\vec{u} = \begin{Bmatrix} u1 & u2 & u3 \end{Bmatrix}^T$, is equivalent to:

$$\begin{bmatrix} k_{e1} & -k_{e1} & 0 \\ -k_{e1} & k_{e1} & 0 \\ 0 & 0 & 0 \end{bmatrix} \begin{Bmatrix} u1 \\ u2 \\ u3 \end{Bmatrix} = \begin{Bmatrix} f1_{e1} \\ f2_{e1} \\ 0 \end{Bmatrix} \tag{2.21a}$$

And

$$\begin{bmatrix} 0 & 0 & 0 \\ 0 & k_{e2} & -k_{e2} \\ 0 & -k_{e2} & k_{e2} \end{bmatrix} \begin{Bmatrix} u1 \\ u2 \\ u3 \end{Bmatrix} = \begin{Bmatrix} 0 \\ f1_{e2} \\ f2_{e2} \end{Bmatrix} \tag{2.21b}$$

Then the forces can be added given the fact that $\overrightarrow{f2} = \overrightarrow{f2_{e1}} + \overrightarrow{f1_{e2}}$ (= 0 at equilibrium) to obtain:

$$\begin{aligned} \vec{f} &= \begin{Bmatrix} f1 \\ f2 \\ f3 \end{Bmatrix} = \begin{Bmatrix} f1_{e1} \\ f2_{e1} + f1_{e2} \\ f2_{e2} \end{Bmatrix} = \begin{Bmatrix} f1_{e1} \\ f2_{e1} \\ 0 \end{Bmatrix} + \begin{Bmatrix} 0 \\ f1_{e2} \\ f2_{e2} \end{Bmatrix} \\ &= \vec{f_{e1}} + \vec{f_{e2}} = \underline{k_{e1}}\vec{u} + \underline{k_{e2}}\vec{u} = \left[\underline{k_{e1}} + \underline{k_{e2}}\right]\vec{u} = \underline{K}\vec{u} \end{aligned} \tag{2.22}$$

$\underline{K}$ is called the stiffness matrix and $\vec{f}$ the load vector. At equilibrium, the system written in full would be:

$$\begin{bmatrix} k_{e1} & -k_{e1} & 0 \\ -k_{e1} & k_{e1} + k_{e2} & -k_{e2} \\ 0 & -k_{e2} & k_{e2} \end{bmatrix} \begin{Bmatrix} u1 \\ u2 \\ u3 \end{Bmatrix} = \begin{Bmatrix} -f1 \\ 0 \\ f1 \end{Bmatrix} \tag{2.23}$$

Which could be solved using $\vec{u} = \underline{K}^{-1}\vec{f}$.

However one can notice that this particular system would have an infinity of solutions as there are an infinity of displacements $\vec{u}$ able to satisfy the prescribed forces (the inverse problem is ill-posed, and in mathematical terms $\det \underline{K} = 0$).

Therefore one has to be careful about which boundary conditions are applied. In this case we might for instance prescribe a fixed displacement at the left node $u1 = d$. In order to enforce this displacement, the following modifications are made:

$$\begin{bmatrix} k_{e1} & -k_{e1} & 0 \\ -k_{e1} & k_{e1} + k_{e2} & -k_{e2} \\ 0 & -k_{e2} & k_{e2} \end{bmatrix} \text{ becomes } \begin{bmatrix} 1 & 0 & 0 \\ 0 & k_{e1} + k_{e2} & -k_{e2} \\ 0 & -k_{e2} & k_{e2} \end{bmatrix}$$

And

$$\begin{Bmatrix} -f1 \\ 0 \\ f1 \end{Bmatrix} \text{becomes} \begin{Bmatrix} d \\ 0 - k_{e1} \times d \\ f1 - 0 \times d \end{Bmatrix}$$

So that the initial system

$$\begin{cases} k_{e1}u1 - k_{e1}u2 = f1 \\ k_{e1}u1 + (k_{e1} + k_{e2})u2 - k_{e2}u3 = 0 \\ -k_{e2}u2 + k_{e2}u3 = -f1 \end{cases} \tag{2.24}$$

becomes

$$\begin{cases} u1 = d \\ (k_{e1} + k_{e2})u2 - k_{e2}u3 = -k_{e1}d \\ -k_{e2}u2 + k_{e2}u3 = -f1 \end{cases} \tag{2.25}$$

The trivial equation $u1 = d$ can be deleted, and the system with 2 equations and 2 unknowns be solved. Because one node is fixed, there will be only one solution satisfying the system.

In order to add a point force at a given node, it is easier and only needs to be added to the load vector at the corresponding index.

2D elasticity with rectangular elements

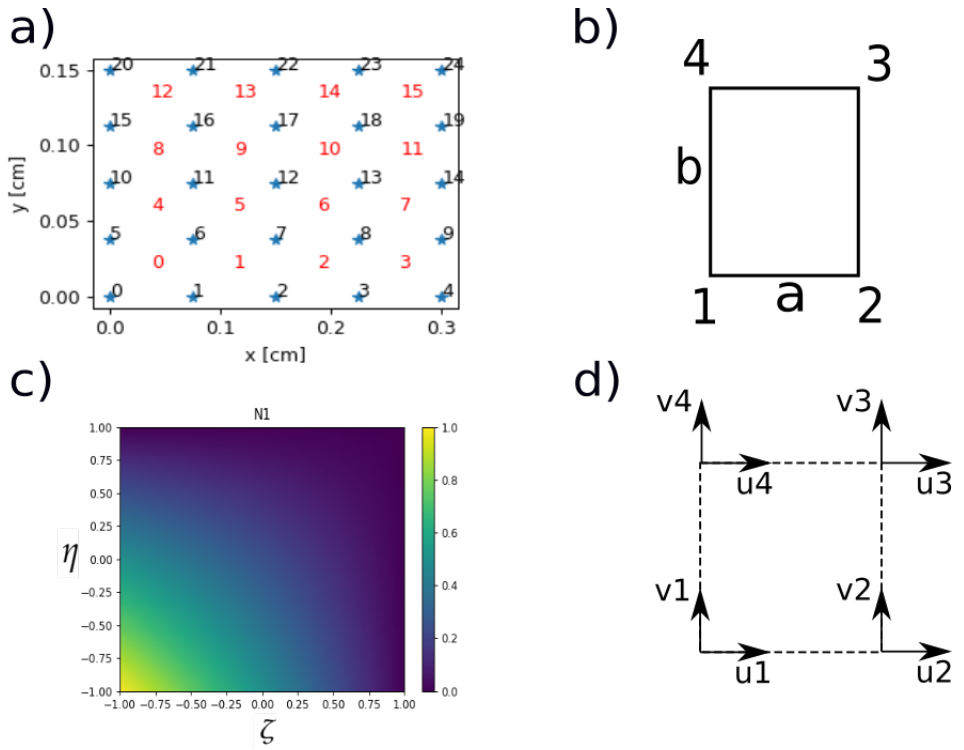

FIGURE 2.16: a) Grid example with global nodes (blue) and elements numbers (red). b) Rectangular element of length a and b in the physical domain. c) Example of shape function N1 in local coordinates d) Local degrees of freedom of an element

For 2D problems using rectangular elements the principle is the same as with the spring example. Starting from the constitutive equations:

$$\begin{cases} \frac{\partial \sigma_{xx}}{\partial x} + \frac{\partial \tau_{xy}}{\partial y} + F_x \\ \frac{\partial \sigma_{yy}}{\partial y} + \frac{\partial \tau_{xy}}{\partial x} + F_y \end{cases} \tag{2.26}$$

Where F_x and F_y are the body forces, using the displacements u and v in x and y direction, equation 2.26 can be written (Smith et al., 2013):

$$\frac{E}{1-\nu^2}\left(\frac{\partial^2 u}{\partial x^2} + \frac{1-\nu}{2}\frac{\partial^2 u}{\partial y^2} + \nu\frac{\partial v}{\partial x \partial y} + \frac{1-\nu}{2}\frac{\partial^2 v}{\partial y \partial x}\right) = -F_x \tag{2.27a}$$

$$\frac{E}{1-\nu^2}\left(\nu\frac{\partial^2 u}{\partial y \partial x} + \frac{1-\nu}{2}\frac{\partial^2 u}{\partial x \partial y} + \frac{1-\nu}{2}\frac{\partial^2 v}{\partial x^2} + \frac{\partial^2 v}{\partial y^2}\right) = -F_y \tag{2.27b}$$

From here the displacements can be approximated using the so-called shape functions. Those shape functions can be polynomials of high-order or linear in the simplest case. They can be defined in a local coordinate system (ζ,η) which maps the physical coordinates (x,y) in a domain comprised between -1 and 1, used for the numerical integration. For 4-node rectangular elements, the linear shape functions N1, N2, N3 and N4 in the local coordinate space have the form:

$$\begin{cases} N1 = (1-\frac{x}{a})(1-\frac{y}{b}) & \equiv \frac{1}{4}(1-\zeta)(1-\eta) \\ N2 = \frac{x}{a}(1-\frac{y}{b}) & \equiv \frac{1}{4}(1+\zeta)(1-\eta) \\ N3 = \frac{x}{a}\frac{y}{b} & \equiv \frac{1}{4}(1+\zeta)(1+\eta) \\ N4 = (1-\frac{x}{a})\frac{y}{b} & \equiv \frac{1}{4}(1-\zeta)(1+\eta) \end{cases} \tag{2.28}$$

An example of shape function is shown in fig. 2.16.c . N1 is for instance equal to 0 at every node except the local node 1 (fig. 2.16.b-c). Using those shape functions, the displacement (assumed linear) inside an element e can be approximated as:

$$u_e(x,y) = \Sigma N_i u_i = \begin{Bmatrix} N1 & N2 & N3 & N4 \end{Bmatrix} \cdot \begin{Bmatrix} u1 & u2 & u3 & u4 \end{Bmatrix}^T \tag{2.29}$$

where u1, u2, u3, u4 are the nodal displacements in x-direction (fig. 2.16.d). A similar relation is valid for v1, v2, v3 and v4, the nodal displacements in the y-direction: $v_e(x,y) = \Sigma N_i v_i$. The nodal displacements in x and y directions are usually called degrees of freedom (dof) and commonly gathered in one single displacement vector $\vec{u} = \begin{Bmatrix} u1 & u2 & u3 & u4 & v1 & v2 & v3 & v4 \end{Bmatrix}^T$.

Then the FEM consists in using those approximations in equations 2.27a-2.27b, and by multiplying 2.27a and 2.27b each by the 4 shape functions, a set of 8 equations necessary to solve for the 8 unknowns in $\vec{u}$ is obtained. Both sides of the equations are then integrated by parts which enables us to avoid having the second derivatives of displacements appearing (otherwise there would be trivial equations 0 = 0 as the second derivative of a linear function would be zero).

Following those steps, we end up with the following set of equations for an element (Szabo and Lee, 1969):

$$\frac{E}{1-\nu^2}\int_0^a\int_0^b \begin{bmatrix} (\frac{\partial N_i}{\partial x}\frac{\partial N_j}{\partial x}+\frac{1-\nu}{2}\frac{\partial N_i}{\partial y}\frac{\partial N_j}{\partial y}) & (\nu\frac{\partial N_i}{\partial x}\frac{\partial N_j}{\partial y}+\frac{1-\nu}{2}\frac{\partial N_i}{\partial y}\frac{\partial N_j}{\partial x}) \\ (\nu\frac{\partial N_i}{\partial y}\frac{\partial N_j}{\partial x}+\frac{1-\nu}{2}\frac{\partial N_i}{\partial x}\frac{\partial N_j}{\partial y}) & (\frac{\partial N_i}{\partial y}\frac{\partial N_j}{\partial y}+\frac{1-\nu}{2}\frac{\partial N_i}{\partial x}\frac{\partial N_j}{\partial x}) \end{bmatrix} dxdy \cdot \vec{u} = \vec{f} \tag{2.30}$$

Which gives an element stiffness matrix $\underline{ke}$ in the matrix form:

$$\underline{ke} = \int \underline{B}^T \underline{DB} dV \tag{2.31}$$

If the terms in $\vec{u}$ are rearranged such that $\vec{u} = \begin{Bmatrix} u1 & v1 & u2 & v2 & u3 & v3 & u4 & v4 \end{Bmatrix}^T$ $\underline{B}$, the matrix containing the shape functions derivatives is given by:

$$\underline{B} = \begin{bmatrix} \frac{\partial N1}{\partial x} & 0 & \frac{\partial N2}{\partial x} & 0 & \frac{\partial N3}{\partial x} & 0 & \frac{\partial N4}{\partial x} & 0 \\ 0 & \frac{\partial N1}{\partial y} & 0 & \frac{\partial N2}{\partial y} & 0 & \frac{\partial N3}{\partial y} & 0 & \frac{\partial N4}{\partial y} \\ \frac{\partial N1}{\partial y} & \frac{\partial N1}{\partial x} & \frac{\partial N2}{\partial y} & \frac{\partial N2}{\partial x} & \frac{\partial N3}{\partial y} & \frac{\partial N3}{\partial x} & \frac{\partial N4}{\partial y} & \frac{\partial N4}{\partial x} \end{bmatrix} \tag{2.32}$$

and using the chain rule:

$$\underline{B} = 2\begin{bmatrix} \frac{1}{a}\frac{\partial N1}{\partial \zeta} & 0 & \frac{1}{a}\frac{\partial N2}{\partial \zeta} & 0 & \frac{1}{a}\frac{\partial N3}{\partial \zeta} & 0 & \frac{1}{a}\frac{\partial N4}{\partial \zeta} & 0 \\ 0 & \frac{1}{b}\frac{\partial N1}{\partial \eta} & 0 & \frac{1}{b}\frac{\partial N2}{\partial \eta} & 0 & \frac{1}{b}\frac{\partial N3}{\partial \eta} & 0 & \frac{1}{b}\frac{\partial N4}{\partial \eta} \\ \frac{1}{b}\frac{\partial N1}{\partial \eta} & \frac{1}{a}\frac{\partial N1}{\partial \zeta} & \frac{1}{b}\frac{\partial N2}{\partial \eta} & \frac{1}{a}\frac{\partial N2}{\partial \zeta} & \frac{1}{b}\frac{\partial N3}{\partial \eta} & \frac{1}{a}\frac{\partial N3}{\partial \zeta} & \frac{1}{b}\frac{\partial N4}{\partial \eta} & \frac{1}{a}\frac{\partial N4}{\partial \zeta} \end{bmatrix} \tag{2.33}$$

The elements of $\underline{ke}$ are then integrated using the gauss-quadrature method: the integral a function $f(x,y)$ can be approximated by the sum of the value of the function at so-called gauss-points f_i multiplied by weights w_i. For rectangular elements the coordinates of the four gauss points in the local coordinate space and the weights are given by table 2.3

ζ_i	η_i	w_i
$\frac{-1}{\sqrt{3}}$	$\frac{-1}{\sqrt{3}}$	1
$\frac{1}{\sqrt{3}}$	$\frac{-1}{\sqrt{3}}$	1
$\frac{1}{\sqrt{3}}$	$\frac{1}{\sqrt{3}}$	1
$\frac{-1}{\sqrt{3}}$	$\frac{1}{\sqrt{3}}$	1

TABLE 2.3: Gauss points coordinates and weights for 4 -nodes rectangular elements

Equation 2.31 can now be rewritten:

$$\int \underline{B}^T \underline{D}\underline{B} dV = \Sigma_i \Sigma_j \underline{B}^T \underline{D}\underline{B}_{ij} det(\underline{J}) w_{ij}$$

where $\underline{J}$ is the Jacobian which contains the ratio between the physical and local coordinates:

$$\underline{J} = \begin{bmatrix} \frac{\partial x}{\partial \zeta} & \frac{\partial x}{\partial \eta} \\ \frac{\partial y}{\partial \zeta} & \frac{\partial y}{\partial \eta} \end{bmatrix} \tag{2.34}$$

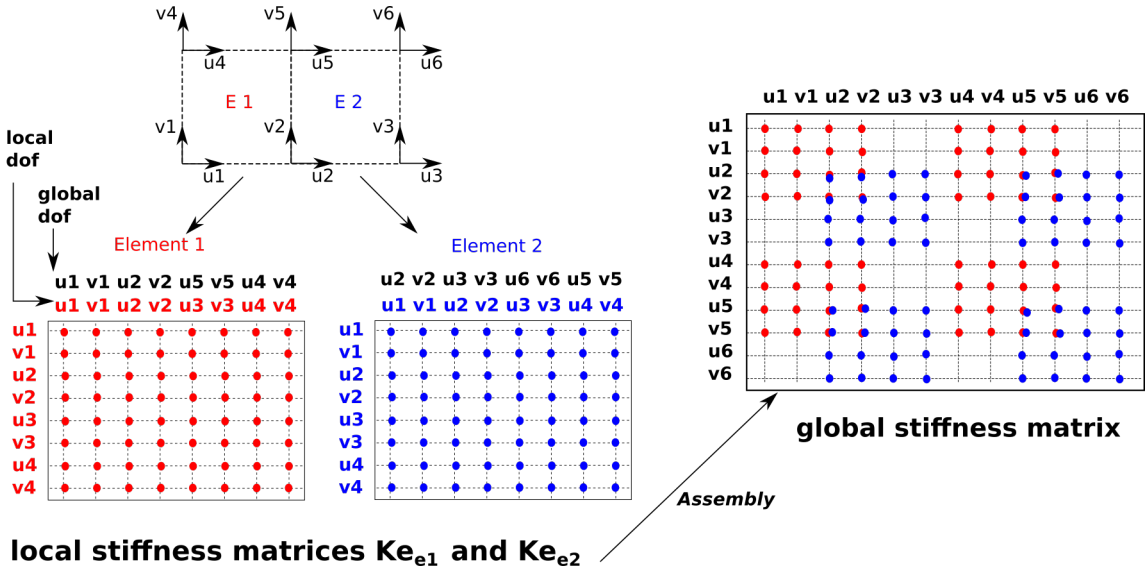

FIGURE 2.17: How to assemble the contribution of 2 elements in a global stiffness matrix. At the locations where there are contributions from several elements, the stiffness matrix values ke_{ij} are summed

The contributions of all the elements are summed in a single global stiffness matrix $\underline{K}$ in the same way as in the example of the spring system (fig. 2.17). All the dof shared between 2 neighbouring elements will have the added contribution of

the 2 elements in the stiffness matrix. It will also be similar to build the force vector and apply the boundary conditions. The system is finally solved using:

$$\vec{u} = \underline{K}^{-1}\vec{f} \tag{2.35}$$

The discontinuous version of finite elements

Until now, the FEM was described for its continuous version, which is assuming that the displacements are continuous in the physical domain. In certain cases and especially for cracks and rupture problems, it is convenient to enable a discontinuity between the elements (corresponding to the location of a precut interface for instance). This numerical scheme is called Discontinuous Galerkin (DG) and I built a python code based on the MATLAB version implemented by Bird et al., 2017 in this thesis (see appendix C for the python scripts). In DG, each element possesses independent dof that are not linked to dof of nearby elements by the volume integral term $\int \underline{B}^T \underline{D}\underline{B} dV$, but by surface fluxes. The assembled global stiffness matrix $\underline{K}$ is therefore a combination of terms coming from the volume integrals and others from the surface integrals. For a domain with $nelx$ elements in x-direction and $nely$ elements in y-direction, the total number of elements $nels$ (hence the total number of volume elemental stiffness matrices $\underline{k}_e^{vol}$) will be $nelx \times nely$, and the total number of faces connecting two elements is $nfaces = 2nels - (nelx + nely)$. Assuming continuity between the elements, $\underline{K}$ can be calculated as (Bird et al., 2017):

$$\begin{aligned} \underline{K} &= \sum_{1}^{nels} \int \underline{B}^T \underline{D}\underline{B} dV + \sum_{1}^{nfaces} \int (C_1 + C_2 + C_3 + C_4) dS \\ &= (\underline{K}_{vol} + \underline{K}_{surf}) \end{aligned} \tag{2.36}$$

where

$$\begin{cases} C_1 = -\underline{B}^{+T} \underline{D}\, \underline{n}^T \underline{N}^+ /2 - \underline{N}^{+T} \underline{n}\, \underline{D}\, \underline{B}^+ /2 + p(\underline{N}^{+T} \underline{N}^+) \\ C_2 = +\underline{B}^{+T} \underline{D}\, \underline{n}^T \underline{N}^- /2 - \underline{N}^{+T} \underline{n}\, \underline{D}\, \underline{B}^- /2 - p(\underline{N}^{+T} \underline{N}^-) \\ C_3 = -\underline{B}^{-T} \underline{D}\, \underline{n}^T \underline{N}^+ /2 + \underline{N}^{-T} \underline{n}\, \underline{D}\, \underline{B}^+ /2 - p(\underline{N}^{-T} \underline{N}^+) \\ C_4 = +\underline{B}^{-T} \underline{D}\, \underline{n}^T \underline{N}^- /2 + \underline{N}^{-T} \underline{n}\, \underline{D}\, \underline{B}^- /2 + p(\underline{N}^{-T} \underline{N}^-) \end{cases} \tag{2.37}$$

The $+$ and $-$ superscripts correspond to the variables in the positive and negative elements around a face, depending on the convention chosen, $\underline{n}$ contains the components of the face normal vector $\hat{n}$, pointing outwards the positive element (see fig. 2.18). p is a penalty term defined as $p = 10\frac{E^*}{h}$. h being the length of the face.

$$\underline{n} = \begin{bmatrix} n_x & 0 & n_y \\ 0 & n_y & n_x \end{bmatrix}$$

And

$$\underline{N} = \begin{bmatrix} N1 & 0 & N2 & 0 & N3 & 0 & N4 & 0 \\ 0 & N1 & 0 & N2 & 0 & N3 & 0 & N4 \end{bmatrix}$$

Those terms are integrated along the surface between two facing elements using 3-points gaussian integration with coordinates and weights summarized in table 2.4. In the example of figure fig. 2.18, ζ is constant for all the gauss points as the surface is oriented vertically; $\zeta = +1$ for the positive element, $\zeta = -1$ for the negative element.

ζ_i or η_i	w_i
$-\sqrt{\frac{3}{5}}$	5/9
0	8/9
$+\sqrt{\frac{3}{5}}$	5/9

TABLE 2.4: Gauss points coordinates and weights for surface terms integration

The assembly procedure is illustrated in fig. 2.18, according to the element topography. The term C1 links only nodes from the positive element, and the term C4 only from the negative element. The terms C2 and C3 are linking nodes from positive and negative elements (see eq. 2.37).

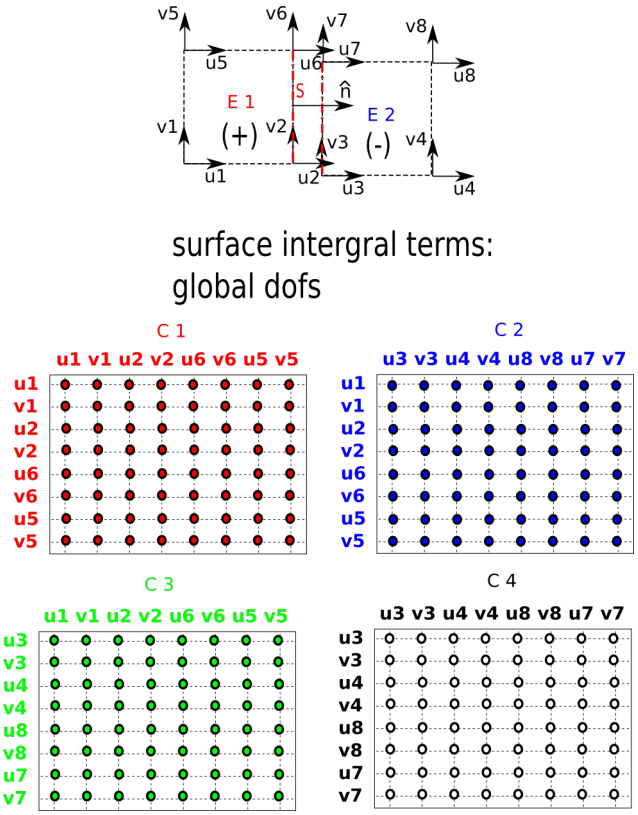

FIGURE 2.18: How to assemble the surface terms C1 to C4 in a global stiffness matrix. At the locations where there is a contributions of several terms, they are summed

For elastodynamic problems the wave equation written from a FEM point of view is:

$$\underline{M}^T \ddot{\vec{u}} + \underline{K}^T \vec{u} = \vec{f} \tag{2.38}$$

If using the centered finite-difference approximation of the time derivative it becomes:

$$\vec{u}_{t+dt} = dt^2 [\underline{M}^T]^{-1} [\vec{f} - \underline{K}^T \vec{u}_t] + 2\vec{u}_t - \vec{u}_{t-dt} \tag{2.39}$$

where $\underline{M}$ is the so-called mass matrix which is assembled in a similar way than for $\underline{K}$, and where the elementary matrices $\underline{M}_e$ are calculated and integrated using:

$$\underline{M}_e = \int \rho \underline{N}^T \underline{N} dV = \Sigma_i \Sigma_j \rho \underline{N}^T \underline{N} det(\underline{J}) w_{ij} \tag{2.40}$$

2.3.3 Overdetermined inversion

Using photoelasticity, it is possible in some cases to obtain informations about the stress field around a crack tip, by inverting the isochromatic fringes (Dally and Riley, 1965). Although it did not work well in the case of the dynamic ruptures, I discuss why in appendix A, and still describe this useful method here.

To understand the inverse problem, it is useful to consider a simple linear fit using the least-square method. Consider a set of points (y_i, x_i) which we want to fit with a function in the form $f(a_1, a_2) = a_1 + a_2 x$. In order to have an optimal fit, we need to adjust the coefficients a_1 and a_2 which minimize the root-mean-squared error $R_2(a_1, a_2) = \sum_{i=1}^{n} [y_i - (a_1 + a_2 x_i)]^2$. The condition to have found a minimum is:

$$\frac{\partial R^2(a_1, a_2)}{\partial a_i} = 0 \tag{2.41}$$

For a linear fit we can thus write:

$$\begin{cases} \frac{\partial R^2(a_1,a_2)}{\partial a_1} &= -2\sum_{i=1}^{n}[y_i - (a_1 + a_2 x_i)] = 0 \\ \frac{\partial R^2(a_1,a_2)}{\partial a_2} &= -2\sum_{i=1}^{n}[y_i - (a_1 + a_2 x_i)]x_i = 0 \end{cases} \tag{2.42}$$

$\Leftrightarrow$

$$\begin{cases} n a_1 + a_2 \sum_{i=1}^{n} x_i &= \sum_{i=1}^{n} y_i \\ a_1 \sum_{i=1}^{n} x_i + a_2 \sum_{i=1}^{n} x_i^2 &= \sum_{i=1}^{n} x_i y_i \end{cases} \tag{2.43}$$

Or written in matrix form:

$$\begin{bmatrix} n & \sum_{i=1}^{n} x_i \\ \sum_{i=1}^{n} x_i & \sum_{i=1}^{n} x_i^2 \end{bmatrix} \begin{Bmatrix} a_1 \\ a_2 \end{Bmatrix} = \begin{Bmatrix} \sum_{i=1}^{n} y_i \\ \sum_{i=1}^{n} x_i y_i \end{Bmatrix} \tag{2.44}$$

It can also be noticed that:

$$\begin{bmatrix} n & \sum_{i=1}^{n} x_i \\ \sum_{i=1}^{n} x_i & \sum_{i=1}^{n} x_i^2 \end{bmatrix} = \begin{bmatrix} 1 & \dots & 1 \\ x_1 & \dots & x_n \end{bmatrix} \begin{bmatrix} 1 & \dots & x_1 \\ . & \dots & . \\ . & \dots & . \\ 1 & \dots & x_n \end{bmatrix} = \underline{G}^T \underline{G}$$

And

$$\begin{Bmatrix} \sum_{i=1}^{n} y_i \\ \sum_{i=1}^{n} x_i y_i \end{Bmatrix} = \begin{bmatrix} 1 & ... & 1 \\ x_1 & ... & x_n \end{bmatrix} \begin{Bmatrix} y_1 \\ . \\ . \\ y_n \end{Bmatrix} = \underline{G}^T \vec{d}$$

Finally the model parameters $\vec{m} = \left\{ a_1, a_2 \right\}^T$ can be found using the familiar equation for inverse problems:

$$\vec{m} = \left[\underline{G}^T \underline{G} \right]^{-1} \underline{G}^T \vec{d} \tag{2.45}$$

where $\vec{d} = \left\{ y_1, ..., y_n \right\}^T$ contains the data points, and $\underline{G}$ contains the partial derivatives of the function to minimize $g_i(x_i, y_i, a_1, a_2, ..., a_k) = y_i - f(x_i, a_1, a_2, ..., a_k)$ with respect to the k model parameters in $\vec{m}$. Those derivatives can be either determined analytically, or using a finite difference approximation. $\underline{G}$ is written in the general form:

$$\underline{G} = \begin{bmatrix} \frac{\partial g_1}{\partial a_1} & \frac{\partial g_1}{\partial a_2} & ... & \frac{\partial g_1}{\partial a_k} \\ \frac{\partial g_2}{\partial a_1} & \frac{\partial g_2}{\partial a_2} & ... & \frac{\partial g_2}{\partial a_k} \\ . & . & . & . \\ . & . & . & . \\ . & . & . & . \\ \frac{\partial g_n}{\partial a_1} & \frac{\partial g_n}{\partial a_2} & ... & \frac{\partial g_n}{\partial a_k} \end{bmatrix} \tag{2.46}$$

In the case of a non-linear inverse problem, some initial guess for the models parameters $\vec{m}_0$ have to be given at first, and then the solution is found iteratively using a root-finding algorithm such as the Newton-Raphson method as described in Dally and Riley, 1965, p 514-515.

The matrix $\underline{G}$ is calculated at a time j like in eq. 2.46, from the vector $\vec{g}_j$ containing the errors between observations and modelled data, and by taking the derivative of these errors with respect to the k model parameters contained in $\vec{m}_j$. We obtain a vector $\vec{\Delta}_j$ containing the corrections to apply to $\vec{m}_j$ using equation 2.47.

$$\vec{\Delta}_j = \left[\underline{G}_j^T \underline{G}_j\right]^{-1} \underline{G}_j^T \vec{g} \tag{2.47}$$

The model $\vec{m}_j$ is thus corrected using:

$$\vec{m}_{j+1} = \vec{m}_j + \vec{\Delta}_j \tag{2.48}$$

The process is repeated, starting again from eq. 2.47 with the new model values in $\vec{m}_{j+1}$ until the solution converges which means until the errors in $\vec{\Delta}_j$ are negligible.

To avoid falling in local minima in the inversion described in appendix A, we also repeat the inversion procedure, starting from different initial guesses.

Chapter 3

Loading rate influence on the nucleation of laboratory earthquakes

This chapter is written in the form of an article, as its content has been published in Journal of Geophysical Research (Guerin-Marthe et al., 2018). It is co-authored with Stefan Nielsen who participated to the data acquisition and made few edits in the text, Stefano Giani and Robert Bird who helped with the development of a Finite Element code, and Giulio Di Toro who provided the funds to buy the laboratory equipment. I did the acquisition, processed the data, made the figures, wrote the Finite Element code in python, and wrote the manuscript. Some elements of the methods section in this chapter are already mentioned in chapter 2, however we now give more emphasis on how the specific set of experiments have been run, in a self-contained form.

Keypoints :

- The nucleation length decreases with loading rate, implying that smaller-size asperities clusters can be triggered by accelerated slip
- The nucleation position localises on high coulomb stress patches with small-scale inhomogeneities at high loading rates
- The measured nucleation length of laboratory earthquakes falls into the range predicted by numerical and theoretical studies

3.1 Abstract

Recent GPS observations of major earthquakes such as the 2014 Chile megathrust show a slow pre-slip phase releasing a significant portion of the total moment (Ruiz et al., 2014). Despite advances from theoretical stability analysis (Rubin and Ampuero, 2005; Ruina, 1983), and modeling (Kaneko et al., 2017), it is not fully understood what controls the prevalence and the amount of slip in the nucleation process. Here we present laboratory observations of slow slip preceding dynamic rupture, where we observe a dependence of nucleation size and position on the loading rate (laboratory-equivalent of tectonic loading rate). The setup is composed of two polycarbonate plates under direct shear with a 30 centimeters long slip interface. The results of our laboratory experiments are in agreement with the pre-slip model outlined by Ellsworth and Beroza (1995) and observed in laboratory experiments (Ohnaka and Kuwahara, 1990; Nielsen et al., 2010; Latour et al., 2013), which show a slow slip followed by an acceleration up to dynamic rupture velocity. However, further complexity arises from the effect of (1) rate of shear loading and (2) inhomogeneities on the fault surface. In particular, we show that when the loading rate is increased from 10^{-2} MPa.s^{-1} to 6 MPa.s^{-1}, the nucleation length can shrink by a factor of three and the rupture nucleates consistently on higher shear stress areas. The nucleation lengths measured fall within the range of the theoretical limits L_b and L_∞ derived by Rubin and Ampuero (2005) for rate-and-state friction laws.

3.2 Introduction

The precursory phase of earthquakes and, more generally, the different phases of the seismic cycle remain in large part poorly understood. However some promising advances have been made in the past decades thanks to fault observations, theoretical and numerical models, and small-scale laboratory experiments.

It is well-known that some faults are able to release a significant portion of the strain energy accumulated during the tectonic loading phase by slow, aseismic creep (Kanamori, 1977; Scholz et al., 1969). The observation of small to moderate earthquakes and repeaters evolving in the area of an impending earthquake, has allowed to infer either the presence of slow slip (Kato et al., 2012; Hasegawa and Yoshida, 2015) or the advancement of a slow rupture front (Bouchon et al., 2011; Michel Bouchon and Schmittbuhl, 2013). More recently, thanks to substantial developments of GPS and continuous GPS networks along with satellite interferometry, it has been possible to use geodetical data in conjunction with seismic signals to highlight the crustal deformation during different stages of the seismic cycle. In a small number of cases so far, an accelerated slip phase preceding large or great earthquakes of several weeks (Ruiz et al., 2014; Ruiz et al., 2017) to months (Socquet et al., 2017) has been identified, often accompanied by seismic swarms triggered as the slip progresses (Kato et al., 2012). The latter may be indicative of the nucleation process and has been interpreted as part of the triggering mechanism of earthquakes (Ruiz et al., 2014; Ruiz et al., 2017). In the later case, the coseismic slip area was smaller and located inside the large nucleation zone that started slipping a few months before. More recently Tape et al. (2018) showed that a M3.7 earthquake in Alaska initiated with the acceleration of a rupture front 22 seconds before the main shock. This last observation concerns a small earthquake rupture and thus provides insight in the rupture process at an intermediate scale between laboratory experiments and great earthquakes.

While the above observations are provoking, they are so far too few to clearly quantify the prevalence of pre-slip, and to demonstrate a statistically significant causality relation between slow-slip and earthquake nucleation. As a consequence, opposing models have been proposed for earthquake initiation: the

pre-slip model of Ellsworth and Beroza (1995) and the cascade model (Olson and Allen, 2005). The main difference between the two models is that in the pre-slip model, the rupture expands until the slipping patch reaches a critical size L_c at which it becomes unstable. In the cascade model, small and large earthquake start in a similar manner, by successive random breaking of asperities eventually leading to a large rupture for which the size cannot be predicted until it stops (Olson and Allen, 2005).

As it has been suggested that a number of large events have been triggered by pre-slip (Ruiz et al., 2014; Ruiz et al., 2017; Tape et al., 2018), it is crucial to understand how large can a slipping patch grow before being likely to become unstable and trigger a major event, and what controls the size of L_c, intended as the size above which a sliding fault patch will start to propagate spontaneously. L_c can be predicted for a few simple models related to earthquake faulting. Assuming that the stress drop inside the slipping patch is known, an estimate of L_c can be obtained based on energy concepts, stemming from the original Griffith criterion for brittle failure (Griffith, 1921), subsequently extended to elasto-plastic materials (Irwin, 1957; Rice, 1968) and to shear rupture on frictional earthquake faults (Andrews, 1976). The resulting L_c decreases with the normal stress and the stress drop within the nucleation patch, and increases with the fracture energy. For a homogeneous fault characterized by a velocity-weakening friction law, the size L_{b-a} of an unstable slipping patch can be predicted (Ruina, 1983; Gu et al., 1984) by stability analysis. Some correspondence between L_{b-a} (obtained in terms of stability) and L_c (obtained in terms of energy balance) must exist and has been explored for particular cases of rate-and-state friction laws (Uenishi and Rice, 2003; Rubin and Ampuero, 2005). Importantly, the study of Rubin and Ampuero (2005) using rate-and-state models shows that L_{b-a} is not unique, but that there exists a range of possible nucleation lengths within the values (L_b, L_∞), corresponding to the lower and upper bounds of the nucleation length predicted, respectively (see discussion section). While these theoretical predictions are roughly matched by experimental observations, a more complex behaviour is observed on experimental and natural faults, possibly due to strong inhomogeneity (Harbord et al., 2017).

Because of the small number of pre-slip observations in nature and the complexity of the physical processes involved at different scales, one way to investigate the dependence of L_c on individual physical parameters is to replicate this slow-slip in controlled laboratory experiments (Ohnaka and Kuwahara, 1990; Kato et al., 1992; Ohnaka, 1992; Latour et al., 2013; Mclaskey and Yamashita, 2017; Xu et al., 2017) and in numerical models (Kato and Hirasawa, 1996; Rubin and Ampuero, 2005; Kaneko and Ampuero, 2011; Kaneko et al., 2016; Kaneko et al., 2017). Latour et al. (2013) evidenced that L_c was inversely proportional to the normal stress using polycarbonate plate as earthquake laboratory analog. The normal stress dependence is supported by theoretical studies using rate-and-state or slip weakening friction laws and crack stability analysis Ruina, 1983. Ohnaka (1992) and Kato et al. (1992) also observed a similar pre-slip in laboratory rupture experiments using granite slabs. The scaling of L_c in those experiments depends on normal stress, fault surface roughness and slip weakening distance D_c, which is the amount of relative slip on a fault needed for the friction to reach the dynamic value. The effect of normal stress is also evidenced in numerical models (Kaneko et al., 2016). But, more than the L_c dependence on normal stress, numerical models also show that increasing the loading rate causes L_c to decrease, using rate-and-state friction laws (Kato and Hirasawa, 1996; Kaneko et al., 2016).

In order to verify this decrease of L_c , we conducted experiments similar to the ones of Latour et al. (2013), but this time investigating the effect of the loading rate on the nucleation length of laboratory ruptures. Even though experiments using granite blocks have already investigated the L_c dependence on loading rate, this was done either by looking at strain gauges signals (Kato et al., 1992), or by observing the transition between stable and unstable behavior of granite slabs of length close to L_c (Mclaskey and Yamashita, 2017). The advantage of the photoelastic technique used here is that the tips of the propagating rupture can be directly tracked, allowing to measure nucleation length and position.

3.3 Materials and Methods

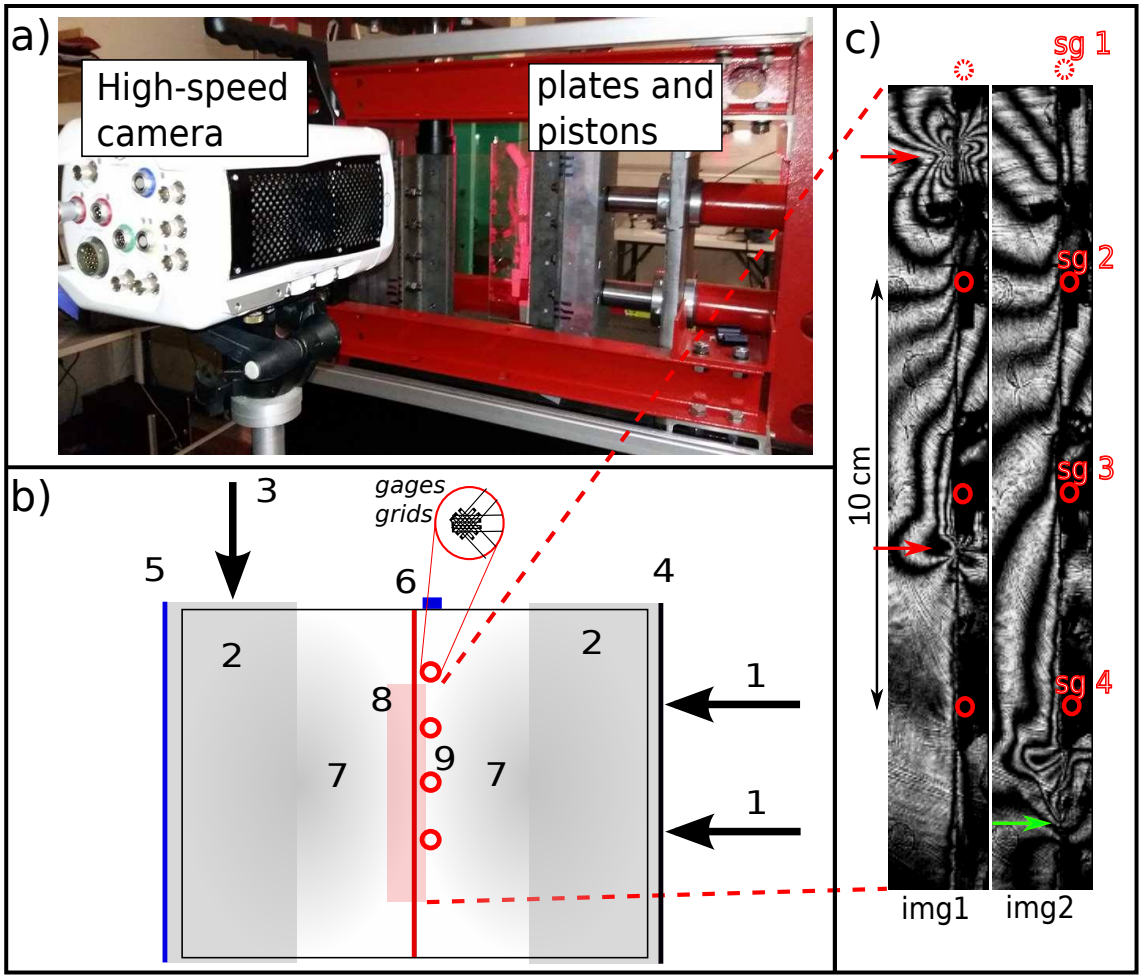

FIGURE 3.1: Photograph and schematic description of the experimental setup. a) Picture of the biaxial press used for the rupture experiments. b) Sketch of the loading and monitoring configuration with the two polycarbonate plates (7) held through metallic clamps (2). Two horizontal pistons (1) apply a distributed normal force through the right-hand clamp edge (4), which is fixed in the vertical direction but allowed to move in the horizontal direction. A vertical piston (3) actuates the shear stress by applying a vertical force through the left-hand clamp edge (5), which is allowed to move vertically along a low friction rail, but is fixed in the horizontal direction. Four strain gauge rosettes (9) indicated by red circles are fixed using cyanoacrylate bond along the 30x1 cm interface (red line) between the two plates. An accelerometer (6) is fixed at the top of the right plate, and a high speed camera captures the rupture events in a 20 cm long window (8) in the middle of the interface. c) Two examples of isochromatic fringe patterns recorded during a rupture. The slipping zone of img1 is situated between the two red arrows that represent the crack tips, or propagating rupture fronts. The green arrow on img2 points at the bottom tip that has transitioned to supershear velocity, while the top tip has propagated outside of the camera field. Again red circles represent the strain gauges, which are numbered sg1-4.

The laboratory setup (fig. 3.1.a and 3.1.b) consists in two rectangular polycarbonate plates 30 x 15 x 1 cm, held in sliding contact across their 30 cm edge. Two horizontal pistons apply a uniform pressure through a metal holder, maintaining the 30 cm by 1 cm contact interface under normal stress. A third piston applies a vertical force on the metal holder of the left-hand plate, thus imposing shear stress on the sliding interface in a simple shear configuration. All pistons are controlled by hand pumps. The two horizontal pistons and the normal stress remain fixed during the shear loading phase leading to the rupture. After each rupture the normal stress is released, the plates are reset to their initial positions, and the normal stress is imposed again for the next experiment. Three strain components are monitored at each of the four strain gauge rosette locations (2 mm away from the fault interface, and equally spaced 5 cm away from each other).

The signals are sampled at 10 MHz and filtered at 500 kHz in order to record the initial, peak, residual and normal stresses before the rupture, respectively τ_0, τ_p, τ_r and σ_n (see fig. 3.2). Because we do not control the exact value of shear loading rate $\dot{\tau}$ when moving the vertical piston using the hand pump, we also use the strain gauges to measure the average loading rate $\dot{\tau} = \Delta\tau/\Delta t$ during the few seconds of the loading phase.

A high-speed camera continuously overwrites a circular buffer, recording at 2.10^5 frames per second. A signal is sent to the camera immediately after the dynamic rupture, allowing to store the frames from the last few seconds before rupture, and up to approximately 0.5 s after. We use the well-known photoelastic properties of the polycarbonate to visualize so-called isochromatic fringes, highlighting the areas of high stress concentration which correspond to the edges of the slipping patch (fig. 3.1.c), as used in previous laboratory rupture experiments (Nielsen et al., 2010; Rosakis et al., 2007). We select the frames where sharp stress variations start to appear along the contact interface (start of nucleation), until the crack propagates dynamically and the tips reach the limit of the camera field. Thus for each rupture experiment, which lasts a few hundreds of micro-seconds, we are able to track the positions of the rupture tips versus time along with the absolute values of stress measured at four locations thanks to the strain gauge

rosettes. The gauges' values can be interpolated to obtain a continuous stress distribution (see fig. 3.3.b and fig. 3.5). The two surfaces in contact were initially smoothed using 400 grit diamond powder and then sandblasted with heterogeneous sand particles to simulate a self-similar roughness in a similar way than in Lu et al. (2010a). Note that before the experiments presented below, several stick-slip events had already been triggered. This might have introduced defects on the simulated fault surface, and would explain why small-scale stress heterogeneities (wavelengths of 4 to 8 mm) are visible in fig 3.8. Those short wavelengths are superimposed to larger normal and shear stress variations which are explained by the loading conditions (see section 4.1.2).

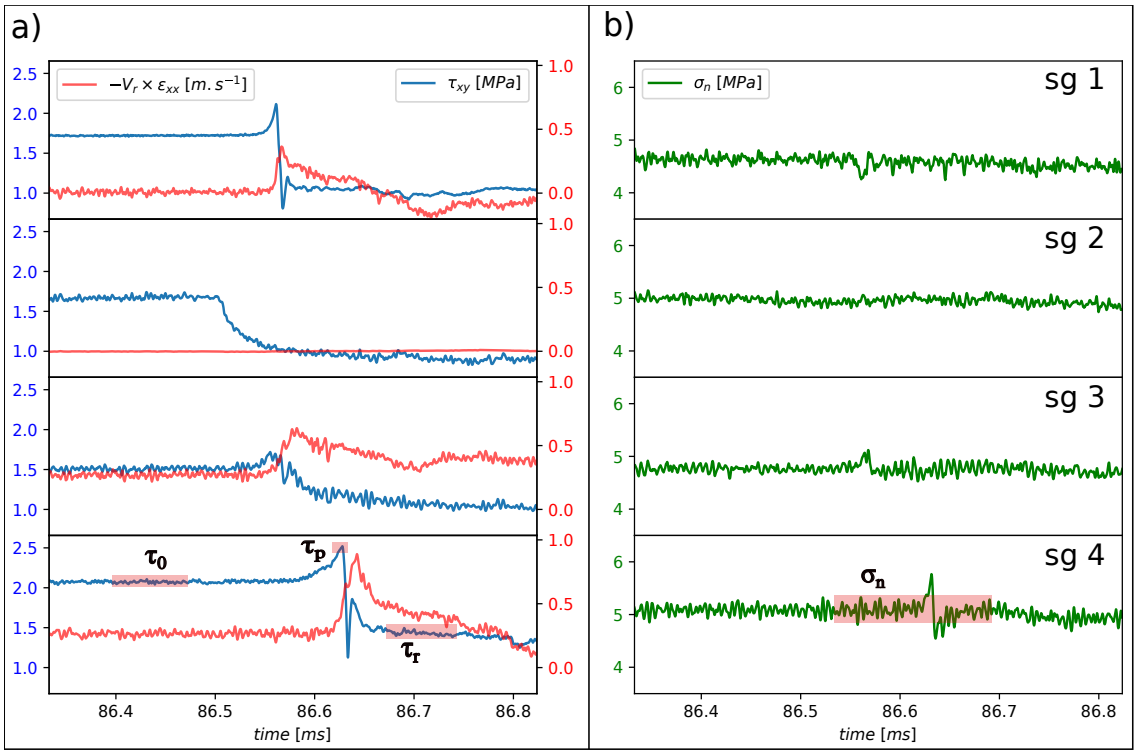

FIGURE 3.2: Example of strain gauge signals recorded during a rupture that initiates close to the strain gauge sg 2. a) Shear stresses τ_{xy} and fault parallel particle velocities $-V_r\epsilon_{xx}$ recorded at the 4 different locations corresponding to sg 1 to sg 4, V_r being the rupture velocity . b) Normal stresses σ_n recorded at the same locations. For one event, the initial shear stresses τ_0 , peak stresses τ_p , residual stresses τ_r and normal stresses σ_n are picked as averaged values in time windows shown on the stress records at sg 4. Note that although σ_n can slightly vary locally at the rupture front, we only pick the averaged value.

3.4 Results

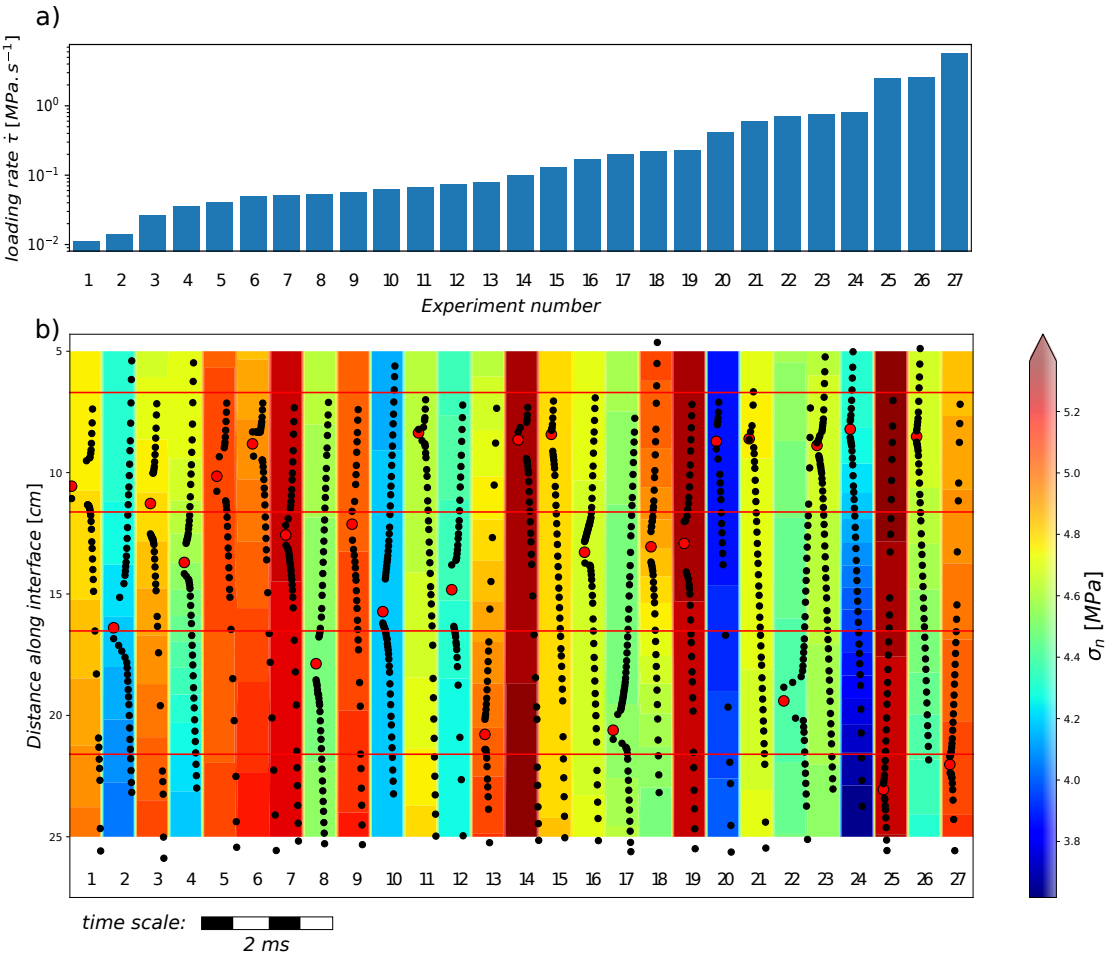

FIGURE 3.3: a) Loading rate for each experiment and b) Corresponding rupture histories presented in individual time windows of 500 μs. The black dots are the positions of the crack tips. The background colors represent the normal stress distribution for each rupture, measured with the four strain gauge rosettes, and interpolated between their positions indicated by the red solid lines. The big red dots are the nucleation positions.

We conducted a total of 27 individual experiments, at imposed loading rates ranging from 0.01 MPa.s^{-1} to 6 MPa.s^{-1} (figure 3.3.a), with normal stresses maintained around 4.7 $\pm$ 0.8 MPa (fig 3.3.b). The key input and output variables are summarized in table 3.1. For each experiment, we present the tracking of the rupture tips positions in individual time windows representing 500 μs. Crack tips are not clearly visible on all frames (due to weak stress concentration or to masking by strain gauge rosettes) which is why there are apparent gaps in picking of the front positions (black dots) in fig. 3.3.b. We took care of performing

the experiments in a random order in terms of the background loading rate, to exclude any possible bias due to progressive sample wear. As a consequence the rupture histories presented in figure 3.3.b have not been run in the same order as presented (by increasing loading rate). The background color represents the normal stress distribution for each individual experiment, interpolated from the four strain gauge rosettes values.

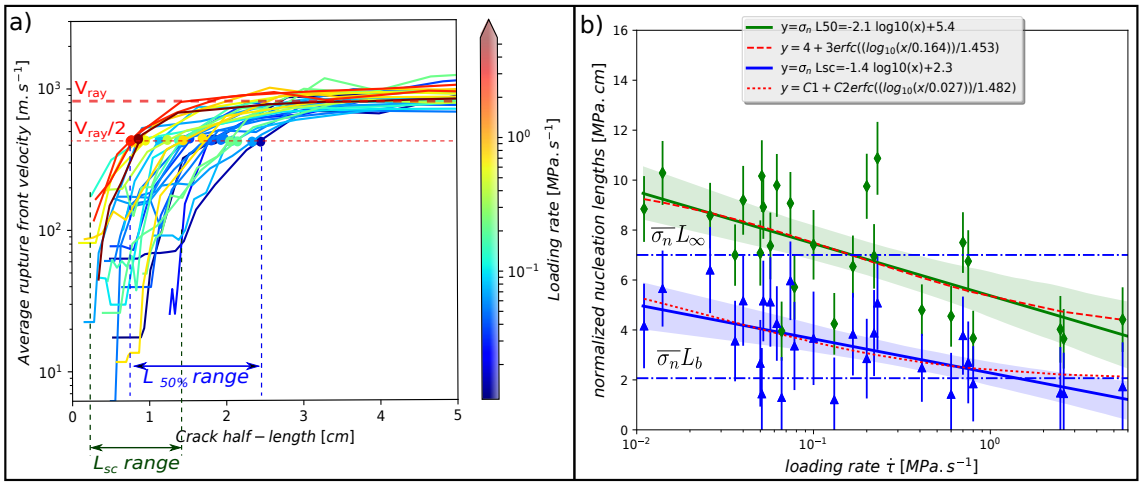

FIGURE 3.4: a) Characteristics of the nucleation phase of each individual rupture experiment under different background loading rates. Warmer colors represent higher loading rates. The dots represent a nucleation length taken arbitrarily as the crack half-length when the average rupture front velocity $\overline{V_r}$ reaches 50% of the Rayleigh wave speed V_{Ray}. b) Normalized nucleation lengths L_{sc} (blue triangles) at the start of the acceleration and $L_{50\%}$ (green diamonds) by the normal stress, as a function of the background loading rate $\dot{\tau}$. The blue and green area represents the uncertainty on the arbitrary linear relations plotted as a solid lines, using a bootstrap method at 95.45% of confidence (2 x std), for $\overline{\sigma_n} L_{sc}$ vs $\dot{\tau}$ and $\overline{\sigma_n} L_{50\%}$ vs $\dot{\tau}$, respectively. The dashed red lines are non-linear fits assuming that the nucleation length tends asymptotically toward limiting values L_b and L_∞ at high and low values of $\dot{\tau}$ respectively.

Using the position of the rupture tips versus time, we can plot the average rupture front velocity $\overline{V_r}$ versus crack half-length (fig. 3.4.a) ($\overline{V_r}$ being the average of the 2 rupture fronts velocities in the case of bilateral ruptures). We see clearly the phase of acceleration of V_r up to about the Rayleigh wave speed $V_{Ray} \approx 820$ m.s^{-1}, i.e., the limiting velocity for subshear ruptures (dashed red line in fig. 3.4). We use V_{Ray} to define $L_{50\%}$ as the crack half-length when $\overline{V_r} = 0.5\, V_{Ray}$. We also observe supershear rupture in some of the experiments (fig. 3.1.c) in particular when the length of the propagating rupture exceeds 5 cm (not shown in

exp. number	exp. name	$\dot{\tau}$ [MPa/s]	order of run	$\overline{\tau_0}$ [MPa]	$\overline{\tau_p}$ [MPa]	$\overline{\sigma_n}$ [MPa]	$\overline{\tau_r}$ [MPa]	L_{sc} [cm]	$L_{50\%}$ [cm]
1	30	0.011	23	1.8	2.1	4.8	1.2	1.7	3.7
2	013	0.014	3	1.4	1.6	4.2	0.9	2.7	4.9
3	32	0.026	24	1.7	2.0	4.9	1.2	2.7	3.6
4	015	0.036	4	1.6	1.8	4.5	1.0	1.6	3.1
5	26	0.04	21	1.7	2.0	5.1	1.1	2.0	3.6
6	34	0.05	25	1.7	2.1	5.0	1.2	1.1	2.9
7	25	0.051	20	1.7	2.0	5.2	1.1	0.6	3.9
8	09	0.052	10	1.5	1.8	4.6	1.0	2.3	4.0
9	19	0.057	16	1.5	1.7	5.1	1.0	2.0	2.9
10	009	0.062	1	1.3	1.5	4.2	0.9	2.0	4.7
11	10	0.066	11	1.6	1.8	4.7	1.1	0.6	1.7
12	27	0.074	22	1.5	1.7	4.3	1.0	2.8	4.2
13	35	0.078	26	1.7	1.7	4.8	1.1	1.3	2.3
14	20	0.1	17	1.6	2.0	5.3	1.1	1.4	2.8
15	13	0.131	13	1.6	2.0	4.8	1.1	0.5	1.8
16	11	0.167	12	1.6	1.9	4.7	1.1	1.6	2.8
17	07	0.2	8	1.4	1.7	4.5	1.0	1.3	4.3
18	017	0.22	6	1.7	1.9	4.8	1.1	1.6	2.9
19	21	0.23	18	1.7	2.0	5.3	1.0	1.9	4.1
20	18	0.41	15	1.2	1.4	3.9	0.8	1.3	2.5
21	16	0.6	14	1.6	1.9	4.7	1.1	0.6	1.9
22	08	0.7	9	1.6	1.8	4.5	1.0	1.7	3.4
23	012	0.75	2	1.4	1.7	4.6	0.9	1.2	2.9
24	019	0.8	7	1.4	1.7	4.0	0.9	0.9	1.7
25	22	2.49	19	1.8	2.1	5.3	1.1	0.6	1.5
26	016	2.6	5	1.6	1.9	4.5	1.0	0.6	1.6
27	37	5.6	27	1.8	2.0	5.0	1.2	0.7	1.7

TABLE 3.1: Summary of the input and output variables of the experiments. From left to right: experiment number, experiment name, loading rate, order in which it has been run, average initial stress (from the 4 different values measured at the 4 strain gauges), average peak stress, average normal stress, average residual stress, nucleation length, nucleation length defined at 50% of the Rayleigh wave speed.

fig. 3.4.a). (The limiting rupture velocity in supershear is the P-wave velocity ≈ 1860 m.s^{-1}, but we always use V_{Ray} for the definition of $L_{50\%}$). Using $L_{50\%}$, the stress concentration at the crack tips is large enough to allow a clearly visible rupture tips in most cases. For comparison to the theoretical predictions L_b, L_{b-a} and L_∞, we also define L_{sc} as the nucleation length at which nucleation starts to accelerate. However, at such early stage of nucleation, the crack tip position is less clear; therefore L_{sc} is poorly resolved, in particular for small nucleation sizes (see lower bound of L_{sc} range, fig. 3.4.a).

We observe a shrinking of the nucleation length with increasing loading rate in accordance to the numerical model of Kaneko et al. (2016). $L_{50\%}$ shrinks from almost 2.5 cm to approximately 0.8 cm when the loading rate is increased from 10^{-2} MPa.s^{-1} to 6 MPa.s^{-1} respectively. Although the variability is high, this shows clearly that $L_{50\%}$ is dependent on the loading rate.

Because the nucleation length is also inversely proportional to the normal stress (see discussion), we normalize $L_{50\%}$ by multiplying it by σ_n. When plotted versus $\dot{\tau}$ the normalized nucleation length decreases with increasing loading rate (fig. 3.4.b). As we have an uncertainty on the nucleation length and on the normal stress interpolated at the nucleation position, we propagate the uncertainty on $L_{50\%} \times \sigma_n$ and plot the error bars. Even though we do not know the exact relationship between normalized $L_{50\%}$ and loading rate, a linear regression shows a clear negative slope:

$$L_{50\%} \times \sigma_n = -2.1 \log_{10} \dot{\tau} + 5.4 \tag{3.1}$$

$L_{50\%}$ is in cm, σ_n in MPa, and $\dot{\tau}$ in MPa.s^{-1}. Dividing equation 3.1 by the average normal stress of $\overline{\sigma_n}$ = 4.7 MPa we obtain:

$$L_{50\%} = -0.44 \log_{10} \dot{\tau} + 1.15 \tag{3.2}$$

The uncertainty on this slope is calculated using a bootstrap method and displayed as a light green area. The regression coefficient is clearly negative meaning that the normalized nucleation length is dependent on the loading rate.

Assuming that the nucleation length L_{sc} tends asymptotically toward the theoretical limiting values L_b and L_∞ at high and low values of $\dot{\tau}$ respectively (see discussion section), we can also obtain an empirical fit using the follwing mathematical form (using erfc to produce tapering at both high and low values of $\dot{\tau}$):

$$\overline{\sigma_n} L_{sc} = c1 + c2 \times \text{erfc}\left(\frac{\log_{10}(\dot{\tau}/c3)}{c4}\right) \tag{3.3}$$

where $c1 = \overline{\sigma_n} L_b = 2.07$ [MPa.cm], $c2 = \overline{\sigma_n}(L_\infty - L_b)/2 = 2.47$ [MPa.cm], $c3 = 0.027$ [MPa.s^{-1}] and $c4 = 1.482$.

A similar relation can be found using $L_{50\%}$ (fig. 3.4.b).

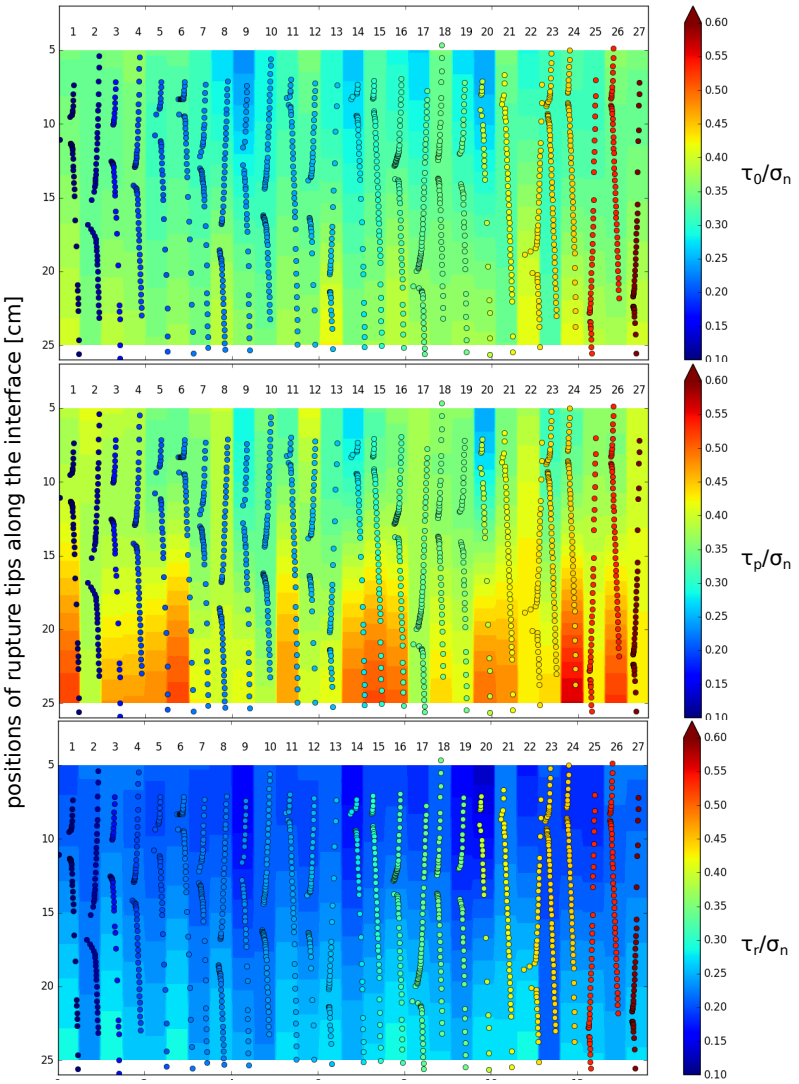

FIGURE 3.5: Maps for each 27 experiments of the friction before, during and after the passage of the rupture front. Friction coefficients are extrapolated between the 4 strain gauges locations, using values picked as in figure 2. The dot colors represent the loading rate and follow the same scale than on fig. 4.a.

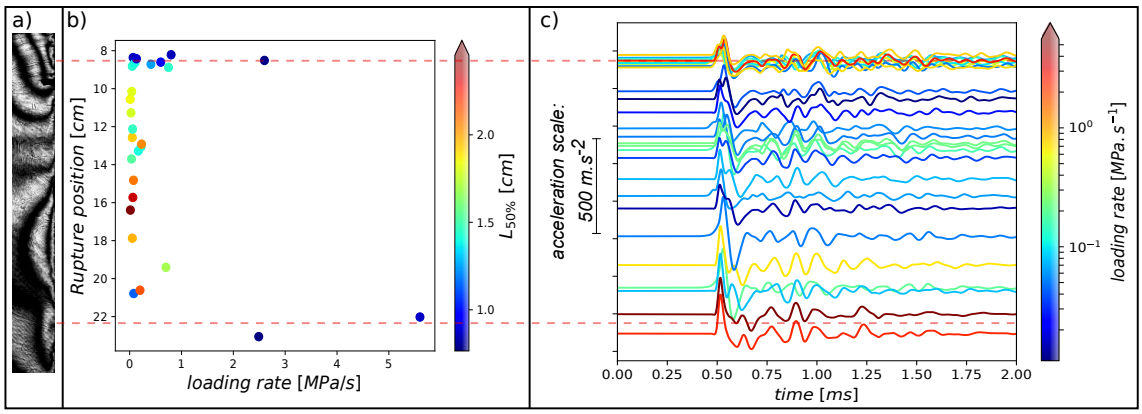

FIGURE 3.6: a) Picture of the typical isochromatic fringe pattern taken approximately 500 μs before nucleation, highlighting high shear and normal stresses areas around 8.5 cm and 22.5 cm. b) Nucleation location of each individual experiment. The nucleation location is taken as the mean value of the first picked positions of the crack tips propagating upwards and downwards along the interface. The dots colour represents the nucleation length $L_{50\%}$ measured as in fig. 3.4.a. c) Accelerations recorded at the top edge of the right plate (see fig. 3.1.2). The initial accelerations are zeros, and an offset is applied to plot the waveforms at the position where the rupture have nucleated.

In addition to the shrinking of L_c with increasing loading rate, we observe that the nucleation position along the interface is not random but also affected by $\dot{\tau}$. Indeed at loading rates over 0.3 MPa.s^{-1} the nucleation localizes only on areas situated around 8.5 cm and 22.5 cm along the interface. The nucleation length L_c is small everytime the rupture nucleates on those patches (fig. 3.6.b), and the accelerations (recorded at the top of the right plate) show that all the ruptures initiating around 8.5 cm have very similar waveforms (fig. 3.6.c). We find that the preferred nucleation sites at high loading rates correspond to areas of relatively higher shear and normal initial stresses by using the typical photoelastic fringes pattern before nucleation (taken approximately 500 μs before the crack tips become visible, as shown in fig. 3.6.a) and the strain gauges data; the method is detailed in section 4.1.2. Although the exact stress distribution is different between experiments (see fig. 3.5), the general fringe pattern before rupture is consistent and always showing the two same high stress areas. The stress variations from one experiments to another are of too short wavelength, or too small magnitude to be quantified using the method described in section 4.1.2. The sparse strain gauge measurements do not enable to resolve sharp stress heterogeneities either.

At low loading rates, the nucleation is observed to start in more homogeneous zones (between 10 cm and 18 cm), with apparent slightly lower initial stress values.

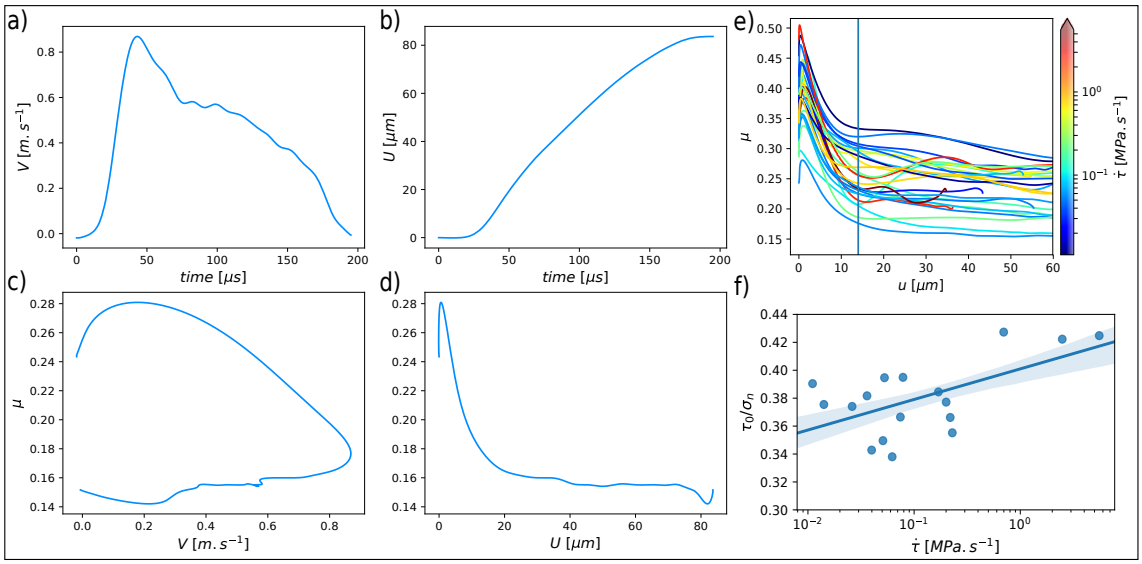

FIGURE 3.7: a) Plot of the local slip velocity V=−2 $V_r\epsilon_{xx}$ (ϵ_{xx} is the fault parallel strain low-pass filtered at 30 kHz) used to calculate (b) the relative displacement U, as detailed in section 2.2.2. The friction evolution is then plotted as a function of (c) the local slip velocity V and (d) the relative displacement U. e) Dynamic slip-weakening friction laws of each experiments. f) Normalized τ_0 vs loading rate for all events excepts the ones having nucleated around 8.5 cm along the interface which are discarded as the stress values are not resolved by the sparse strain gauge measurements.

Finally, we attempt to derive the dynamic slip-weakening friction laws of each rupture (fig. 3.7.e) using the method described in section 2.2.2 (eq. 2.15). From the camera data we select strain gauges that recorded ϵ_{xx} when the rupture front attained a quasi-static propagation velocity $V_r \approx V_{Ray}$, and use the measured velocity to calculate u. Filtering the signal at 30 kHz and plotting the friction evolution versus slip for each experiment indicates a slip dependence of friction with a consistent critical slip weakening distance $D_c \approx 14\ \mu m$ (fig. 3.7.e). However there is no clear trend concerning the slip weakening dependence of friction with regard to the loading rate. This should be expected as the dynamic friction is weakly related to the quasi-static friction law state variables and therefore to the loading history. To quantify what happens during the quasi-static stage of rupture, we use the values of τ_0 and σ_n interpolated at the nucleation position

(fig. 3.5) and plot their relation with $\dot{\tau}$ (fig. 3.7.f). The events nucleating on the high stress area around 8.5 cm along the interface are discarded as the interpolated stress distribution using the strain gauges can clearly not resolve the stress field visible on the isochromatics (fig 3.6.a). The ratio τ_0 / σ_n seems to increase with loading rate, which is consistent with the rate effect of rate-and-state friction laws. A possible microphysical interpretation is that locked micro-contacts across the sliding surface deform plastically under shear; in that case their shear stress is expected to increase with strain rate. We can also infer that if the higher stresses around 8.5 cm would be properly resolved by the strain gauges, this would add more point in the upper right part of the graph fig. 3.7.f.

3.5 Discussion

We now discuss our observations on the size of experimental nucleation to the theoretical predictions that can be made using stability analysis and assuming some type of rate-and-state frictional behavior.

Because the stability analysis does not consider a change in the remote load, it is expected that those experiments where the loading rate is the smallest should be closer to the prediction and differ increasingly with loading rate. However we remark that other differences between theory and model may alter the behavior. First, inhomogeneity of the simulated fault will arise due to stress fluctuations, slight changes in frictional properties and imperfections in the slip surface due to non-planarity, wear or microcracks. Second, the actual frictional behavior of the simulated fault may not be perfectly matched by the specific rate-and-state friction that is being assumed in the stability analysis.

In the rate-and-state friction framework, the friction coefficient can be expressed as in Ruina (1983):

$$\tau = \sigma_n \left(\mu_0 + a \ln \left(\frac{V}{V_0} \right) + b \ln \left(\frac{V_0 \theta}{d_c} \right) \right) \tag{3.4}$$

where for the aging law:

$$\frac{d\theta}{dt} = 1 - \frac{V\theta}{d_c} \tag{3.5}$$

and for the slip law

$$\frac{d\theta}{dt} = -\frac{V\theta}{d_c} \ln\left(\frac{V\theta}{d_c}\right) \tag{3.6}$$

Where σ_n is the normal stress, a and b are the rate and state constitutive parameters, V is the slip rate, μ_0 is the reference friction coefficient at the reference slip rate V_0. d_c is a characteristic slip.

Although no simple analytical solution exists for these laws, the expected critical nucleation length at which a slipping zone becomes unstable has been discussed by several authors (Ruina, 1983; Dieterich, 1992; Rice, 1993; Uenishi and Rice, 2003; Rubin and Ampuero, 2005; Ampuero and Rubin, 2008; Fang et al., 2010). Because of the non-trivial evolution of the coupled parameters θ and V along a fault obeying a rate-and state law, the nucleation history and therefore the critical nucleation length can be significantly different depending on which initial and loading conditions are used in numerical models (Rubin and Ampuero, 2005; Fang et al., 2010). Using a simple spring-slider model and linear stability analysis, Ruina (1983) and Rice (1993) have shown that the critical stiffness of a patch was given by $k_c = (b-a)\sigma_n/d_c$, giving a critical nucleation length $L_{b-a} = G^* d_c/((b-a)\sigma_n)$, G^* being the effective shear modulus for in-plane stress, $G^* = G/(1-\nu)$. Rubin and Ampuero (2005) also examined in detail the nucleation of rate and state faults and showed that the variable $\Omega = V\theta/d_c$ played a crucial role in the process. They found that depending on the value of Ω at the time of nucleation, on the ratio a/b, and on the state variable evolution law chosen (slip or aging law), different expression for the nucleation length could be expected (Rubin and Ampuero, 2005; Ampuero and Rubin, 2008). In particular, when $\Omega \approx 1$, close to steady-state, the nucleation length reaches an upper bound $L_\infty = G^* d_c/\pi \times (b/(\sigma_n(b-a)^2))$. The same scaling in $b/(b-a)^2$ can be found in the critical length derived by Andrews (1976) using a slip-weakening law and an energy criterion $L_{Andrews} = 2G^* D_c/\pi \times (\tau_p - \tau_f)/(\tau_0 - \tau_f)^2$. In the case where the nucleation process is fast enough (for example considering a fault that has not recently rupture and with high slip rates), $\Omega \gg 1$ and does not have the time to decrease inside the slipping area unlike for a slow nucleation process. In this

Parameter	Value	Unit
μ	0.96	GPa
ν	0.35	
d_c	2×10^{-7}	m
σ_n	4.7	MPa
a	0.01	
b	0.0144	

TABLE 3.2: Parameters used to estimate the nucleation lengths L_b, L_{b-a} and L_∞. ν is the Poisson's coefficient.

case the nucleation zone shrinks to a minimal value of $L_b = G^* d_c/(b\,\sigma_n)$. Uenishi and Rice (2003) and Dieterich (1992) also showed that in the case $\Omega \gg 1$ the rate-and-state law can be approximated as a slip-weakening law, and the critical nucleation length scales as b^{-1}. It has also been remarked that low ratios of a/b favor a nucleation patch of size L_b while larger ratios of a/b favor the expanding crack case growing up to a critical length L_∞ (Rubin and Ampuero, 2005) unless Ω is very large at the time of nucleation. Finally, by comparing the two evolution laws, Ampuero and Rubin (2008) found that when $\Omega \gg 1$ they gave similar results, while when $\Omega \approx 1$ the slip law produced unidirectional rupture propagation only.

In order to compare the experimentally determined nucleation lengths to the theoretical estimates, we use the values from Kaneko et al. (2016) who modeled similar experiments (Latour et al., 2013) that were run with a loading rate of $\dot{\tau}$ = 0.36 MPa.s^{-1}. The values are summarized in table 3.2. However, it is important to point out that in Latour et al. (2013) both shear and normal stresses were time dependent due to the oblique fault in the experimental setup. Also, we use the ageing law to estimate the nucleation length and to compare it to L_b and L_∞ derived by Rubin and Ampuero (2005). Those values do not necessarily hold for the slip law and it is not clear which law would be the most representative of the experiments in this study.

Using those parameters we obtain $L_b = 0.44$ cm, $L_{b-a} = 1.43$ cm and $L_\infty = 1.49$ cm. The measured values L_{sc} (fig. 3.4.a) are comprised between 0.25 cm and 1.4 cm, close to the predicted range bounded by L_b and L_∞. We do not know what would happen for a larger range of experimental loading rates values, however,

we can infer that the values taken by L_{sc} would tend asymptotically toward the bounds L_b and L_∞ for $\dot{\tau} \leqslant 6$ MPa.s^{-1} and $\dot{\tau} \geqslant 0.01$ MPa.s^{-1}, respectively. Using the energy criterion of Andrews (1976), along with our averaged values of $\overline{\tau_0} = 1.58$ MPa, $\overline{\tau_p} = 1.84$ MPa , $\overline{\tau_f} = 1.05$ MPa and $\overline{D_c} = 14$ μm from the experimentally determined friction law (fig. 3.7.e), we obtain $L_{Andrews} = 3.7$ cm which is slightly more than twice the maximum value L_∞. An important result of this study is that we are able to obtain nucleation lengths ranging from the minimum to the maximum values predicted by the rate-and-state laws only by varying the loading rate. Even though this parameter is often neglected in theoretical studies to obtain analytical solutions of rate-and-state laws, $\dot{\tau}$ seems to have a great influence on the path taken by the coupled parameters θ and V which ultimately control the nucleation length. In fact the loading rate itself may not be the determining factor, but rather the greater acceleration resulting from the imposition of a high loading rate starting from close to zero velocity, thus forcing the system away from the steady-state. In particular, if inside the nucleation patch Ω becomes $\gg 1$ due the sudden increase of velocity V, and if the state variable θ does not have the time to evolve during the nucleation phase due to a high loading rate, Ω will remain $\gg 1$ by the time of instability, in which case a small nucleation length close to L_b is to be expected.

In addition to the dependence of L_c on $\dot{\tau}$, we also observe a dependence of the nucleation position (see fig. 3.6). Indeed, while the ruptures nucleate more or less randomly along the interface at low $\dot{\tau}$, as we exceed a value of $\dot{\tau} \approx 0.3$ MPa.s^{-1} the rupture initiates systematically within two localized patches positioned at 8.5 and 22.5 cm along the interface. By using a finite element model later in chapter 4 to match the observed fringes, we show that they seem to correspond to zones of high coulomb stresses, where the nucleation is thus likely to initiate (see fig. 4.12 of section 4.1.2). Previous studies already showed that the initial stress distribution (Kato and Hirasawa, 1996) and frictional parameters a and b (Kawamura and Chen, 2017; Ray and Viesca, 2017) would influence the rupture nucleation, but the role of the loading rate was not clear. In more recent studies, Xu et al. (2017) who observed a similar negative dependence of Lc with $\dot{\tau}$, showed that the spatial distribution of the nucleation zones of stick-slip events

were also influenced by $\dot{\tau}$. However in their case the effect was the opposite compared to our experiments: the nucleations occurred all within the same patch for loading rates of 0.01 mm.s^{-1} and 0.1 mm.s^{-1}, but started to be located randomly at 1 mm.s^{-1}. This contrast between the experiments presented here and the results of Xu et al. (2017) could be explained by a different frictional evolution of the pre-cut surfaces between experiments using granite samples (possible frictional melt during weakening phase which would solidify during the healing process) or polycarbonate in our study (no melt during dynamic ruptures, but rather elasto-plastic deformations). In addition, between each event we reset the plates to their initial positions and wait approximately 20 seconds in order for the interface to heal while in the case of Xu et al. (2017), each experiment at a given loading rate comprises a continuous series of stick-slip instabilities.

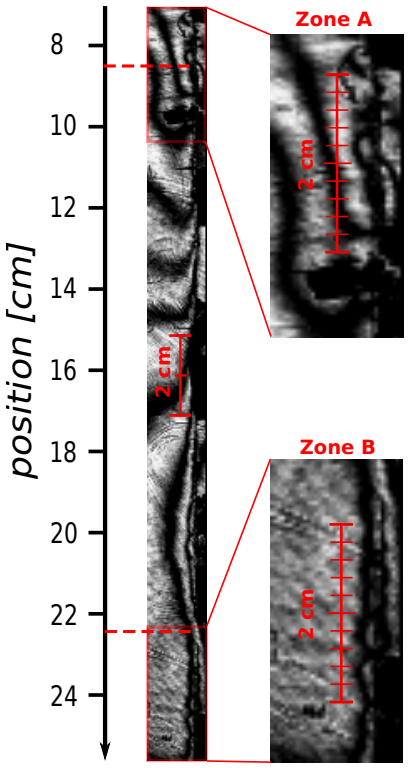

FIGURE 3.8: Zoom-in of the photoelastic fringes located around the high stress areas (zones A and B), showing short wavelength variations of stress between 4 and 8 mm, compared to the smoother distribution at the center of the frame.

Although we do not have a clear explanation why some rupture would nucleate in zones of lower coulomb stress, it is very likely that there exist smaller stress heterogeneities that we are not able to resolve with the sparse strain gauge

measurements or on the isochromatic fringes, and which may vary from one experiment to another influencing the nucleation position; the nucleation may start at some sites where locally high coulomb stress is not resolved by our measurements. The discussion in section 4.1.2 gives only an general idea of the stress distribution along the interface, but do not enable to resolve very small stress variations, or to compare quantitatively the initial stresses of different experiments. We also note that the wavelength of the stress heterogeneity along the interface may play a role in the nucleation localisation. Indeed, in the preferred nucleation zones A and B (see fig. 3.8), a cluster of heterogeneities of smaller wavelength compared to the rest of the interface (4 to 8 mm) is visible in the photoelastic fringes. One hypothesis is that fast stressing would favour the instability closer to small-scale inhomogeneities, while gradual stressing favours the development of pre-slip on larger, homogeneous patches. This could be the case if the stress redistribution during the rupture preparation phase followed a diffusive process, because the diffusion time is proportional to the square root of the inhomogeneity wavelength. Under slow loading the small wavelength heterogeneities would have time to disappear, favouring the development of larger and longer-lasting stress variations. In this study, we have no direct experimental evidence of such process other than the presence of small-scale heterogeneity as illustrated in fig. 3.8, and at time of failure, the level of small-scale heterogeneity appears to be the same in either fast or slow loading conditions. However, as mentioned earlier, it is difficult to make an accurate quantitative analysis based on the photoelastic images alone, and the stress is measured only at the four sites which were instrumented with strain gauges. Also, we can visualize only the main rupture at a late nucleation stage: some rate-dependent slip may occur during the previous seconds of loading which are not captured. Numerical experiments using heterogeneous a and b values and/or heterogeneous initial stress distribution along with varying loading conditions (different loading rates and hold times) would be needed to better understand the influence of the loading rate on the nucleation position.

Another difference with the results of Xu et al. (2017) has to do with the rupture speed dependence with loading rate. While Xu et al. (2017) observe a clear

rupture speed dependence, it is a bit less visible in our experiments (even though some slight dependence can still be seen in fig. 3.4). Indeed, in Xu et al. (2017), the rupture speed does not seem to reach consistently the limiting speed V_{Ray}, unlike what we observe. As the spatial resolution in their experiments is lower, maybe the rupture sometimes switches temporarily to supershear fronts which is not visible, and there could also be 3D effect with only an apparent rupture speed measured. In our experiments, the setup is clearly 2D, and the rupture propagates along a line rather than a plane. It follows a classical evolution, reaching rapidly V_{Ray}, and sometimes switching to supershear. Even though the threshold for the limiting speed is roughly the same around 820 m/s regardless of the loading rate applied in our experiments, what we see is that this threshold is reached earlier in space and time at high loading rate, and the same can be said for the transition to supershear. This dependence of the transition to supershear with loading rate is not discussed here, but could be the object of further studies.

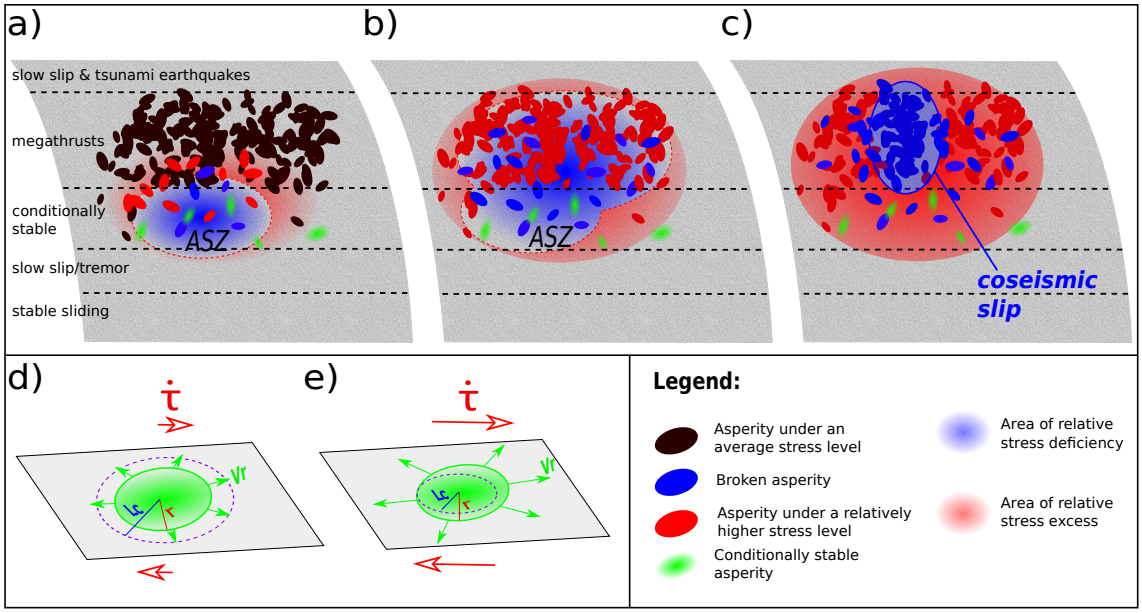

FIGURE 3.9: Cartoon illustrating how the loading rate may locally increase in a slab close to rupture (a,b,c), and how such loading rate increase can induce seismic rupture of conditionally stable asperities (d,e). a) An Apparent Slipping Zone (ASZ) expands from the conditionally stable part, slowly releasing stress in the blue area, and increasing it outside in the red area. Blue asperities are failing; red asperities are locked and accumulating stress; black asperities (located further away) are not yet significantly affected by the stress variations; green asperities are conditionally stable. The conditionally stable asperities (green) do not fail seismically at this stage because their radii r are smaller than L_c. b) The ASZ slowly expands, inducing an increase in both load and loading rate in the surrounding area. This activates seismic failure of either previously locked asperities, or of previously aseismic, conditionally stable asperities (green) due to the shrinking of L_c below their radius r. c) Final stage of nucleation for a large earthquake. A dense cluster of asperities fail jointly (cascade or pre-slip model), further accelerating load around the slip area and finally triggering a large seismic rupture. d) When the loading rate is relatively low (stage a), the conditionally stable asperities slip aseismically as L_c is larger than the asperity radius r. e) When the loading rate increases (stages b and c), the previously aseismic asperities might start to fail seismically if L_c shrinks and becomes smaller than r.

To understand what those experimental results can mean for real earthquakes, it is important to have a global picture of how the interface between plates behaves. From recent observations where pre-slip was detected before an earthquake by inverting GPS signals (Ruiz et al., 2014; Ruiz et al., 2017), a large Apparent Slipping Zone which we will refer to as ASZ appears to be activated around the future epicenter of the earthquake. In order to understand why this ASZ

(interpreted as the preseismic slip) is larger than the coseismic slip, it is important to imagine this ASZ as a highly heterogeneous patch actually composed of smaller locked (or rate-weakening) and creeping (or rate-strengthening) patches (see fig. 3.9.a), as suggested by Socquet et al. (2017). Those patches are progressively activated as the ASZ expands (fig. 3.9.b), some asperities (intended as either conditionally stable or unstable velocity-weakening patches) might fail (foreshocks), releasing stress locally and in the surrounding creeping material, while others might remain locked and build-up stress. It has been observed that this apparent homogeneous ASZ is not only discontinuous in space, but also in time (Frank et al., 2017). The remaining locked asperities inside the ASZ will still be progressively loaded as it expands, and if a large cluster of them breaks (see fig. 3.9.c), this would be the main shock of an earthquake and possibly a foreshock of a next one.

In our case, it is hard to tell if the L_{sc} measured from the experiments (a few centimeters) can be extrapolated to infer the size of the ASZ which can reach a radius of several tens of kilometers (Ruiz et al., 2014). Indeed, the ASZ is very heterogeneous and experiences much more complexity in the frictional evolution than in the controlled laboratory experiments. But considering that the ASZ may be close to velocity-neutral, with an average of (a-b) close to 0, the estimates L_{b-a} could be infinitely large.

Contrary to the observations reported by Ruiz et al. (2014), the conditions under which the experiments are conducted here do not appear to result in a large creeping patch with locked asperities, but rather in a locked fault with a localised pre-slip patch which grows into a dynamic rupture, corresponding rather to the observations of Tape et al. (2018) for a M3.7 asperity. We can therefore discuss the possible effects of a shrinking nucleation size under accelerated loading rate in some natural contexts, for example, linking the natural earthquake nucleations described by Ruiz et al., 2014 and Tape et al., 2018 or to explain the appearance of aftershocks following the 2011 M9.0 Tohoku-oki earthquake, in places where only very few earthquakes had been observed during the last 88 years (Hatakeyama et al., 2017).

A locked asperity on a creeping fault could fail aseismically: if L_c were larger than the size of the asperity, the slip would not accelerate up to seismic velocities needed to radiate waves (Mclaskey and Yamashita, 2017) (see fig. 3.9.d). However, if the loading rate in the vicinity of this patch is suddenly increased, L_c could decrease below the asperity dimensions and the patch could become seismic (see fig. 3.9.e). As noted by Mclaskey and Yamashita (2017) this model is consistent with the observations of Wech and Bartlow (2014) who evidenced a correlation between slow slip rate and the number of tremors in Cascadia, considering that a subduction interface can be composed of a large population of those patches oscillating between stable and unstable behavior. As the ASZ undergoes accelerated creep, the local loading rate on the smaller locked asperities increases and this could trigger their seismic rupture during the preseismic interval. In the postseismic phase, as long as the accelerated creep continues, the small asperities may still undergo seismic rupture as observed in the seismic cycle (Yao et al., 2017), and aftershocks could appear in conditionally stable areas following the increase of loading rate as discussed by Hatakeyama et al. (2017).

Chapter 4

Numerical models of rupture and loading conditions of biaxial experiments

This chapter aims mainly at helping to understand the results of the analogue rupture experiments from chapter 3. It is divided into a static models section and a dynamic models section.

The static part is used to benchmark the FEM base code (including the part written to calculate stresses and strains from a 2-dimensional displacement field) using the analytical solution for a mode I crack under a uniform remote stress. The way I deal with contact problems in finite elements is introduced, and is the basis of a code in developement simulating dynamic ruptures (see appendix C). I also use the static model to infer the initial stress distribution in the experiments described in chapter 3. This constitutes an appendix of the published article Guerin-Marthe et al., 2018. Finite differences are used to model the dynamic ruptures, and enable to better understand the evolutions of slip, velocities and stresses along the fault, in a similar manner to what has been measured by the strain gauges in chapter 3. Finally, I verify and discuss the method used in chapter 3 to estimate the slip dependant friction law.

The reader can refer to sections 2.3.2 and 2.3.1 for the general theory of FEM, DG and finite differences. Here I only focus on the code adaptations to model the experiments. Altogether, this can be used as a tutorial to implement FEM models, and adapt them to simulate 2D static elasticity, or dynamic ruptures.

4.1 Static model

4.1.1 Crack model and benchmark

The polycarbonate plates are modelled using Finite Elements and linear elasticity. We need to benchmark the numerical model, and therefore we verify that when the model is deformed, displacements and stresses are consistent with linear elasticity and LEFM theory.

Model verification

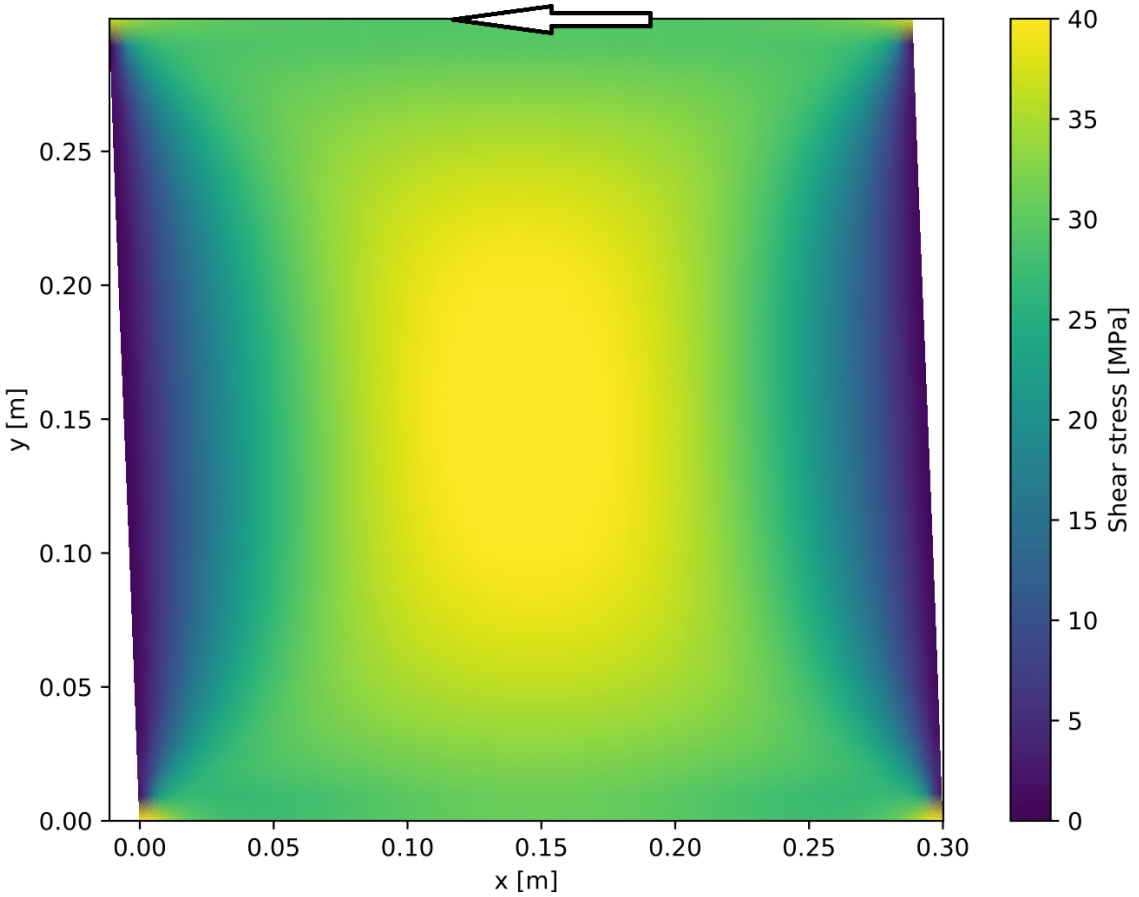

FIGURE 4.1: Simple shear static simulation, applying a negative horizontal displacement at the top edge of the elastic domain, and zero horizontal displacement at the bottom edge. The vertical displacement are also kept to zero.

The first thing I do is to check that the way displacements and forces are applied to the edges of the domain is correct, as well as the way stresses are calculated. This is done by creating a simple shear model, where the left and right boundaries

are left stress-free, and uniform displacements dx corresponding to a uniform pressure P_h of 28 MPa (arbitrary) are applied on the top edge. The displacements on the bottom edge in both directions are fixed to zero. dx is calculated for given values of E, ν and Ly (the height of the domain) using (see fig. 1.14 and eq. 1.7):

$$dx = \frac{L_y \times P_h}{E/(1+\nu)} \tag{4.1}$$

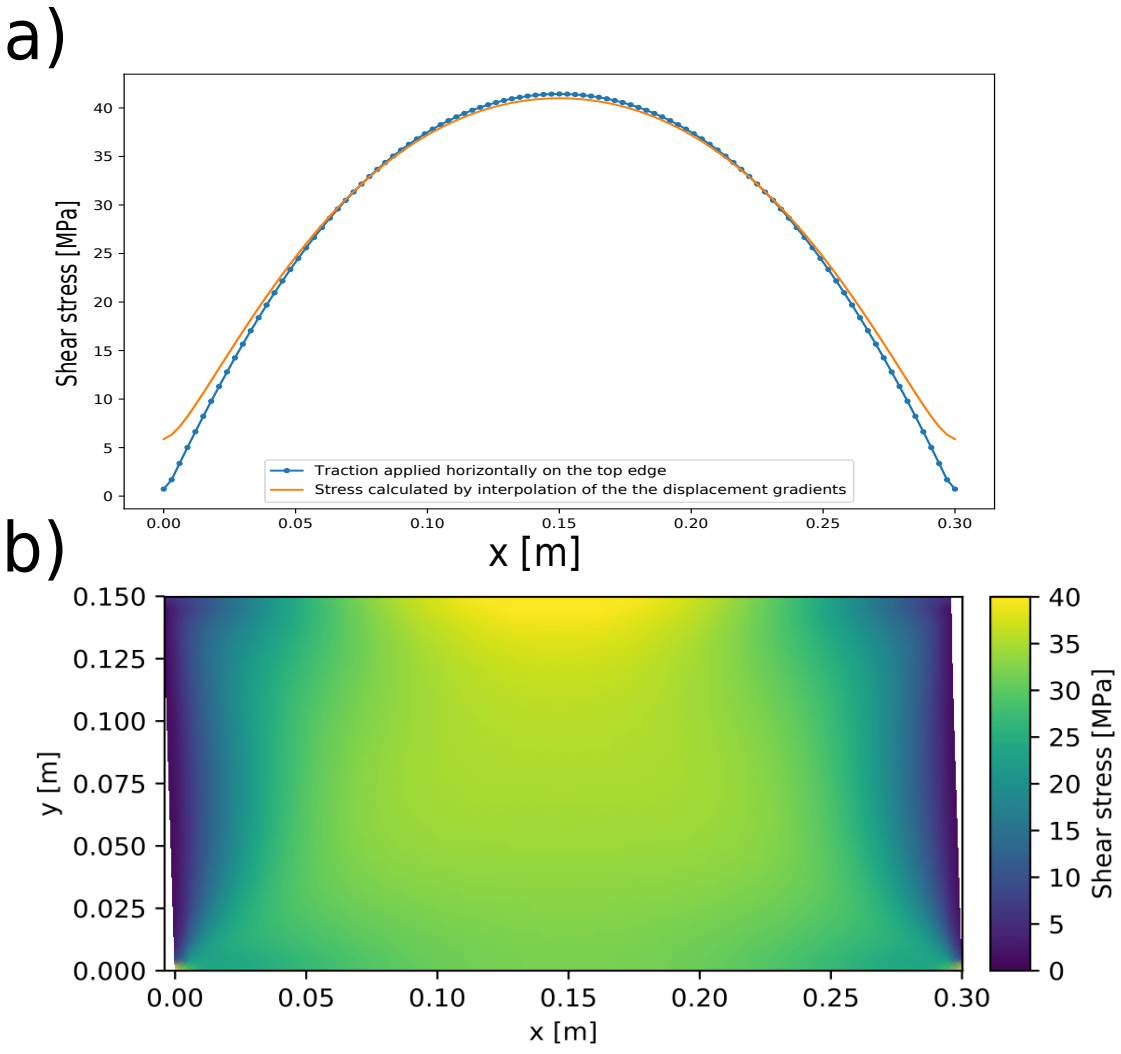

FIGURE 4.2: a) The blue line corresponds to the shear stress measured in the middle of the 30 by 30 cm elastic domain (0<x<30 cm, y=15 cm in figure 4.1). Those shear stresses are then applied as horizontal tractions at the top boundary of a half-domain, 30 by 15 cm. b) Stresses measured in the half-domain by using the interpolated displacements. The displacement of the left, bottom and right edges are measured in the model of figure 4.1, and then imposed on the half-domain model. The stresses calculated at y = 15 cm are also plotted in a) (orange solid line) to be compared to the applied tractions.

The stresses are calculated using eqs. 1.4 and 1.8 for the plane stress case (chapter 2), and are plotted in fig. 4.1. As expected, the stresses are higher in the middle of the domain, and go to zero at the stress-free edges. A stress profile at $y = 15$ cm and $0 < x < 30$ cm is plotted in fig. 4.2.a (blue line).

Now if the domain is "cut" in half, along $y = 15$ cm, if the displacements are kept the same than on fig. 4.1 at the left, bottom and right edges, and if the shear stress profile measured in the full domain (blue line fig. 4.2.a) is applied as horizontal distributed forces on the top edge of the half-domain, we expect to find a consistent stress distribution (fig. 4.2.b). We can check that the tractions applied (blue line fig. 4.2.a) and the stress measured (orange solid line fig. 4.2.a) are indeed very similar, at the exception of the left and right edges ($x = 0$ cm and $x = 30$ cm), where a difference of 5 MPa is observed. It is likely due to interpolation approximations close to the model's edges.

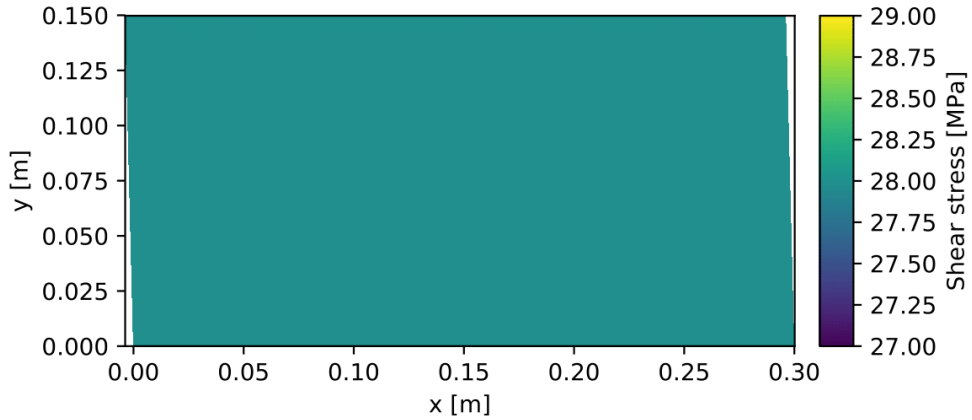

FIGURE 4.3: Static simulation on a half-domain where the displacements on the left, bottom and right edges are imposed given theoretical values for a simple shear case. On the top edge the corresponding uniform distributed load is imposed (28 MPa in this case). The uniform stress calculated on the whole domain evidences the consistency between the theory, the simulation, and the stress and strain calculations.

Finally, if instead of the bell shaped curve I apply a uniform pressure of 28 MPa on the half-domain's top edge, while fixing all the other edges displacements at the values corresponding to the theoretical simple shear case, it results in an expected homogeneous shear stress field (see simulation in fig. 4.3).

Convergence analysis for a mode I crack model

I start by modelling a static crack in tensile-opening mode. This enables to introduce the way I deal with contact problems which is based on the idea of fictitious springs linking two elastic domains. The same concept is used in the FEM code simulating dynamic rupture which is only mentioned in the appendix C (it is still under development).

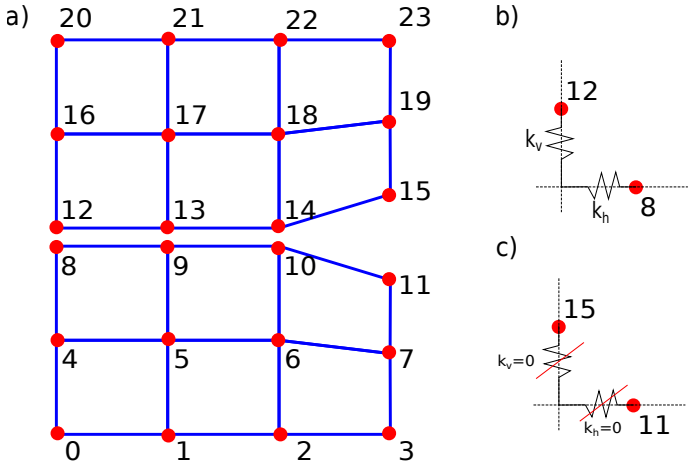

FIGURE 4.4: a) Sketch of the grid setup used for the contact problem and crack simulation. The elastic domain is separated into two elastic domains on both side of an interface where the nodes are split. Inside a domain the nodes are linked by the standard continuous FEM terms, and by fictitious springs at the interface. b) Fictitious springs are maintaining the vertical and horizontal dof of two opposing nodes together as one in case of contact (spring stiffnesses are arbitrarily high). c) Case of mode I open crack where the springs are "cut", which is equivalent to setting their stiffnesses to zero.

In order to model the experiment composed of two elastic plates (see chapter 3), I start by splitting the nodes in the middle of the domain (see fig. 4.4.a). This enables to have a possible discontinuity between elements, similarly to the DG method described in section 2.3.2 of chapter 2. In DG, even though a discontinuity between the elements is allowed, modelling continuous elastic domains might still be needed, in which case additional terms are added to link opposing surfaces (eq. 2.37 in section 2.3.2). The latter have the following form:

$$C_1 = -\underline{B}^{+T}\underline{D}\,\underline{n}^T\underline{N}^+/2 - \underline{N}^{+T}\underline{n}\,\underline{D}\,\underline{B}^+/2 + p(\underline{N}^{+T}\underline{N}^+) \tag{4.2}$$

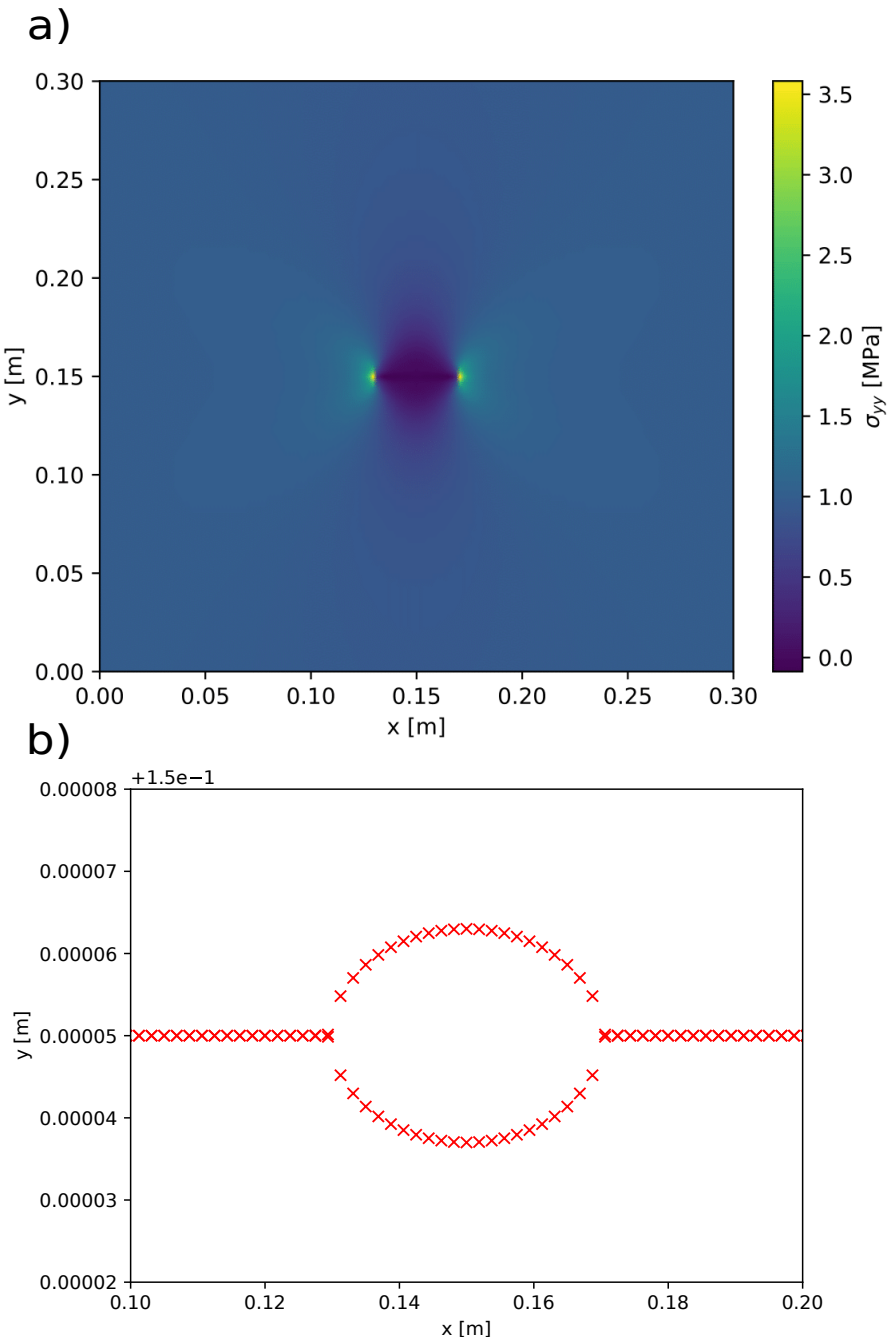

FIGURE 4.5: a) Mode I crack simulation with a remote tensile stress σ_{yy} = 1 MPa. b) Zoom on the split nodes at the interface around the 4 cm long crack.

$(\underline{N}^{+T}\underline{n}\,\underline{D}\,\underline{B}^{+}/2)$ and $(\underline{B}^{+T}\underline{D}\,\underline{n}^{T}\underline{N}^{+}/2)$ are corrective terms added to enforce interaction between elements, and $p(\underline{N}^{+T}\underline{N}^{+})$ is the term weighing the most in the calculations, to link opposing surfaces. It is equivalent to add fictitious springs between opposing nodes as illustrated in figure 4.4.b. Some terms ($\pm k_v$) are linking the vertical dof while others ($\pm k_h$) are linking the horizontal ones. Note that in DG, the arbitrarily high penalty value p corresponds to the fictitious spring

stiffness. It is generally in the order of magnitude of E, if it is too low the simulation is not accurate, and if it is too high, the global stiffness matrix may become singular.

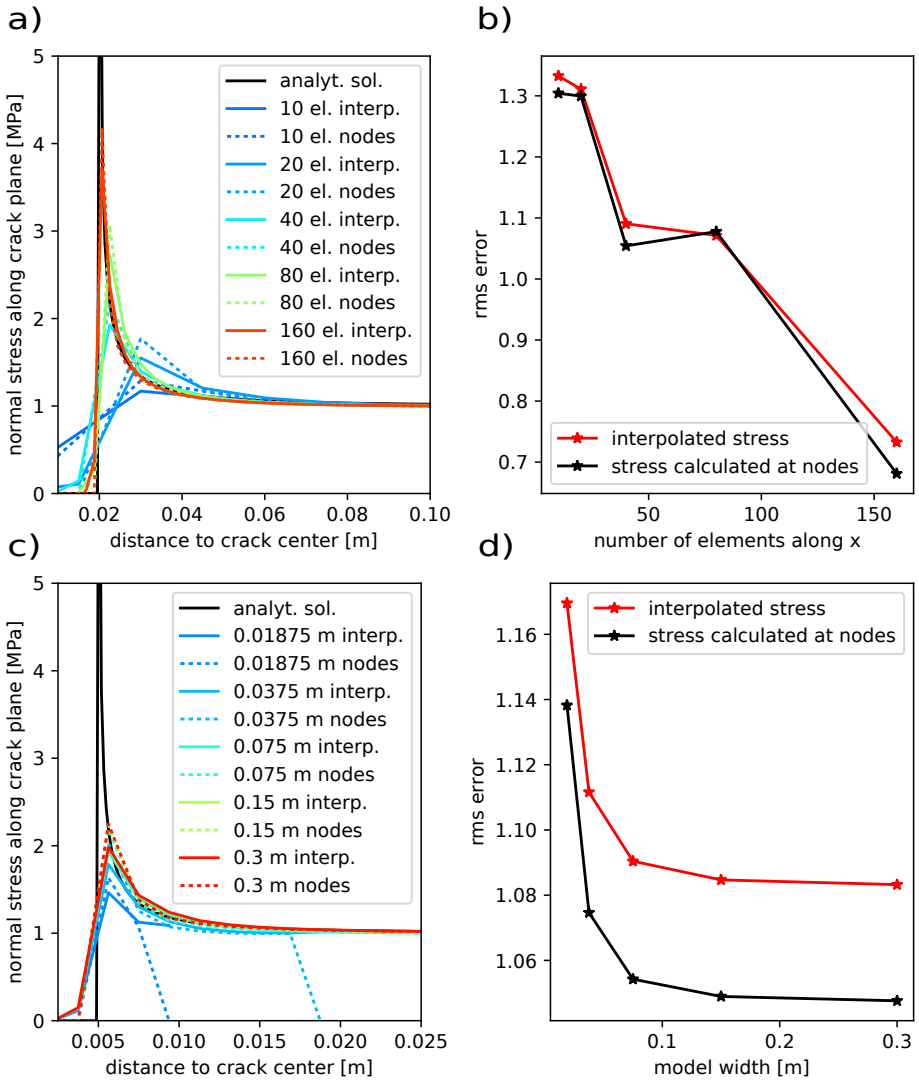

FIGURE 4.6: Convergence analysis using the crack simulation. a) Comparison between the analytical solution of σ_{yy}(x) in the vicinity of a mode I crack under uniform remote stress σ^{∞}_{yy}, and simulations using an increasing number of elements in both x and y directions. b) Associated rms errors. c) Same comparison, but this time increasing the ratio (domain width)/(crack width), and keeping the same elements dimensions, and the same crack width. d) Associated rms errors. In a) and c) the solid lines correspond to the stress values calculated using displacements interpolation in 2D. The dashed lines correspond to the stress values calculated using the relative vertical displacement between two opposing nodes, and the fictitious spring stiffness.

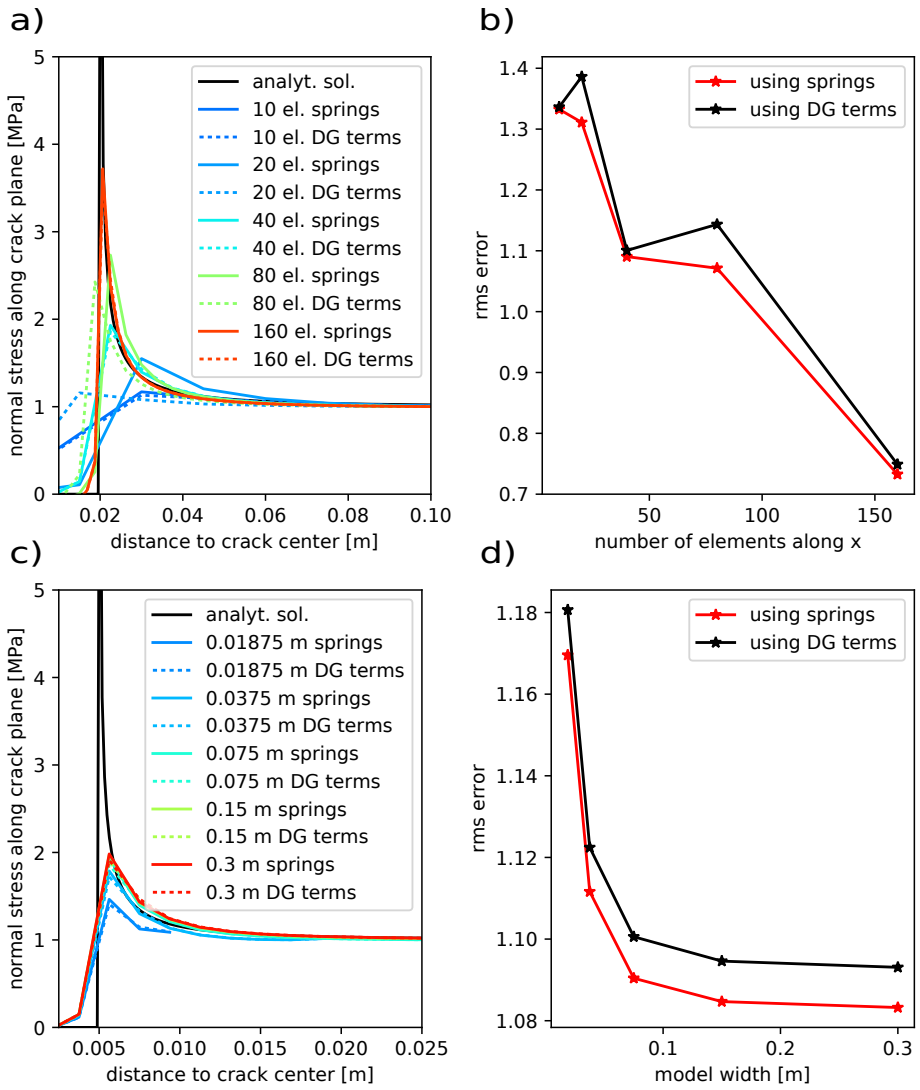

FIGURE 4.7: See caption of fig. 4.6. However, this time the solid lines correspond to simulations using fictitious springs at the split nodes while the dashed lines correspond to simulations using DG terms between the opposing faces. All the stresses are calculated from the displacements interpolation in 2D.

Using these fictitious springs, it is relatively easy to model a crack. At least for mode I, the only things needed to be done is applying displacements at the top and bottom edges of the domain corresponding to a uniform traction (1 MPa in the simulation of fig. 4.5.a), and add stiffness terms $\pm k_v$ and $\pm k_h$ corresponding to springs all along the interface, except where the crack is defined (equivalent to set $k_v = k_h = 0$). By doing so, I allow the two surfaces inside the crack to be completely detached (see fig. 4.5.b). As expected, the stress concentration is also very high at the crack tips (see fig. 4.5.a), and the values of $\sigma_{yy}(x)$ along x in the vicinity of the crack tip can be compared to the analytical solution which has the

form (Broberg, 1999):

$$\sigma_{yy}(x) = \frac{\sigma_{yy}^{\infty}}{\sqrt{1-\left(\frac{a}{x}\right)^2}} \tag{4.3}$$

Where a is the crack half-length, σ_{yy}^{∞} is the remote stress, and x = 0 at the center of the crack.

Note that for x $\approx a$, this expression becomes equivalent to the form of the near-field stress equations 1.12, with an amplitude dependence in $1/\sqrt{r}$, where r is the distance to the crack tip. Indeed, starting from eq. 4.3, taking x=a+r, and using Taylor expansions to show that $1 - a^2/(r+a)^2 = 2r/a + \mathcal{O}(r^2)$ for r ≈ 0, we obtain:

$$\sigma_{yy}(x) = \sigma_{yy}^{\infty}\sqrt{\frac{a}{2r}} \tag{4.4}$$

I check that the solution converges when increasing the number of elements (figs. 4.6.a-b and 4.7.a-b), or when increasing the domain width and keeping a and the number of elements inside the crack constants (figs. 4.6c-d and 4.7.c-d). I also compare the stress values calculated using the interpolation of the displacement field, to the values given by the relative displacement Δu between nodes. Indeed, the traction at a given node along the interface is directly proportional to the fictitious spring stiffness k, and given by $f = k\Delta u$. Figure 4.6 corresponds to two sub-domains linked by fictitious springs, while figure 4.7 corresponds to two sub-domains linked by DG terms. It can be seen that for a high enough number of elements, the different ways to obtain the stress, and the DG or spring stiffness terms are giving the same results (see fig. 4.6.a-b and 4.7.a-b).

4.1.2 Initial stress distribution of dynamic ruptures inferred from photelastic fringe patterns coupled with finite element models

This section aims at discussing what is the stress distribution along the interface between the two polycarbonate plates, just before a rupture, using the photoelastic fringe patterns and FEM, in order to support the measurements of chapter 3.

As described in section 2.1.1, the setup is composed of two polycarbonate plates 15 cm wide by 30 cm long, and 1 cm thick (see figure 4.8). They are clamped by two metallic frames overlapping them over a width of 7.5 cm, on each side of the setup. Then two pistons are applying a normal force by pushing uniformly on the right edge, 30 cm long. Once under normal load, a fault parallel shear stress is applied by pressing the left clamping frame downwards. Although the setup seems simple, further complexity arises from the fact that the plate might actually not be clamped uniformly within the width of the metallic frame. This can generate different loading conditions, therefore different stresses at the interface.

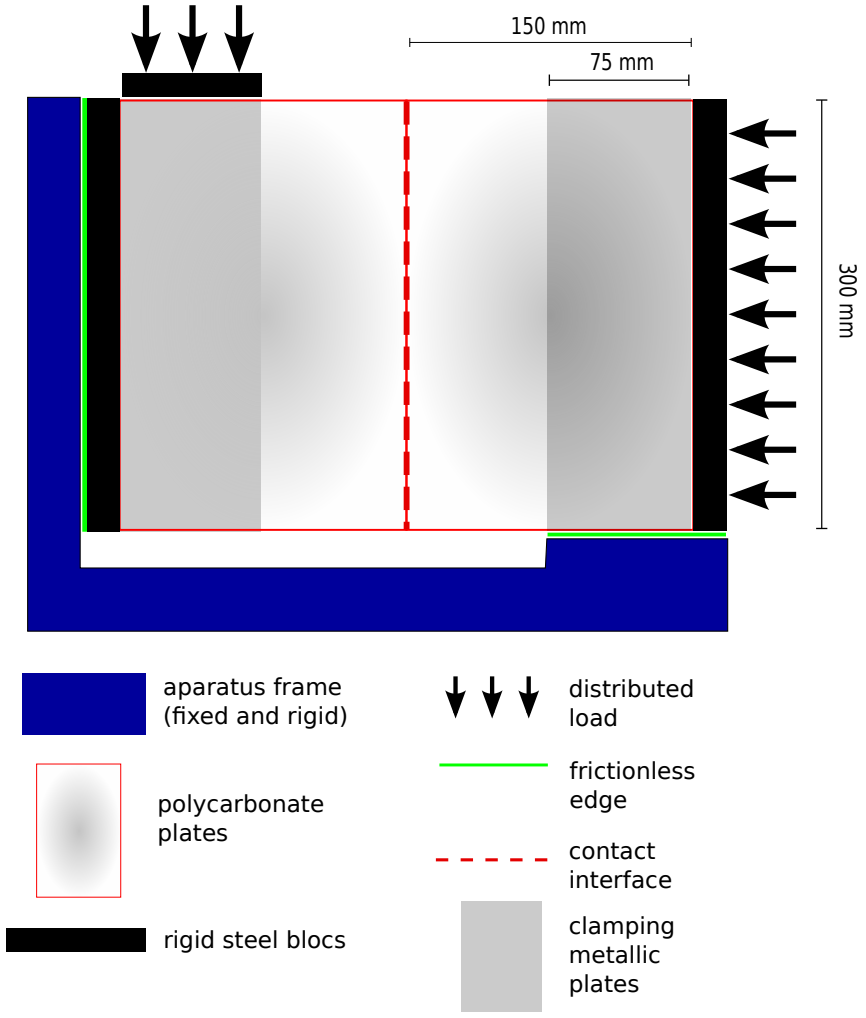

FIGURE 4.8: Sketch of the experimental setup and boundary conditions of the model

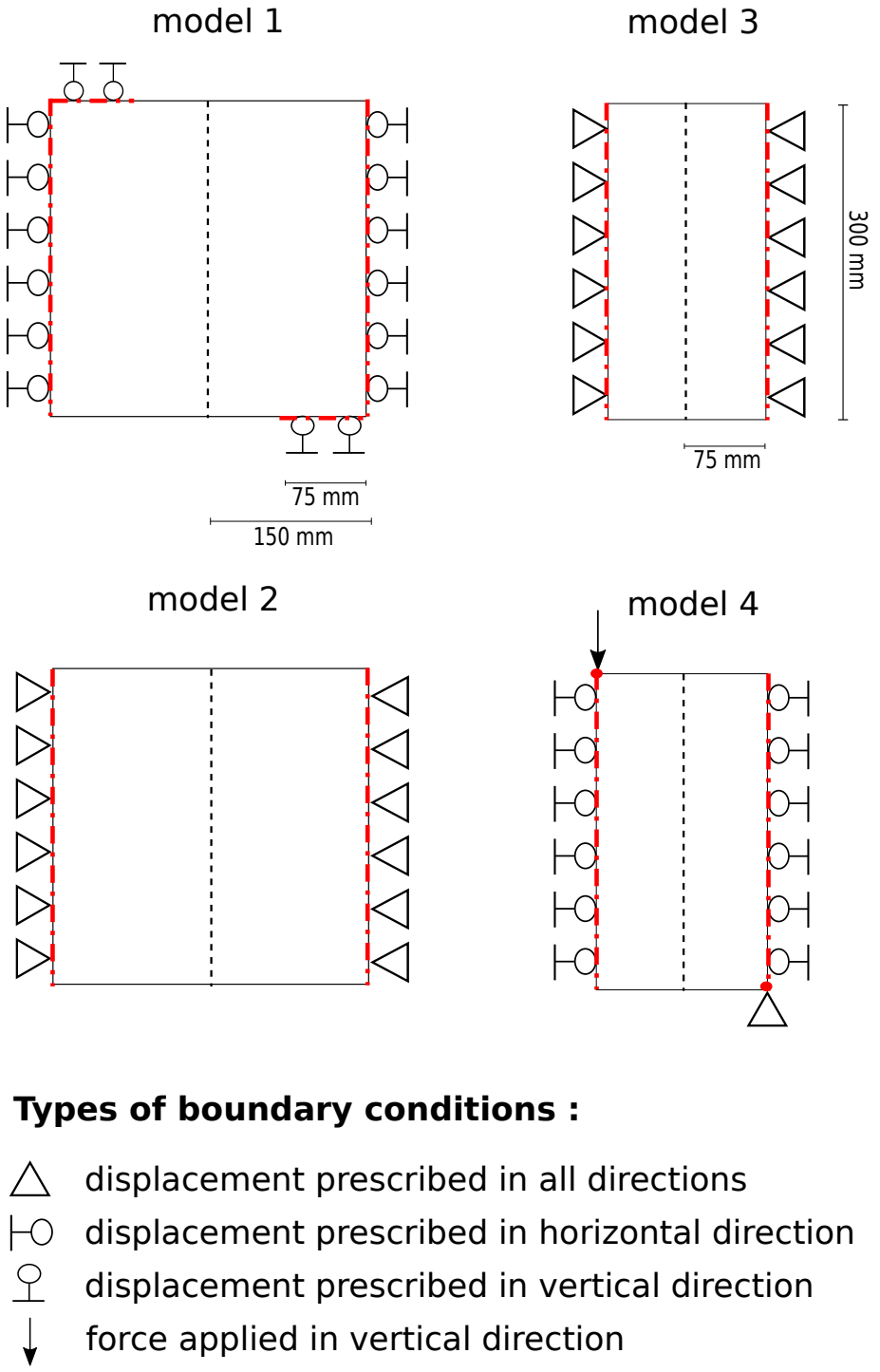

FIGURE 4.9: Different types of numerical models used to generate shear stress at the interface (dashed line)

In order to discuss which loading configuration is the best suited to represent the experiments, I perform finite element simulations using different boundary conditions as described in figure 4.9. Note that if the plates were perfectly maintained within the metallic clamp, I would only need to model two elastic domains

7.5 cm wide and 30 cm long (models 3 or 4 fig. 4.9). But if they are allowed to move inside the clamps, it might resemble rather models 1 and 2 of fig. 4.9.

Using the loading configurations illustrated in fig.4.9, I first adjust the magnitude of the forces or displacements to match roughly the strain gauge measurements of shear and normal stresses to the stresses calculated in the middle of the FEM models (dashed lines fig. 4.9). At this stage it can be observed that for models 1 and 2 (30 by 30 cm) the shear distributions along the interface tend toward parabolic-like shapes, and as the models are shortened (models 3 and 4), corners start appearing at the edges (fig. 4.10). In all the cases the shear stress goes down to 0 at the edges, which is to be expected at stress-free boundaries. The normal stresses are more homogeneous and more or less similar between the different simulations except for the model 4 where point loads are applied. All the normal stress distributions present corners where the stress drops roughly 7 cm away from the edges. Model 4 is the one which seems to match best the shear stress distribution, while the normal stress distribution is better represented by the other models.

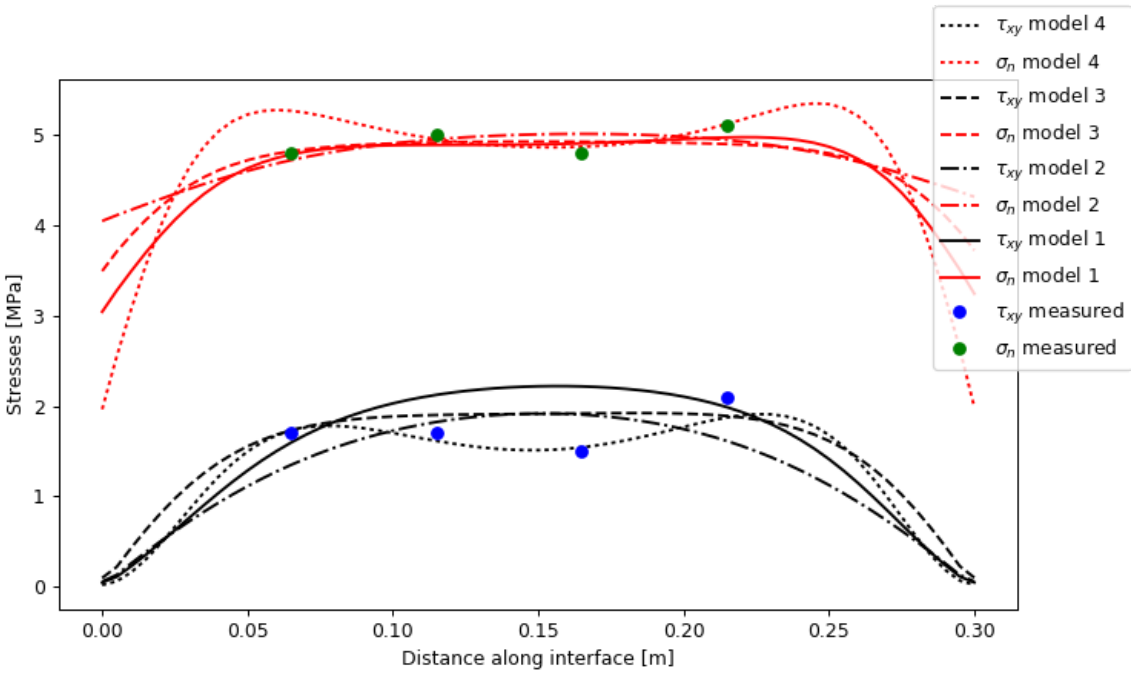

FIGURE 4.10: Shape of shear stresses generated at the interface by each of the 4 loading configuration, and strain gauge point measurements of shear stresses.

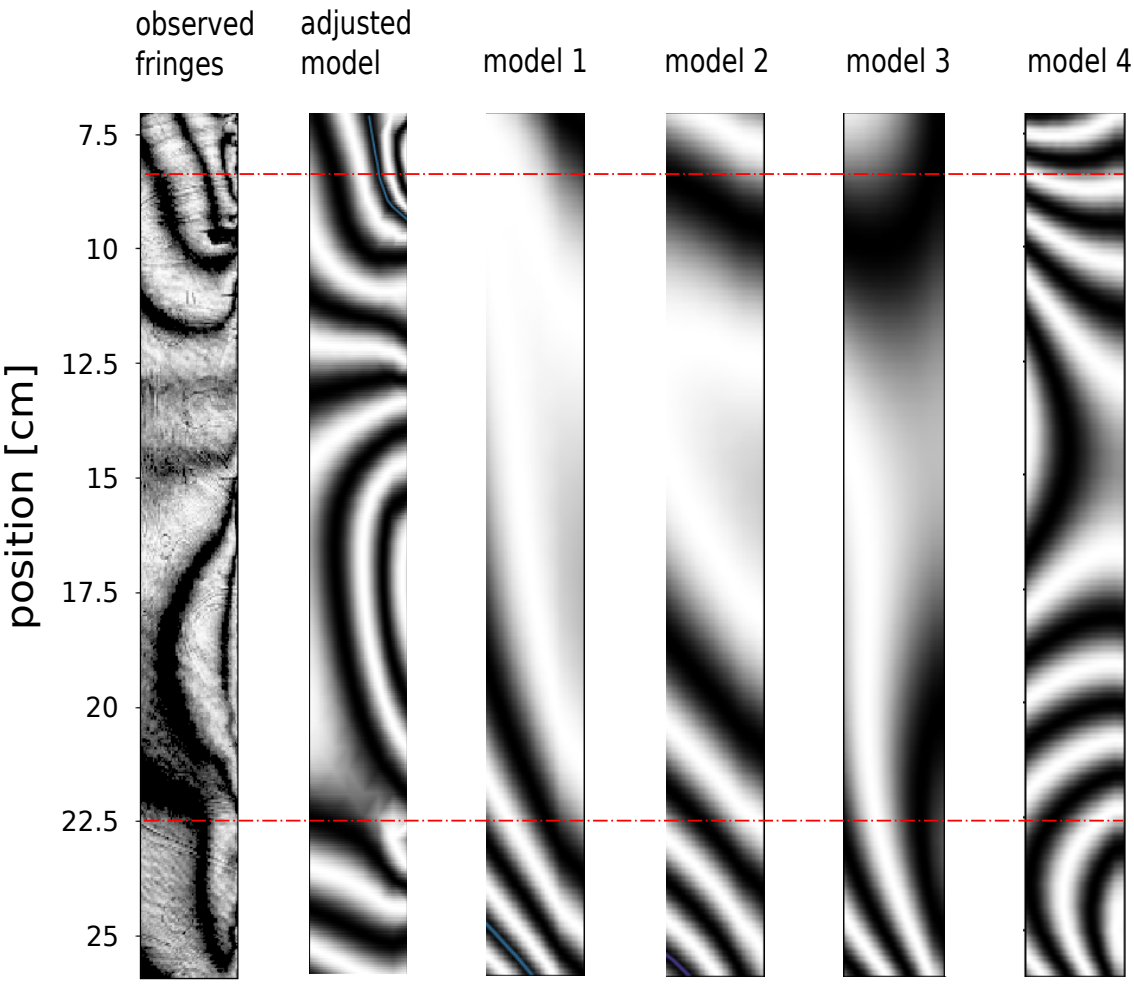

FIGURE 4.11: Fringe patterns simulated in the zone corresponding to where the experimental fringes have been filmed

In order to compare the models to the experimental data, I simulate the isochromatics that the shear and normal stress values measured at the interface would generate if they are applied as tractions along the 30 cm long edge of one single plate, taking a fringe value f_σ= 4000 N.m^{-1}. The opposite edge is left with the same boundary type as it is in figure 4.9. The patterns of the 4 models are compared to each other, to a fifth model where shear and normal stresses were manually adjusted to match the isochromatics (see fig. 4.12), and to a typical snapshot of fringe pattern before a rupture (fig. 4.11). The boundary conditions of the fifth model are like the model 3 on the right edge (fixed in all directions). Models 1 and 2 are far from matching the isochromatics, while models 3 and 4 are a better starting point. It is thus important to consider the plates as shortened to

half their original width as they are clamped between the metallic frames. Then starting from model 3 and by manually adjusting the tractions at the left edge, I manage to obtain a fringe pattern qualitatively similar to the one observed (adjusted model and observed fringes in fig. 4.11). This requires two peaks of shear stress at approximately 8 cm and 23 cm along the interface, while the normal stress is more homogeneous, and only dropping slightly on the edges according the model of fig. 4.12.

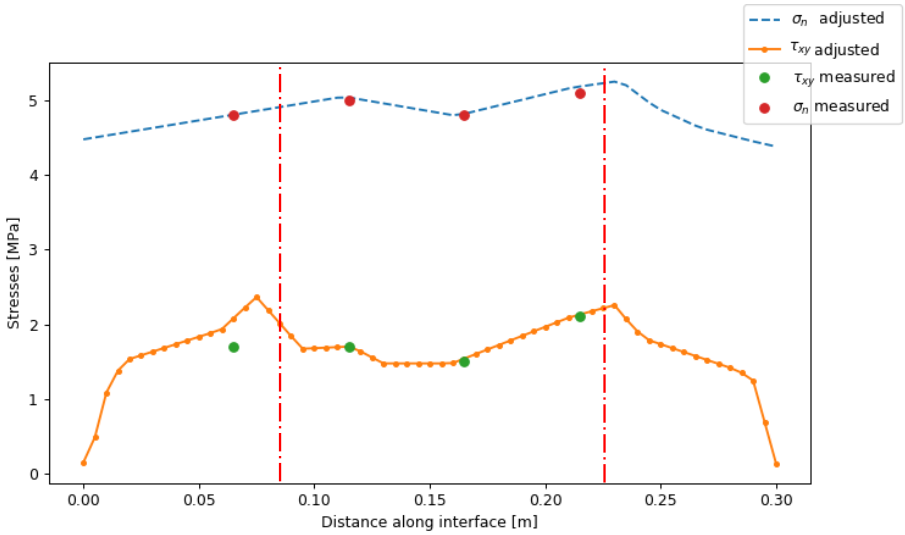

FIGURE 4.12: Manually adjusted tractions at the interface to qualitatively fit the fringes

The adjusted model is consistent with the observed nucleation positions at 8.5 cm and 22.5 cm as the coulomb stress of the model $\tau_{coulomb} = \tau_{xy} - \mu\sigma_n$ is close to zero at those locations (see fig. 4.13). The rupture is therefore more prone to start from those 2 locations.

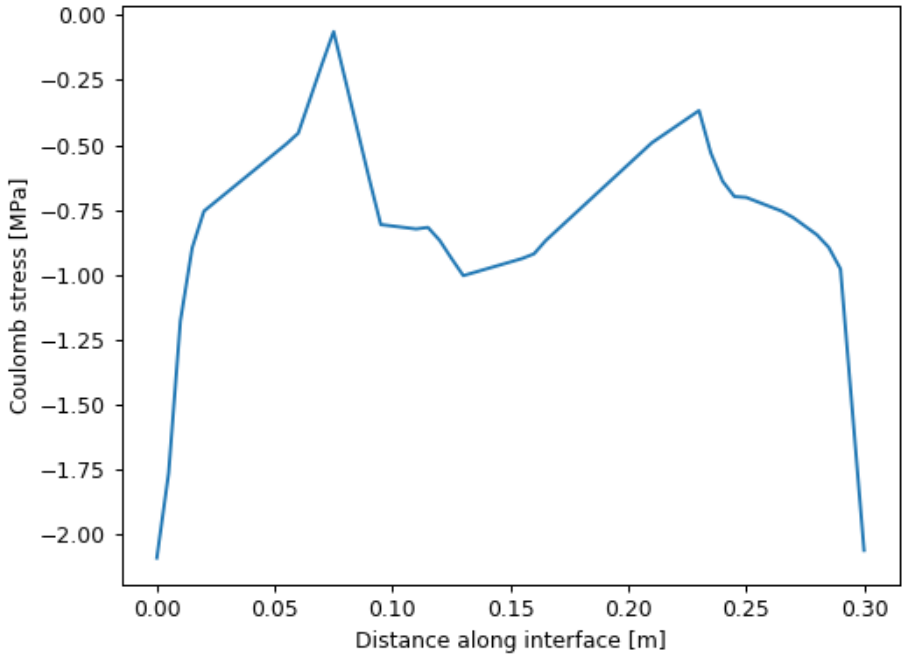

FIGURE 4.13: Coulomb stress from the adjusted model using a friction coefficient $\mu = 0.5$. The closer $\tau_{coulomb}$ is to 0, the closer to failure this point is.

The result of this section highlighting the two areas of high coulomb stress is non-unique in the sense that a same fringe pattern can be created by different shear stress distributions; the concentrated fringes could also highlight areas of low shear stress. Nevertheless, after having adjusted manually the stress distribution several times, low stress values around 8 cm and 23 cm never enabled to obtain a good match between modelled and experimental fringes. It does not fit well with the strain gauge data either, and it is less consistent with the fact that those areas are the preferred nucleation sites of the ruptures.

It should also be mentioned here that I explored other ways to match the fringe pattern between simulations and experiments, rather than trying manually to adjust the forces. As I did not obtained better results, the latter are not shown here, but I can describe briefly the methods used. I started by defining a straightforward misfit function, as the sum of the difference between simulated and measured light intensities, for all the pixels. Then, I searched randomly in the parameter space which forces would minimise the misfit. This did not give conclusive results as the misfit function defined this way does not tell exactly how close to the real solution the model is: two very similar fringe pattern can

give two very different misfit values if the fringes are sightly shifted so they become in phase opposition. From this observation, I chose to look rather at the envelope of the fringes by taking the Hilbert transform of the pictures and the models. I also defined the misfit function as the different between the two, and searched randomly in the parameter space. This gave results qualitatively similar to the one when adjusting manually the forces at the interface, but no better... One thing that would probably work better is to use the same misfit function (difference between the simulated and measured fringes' envelopes), and carry a proper inversion (steepest gradient for instance), similarly to what has been done in appendix A.

4.2 Dynamic rupture

In order to model the dynamic ruptures, I use finite-differences which are less computationally expensive, and easier to implement compared to FEM. The code used is reproduced from Virieux and Madariaga, 1982. More details on the 2D discretized wave equations used are given in section 2.3.1 of chapter 2 (eqs. 2.17). Along the fault I prescribe the initial shear stresses, and a patch is defined, of a half-width corresponding to L_c, were the shear stress is forced to drop. This stress drop induces opposing slip velocities on the two opposing sides of the interface. A relative slip along the interface therefore increases progressively, making the stress drop further, according to a linear slip-weakening friction law (see section 1.4) (a residual stress τ_r is also defined, minimum that the shear stress can reach). As the stress drops inside the crack or ruptured area, it increases outside, at the tips. A peak stress τ_p is defined as our rupture criterion: when τ_p is reached at the crack tips, the crack is allowed to expand and accelerate. I also prescribe the loading rate $\dot{\tau}$ at which the shear stress in the non-ruptured area increases. The initial stress drop needed for the rupture to initiate actually corresponds to the difference between the increased shear stress outside the ruptured area, and the shear stress inside the initial ruptured area. In the models presented in this section, for $\dot{\tau}$ up to 10 MPa/s, stress variation induced by the loading rate rapidly become negligible in the nucleation process.

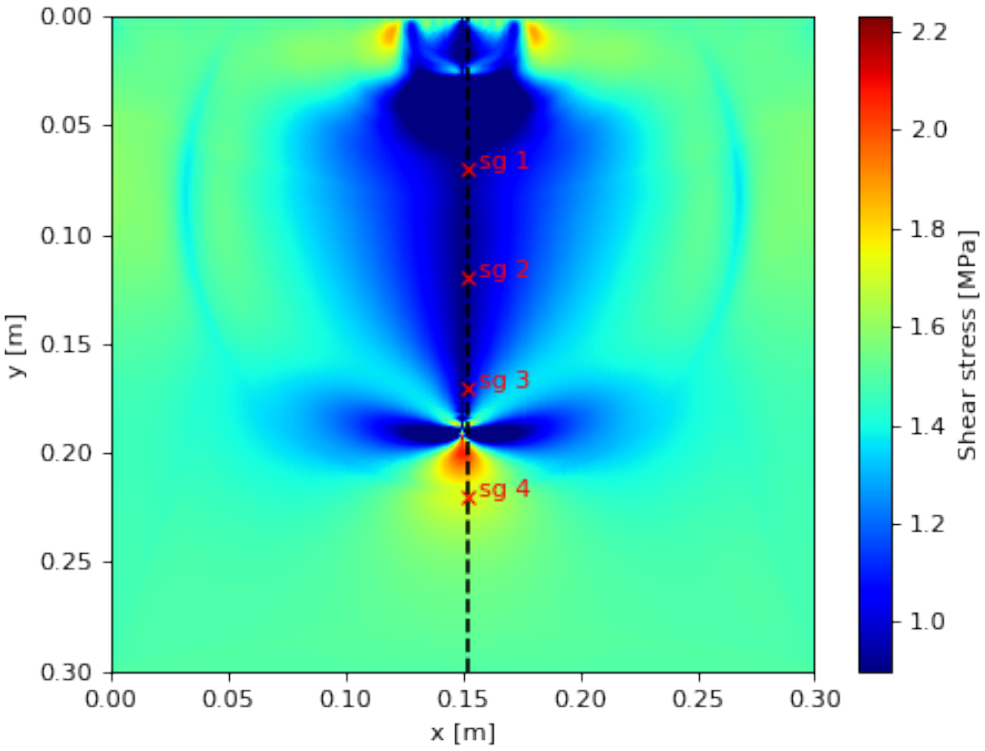

FIGURE 4.14: Shear stress distribution during a sub-shear rupture, in the 30 by 30 cm domain (parameters corresponding to model 1 in table 4.1), simulating a dynamic rupture similar to the ones observed in the laboratory, using the biaxial shear apparatus. Time-dependant modelled signals are recorded 2 mm away from the fault, at the positions corresponding to the strain gauges in the experiments of chapter 3 (sg 1, sg 2, sg 3 and sg 4).

In order to be comparable to the experiments, I use a similar geometry and similar material properties than the polycarbonate plates. The Young's modulus E = 2.6 GPa, and the Poisson's ratio ν = 0.35, which gives a S-wave speed V_S = 893 m/s. The grid is 30 by 30 cm with a fault parallel to the y-axis, at x = 15 cm. The horizontal (fault perpendicular) edges are stress-free, while the displacements on the fault parallel edges are fixed to zero. Displacements, velocities and stresses are stored at the corresponding strain gauge locations (sg 1, sg 2, sg 3 and sg 4) in the experiments (see fig. 4.14), 2 mm away from the fault. An example of typical shear stress field recorded during a rupture is shown in fig. 4.14. Three different models are used in this sections, and the parameters are summarized in table 4.1. Model 1 is used to look at the friction dependence on slip, to see if the

steady-state approximation made to plot the friction law described in chapter 2 and used in chapter 3 is valid. This model has the advantage to simulate a rupture propagating at constant velocity for a long time. Model 2 is a model where we adjusted manually the simulation parameters in order to fit the experimental data. Model 3 is used to verify that the loading rate applied does not affect the simulations when using a linear slip-weakening law. It simulates a clear supershear transition, and makes it easy to verify that it happens at the same time for different loading rates.

Parameters:	model 1	model 2	model 3
E [GPa]	2.59	2.59	2.59
ν	0.35	0.35	0.35
ρ [kg.m^{-3}]	1200	1200	1200
L_c [cm]	2.05	1.45	2.5
τ_p [MPa]	2.23	2.23	2.15
τ_0 [MPa]	1.5	heterogeneous	1.5
τ_r [MPa]	0.9	0.9	0.9
D_c [μm]	12	9	15
S	1.22	≈ 1.22	1.08
κ	1.93	≈ 1.82	2.0
dx [mm]	0.5	0.75	0.6
nx = ny	600	400	500
dt [μs]	0.076	0.114	0.090
t_{max} [ms]	0.4	0.7	0.4
$\dot{\tau}$ [MPa/s]	1.0	0.07	variable

TABLE 4.1: Summary of parameters used in finite difference models

In order to compare the experiment and numerical models, I change the model parameters by trial and error (model 2 in table 4.1) in order to fit the strain gauge data (see fig. 4.15). The initial shear stress distribution $\tau_0(y)$ is fitted with a 5^{th} order polynomial function, so that I obtain a continuous initial shear stress which passes by the experimental values recorded by the strain gauges (see fig. 4.16,

stress profile at a time = 0 ms). A very good correlation between the signals is obtained, although the peak stress arrives earlier for sg 4, indicating a slightly earlier transition to supershear in the model, compared to the experiments.

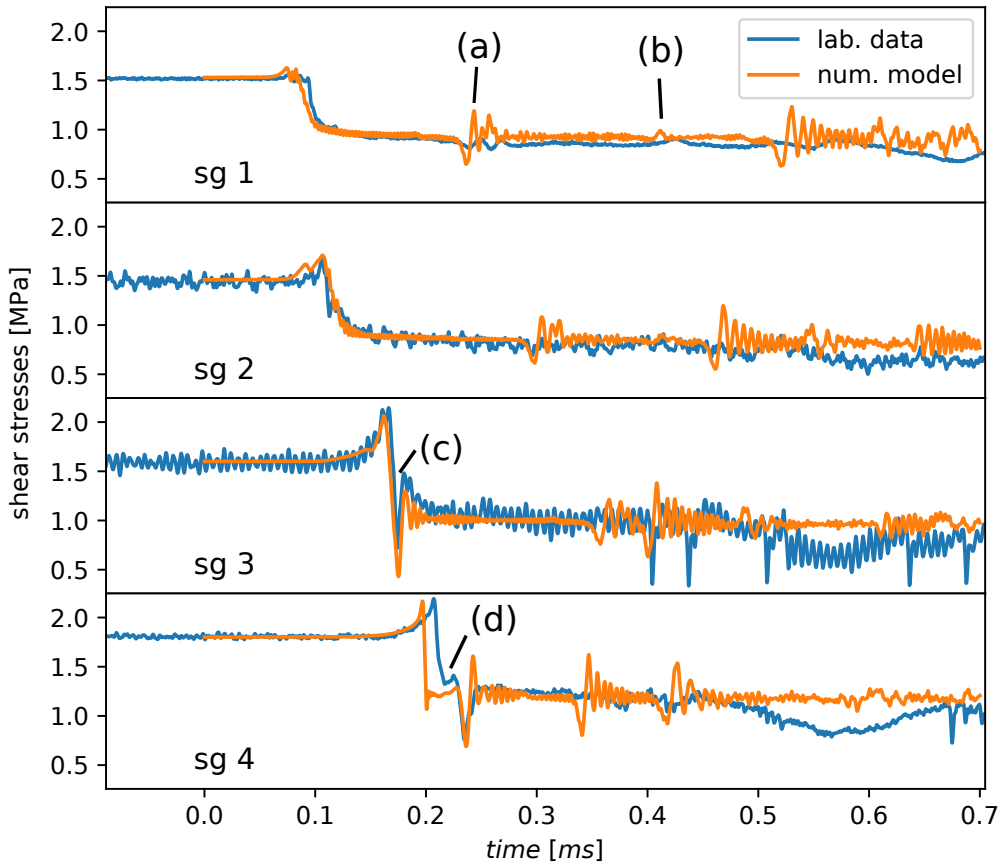

FIGURE 4.15: Comparison between experimental strain gauge signals and modelled ones (parameters corresponding to model 2 in table 4.1), for a supershear case.

When using the numerical simulation results, the shear stress signals from strain gauges in the experiments are easier to interpret. By looking at the along-fault shear stress profile (2 mm away from it) plotted versus time (fig. 4.16), we can better identify what is recorded by the gauges in fig. 4.15. On sg 1 for instance, we clearly identify the reflected supershear and subshear fronts from the top of the model, arriving around 0.25 μs (a), and a positive pulse around 0.45 μs corresponding to a reflection on the vertical edges (b). At sg 3, we observe a

typical subshear rupture front, with a significant stress drop separating two stress peaks (c). This drop does not exists on the fault itself (fig. 4.18.d), but is measured due to the shear stress field complexity away from the fault (see fig. 4.14). It can also be seen from the theoretical solution of stress away from the fault for a dynamic crack propagating at constant speed (eqs 1.12 and 1.15; a plot example using those equations is shown in appendix A, fig A.3.c). Finally, sg 4 records a delay between the first shear stress peak and the following stress drop (d). This delay is longer for a longer time since the transition to supershear. This typical observation enables to clearly identify supershear ruptures thanks to strain gauges, and to have an idea of when and where the transition occurred.

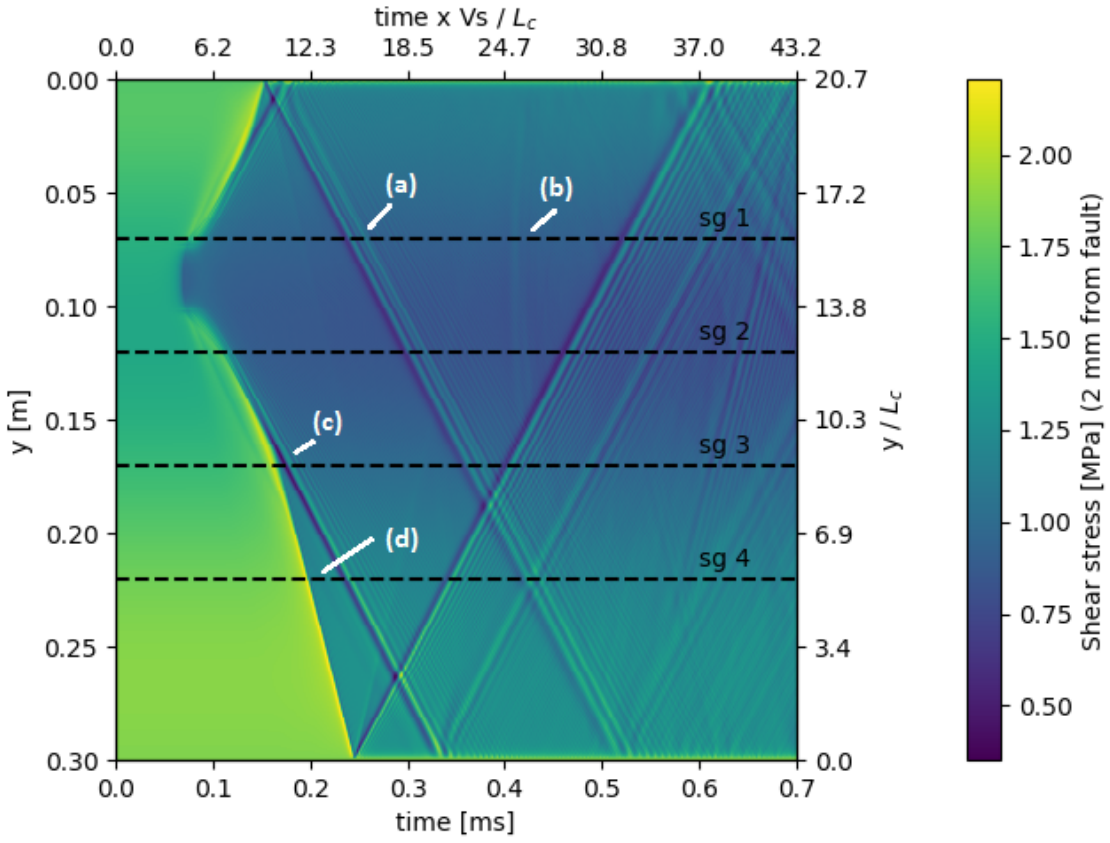

FIGURE 4.16: Time evolution of the shear stress profile 2 mm from the fault during a supershear rupture, and adimensional axes. Reflected waves are clearly visible on the figure.

The transition to supershear is controlled by the dimensionless prestress ratio $S = (\tau_0 - \tau_r)/(\tau_p - \tau_r)$ which gives the ratio of stress increase needed at the crack tips to stress released inside the crack. The lower S, the more likely

to have a supershear transition. Supershear velocities are bounded by the so-called Eshelby velocity equal to $\sqrt{2}V_S$, and the P-wave velocity V_P, which can be verify in the finite-difference models. The other nondimensional length used for normalizing the axes of fig. 4.16 is the critical nucleation length L_c. The way I set up the models, this corresponds to the initial half-crack length. In the case where the initial stress drop inside the slipping patch equals $\tau_p - \tau_r$, L_c would correspond to $L_{Andrews}$ discussed in chapter 3. We recall that $L_{Andrews} = 2G^* D_c/\pi \times (\tau_p - \tau_f)/(\tau_0 - \tau_f)^2$ where $G^* = G/(1-\nu)$ (Andrews, 1976), and in which the prestress ratio S also appears.

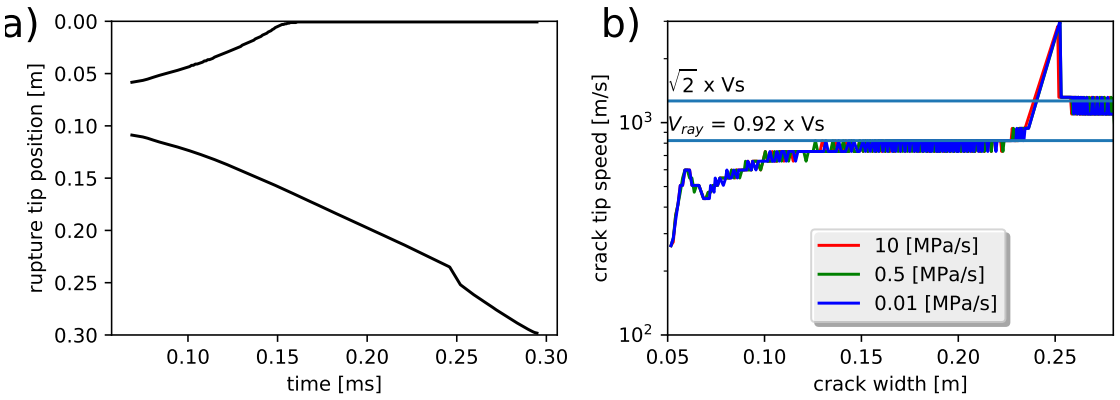

FIGURE 4.17: a) Track of rupture tips during a numerical simulation of dynamic rupture. I call crack the slipping zone delimited by the tips position potted as solid lines. The rupture transitions to supershear after 0.25 ms. b) Speed of the crack tip propagating downwards, versus crack width. The velocity peak around 0.25 ms is an artefact, as the rupture tip "jumps" ahead in a discontinuous fashion.

In the numerical models, the loading rate $\dot{\tau}$ controls the time needed to start the dynamic rupture, for given values of τ_p, τ_0 and τ_r, and D_c affects how fast the rupture accelerates. In model 3 (see table 4.1), I check that the loading rate $\dot{\tau}$ applied does not affect significantly the simulations once the rupture accelerates (fig. 4.17). Indeed, although the shrinking of L_c with $\dot{\tau}$ has been experimentally observed in chapter 3, and explained with rate-and-state laws, it is theoretically shown that loading conditions should not affect L_c when using a linear slip-weakening friction law (Uenishi and Rice, 2003). For loading rate values around several GPa/s however, regardless of the friction law used, a non-negligible shear stress amount added between each time step could bring a large portion of the

fault over τ_p therefore affecting the dynamic rupture. The value of $\dot{\tau}$ does not change the simulation results for the loading rates range considered, between 0.01 and 10 MPa/s (fig. 4.17.b). It would be different using rate-and-state friction laws, as shown in Kaneko et al., 2016, where in this case $\dot{\tau}$ would affect L_c.

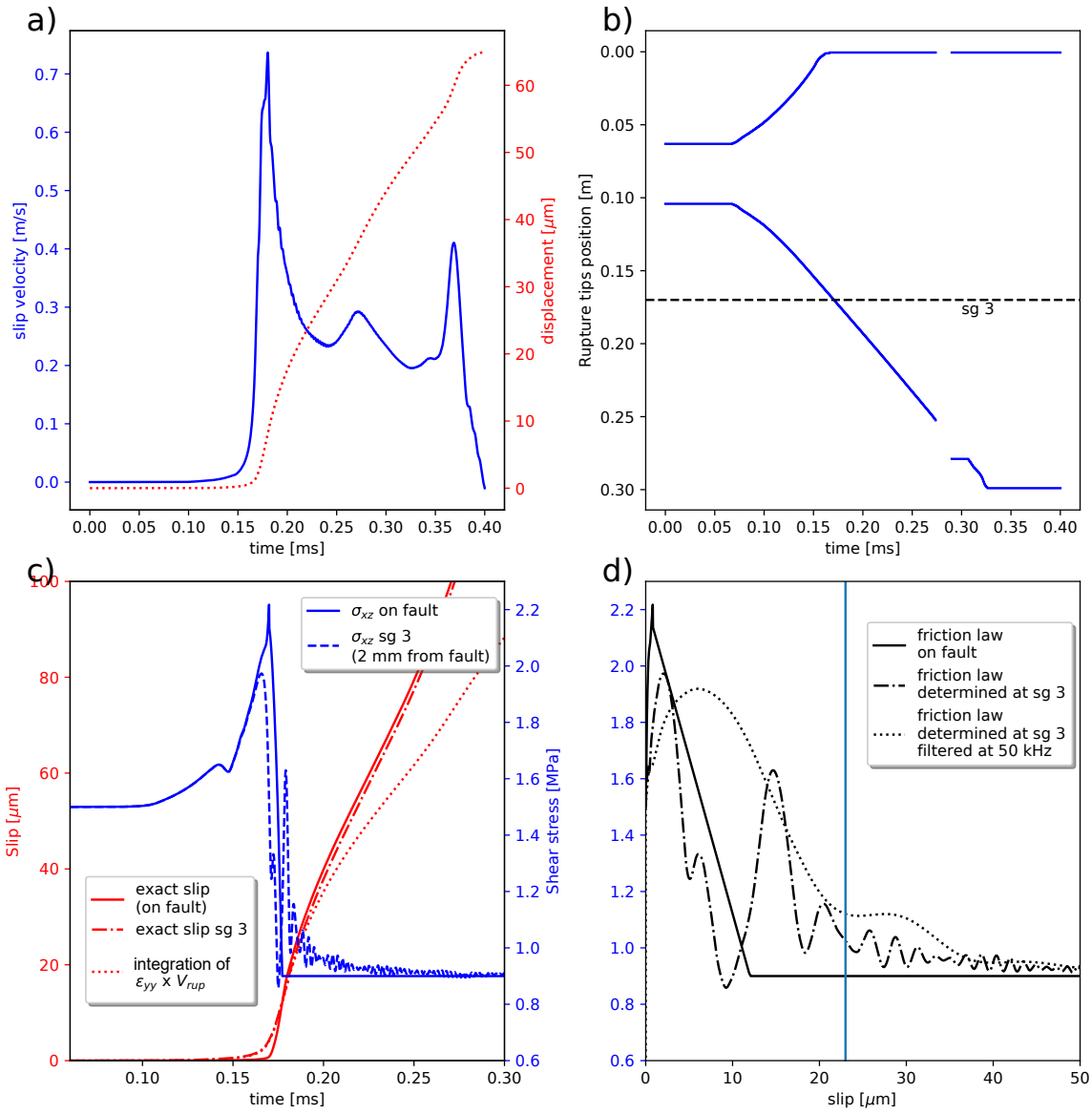

FIGURE 4.18: a) $\epsilon_{yy} \times V_{rup}$, 2 mm away from the fault, recorded at sg 3 during a rupture propagating at constant speed. The displacement is calculated by integrating $2 \times \epsilon_{yy} \times V_{rup}$. b) Track of rupture position versus time. The discontinuity corresponds to a supershear transition. c) Comparison of shear stress and slip measured exactly on the fault, or 2 mm away. The slip 2 mm from the fault can be calculated by integrating the velocity in the model, or by integrating $2 \times \epsilon_{yy} \times V_{rup}$. d) Comparison between the exact friction law on the fault, the one derived by measuring ϵ_{yy} 2 mm away, and the one using the same one, using a shear stress filtered with a 50 kHz low-pass.

An important point of this section however is to validate and discuss the method used in section 2.2.2 to determine the friction law governing the stress evolution during a shear rupture. I use the model 1 for which the simulation parameters are given in table 4.1.

It can be shown mathematically that when a rupture front propagates at a constant speed V_{rup} (see fig. 4.18.b), taking the crack tip position as the reference position and assuming a steady-state strain field, one can obtain the strain variations in space from the strain variation in time. As detailed in section 2.2.1 of chapter 2, the fault parallel strain ϵ_{yy} can be used to calculate the local particle velocity u_y (fault parallel component), using $u_y = \epsilon_{yy} \times V_{rup}$. The slip velocity $V(y,t) = \partial u_x/\partial t$ is therefore equal to $2 \times \epsilon_{yy} \times V_{rup}$, and the local relative displacement on the fault is $U(y,t) = \int 2 \times \epsilon_{yy} \times V_{rup}$ dt (fig. 4.18.a).

If this method works theoretically, further complexity is expected in practice, particularly because of the difficulty to measure shear stress σ_{xy} and fault parallel strain ϵ_{yy} exactly on the fault.

When comparing the signals exactly on the fault, and 2 mm away from it (fig. 4.18.c), it can be seen that when using ϵ_{yy} away from the fault, $U(y,t)$ is overestimated at the beginning (fig. 4.18.c, red dotted curve). This leads to an apparent slip-hardening phase which is not necessarily realistic (fig. 4.18.d, dashed line, between 0 to 8 μm of slip). Moreover, it can be problematic if we want to recover the friction law, because of the shear stress drop near the rupture tip when measured at a finite distance from the fault plane (see figs 4.15-(c) and 4.18.d). This issue has been bypassed by using a lowpass filter in chapter 3, and the filtering effect is shown in fig. 4.18.d. What can be seen is that the critical slip weakening distance D_c previously estimated in chapter 3 from the filtered friction law around 12 to 14 μm is likely overestimated by a factor 2 (fig. 4.18.d). Interestingly, if using a corrected value for D_c around 6 to 7 μm, the nucleation length estimate $L_{Andrews}$ would be around 1.5 cm for the results of chapter 3. This would be much closer to the upper bound of the experimentally measured nucleation lengths, and to L_∞, compared to the 3 cm previously estimated.

Finally, I look at the slip velocity dependence of friction, by comparing the experiments and the model at sg 3, using the parameters of model 2 in table 4.1

(see also fig. 4.15 from the same simulation). It shows that the real slip increase on the fault comes later, and that the peak velocity is higher (fig. 4.19.a). Therefore, using experimental data, the method would tend to give an underestimated peak velocity (fig. 4.19.a). However, in spite of noisy strain gauge signals, this shows that 2 mm away from the fault, the experimental and modelled data give a similar friction versus slip velocity $V(y,t)$ relation. The slope $\partial\sigma_{xy}(t)/\partial V(y,t)$ is also well estimated (fig. 4.19.b).

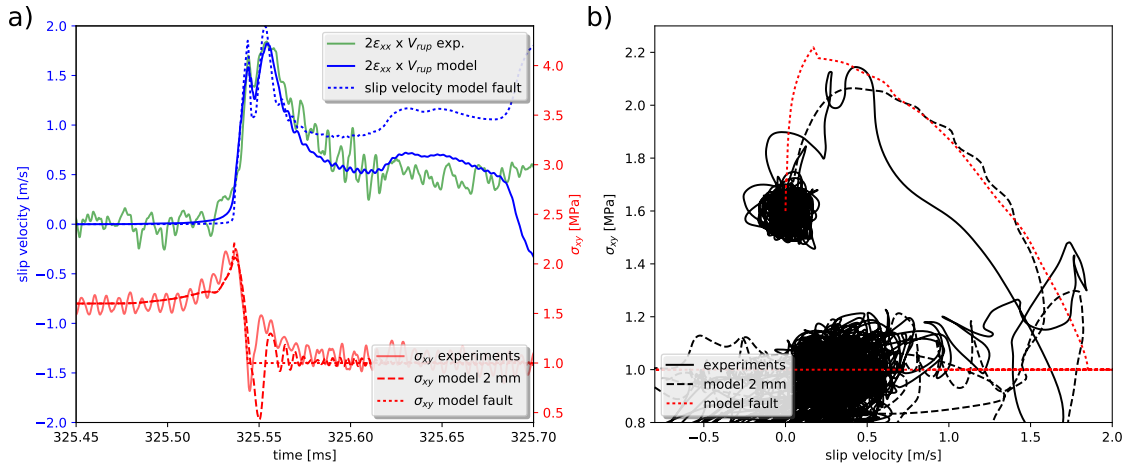

FIGURE 4.19: a) $2 \times \epsilon_{yy} \times V_{rup}$ estimated in the experiments with strain gauges, or in the numerical model, and exact slip velocities on the fault and 2 mm away from it. Shear stresses from the experiments, on the fault in the model and 2 mm away from it are compared. b) This gives 3 different relations for the velocity dependence of friction: the exact one on the fault in the model, the one determined experimentally, and the one calculated in a similar manner using the numerical model values of ϵ_{yy} and σ_{xy}

Chapter 5

Dynamic friction of rocks at crustal pressure conditions

This chapter aims at verifying the influence of loading rate and healing time on the laboratory faults' stability under crustal pressure conditions, using Westerly granite samples. It also provides a deeper understanding on the loading setup used by C. Harbord in his PhD thesis (Harbord, 2018) who investigated the stability of different types of rocks, and for different confining pressure and roughness conditions. The setup previously designed and used in Harbord, 2018 has been adapted it in order to enable placing up to 6 strain gauges along a 4 cm long simulated fault, by transmitting signals via anodized wires in sealed epoxy filled feed-through. This chapter is written in the form of an article as, even though the results are preliminary, some of its content is publishable or can be used as supporting information for a publication concerning similar experiments.

Keypoints :

- A setup has been adapted in order to enable placing up to 6 rosette strain gauges along a 4 cm long simulated fault, during a dynamic rupture between granite slabs, under crustal pressure conditions.
- Healing time and loading rate are both influencing the stability of laboratory faults under 50 MPa of confining pressure.
- The apparent friction coefficient, when compared similar rate-and-state experiment, can be lower than typical Byerlee values of 0.6 to 0.8, and depends on the contact interface roughness and on the loading conditions.

5.1 Abstract

Laboratory experiments of rock friction are an essential tool used to better understand the seismic cycle. A large number of published experiments on the frictional behaviour of laboratory faults were traditionally conducted under relatively low normal stress, and only an average friction coefficient was measured (using the axial load and confining pressure values), although friction is expected to be heterogeneous along the contact interface. By positioning various sensors along the interface (displacement sensors, strain gauges or accelerometers for instance), it is possible to understand in much more detail the processes at the origin of earthquakes in comparison with experiments where only the apparent friction is measured from the forces applied at the model's edges. When performing experiments under high confining pressures, more representative of the seismogenic conditions in the Earth's crust, instrumenting the samples becomes challenging. Here we present a setup designed to allow the positioning of several strain gauges on granite samples, and inside a pressure vessel. The experiments are performed under confining pressures up to 100 MPa, and show that the loading rate and healing time have an effect on fault stability, in accordance with previous studies. This effect is interpreted in light of previous work using rate-and-state friction. We also measure stress variations which are only recorded locally by the strain gauges during slow events, probably caused by inhomogeneous small scale slip at the interface. Finally, we obtain low apparent friction values which might be explained partly by complex loading conditions creating a heterogeneous normal stress along the contact interface, but also very likely by the roughness of the precut surfaces, in agreement with collateral experiments (personal communication from T. Tesei).

5.2 Introduction

An important challenge in seismic hazard assessment is to understand what controls the stability of natural faults. Rate-and-state laws (where rock strength depends logarithmically on the healing time and strain rate) offer a popular framework to interpret laboratory and natural observations (Scholz, 1998). From such laws, the critical nucleation length L_c of a slipping patch at which a rupture accelerates can be derived (Ruina, 1983). Several laboratory studies have investigated the stability of rocks under relatively low confining pressure (Mclaskey and Yamashita, 2017; Xu et al., 2017; Marone, 1998b; Kato et al., 1992). They showed that when the estimated L_c is larger than the sample length l, the simulated fault is stable, and it becomes unstable at higher loading rates and healing times, in which case $L_c < l$. These studies are supported by theoretical (Rubin and Ampuero, 2005; Fang et al., 2010) and numerical work (Kaneko et al., 2016; Kato and Hirasawa, 1996). In chapter 3 (Guerin-Marthe et al., 2018) we also showed evidence of the shrinking of the critical nucleation length L_c with loading rate, by measuring it directly in photoelastic experiments using polycarbonate plates. Similar measurements of L_c can be made with a dense array of strain gauges positioned along the interface between rock slabs (Xu et al., 2017). Local stress measurements are also important in order to understand the sample's non-trivial loading conditions (Guerin-Marthe et al., 2018). Although it is relatively easy to make these measurements at low confining pressures, instrumenting the samples becomes challenging at high confining pressures, inside a vessel. In this preliminary study, I successfully test a way to obtain such dense measurements by transmitting strain gauge signals via anodized wires inside a pressure vessel. I also demonstrate the loading rate and healing time influence on fault stability, even under crustal pressure conditions under which complex weakening mechanisms are likely to take place (Rice, 2006). To the author's knowledge this has not been done yet at such pressure conditions. Moreover, most of the experiments investigating rate-and-state parameters are usually conducted by imposing velocity steps where the fault is always sliding (Dieterich, 1979; Marone, 1998a). This is

partly because the current rate-and-state mathematical formulation does not allow for realistic friction values at zero sliding velocities, which is not consistent with the fact that natural faults can be completely locked before breaking into an earthquake following a sudden increase of tectonic loading. In this study, slide-hold-slide types of experiments are run in order to be consistent with chapter 3, and with natural faults' loading conditions.

5.3 Material and methods

The setup consists of two granite slabs 40 x 4 x 20 mm each, held in sliding contact across a 40 x 20 cm interface (fig. 5.1.a). Surfaces are polished with a 400 grit diamond powder (particle sizes: 18.3 microns), and then a 800 grit sandpaper (particle sizes: 7.8 microns). They are fixed on reinforced stainless steel holders which load the samples in a quasi-direct shear configuration. Two strain gauges (fig. 5.1.a-(2)) were also placed along the 4 x 40 cm face of one sample. Anodized cables (fig. 5.1.a-(3)) are then soldered on the fault parallel and diagonal components (45° from the fault). The voids are filled with silicon spacers (fig. 5.1.a-(1)), and everything is wrapped in Teflon sheets and slid into a Nalgene™ plastic jacket (fig. 5.1.b). A hole is pierced in the jacket in order for the anodized wires to be passed through it. The hole is later sealed with soft Loctite® Hysol 9455 flexible epoxy (fig. 5.1.b-(6)) and the wires are connected on soldering pads fixed on the jacket (fig. 5.1.b-(7)). The jacket is then inserted in a metallic sample assembly (fig. 5.1.c), and both ends are sealed with o-rings when pressure is applied. The left part of the sample assembly (as shown in fig. 5.1.c) goes inside the vessel. The fault's normal stress is controlled by the confining pressure, and the shear stress is applied by pushing the left part of the sample assembly rightward on fig. 5.1.c, while the cap on the right is fixed on top of the vessel. Others anodized cables coming from outside the vessel (fig. 5.1.c-(9)) are fed through a hollow conduit (fig. 5.1.c-(8)) and connected to the soldering pads (fig. 5.1.b-(7)). The feed-through are filled with high shear resistance Permabound® ET5428 two-part epoxy (fig. 5.1.d-(10)) in order to resist confining pressures up to 250 MPa (tested up to 150 MPa for 30 minutes).

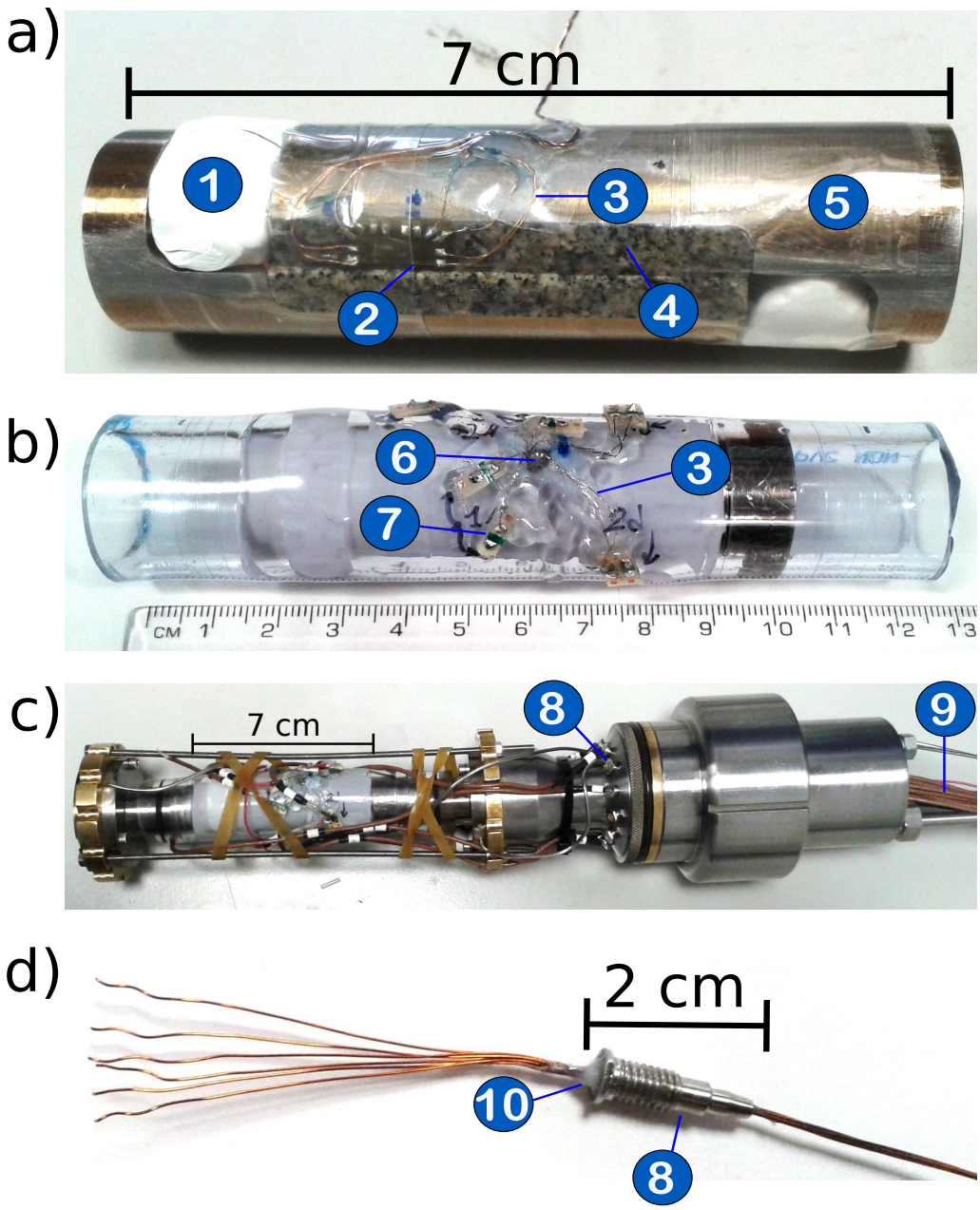

FIGURE 5.1: Sample preparation for the triaxial apparatus. a) Slabs of granite (4) instrumented with strain gauges (2) and fixed on reinforced stainless steel holders (5). The voids are filled with silicon spacers (1), and the gauges are connected via anodized wires (3) soldered manually onto them. b) Slabs and holders wrapped into a Nalgene^{TM} tubing. The anodized wires (3) are passed outside the jacket via a hole later filled with soft epoxy (6), and are connected on soldering pads (7). c) Everything is inserted in the sample assembly. Feed-through (8) connect the wires from inside the pressure vessel to the outside (9). d) Detail of the hollow feed-through where anodized wires transmit the signal, while the sealing is obtained by filling the hole with hard epoxy.

Note that in the experiments presented in this study, only one strain gauge centred 13 mm away from the sample edge and 1.5 mm from the fault ended up

working. Indeed soldering manually wires on the tiny soldering pads is technically very challenging, and connections often fail. We may also lose the signals in the case where the anodization is scratched and wires touch the sample assembly frame.

In the following experiments, the variable loading rate is applied by controlling the tension applied to an axial displacement LVDT actuator, moving the loading column upwards (see sketch and pictures of the machine in chapter 2). A raw displacement d_{raw} is calculated given the number of rotations of the actuator, but in order to compute the actual shortening of the prepared sample (fig. 5.1.a), it is necessary to correct for the machine stiffness $k_{machine}$ = 180 kN/mm given a measured axial force F using $d_{corr} = d_{raw} - F/k_{machine}$. An average shear stress $\overline{\tau_{xy}}$ on the fault (width w and length l) can be calculated using:

$$\overline{\tau_{xy}} = \frac{F}{w \times (l - d_{corr})} \tag{5.1}$$

And we assume $\sigma_n = P_{conf}$

5.4 Results

5.4.1 Overview of experiments

Two experiments are presented here: E1 and E2. E1 is designed to verify the loading rate dependence of nucleation length by looking at the stability of laboratory faults under a confining pressure of 50 MPa, sheared by displacing a loading column at different rates (see fig. 5.3). E2 (see fig. 5.4) is more focused on the role of healing time in laboratory fault's stability. We also look at the evolution of rock strength for different loading rates and healing times, and compare the stresses measured by the loading column's load cell to the local strain gauge measurements (figs. 5.8 and 5.9). There are a total of 20 recorded events, of which some are 'silent', meaning they produce a modest stress drop, and no audible acoustic emission ((4) and (8)). For E1 and E2, we calculate the friction coefficient using the ratio of shear stress $\overline{\tau_{xy}}$ to confining pressure (equivalent to normal stress). The displacement d_{corr} (average slip on the fault) and the loading rate $\dot{\tau}$ are also

Tension applied [V]	0.5	0.7	0.9	4	8
Displacement rate [μm/s]	0.2	0.6	1.0	5.6	11.0
Loading rate [MPa/s]	0.02	0.044	0.068	0.35	0.73

TABLE 5.1: Equivalence between displacement and loading rates, and voltage applied to the actuator

indicated. $\dot{\tau}$ is measured directly on the linear loading phases of shear stress records (see fig. 5.3.a): we simply divide the variations of shear stress $\Delta\overline{\tau_{xy}}$, by the time interval Δt. During the 'stick' phases, it can be verified that the medium composed of the granite slabs in contact is linearly elastic, by dividing the displacement rate $\dot{d} = \Delta d_{corr}/\Delta t$ (see fig. 5.3.b) by the loading rate $\dot{\tau} = \Delta\overline{\tau_{xy}}/\Delta t$ (fig. 5.2.a), and showing that $\dot{d}/\dot{\tau}$ is constant (fig. 5.2.b). The relations between displacement and loading rates versus applied tension are also quasi linear (fig. 5.2.a). The values of loading rate given later in figs. 5.3.b and 5.4.b are therefore taken from table 5.1, and are known during the experiments as we know the exact voltage applied to the loading column. These values correspond to the slope during the loading period, where the shear stress increases linearly with time.

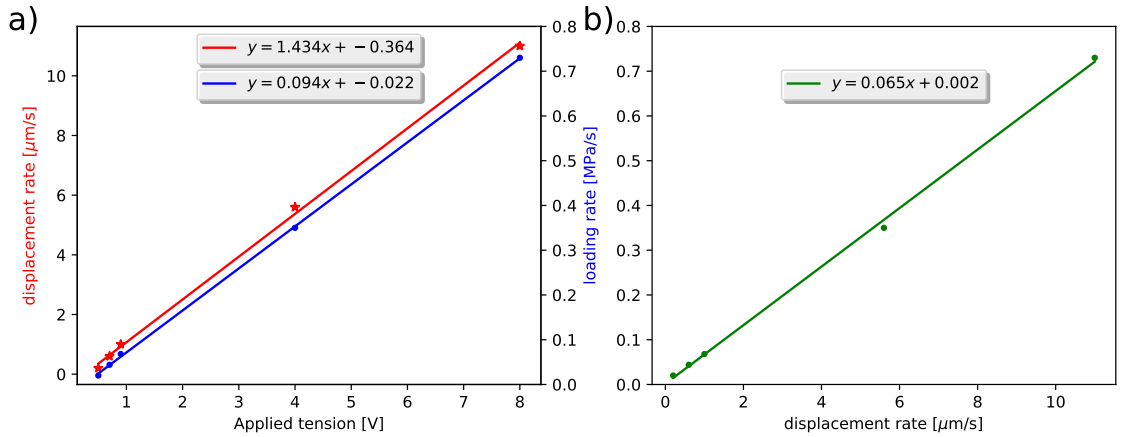

FIGURE 5.2: a) Measured displacement and loading rates versus tension applied on the axial displacement LVDT actuator. b) Relation between experimental measurements of displacement rates and loading rates.

E1: Effect of loading rate

In E1 (fig. 5.3), the confining pressure is maintained constant at 50 MPa, and the sample is sheared at rates ranging from 0.02 to 0.73 MPa/s. The hold time is also kept constant at 5 minutes between two successive loading phases. The main result of this experiment is a transition from stick-slip to slow events at low loading rates, between 0.02 and 0.044 MPa/s here. The apparent friction coefficient ($\overline{\tau_{xy}}/P_{conf}$) tends to increases during the experiment, from $\mu = 0.3$ to $\mu = 0.4$, and we do not observe a link between loading rate and stress drop. The relatively low values of μ (typical values of friction for rocks are around 0.6 to 0.8) can be attributed to the very smooth polishing of the samples' surfaces at 800 grit, or to coulomb stress variations induced by the loading conditions. This will be discussed in more detail in the next chapter.

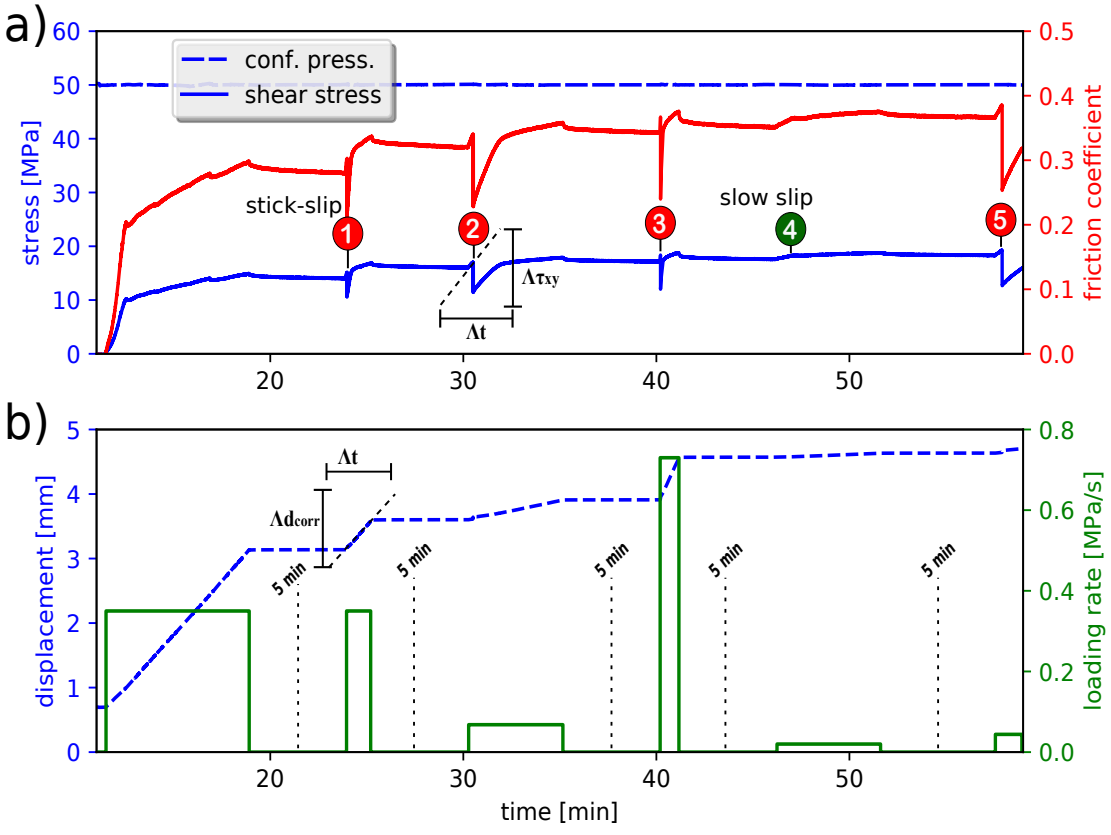

FIGURE 5.3: Experiment 1 (E1): Overview of triaxial experiment using different loading rates. a) Evolution of the friction coefficient calculated using shear stress and confining pressure. Out of the 5 events, (1), (2), (3), (5) are pure stick-slips (red color) while (4) is a slow slip event (no audible acoustic emission; green color). b) Piston displacement versus time, associated loading rate and hold times.

E2: Effect of healing time

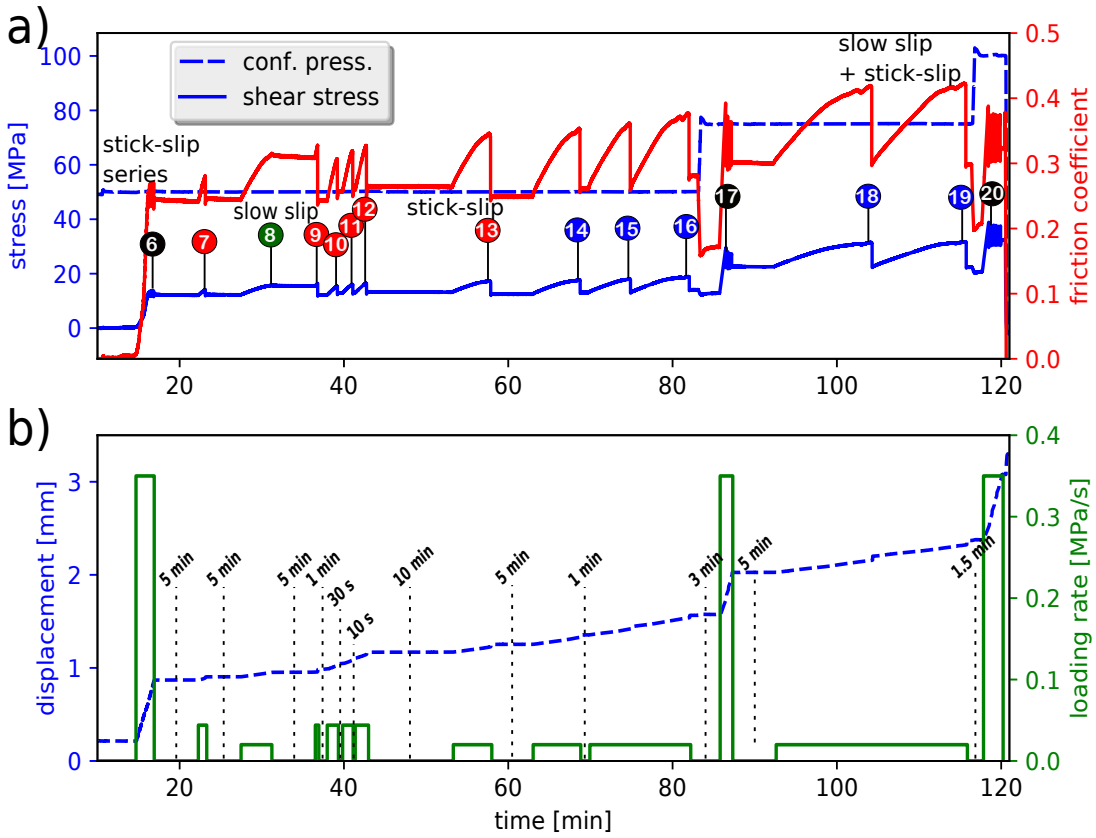

FIGURE 5.4: Experiment 2 (E2): Overview of triaxial experiment using different hold times, loading rates and confining pressure. The events labelled with blue color are qualified as 'slow slip + stick-slip'. See legend of fig. 5.3 for more details.

In the second experiment E2 (fig. 5.4), we also start with a constant confining pressure of 50 MPa. The sample is initially loaded at 0.35 MPa/s, and we then decrease the loading rate until we observe the same transition from stick-slips to slow events between 0.02 and 0.044 MPa/s. From there we look at how the healing time affects the simulated fault's stability, at 0.044 MPa/s first and then 0.02 MPa/s. We always get stick-slips at 0.044 MPa/s with healing times of 5 min., 1 min., 30 s and 10 s, therefore we continue with a lower loading rate of 0.02 MPa/s. We get a clear stick-slip after 10 min. of hold (event 13), while for events 14, 15 and 16, shear stress oscillations probably caused by some slow slip start appearing for the subsequent shorter hold times of 5 min., 1 min., and 0 s (no hold). We qualify those events as 'slow slip + stick-slip' as they start by low

amplitude stress oscillations, but still end up with a large stress drop, generating an audible acoustic noise. Fig. 5.5 presents the different types of events, which can easily be classified by plotting the time derivative of the shear stress variations, or stress rate (red curves). The presence of slow slip is detected when the stress rate increases after having decreased, during a period of constant displacement rate of the loading column (events 8 and 14, figs. 5.5.a and 5.5.b). When the event is silent, and with a low amplitude stress drop following the peak stress, I call it only slow slip (events 8, fig. 5.5.a), while when there is a large stress drop and an audible acoustic noise following the stress rate oscillations, I call it "slow slip + stick-slip" (events 14, fig. 5.5.b). When the stress rate variations are monotonous during the loading phase, and followed by a large stress drop, I call the events stick-slips (events 13, fig. 5.5.c).

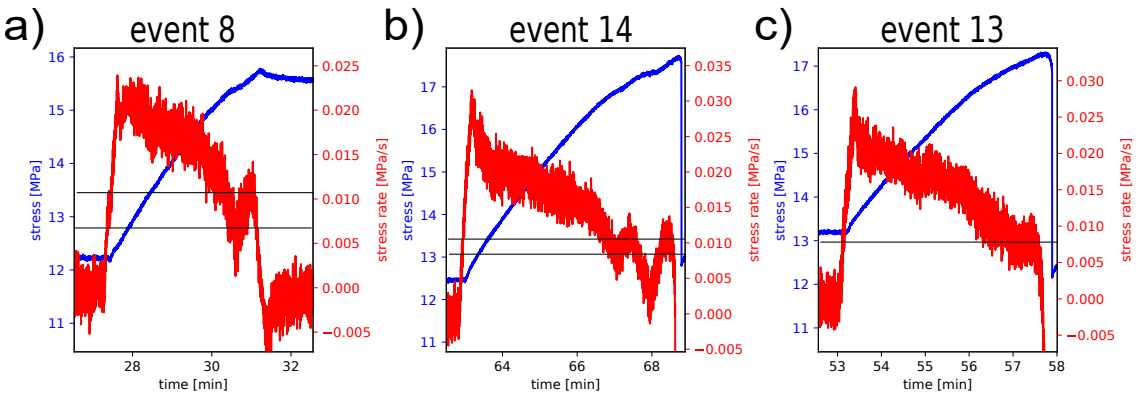

FIGURE 5.5: Different types of events observed in the triaxial shear apparatus. a) Slow slip, b) Slow slip + stick-slip, c) Stick-slip.

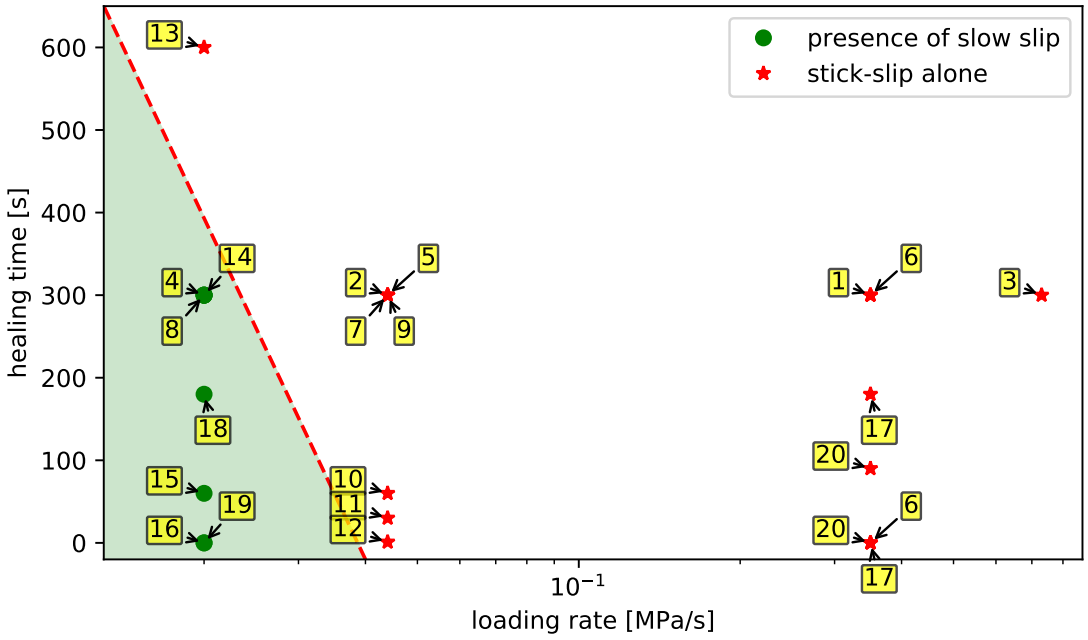

FIGURE 5.6: Effect on healing time and loading rate on the stability of the simulated faults in the triaxial pressure vessel. The yellow labels are the events number. The green area is where some slow slip is observed.

The confining pressure is then increased to 75 MPa (events 17, 18 and 19), we load the sample at 0.35 MPa/s and trigger a series of stick-slips (events 17). Next we hold during 5 min. and apply a loading rate of 0.02 MPa/s for 30 min. during which we records two 'slow slip + stick-slip' events (events 18 and 19), similar to events 14, 15 and 16.

Events 6, 17, and 20 are series of spontaneous stick-slips obtained at $\dot{\tau}$ = 0.35 MPa/s for confining pressures of 50, 75 and 100 MPa, respectively (black color in fig 5.4), which will be discussed along with the strain gauge data in the next section.

We summarize the results of E1 and E2 in fig 5.6 where we observe that slow slip occurs at low loading rates and short healing times (green area in fig 5.6), compared to pure stick-slips.

5.4.2 Strain gauge data

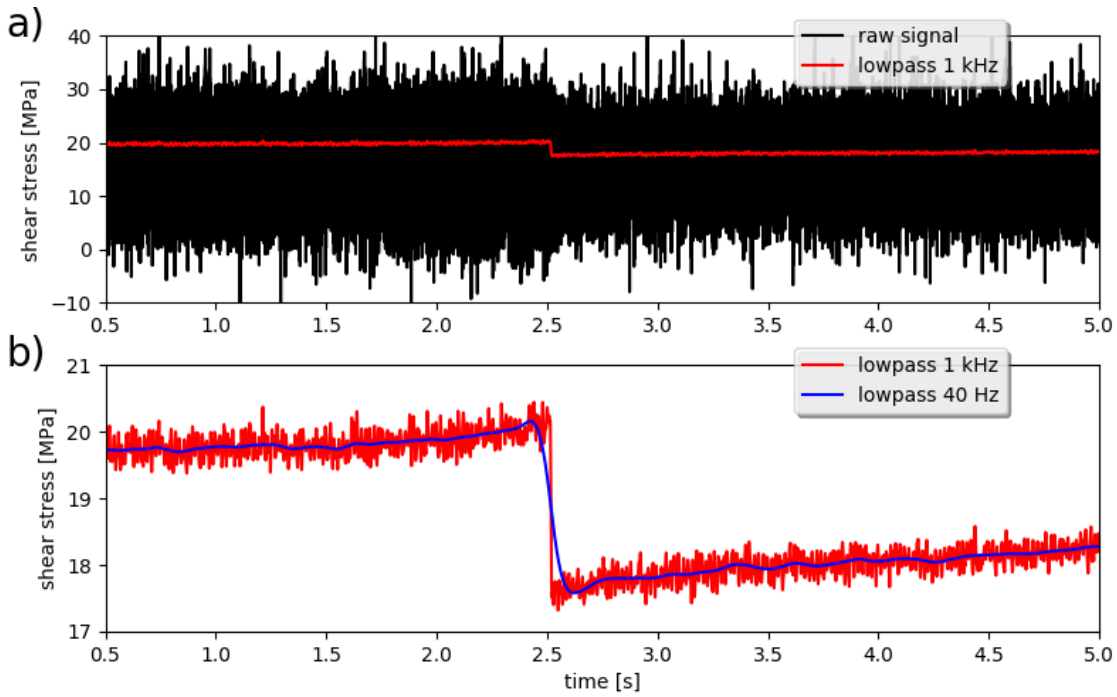

FIGURE 5.7: a) Raw measurement of shear stress for the first event of (17), and signal filter at 1 kHz. b) Signal filtered at 1 kHz with a visible 50 Hz noise, and signal filtered at 40 Hz.

This section presents the strain gauge data obtained locally on the sample for E2, 13 mm away from the edge, and 1.5 mm away from the interface (see figs 5.1.a and 6.1).

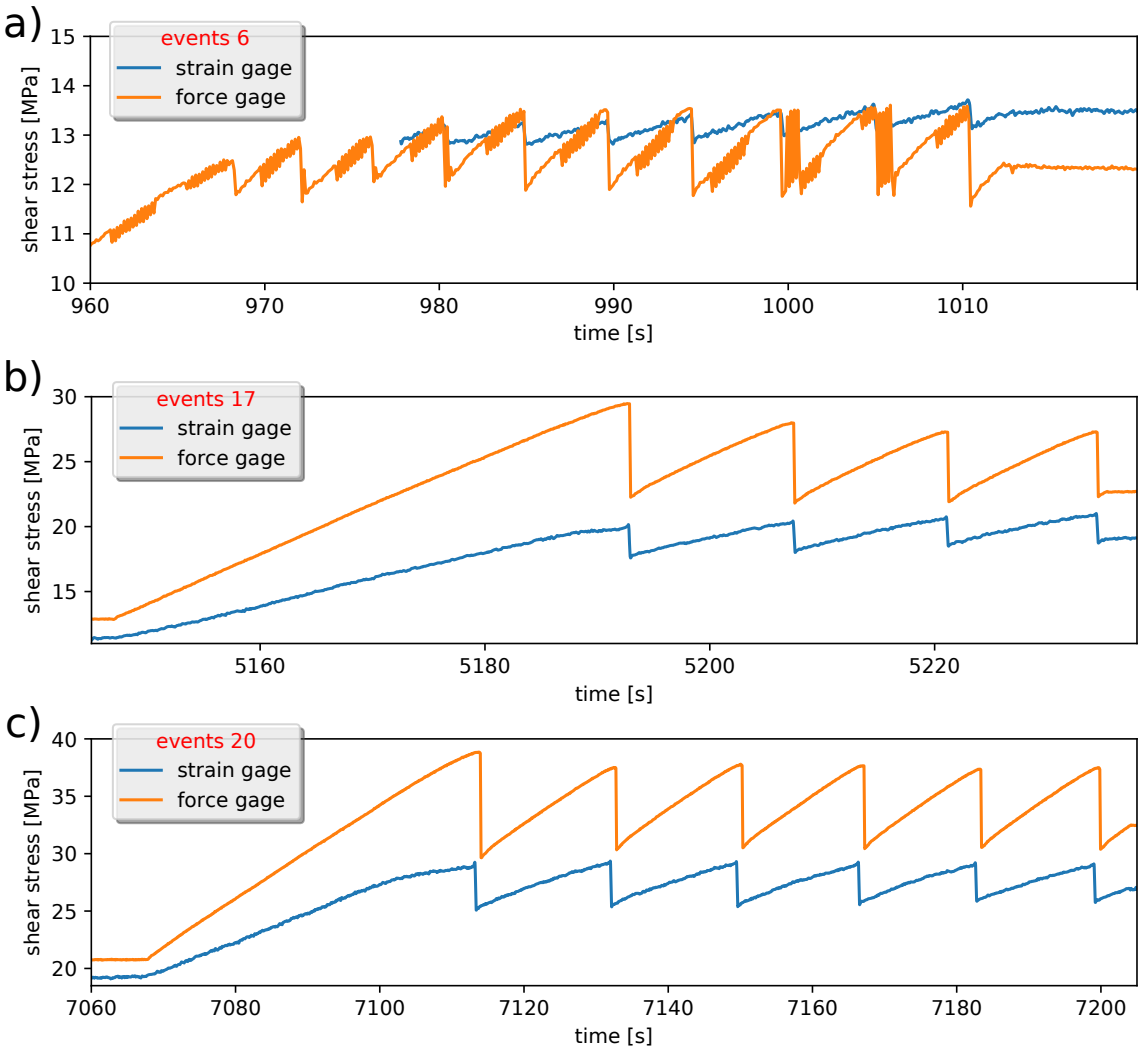

FIGURE 5.8: Series of spontaneous stick-slips recorded by the load cell and strain gauges (filtered at 40 Hz) at confining pressures of 50 MPa (a), 75 MPa (b), 100 MPa (c), for events 6, 17 and 20, respectively.

In the experiments, the noise is very high, probably because of a bad insulation of the anodized connections combined with a high level of electromagnetic noise. Previous tests without anodized wires seemed to result in a better signal-to-noise ratio (Harbord et al., in prep.). In order to detect shear stress variations of less than 1 MPa hidden in noise induced variations of $\pm$ 20 MPa in the raw signal originally sampled at 1 MHz, we apply a lowpass butterworth filter. The effect of the filter is shown in fig. 5.7. The stress drop starts to be clearly visible when using a lowpass at 1 kHz (fig. 5.7.a). However the powerline 50 Hz noise is still visible, and inducing variations up to $\pm$ 0.5 MPa on the shear stress record, which is why we use a 40 Hz lowpass filter in the figures presented below.

Even though the initial aim was to investigate the dynamic friction of granite by looking at the slip-pulse lasting a fraction of a millisecond, the low signal to noise ratio does not enable to record such short features (we also check that no pulse is visible in the data filtered at 50 kHz). Instead it provides a local shear stress variations measurement which can be compared to the apparent shear stress derived from the load cell's axial force record.

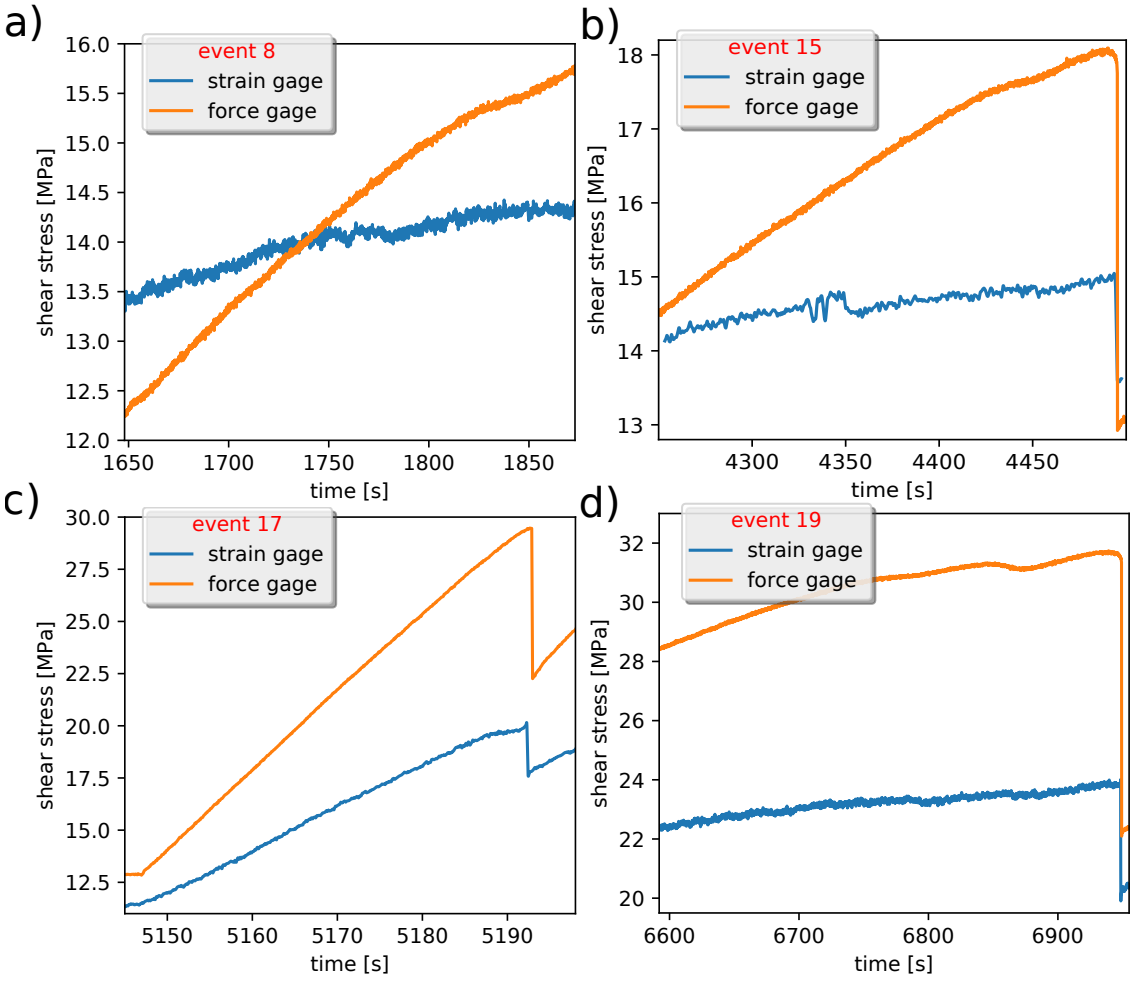

FIGURE 5.9: Zoom on individual events. (a) is a stable, silent event, c) is a stick-slip, (b) and (d) are oscillating and therefore close to the transition toward stable behaviour.

What we observe is that in general the shear stress recorded by the rosette strain gauge is lower than the stress calculated from the force gauge (figs 5.8 b-c, and 5.9.b-c-d), except at the start of the experiment, in the initial loading phase, for events 6 and 8 for instance (figs 5.8 a, and 5.9.a). The local loading rates and stress drops are also lower.

During spontaneous stick-slip series, the magnitude of stress drop increases at first (fig. 5.8.a), but tends to decrease and then stabilize at a later stage, for events 17 (fig. 5.8.b) and 20 (fig. 5.8.c).

Looking at individual events, we see that during silent or transitional events (8, 15 and 19 in figs 5.9.a, 5.9.b and 5.9.d, respectively) the strain gauge picks up local shear stress variations which are not measured by the force gauge, on top of the larger period oscillations. Also, the local shear stress rate sometimes decreases during a yielding phase before increasing again few seconds before the main stress drop, as observed during the first stick-slip of event 17 (5.9.c).

5.5 Discussion

The noise in the signal hides any information concerning the dynamic rupture front propagation, and restricts this study to longer wavelength signals. This should be improved in the future by insulating better the wires. We should also be able to put a large number of strain gauges along the interface, providing that several of the feed-through are made and in working order.

At the moment we still observe interesting features such as a decrease of shear stress rate for event 17 in fig 5.9.c, followed by a rate increase before the stress drop (we can also see it in some other events of figs 5.8.b and 5.8.c). This suggests that some pre-slip measured by the strain gauge only takes place locally, and is too small to be measured by the axial load cell. Then, some accelerating slip might localize further away from the strain gauge in a patch corresponding to the nucleation area, concentrating stress at its edges. As the slipping patch expands, if the strain gauge it located initially outside of it, it will sense an increase of shear stress as the rupture front approaches, followed by a sharp stress drop when the gauge suddenly becomes located inside the dynamically slipping patch.

In a stick-slip event close to instability (events 15 fig 5.9.b) and during the 'slow slip + stick-slip' event 19 (5.9.d) we also observe small local stress drops which are not sensed by the axial load cell. This may be indicative of small dynamic slip patches, occurring on areas representing only a fraction of the 8 cm^2

total sample's surface. A large population of them could create a global progressive weakening of the surface, while creating small local stress drops. Such local events clusters in space and time could also explain the oscillations recorded by the axial load cell, and discussed in Baumberger et al., 1999 in terms of rate-and-state parameters. These preliminary results indicate that the slip distribution is highly inhomogeneous during the pre-slip phase. Understanding the slip distribution of heterogeneity during ruptures is a challenging and possible path for future research.

Finally, looking at the slide-hold-slide experiment E1 run at a confining pressure of 50 MPa, where the hold time is constant (5 minutes) and the sample is loaded with different stressing rates (fig. 5.3), we see a clear influence of the loading rate. Indeed, a transition between stick-slip behaviour and slow slip is observed between 0.044 MPa/s and 0.02 MPa/s. The same transition is observed in E2 (fig. 5.4). Moreover, E2 evidences that larger hold times also favour instability in accordance with previous studies run at lower normal stresses(Marone, 1998b; Mclaskey and Yamashita, 2017). This effect is visible at a loading rate of 0.02 MPa/s, when comparing event 13, a stick-slip triggered after hold time of 10 min, and the 'slow slip + stick-slip' event 16, run at the same loading rate, without hold period.

The latter observations can be explained in term of critical nucleation length L_c derived from rate-and-state laws, as discussed in chapter 3. The explanation can also be visualized using the model results of Fang et al., 2010, using a diagram of shear stress evolution versus slip rate during a typical stick-slip cycle, simulated with rate-and-state laws (Mclaskey and Yamashita, 2017). Fig. 5.10, reproduced and modified after Mclaskey and Yamashita, 2017, shows the path taken by shear stresses and slip rates, for different healing times and loading rates. Typically (path (a)), the shear stress increases during the loading phase, in the interseismic period with low slip rates, reaches the static friction threshold and starts to decrease with increasing slip-rate slowly at first (nucleation) and faster during the coseismic phase. The shear stress stays steady during the following hold phase. In the diagram, the system becomes unstable when brought well above steady-state. Stable events would be plotted as a point along the steady-state line, or low

amplitude oscillations around it with low slip rate values.

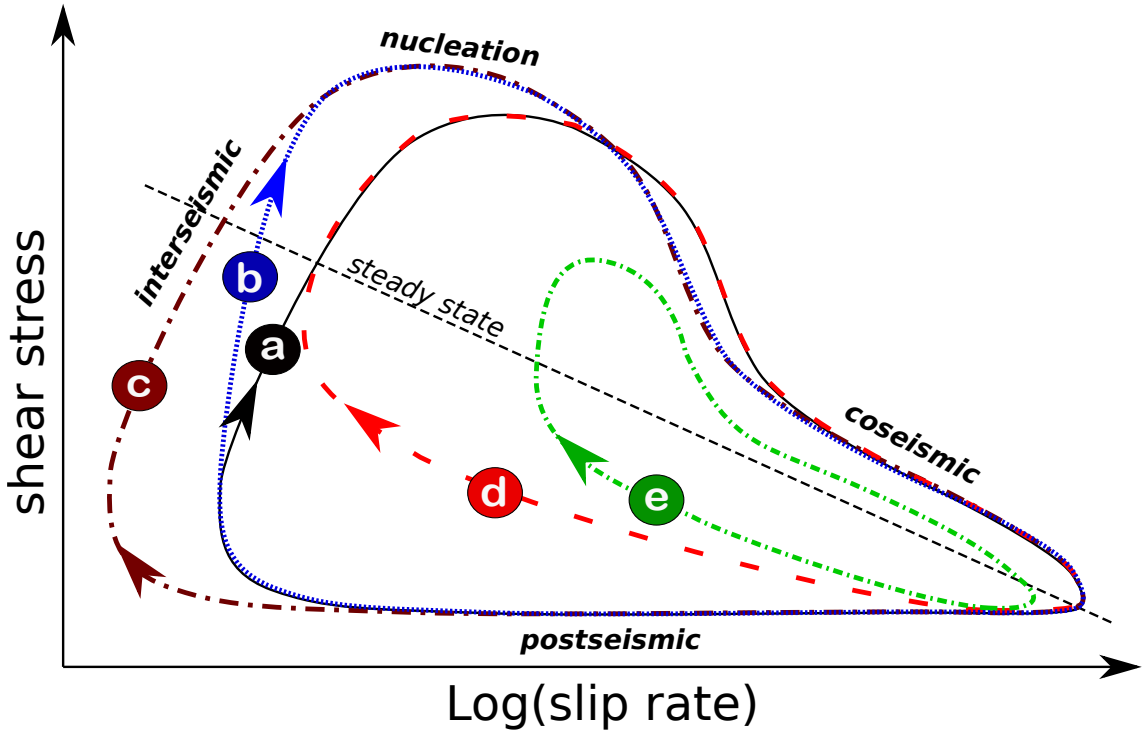

FIGURE 5.10: Paths taken by frictional interfaces during stick-slip cycles in a shear stress versus log(slip rate) diagram, reproduced after Mclaskey and Yamashita, 2017. (a) Reference path. (b) With increased loading rate. (c) With increased hold time. (d) Without hold. (e) Without hold, at higher loading rate

When the interface is loaded faster (path (b)) after a significant hold time, the shear stress increases faster for a given slip rate, and the peak stress is also higher due to the strain rate dependence of stress (Kato et al., 1992; Marone, 1998b). This brings the system further from steady-state which becomes therefore more unstable ($\Omega \gg 1$), resulting in a smaller L_c, as discussed in chapter 3 for the biaxial experiments. A similar effect can be obtained if instead of increasing the loading rate we increase the healing time (path (c)).

In the case where we observe series of spontaneous stick-slips conducted under constant large loading rate, the fault's behaviour might be different. From the numerical model of Im et al., 2017, at least the first event generates a large stress drop $\Delta\tau$, as the contacts are relatively strong ($\Omega \gg 1$, see discussion of chapter 3), while for the following ones (for which the contact population has been renewed), the stress drop is smaller, and L_c larger ($\Omega \approx 1$). It seems to be what we also observe in the stick-slip series 17 and 20 (figs. 5.8.b and 5.8.c). The first

event of the series might follow path (b) after a long hold time, while the following might tend toward path (e). The peak stress seems to rather increase during spontaneous stick-slips at low loading rates (events 13, 14, 15 and 16, in E2, fig. 5.4), and the stress drop is more or less constant. It would correspond to path (d) in the diagram of fig. 5.10. Note that things might be more complex at the start of the experiment (event 6, fig. 5.4), when the surface is strengthening and gouge or frictional melt may be produced.

Chapter 6

Numerical models of triaxial experiments

In chapter 4, finite-difference and finite element methods were used in order to model the loading conditions and dynamic rupture propagations observed in the biaxial experiments of chapter 3. In this chapter, I use the same numerical schemes in order to better understand the experimental data from the triaxial experiments of chapter 5.

6.1 Loading conditions

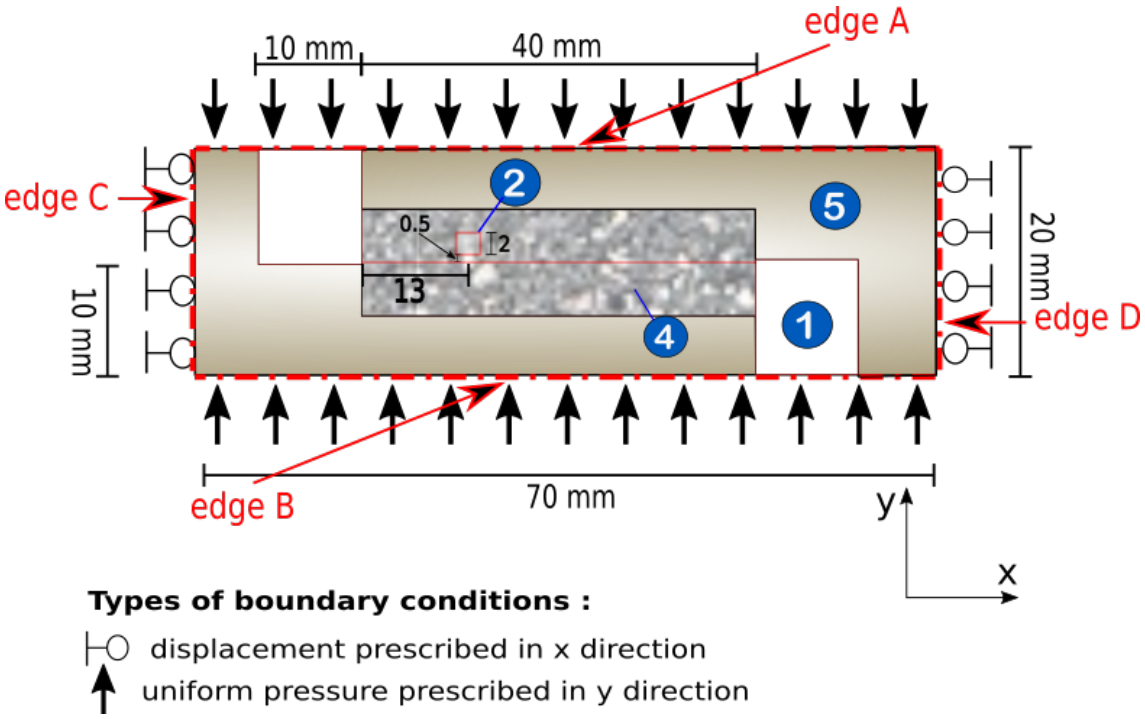

FIGURE 6.1: Boundary conditions and materials of the FEM setup used to model the triaxial loading conditions (see fig. 5.1.a for more details)

In order to better understand the low friction values of 0.3-0.4 and the lower shear stress values recorded locally by the strain gauges compared to the apparent shear stress (obtained by dividing the axial load force values by the sample surface), I run FEM models of the loading conditions for the triaxial experiment. Although it does not explain everything, the static simulation presented here is still useful in order to interpret better the recorded shear stresses from strain gauges and from the axial load measurements in chapter 5.

The cylindrical shape of the sample and the steel holders described in chapter 5 (fig 5.1.a) is approximated by a 2D plane strain model of its central section (fig. 6.1). As we are interested in what happens within the 4 cm long, 2 cm wide, and 8 mm thick granite material, the plane strain assumption is reasonable. Because of the relatively higher stiffness of the stainless steel holders, we assume that the stress distribution in the granite material is the same for any section taken along the 2 cm width of the samples. We also note that even thought 2D models

using the plane-stress assumption are not shown here, they give similar results compared to the plane-strain case.

The model is composed of 3 different elastic materials in order to make it as realistic as possible (the two granite slab are modelled as one single elastic domain): stainless steel (E = 200 GPa, ν = 0.3), soft silicon (E = 0.1 GPa, ν = 0.4), and granite (E = 50 GPa, ν = 0.25). In order to simulate the confining pressure, distributed forces are prescribed on edges A and B, at the dof in y direction, while the dof in x direction are free. It corresponds to a pressure of 50 MPa. And in order to simulate the axial load, displacements in x direction of 0 μm and -60 μm are prescribed on edges C and D respectively, while the dof in y direction are left free. It corresponds to an average axial pressure of approximately 49 MPa (and to an axial force of F = 986 kN). From those values, if using the same calculation as used to estimate the friction in the triaxial experiments, the average shear force along the interface would be equal to F/S = 25 MPa, corresponding to a friction of 0.5.

For this model, I plot the distribution of shear stress τ_{xy} (fig 6.2.a), normal stress σ_{yy} (fig 6.2.b), and fault parallel stress σ_{xx} (fig 6.2.c). I indicate the averaged stress values $\overline{\tau_{xy}}$ and $\overline{\sigma_{yy}}$ inside the strain gauge area ($\overline{\tau_{xy}}$ = 6 MPa and $\overline{\sigma_{yy}}$ = 38 MPa), and along the granite slabs interface ($\overline{\tau_{xy}}$ = 13 MPa and $\overline{\sigma_{yy}}$ = 58 MPa). I also indicate in fig 6.2 the average pressure $\overline{\sigma_{xx}}$ = 49 MPa along edge D, corresponding to the axial force $\vec{F_x}$ measured in the triaxial experiments, if timed by the edge length of 0.02 m.

The shear and normal stress values (τ_{xy} and σ_{yy}) along the line which would correspond to the contact area between the granite slabs (solid red lines in fig 6.2) are plotted in fig 6.3. The ratio τ_{xy}/σ_{yy}, and the coulomb stress $\tau_{coulomb}$ along the same line are also indicated.

The main result from the simulation is that both shear and normal stresses, τ_{xy} and σ_{yy}, are heterogeneous along the interface line with peak values at the edges. The coulomb stress $\tau_{coulomb}$ is also much higher in those areas and closer to 0 (taking a friction coefficient of 0.4, maximum measured in chapter 5), enough to reach the static friction of the samples, meaning that some slip is very likely to take place from one of the edges or both. As the edges would slip, the stress

would redistribute and it is not really clear how in this study (dynamic simulations with the FEM model would be useful). Also in the case where the friction coefficient is higher, in the order of 0.8, the coulomb stress distribution is different, and does not necessarily peak at the edges.

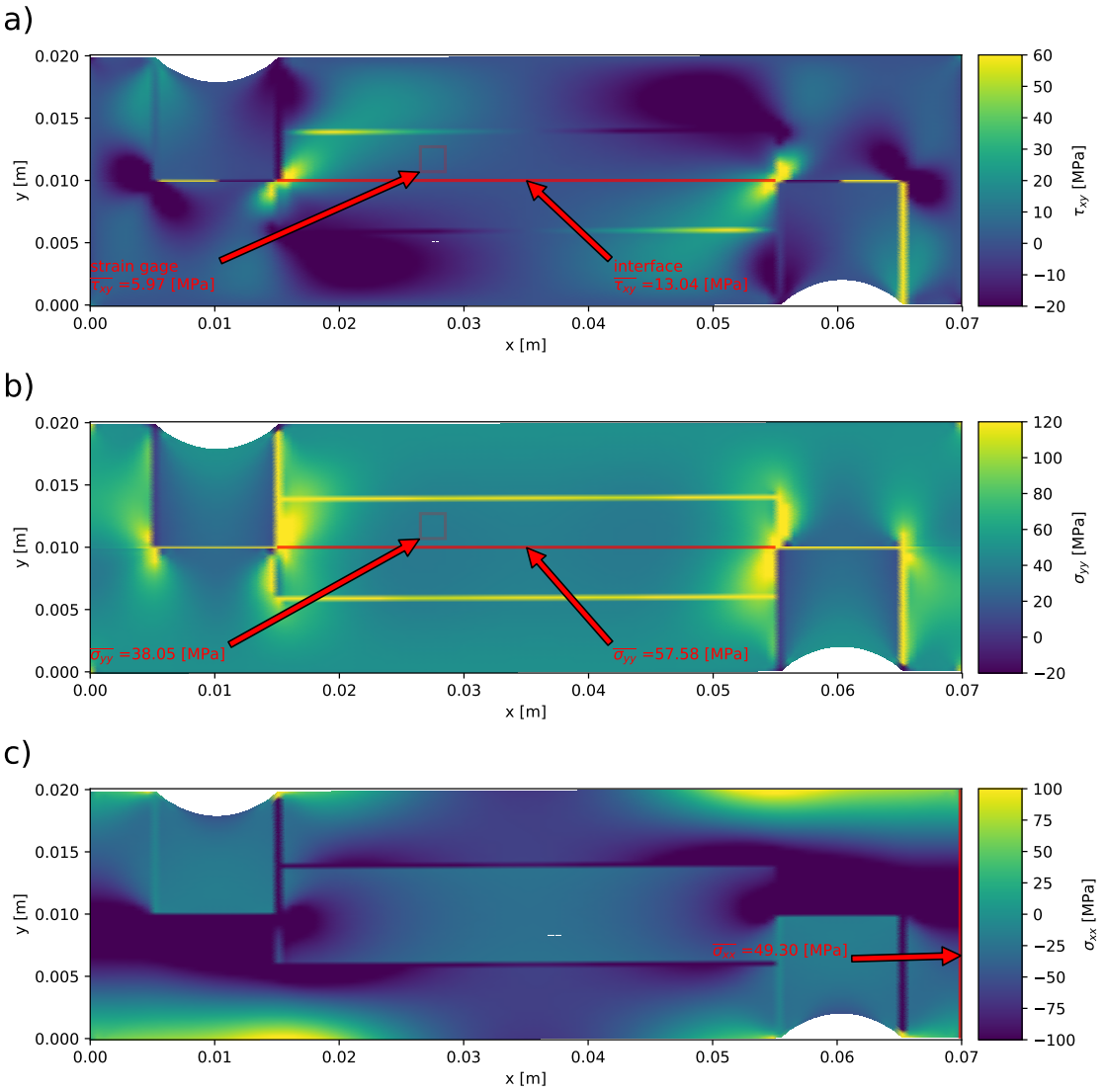

FIGURE 6.2: FEM model of the triaxial experiments loading conditions. a) Shear stress τ_{xy} distribution. b) Normal stress σ_{yy} distribution. c) Fault parallel stress σ_{xx} distribution. In a) and b), the averaged stress values along the line corresponding to the granite slabs contact interface, and the average stresses inside the strain gauge grid area are indicated. In c), the average pressure $\overline{\sigma_{xx}}$ along edge D of the model is shown.

Looking at the absolute stress values in the model, it indicates that although an apparent ratio τ_{xy}/σ_{yy} of 0.5 is measured by dividing shear stress (axial force

divided by sample's contact surface), by the confining pressure, the values recorded by the strain gauge and the actual average stress values along the interface are different, at least for a completely locked interface. Here the ratio τ_{xy}/σ_{yy} at the strain gauge would be equal to 6/38 = 0.16, and would be 13/58= 0.22 on average along the interface. Note that in the triaxial experiments, $\sigma_{yy} = \sigma_n$ is assumed to be constant to simplify the stress measurements with the gauges. It would be important in the future to actually measure the normal stress as it is heterogeneous along the contact interface and not equal everywhere to P_{conf}, making some assumptions wrong.

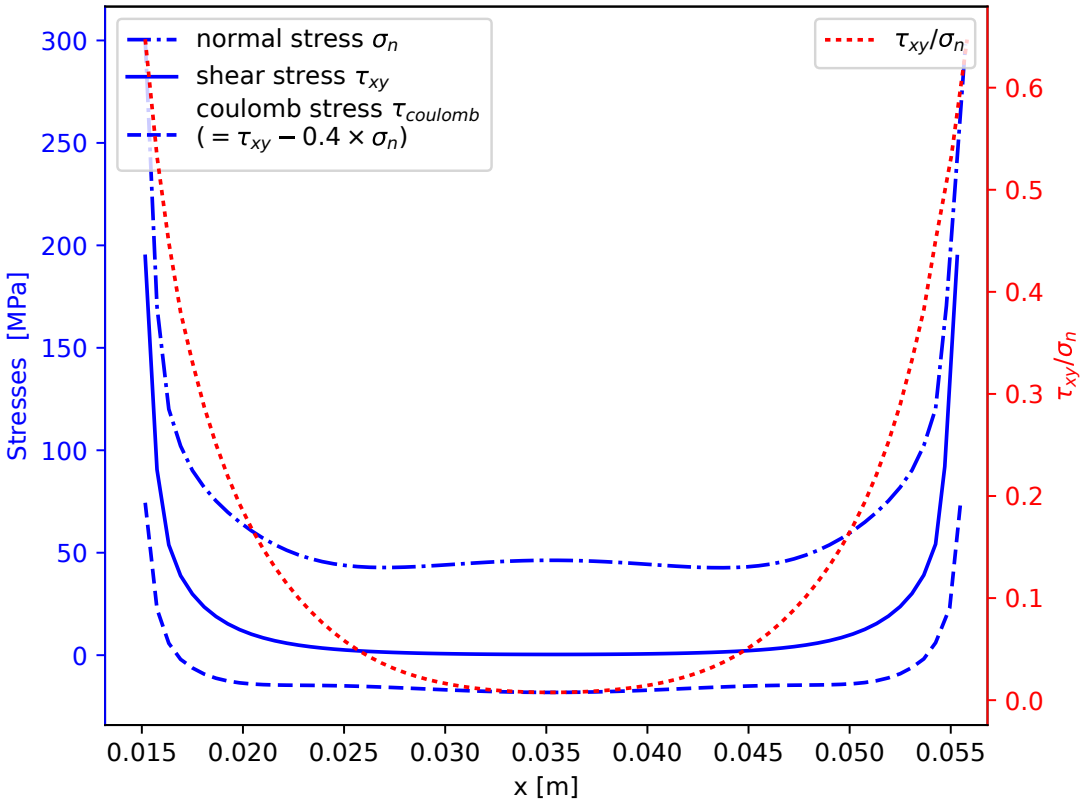

FIGURE 6.3: Stresses along the interface of the FEM model for the triaxial experiments

To come back to the comparison with the experimental results, the FEM model may explain partly why the apparent friction coefficient measured using the axial force can be low, while higher ratios τ_{xy}/σ_{yy} can locally be reached at the interface's edges, enough to start a rupture (however, it does not mean that the rupture

could propagate further, as the energy released at the crack tips might not be sufficient to overcome static friction). At the stage where the interface has not slipped yet, the value of τ_{xy}/σ_{yy} recorded by the strain gauge could be even lower. If the rupture happened so fast that the peak stress would not be recorded in the filtered signal at 24 Hz, that could explain our observations. However, in the case of a silent event where the shear stress is redistributed slowly, the lowpass filter should not hide the peak stress, therefore giving a value more similar to the actual average one along the interface. In order to understand how the stress is redistributed during a rupture, dynamic simulations using the same FEM model would be needed.

In addition to the complexity of loading conditions, it has been shown that the roughness also affects the friction values. Indeed the measured friction during such experiments can decrease from 0.6 at 100 grit, down to 0.3 at 800 grit (personnal communication from Telemaco Tesei). From the results of this chapter and chapter 5, we see that more data need to be analysed, and if possible dynamic FEM models to be run in order to fully understand the laboratory data.

6.2 Dynamic simulations and friction law

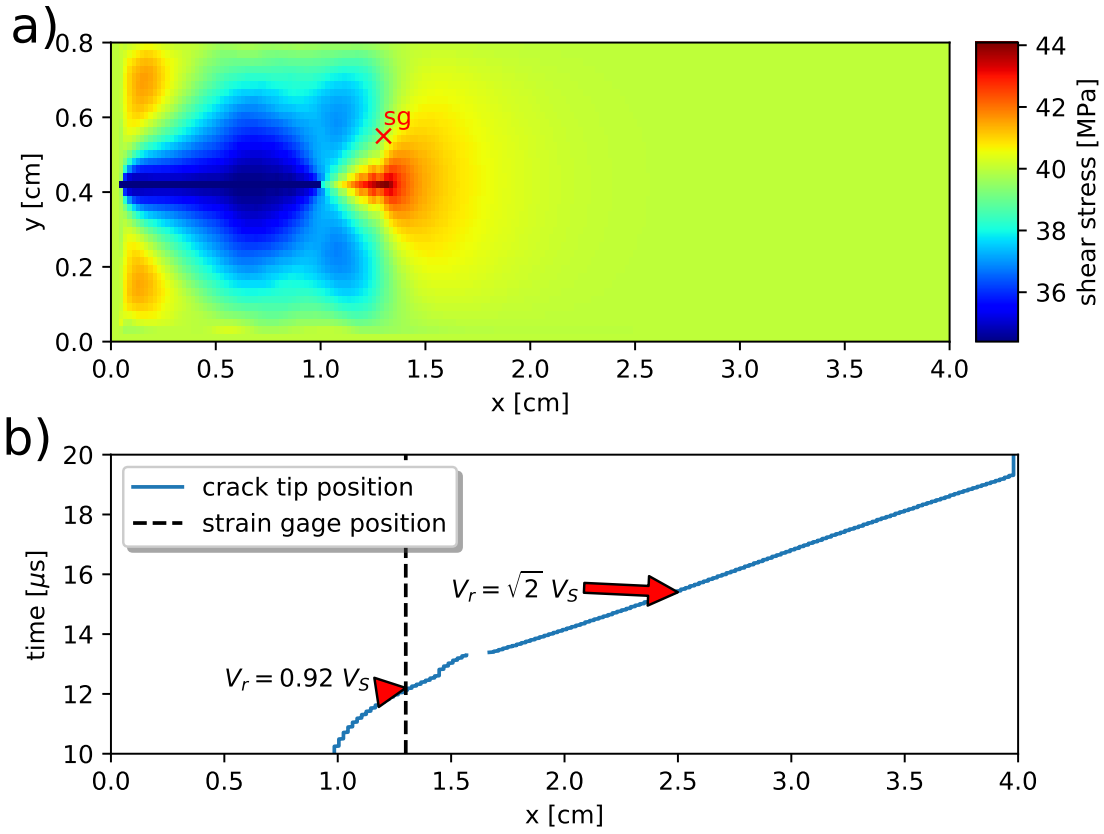

FIGURE 6.4: a) Snapshot of the shear stress field during the passage of rupture front in the vicinity of the strain gauge b) Track of rupture tip; it transitions to supershear around 1.7 cm.

In section 4.2 of chapter 4, I used finite-difference dynamic models in order to verify and discuss the method (in section 2.2.2) used to experimentally determine friction laws of analogue materials such as polycarbonate plates in a biaxial configuration. Although this is a useful validation step for the method, friction laws derived for polycarbonate at normal stresses of a few MPas are of limited interest for the rock mechanics community. This section aims at checking if the same method can be applied to the triaxial experiments presented in chapter 5, where westerly granite slabs are sheared under confining pressures of several tens of MPa. Because of the high noise level in strain gauge signals presented in chapter 5, it is impossible to compare them to numerical models of dynamic rupture. However, the latter are also developed in order to be used as supporting

information of the manuscript Harbord et al. (in prep.), where the less noisy data obtained enabled to use the method from section 2.2.2 to relate friction to slip and slip velocity in triaxial experiments.

The finite difference model is the same than the one in section 4.2, with the same type of linear slip-weakening friction law. The geometry is different, as well as other parameters which are summarized in table 6.1. Their values are adjusted so that as the rupture front passes next to the strain gauge (see fig. 6.4.a-b), the rupture velocity V_r is equal to V_{ray}, and is constant. Only the domain corresponding to the granite slabs (8 by 40 mm) is modelled, and it is assumed that the rupture starts from one of the edges, in accordance to the model results of section 6.1. For simplicity, stress free boundary conditions are imposed at the model edges (note that imposing fixed boundary conditions on the edge of a thin model tends to make the rupture stop prematurely) . The critical slip weakening distance of the model D_c is 2.4 μm, which is the same order of magnitude as the values determined experimentally by Ohnaka, 2003.

parameters		parameters	
E [GPa]	50	S	0.79
ν	0.25	κ	1.31
ρ [kg.m^{-3}]	2700	dx [mm]	0.5
L_c [cm]	0.5	nx	200
τ_p [MPa]	45	ny	40
τ_0 [MPa]	40	dt [μs]	0.012
τ_p [MPa]	35	t$_{max}$ [ms]	0.04
D_c [μm]	2.4	$\dot{\tau}$ [MPa/s]	30

TABLE 6.1: Summary of parameters used in the finite difference model of section 6.2

In figure 6.5, I plot the simulated shear stresses, slip and slip velocities which would be recorded by a strain gauge 1.3 cm from the domain's left edge, and 1.5 mm from the fault line (similarly to the static models of section 6.1). When calculated away from the fault, the slip velocity is obtained using $V(x,t) = 2\epsilon_{xx}V_r$, and

the displacement is the time integral: $U(x,t) = \int (2\epsilon_{xx} V_r) dt$. The shear stresses are explicitly calculated in the stress-velocity formulation of the model, and the values of slip and slip velocity on the fault are also the ones taken directly from the model.

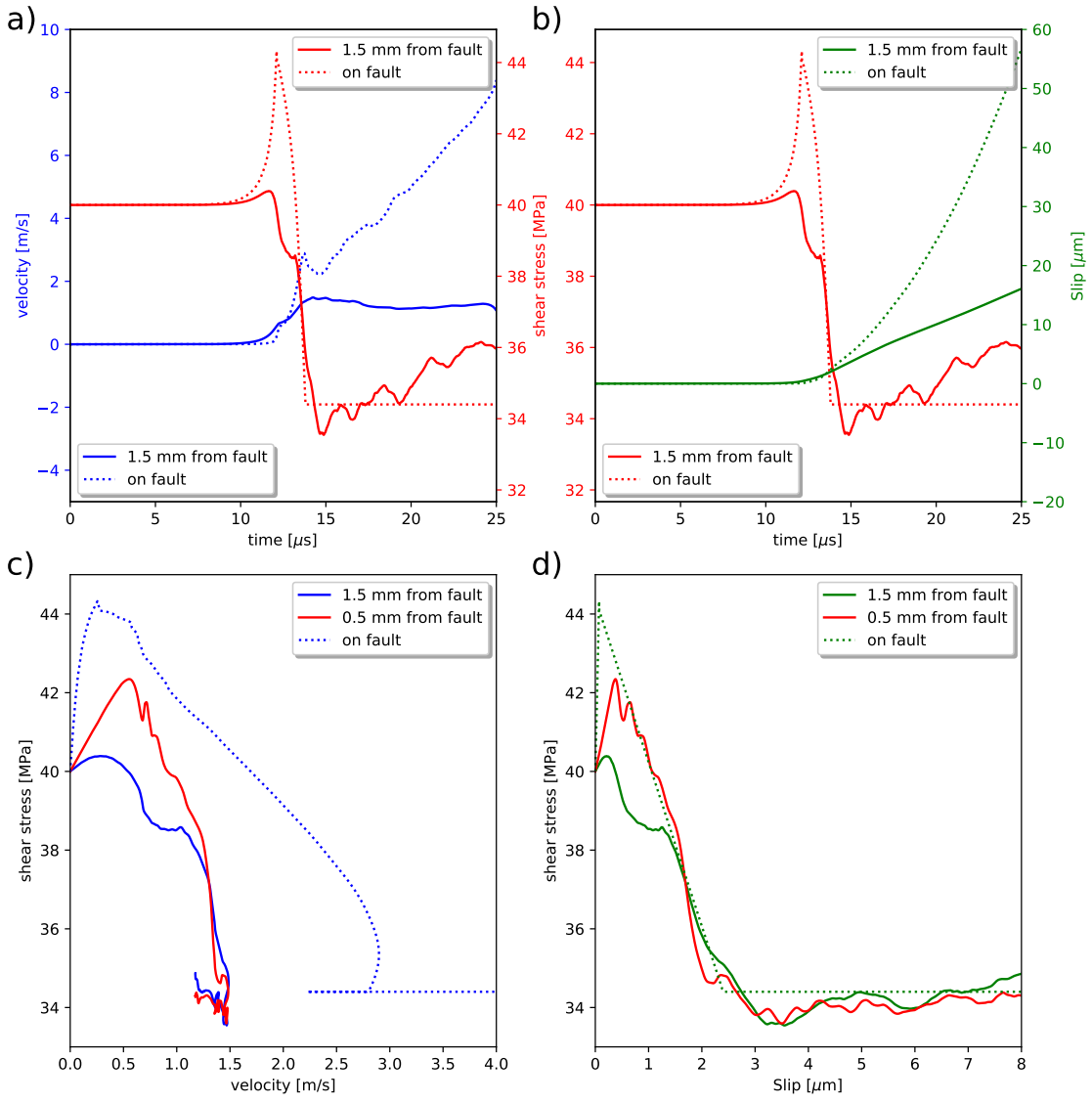

FIGURE 6.5: a) Shear stresses and slip velocities (2 ϵ_{xx} V_S) recorded at the strain gauge position and on the fault. b) Shear stresses and slip ($\int$ $(2\epsilon_{xx} V_S)$ dt) recorded at the strain gauge position and on the fault. c) Shear stress versus slip velocity using model values on the fault, 0.5 mm and 1.5 mm away from it. d) Shear stress versus displacement on the fault, 0.5 mm and 1.5 mm away from it.

In figure 6.5.a, it can be seen that 1.5 mm away from the fault, the peak of shear stress is almost not recorded. The slip is also overestimated at the beginning, and underestimated around 15 μs, from where the signals start to diverge

significantly. This makes the peak velocity underestimated by a factor 2, and the stress drop by a factor 1.5, away from the fault, when plotting the slip velocity dependence of friction (fig. 6.5.c). The fit seems better when looking at the slip-weakening friction law (fig. 6.5.d). This is because although the slip velocity is overestimated at the start, and underestimated after, it compensates when integrating to get the relative slip, and by the time the shear stress has dropped to its residual value τ_r, the amount of slip determined is roughly correct, and corresponds to D_c. If it was possible experimentally to place a strain gauge 0.5 mm from the fault, the peak shear stress τ_p would be resolved better (figs 6.5.c and 6.5.d), however, the peak of slip velocity would still be underestimated (fig 6.5.c).

Chapter 7

Conclusions and perspectives

7.1 Thesis summary

In this thesis, I have used laboratory analogues, alongside with static and dynamic numerical models in order to determine which factors could influence earthquake nucleation. While static numerical simulations were used to understand the complex loading conditions in experiments, and therefore their potential influence on the results, dynamic simulations were compared to laboratory data in order to validate the experimental methods used to measure the frictional dependence on slip and slip velocity.

After an introduction to earthquake studies in chapter 1, and the description of the laboratory and numerical models in chapter 2, we looked specifically at how the earthquake nucleation size was affected by the loading rate $\dot{\tau}$ in chapter 3, and published the results in Guerin-Marthe et al., 2018. Photoelastic experiments of dynamic shear rupture with polycarbonate plates as analogue material were conducted, and filmed at 200000 fps. They enabled us to directly track a rupture front propagating, and therefore to directly measure the nucleation length L_c of laboratory ruptures under varying shear loading rates, corresponding to varying tectonic loading rates in nature. The main result was that a decrease of L_c by a factor of 3 was observed when $\dot{\tau}$ was increased by almost 3 orders of magnitude, from 10^{-2} MPa/s to 6 MPa/s, which is in agreement with previous laboratory results (Mclaskey and Yamashita, 2017; Xu et al., 2017), and numerical studies (Kato and Hirasawa, 1996; Kaneko et al., 2016), suggesting the same effect. This result was interpreted in a rate-and-state frictional framework, and

in particular clarifications were made concerning the fact that at at low loading rates, a crack or slipping patch tends to grow up to a critical size before acceleration, which corresponds to the quasi-static value for a critical nucleation length $L_{Andrews}$ derived by Andrews, 1976, or L_∞ derived by Rubin and Ampuero, 2005. At higher loading rate, when the state of the surface represented by the variable θ in the rate-and-state framework does not have the time to evolve significantly by the time of nucleation, L_c might shrink down to a lower bound called L_b (Rubin and Ampuero, 2005). Although there is a clear negative trend for the relation L_c versus $\dot{\tau}$, a high variability is present and likely amplified by the initial stress heterogeneities combined with variable nucleation positions along the 30 cm long contact interface. We observed that the nucleation of laboratory ruptures initiated consistently around 8 cm or 22 cm along the interface for high loading rates, while being randomly distributed for low values of $\dot{\tau}$. It is not fully understood why, but we suggest that this might be linked to the size distribution of stress heterogeneities, as small wavelength heterogeneities are visible in the initial fringe pattern around 8 and 22 cm compared to larger wavelength along the rest of the interface. Finally, we discuss the implication of the shrinking of L_c with $\dot{\tau}$ in a natural context. Taking the example of subduction zones, we argue that if the loading rate is suddenly increased locally (eg. in the case of a nearby dislocation), a smaller L_c would mean that a patch initially stable could become unstable and release seismic radiations as its size would be superior to the nucleation length. Seismicity could therefore appear in slab regions which were usually silent, according to the observations of Hatakeyama et al., 2017.

In chapter 4, I built a finite element model with simple quadrilateral elements in order to understand the effect of loading conditions on the initial stress field in the elastic plates, just before the nucleation phase. By prescribing specific boundary conditions at the FEM models' edges, both displacements and tractions, I was able to simulate a fringe pattern which matched the experimental observations of isochromatics. The model was compared to fringe patterns in frames taken just before the rupture started to propagate, and in which the isochromatics were therefore representative of the initial stress distribution. This enabled us to evidence two area of high shear and coulomb stresses, corresponding to the

preferred nucleation sites at high loading rates. The results from this technique explain why a rupture would initiate on those patches, as observed in chapter 3, but the difference of initial fringe patterns from one rupture to another is so small that it cannot be used to quantitatively compare experiments (the pictures of the initial fringe patterns are available, and can be found in the online repository http://doi.org/10.5281/zenodo.1438477). It is not accurate enough either to resolve the small wavelength stress heterogeneities observed. The second part of the chapter focused on the dynamic rupture propagation, and aimed at verifying that the stress variations measured experimentally could be reproduced and understood thanks to numerical models. I built a finite difference model based on the method described in Virieux and Madariaga, 1982, and implemented a slip-weakening friction law for simplicity, and because it is consistent with the experimental observations. Indeed, in chapter 3, the fault-parallel stress had been used in order to estimate the relative slip along the laboratory fault, and showed a clear dependence of friction with it. I could also estimate the so-called slip-weakening distance D_c corresponding to the relative slip needed for the friction to reach its dynamic value. D_c of the same order of magnitude was used as a parameter for the dynamic simulation, and it resulted in a very good match with the experimental data, including in the case of supershear ruptures. However, by using the same method in the numerical model, and filtering the signals with a low-pass to estimate the friction dependence on slip (as it was also done for the experimental data), I showed that D_c was likely to be overestimated by a factor two in chapter 3. Therefore it explained why the estimated $L_{Andrews}$ was about twice L_∞. Correcting $L_{Andrews}$ from chapter 3 makes the experimental measurements of nucleation length even more consistent with crack stability theory.

The birefringent properties of polycarbonate were used in chapter 3 in order to measure directly the nucleation length in photoelastic experiments. It was a useful setup to evidence the nucleation length dependence on loading rate, to understand how the stress evolves during a dynamic rupture, and to test a new method to determine the relation of friction versus relative slip. However, the frictional properties of polycarbonate at relatively low pressures around 5 MPa is of limited interest to infer processes happening on real faults. Chapter 5 aimed at

studying the stability of laboratory faults, and the dynamic evolution of friction under more realistic conditions. Friction experiments using granite slabs polished with a 800 grit sandpaper, were conducted in a vessel applying confining pressures between 50 and 100 MPa, representative of the Earth upper crust. One of the results was that increasing healing time and loading rate favoured instability, which had only been evidenced at lower and therefore less realistic pressure conditions, by other studies such as the one of Mclaskey and Yamashita (2017). I also developed a methodology to place strain gauges onto the samples, inside the pressure vessel, and showed that this worked with one strain gauge. Providing that the noise can be reduced and more strain gauge fixed along the slabs interface, it should enable to record the shear stress evolution during the dynamic rupture, estimate the nucleation length, and look at the friction dependence on slip and slip velocity. When comparing the friction values from the strain gauge to the apparent one using the axial load force values , it can be seen that the strain gauge picks up more details, even when filtered at 24 Hz to reduce the noise, and that the local friction values are lower than the apparent ones.

Chapter 6 enabled to clarify the latter observations from chapter 5. I used FEM to model realistic loading conditions of the quasi direct shear configuration used to apply shear stress along the granite blocks' contact interface, including domains representing the sample holders, and silicon spacers. This evidenced in particular two areas of higher coulomb stress values at the samples edges from where the rupture was likely to initiate in this configuration. In those areas, ratios τ_{xy}/σ_n around 0.6 could be reached, and some slip could initiate although the apparent friction measured was much lower. This could partly explain the low apparent friction measured in the triaxial pressure vessel during dynamic stick-slips, but not during slow events. I argue that instead the low friction values are more likely to be due to the very smooth surfaces of our samples (polished at 800 grit), as it has been observed in preliminary studies to significantly lower friction values. The second part of this chapter used the finite difference code in the same way that it was used it in chapter 4, to look at how well the friction dependence on slip and slip velocity could be recovered when using the fault parallel strain. Because the geometry and material property are different compared with chapters 3

and 4, the dynamic rupture is also different, and more affected by the reflections on the edges. This study was therefore necessary to check if the method used to estimate the friction laws in the biaxial configuration with polycarbonate plates could also be used for smaller samples in the triaxial configuration. Although this could not be directly compared to the experimental data of chapter 6 because of noisy signals, this is being used for another study in collaboration with C. Harbord (Harbord et al., in prep.). The main results from the numerical model were that the peak stress is always underestimated by the strain gauge measurement if the latter is placed too far from the contact interface, which is expected. Secondly, when plotting shear stress versus slip velocity, the maximum slip velocity is underestimated by a factor 2. And finally, when plotting shear stress versus slip, the critical slip weakening distance D_c is well estimated although a strengthening phase appears, and is an artefact due to the overestimated slip as the rupture front approaches.

7.2 Discussion

The main result of this thesis is the loading rate effect on the nucleation size of laboratory earthquakes. This section aims at clarifying what this result means for very complex natural systems, how it helps for earthquakes prediction, and how it relates to the cascade versus preslip models debate.

When an interface is composed of a strong population of contacts (i.e. after a long healing time), under a high loading rate, the nucleation length of the rupture L_c tends to be smaller. This can be intuited by considering plasticity theory, where stress increases with strain rate. The faster the shear stress is applied, the more the contacts will resist this applied stress. And when some slip eventually occurs, the whole fault has reached a higher level of potential energy: a smaller nucleation zone is required for the rupture to accelerate and propagate further.

In the laboratory, if the nucleation length is larger than the sample, there is no acoustic emission, only slow slip. In nature, this means that if there is an asperity (a rate-weakening patch embedded in a rate strengthening surrounding medium) smaller than the nucleation length, then the latter will fail aseismically. On the

other hand, if following a sudden increase of loading rate, which can be the case during the immediate post-seismic phase, the shrinking of L_c might make the asperity to fail seismically.

Although this possibly works for an asperity of a few kilometres of diameter as in Tape et al. (2018), where the slow slip is interpreted to start from the outside edges of the asperity, it is hard to imagine than the slow slip observed in the experiments and the large slow slip zone hundreds of kilometres wide measured before large megathrusts (Ruiz et al., 2014; Ruiz et al., 2017) (referred to as ASZ for Apparent Slipping Zone in chapter 3) are comparable. Indeed, the preslip zone in the latter case is very heterogeneous, and larger than the coseismic slip area. Nonetheless, the size of the ASZ is likely to be in some cases a proxy for the following megathrust magnitude, as the energy accumulated on the locked patches within the ASZ will be proportional to its size.

On top of the complex rheology and geometry of the fault zones, other factors complicate the picture, making the loading rate effect on the nucleation size perhaps negligible. Indeed, there can be migrations of fluids driving the rupture, and for which the path is hard to predict. In the case of a complex fault network, it has also been shown with rate-and-state simulations, that the interactions between the faults could generate on a same network sometimes seismic, sometimes aseismic ruptures (Romanet et al., 2018). The normal stress variations during a slip episode are also likely to affect significantly the nucleation length, sometimes more than the loading rate, depending on the geometry of the fault and the direction of slip. Finally, as discussed in chapter 5, L_c decreases only when the loading rate is increased after a long healing time. If the loading rate is constantly high, then it tends to stabilize the fault instead.

In any case, slow slip is a very important phenomenon to study in order to understand earthquakes, and the seismicity patterns. It is very likely that before any earthquake, some slow slip occurs at various scales, even if it is not necessarily possible to detect it yet. What influences it depends largely on the geological setting, and what does it tell us about what follows is a tricky question. The 2016 Mw 7.8 Kaikōura earthquake is a good example to show that on a continental fault, even if some slow slip had occurred on the first fault that ruptured, it

would have been almost impossible to predict the following ruptures on a large network of faults, resulting in a Mw 7.8 earthquake (Ulrich et al., 2019).

Following the recent insights into earthquake nucleation (Ruiz et al., 2014; Ruiz et al., 2017; Tape et al., 2018; Ulrich et al., 2019), one can say that there are as many models as there are earthquakes. However, we see that the pre-slip and cascade models are compatible, and what makes one predominate over the other is not only the complexity of the system, but also the scale at which it can be observed. Before earthquake prediction can be achieved, we need very high resolution data to detect slow slip at the smallest scale possible, and also earthquake simulations incorporating complexities of faults (rheology, fault network, off-fault damage, pore fluids, etc..). It is not only complicated to implement, but also computationally expensive, especially considering the ranges of time and length scales involved.

7.3 Further work

When doing research, it seems that we are always asking more questions than answering them, and earthquake science is certainly not an exception. Even in simplified models of earthquake rupture, there is a lot more that can be done.

In this PhD, I built numerical models in order to better understand the experiments. A simple slip-weakening friction law was used as it worked well to match the experimental data. I did not use the models in order to show the nucleation length dependence on loading rate as it had already been done, although it would still be interesting to implement rate-and-state friction laws in order to match better the experimental observations. In particular, I believe that developing further the code **DG_version4_(dyn_forces).ipynb** from appendix C (in which I use FEM with two continuous domain separated by split nodes at the interface to prescribe traction once the static friction is reached) would give very realistic results for single rupture events, as long as the displacements are small. Ageing or slip versions of the rate-and-state friction laws could be used, but it would be even better to implement the power law version of it (ongoing work by James Moore and Stefan Nielsen) which allows for zero slip velocities.

Improving the Digital Image Correlation (DIC) technique would also be interesting in order to look at the loading conditions of the samples, the initial stresses, and the subsequent dynamic rupture. At the moment, although the preliminary results are promising (see examples in appendix B), the noise could be greatly improved, by improving both the laboratory setup (more homogeneous light, more contrast between the black dots pattern and the rest of the plates), and the way the data is processed (higher order shape functions to match the patterns, filters, etc...). The inversion technique which consists in using the photoelastic fringe pattern to find the initial stress conditions of the experiments as described in chapter 4 would benefit from some improvements too. By taking the Hilbert transform of the gray level instead of the gray level values themselves, and using the strain gauge signals at the same time should make the inversion mode robust.

Finally, one of the most recent and promising techniques for probabilistic short-term earthquake forecasting which has unfortunately not been explored during the thesis is machine-learning. It has been applied successfully to predict the stress drop and timing of stick-slips in rock friction experiments by Rouet-Leduc et al., 2017, and has started to be applied to natural events (Rouet-Leduc et al., 2018). This could also be applied and tested for the photoelastic experiments of chapter 3. Indeed, it is likely that some information about the initial stresses which is challenging to quantify using classic inversion techniques (see appendix A) is contained in the isochromatic fringes. For instance, frames could be given to a machine-learning algorithm, which is trained to return the critical nucleation length, or another frame of the sequence from the same rupture event. The stress information contained by the strain gauges could also be provided. In the case of successful results, we could test the same method using InSAR or strainmeters data, in order to verify if when some pre-slip is detected during the nucleation phase of an earthquakes, it contains informations about the stresses during the dynamic rupture.

Appendix A

Inversion of photoelastic fringes

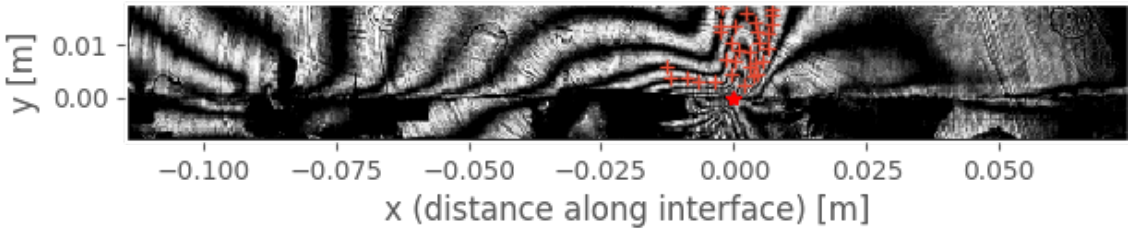

FIGURE A.1: Scaled picture of isochromatics during a dynamic rupture, where we assign manually fringe number values at points picked along the fringes.

A natural question which arises when hearing about photoelastic studies is if we can get quantitative data from isochromatics. During the dynamic rupture experiments presented in chapter 3, the isochromatics are used to track the rupture tips, but do not provide absolute values of shear and normal stress (given by strain gauges instead). Therefore, it seems that a lot of the information contained in the movies is not used. This section discusses why inverting fringes in such experiments is challenging in practice. The script used here to run the inversion is accessible online (see appendix C)

The commonly used inversion procedure is described in chapter 2.3.3. Dally and Riley, 1965 explains more specifically how to invert isochromatics for static cracks, using optics equations from section 2.2.1, and the theoretical static stress field in eq. 1.12, resulting in eq. 1.14. From these equations, a fringe number N can be calculated at any position in the vicinity of a mixed-mode crack, for given values of stress intensity factors K_I, K_{II} and remote stress σ_{0x}.

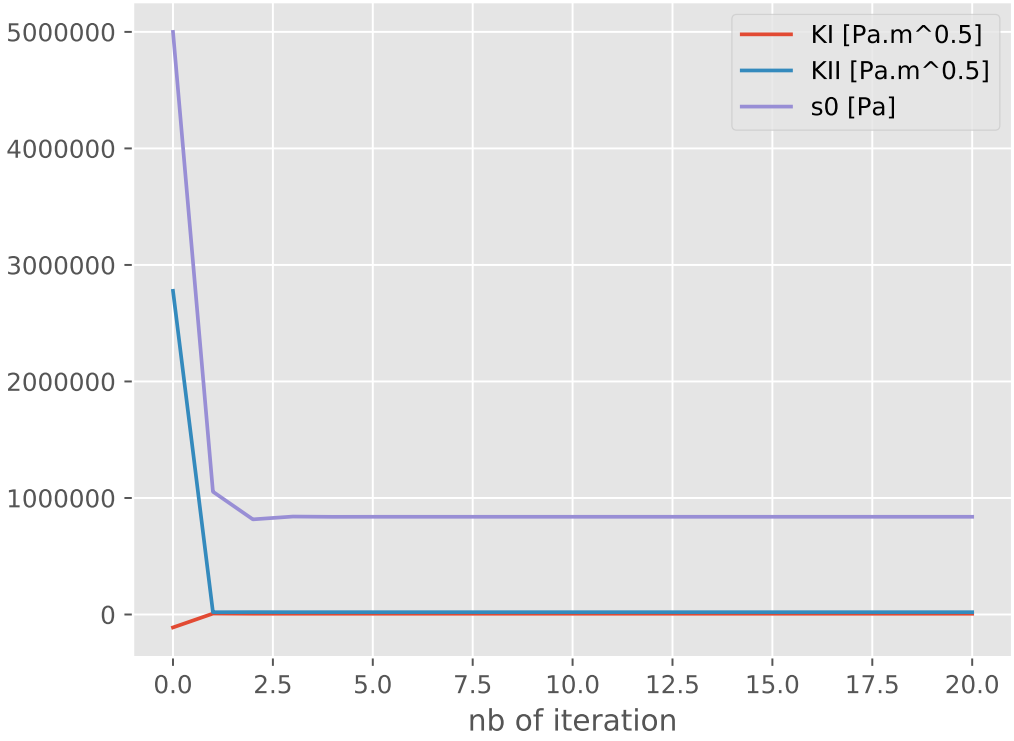

FIGURE A.2: Convergence of inverted parameters K_I, K_{II} and S_{0x}

In order to invert dynamic fringes, I use eq. 1.15 for a mixed-mode dynamic crack, and the optics equations of section 2.2.1. In a similar manner N can be obtained at any position, as a function of K_I, K_{II} and σ_{0x}. In the inversion code, K_I, K_{II} and σ_{0x} are the parameters to invert, in order to minimize the difference between the computed fringe number, and the fringe number which has to be assigned manually.

In order to run the inversion, a fringe number needs to be given at points picked along fringes in the original picture. There need to be more points than parameters to invert, which is why the technique is called over-determined inversion.

Once these data are provided, the code can be run until the solution converges, usually after a few iterations (see fig. A.2). One of the problems is that it is impossible to know the absolute fringe numbers on fig. A.1. Instead we only know from the theoretical equations that the fringe number should decrease away from the

crack tip. The direction of fringe number increase is harder to guess elsewhere in the domain, as heterogeneities create a complex pattern, and there might be saddle points.

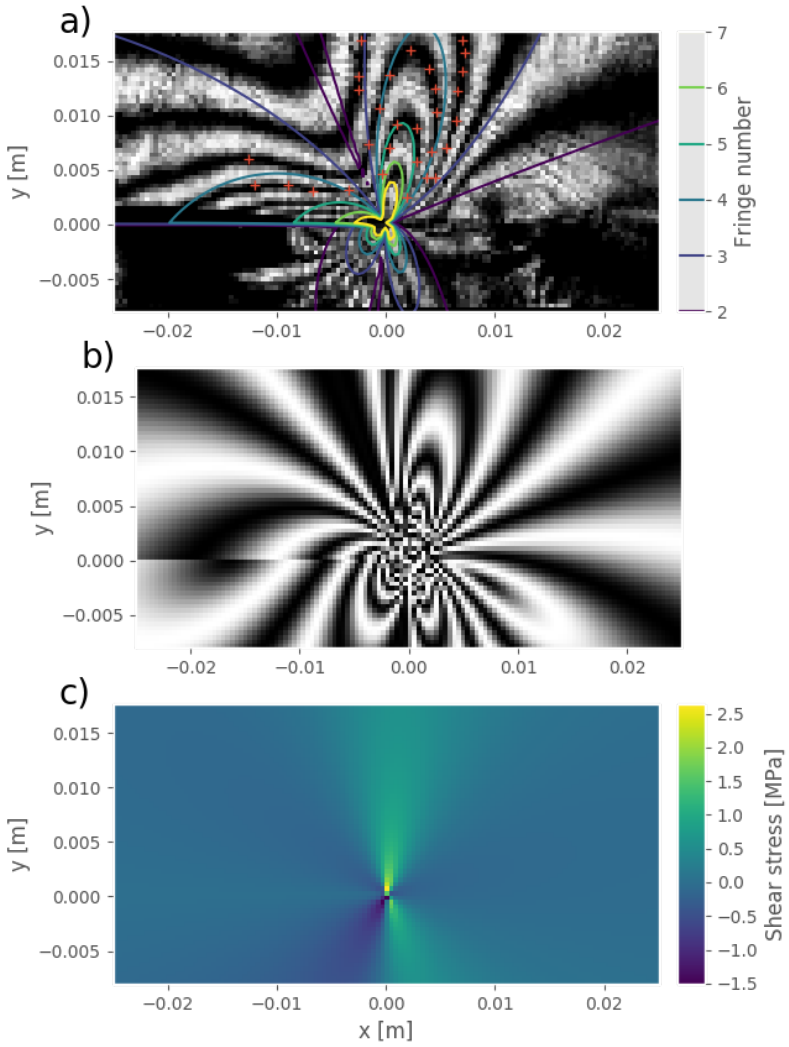

FIGURE A.3: a) Inverted fringes compared to original ones, and picked points. b) Inverted synthetic fringes. c) Inverted shear stresses.

From K_I, K_{II} and σ_{0x}, I compute the inverted fringe number, and superimpose it to the original picture in fig. A.3.a . It can be seen that fringes 4, 5 and 6 roughly match the original pattern, while the others fringes obtained do not fit well. This is also visible on synthetic fringes computed from N and the optics equations, fig. A.3.b . If this method was accurate, the full stress field would be obtained directly. An example is given for the shear stress in fig. A.3.c (as the absolute fringe number is not known, the absolute values of stress are likely to be wrong

too). A big issue with the method also comes from the theoretical dynamic crack equations (eq. 1.15), which assume a negligible process zone length X_e. This is clearly not the case in our experiments, and it is the reason why there is no singularity at the crack tips: the fringes on fig. A.3.a do not join at the tip, unlike on the synthetic fringes of fig. A.3.b. Using the time difference $\Delta t \approx 15\,\mu$s between the peak stress and residual stress recorded by the strain gauges, and a rupture velocity $V_r = 820$ m/s, an estimate of the process zone can be given by $X_e = V_r \times \Delta t = 12$ mm, which is non-negligible compared to the fringes size.

What I could also have done to quantify the fracture energy U_s is to take directly the strain gauge signals 2 mm away from the fault, knowing the the rupture velocity V_r, in a similar way than what has been done in Svetlizky et al., 2016.

Appendix B

Digital Image Correlation

As discussed in appendix A, although the photoelastic method is a very useful tool which has been applied successfully in chapter 3, it has limitations when it comes to measure the full displacement and stress fields, during dynamic rupture experiments. In this section, without going into detail, I briefly explore a DIC technique in order to track the particle displacements on the polycarbonate plates before and during a dynamic rupture. A similar technique has already been successfully applied to rupture dynamics, in the recent study of Rubino et al., 2017. Here I show that even being at the limit of resolution, I obtain some promising results which seem consistent with the strain gauge data from chapter 3.

B.1 Checking the loading conditions of the biaxial experiments

I start by checking the loading conditions created by the biaxial press, already discussed in chapters 3 and 4. In section 4.1.2, I matched the isochromatics of a FEM model to the experimental picture of the fringes at the end of the loading phase and just before a rupture. This suggested two areas of higher coulomb stress from where the rupture consistently nucleated at high loading rates. Using DIC, I want to check if a similar initial stress distribution can be evidenced.

The DIC technique enables to track the motion of particles between two images. The images are fractioned into smaller areas, and the correlation algorithm finds the relative vertical and horizontal displacements of the same neighbourhood of pixels in the two images which give the best match.

I use the MATLAB based free software Ncorr in order to obtain the vertical and horizontal displacement fields u_x and u_y (see fig. B.1) from which strains ϵ_{xx}, ϵ_{xy}, ϵ_{yy} and stresses σ_{xx}, σ_{xy}, σ_{yy} can be estimated (see fig. B.2). Similar results can be obtained with the Image_Correlator.class plugin from the open-source software ImageJ. From the initial and the deformed pictures, normal stresses around 5 to 15 MPa and shear stresses around 2 to 6 MPa, the displacement gradients needed to be resolved are around a few micrometers per centimetre. The frames are 200 by 992 pixels with a resolution of 33 px/cm.

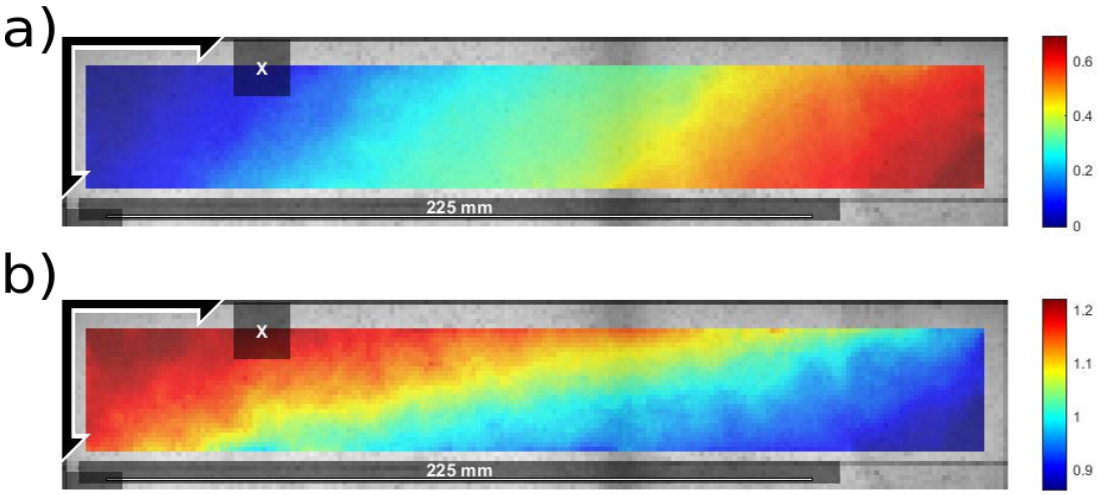

FIGURE B.1: a) Initial horizontal (a) and vertical (b) displacements measured with DIC, u_x and u_y respectively.

Fig. B.2 presents the stresses recovered from the displacement gradients, taking elastic moduli $E = 2.59$ GPa, and $\nu = 0.35$. While the displacement field seems well resolved, the stresses are more noisy as the displacement gradients are used in this case. A profile of shear and normal stresses close to the interface is shown in fig. B.3.a. The normal stresses go up to 17 MPa in the middle if the interface, and are around 5 MPa close to the edges. The shear stress is around 1 MPa at the edges and in the middle of the profile, but exhibits to areas where it peaks at 3 to 4 MPa. The general stress distribution is consistent with what I inferred using the FEM model of section 4.1.2, showing a bell shaped normal stress distribution, and two areas of high shear stress around 8 and 20 cm from where the rupture is likely to start, because of high ratios of σ_{yx} / σ_{yy}. However it is hard to believe

that the shear stress is almost zero in the middle of the interface, because it is not consistent with the numerical model, or with the strain gauge measurements. It it likely due to noisy displacement gradients.

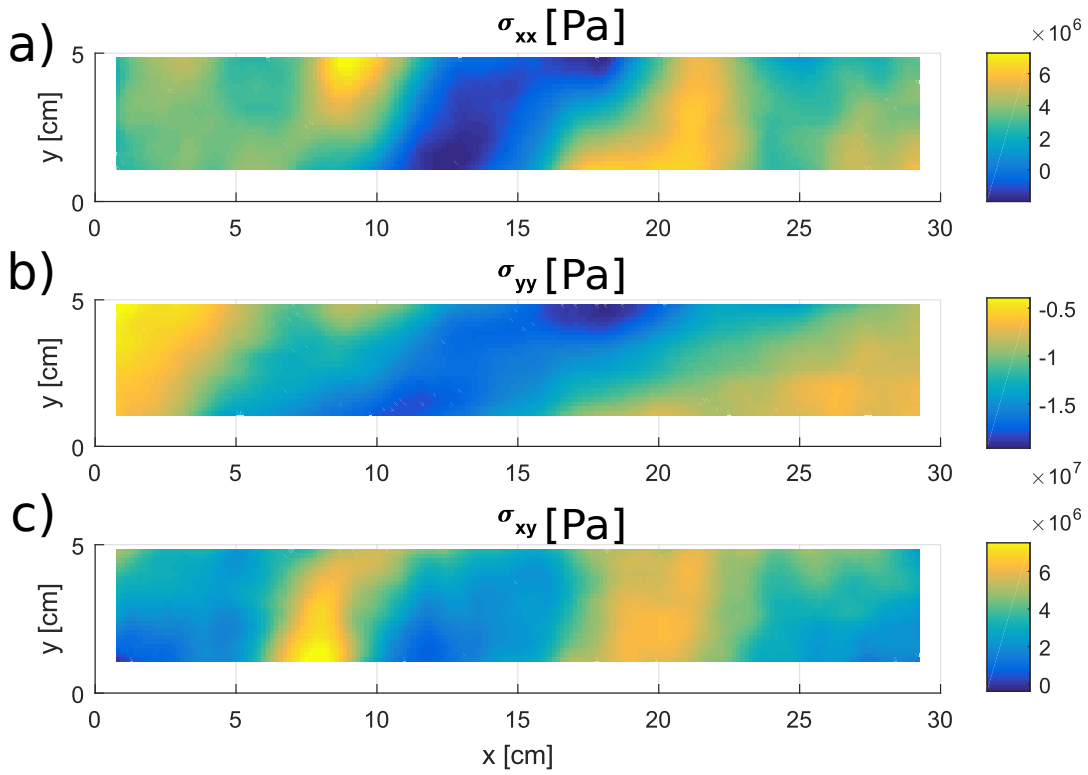

FIGURE B.2: Initial stresses: a) fault parallel; b) fault perpendicular (normal); c) shear.

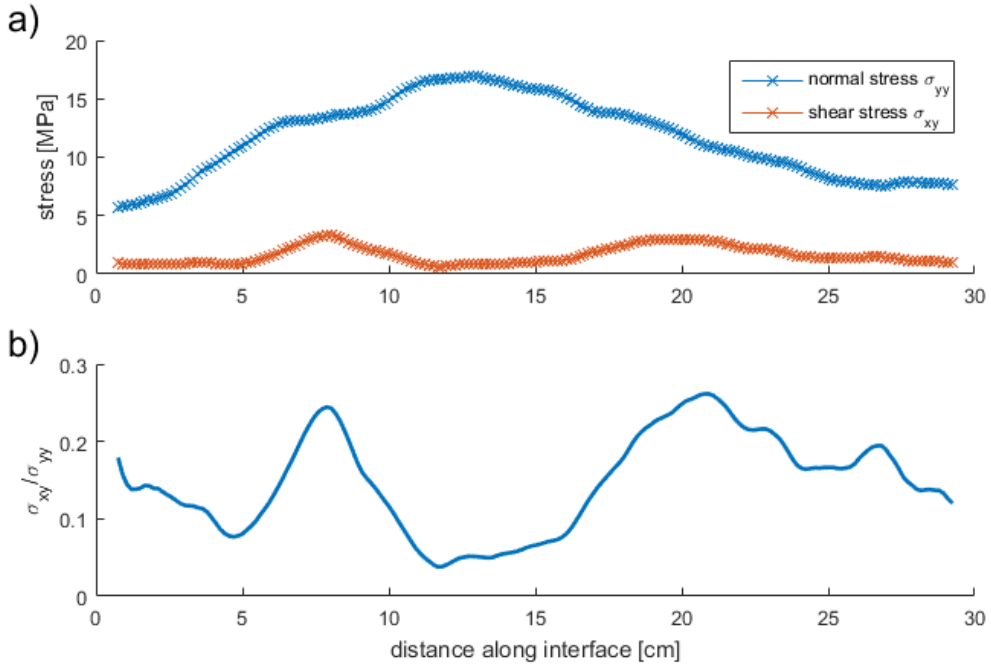

FIGURE B.3: a) Shear and normal initial stresses in the vicinity of the interface. b) Ratio shear to normal stresses.

B.2 Is is possible to see the dynamic rupture propagation?

The second application of DIC tested in the appendix is the visualization of a dynamic rupture propagating at the interface between the polycarbonate plates. I recorded a movie at 60000 fps with a frame dimension of 120 by 992 pixels and the same resolution of 33 px/cm. In this case I am interested in the relative displacement between the two plates. Therefore, I subtract the displacement profile on one side of the interface, to the displacement on the other side between two successive frames, 16.7 μs apart. The cumulative relative displacement along the interface over time is calculated and shown in fig. B.4.

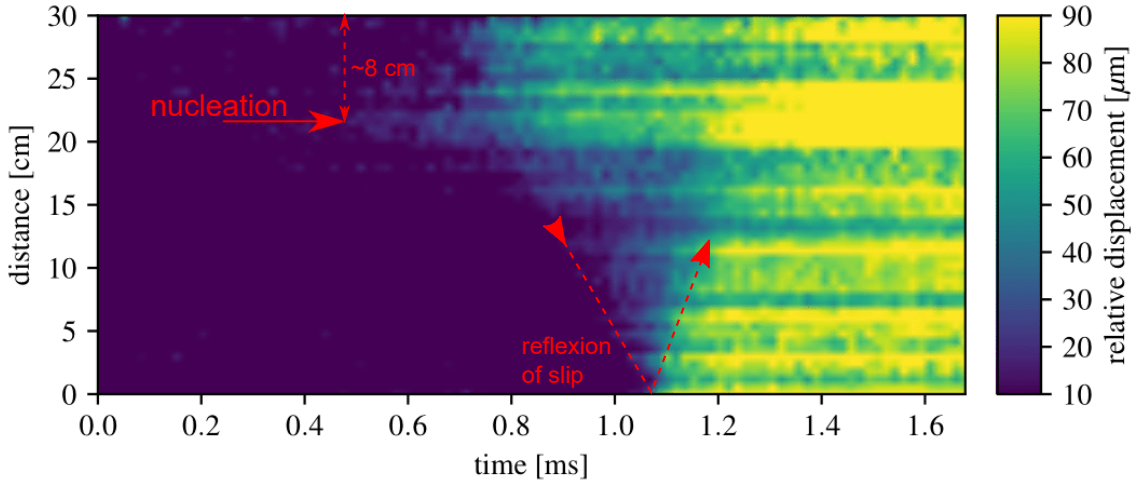

FIGURE B.4: Relative displacement versus time along the interface during a dynamic event in the biaxial machine, obtained with DIC technique.

A nucleation phase is clearly visible, and is followed by the dynamic rupture. Several things are consistent with the biaxial experiments of chapter 3 and help to understand them. First, the nucleation initiates roughly 8 cm away from the edge, which is what is observed with photoelasticity, and is attributed to high values of coulomb stress in those places. Second, the total displacement is around 80 μm, and takes place in a fraction of millisecond, which is roughly what I measured when plotting the dynamic friction evolution of polycarbonate using strain gauges in chapter 3.

Finally, a very useful result is that we now see that we have a relative slip propagating downwards at V_r, and reflected upwards when it reaches the plates' edges. It means that going further from the bottom edge of the interface, the slip starts occurring in two phases. This is also what can be seen, when looking back at the fault parallel strain recoded during the ruptures of chapter 3: the slip pulse is progressively split. We have two peaks recorded by the strain gauges close to the nucleation position, while all the slip happens at once close to the edge where the rupture is reflected.

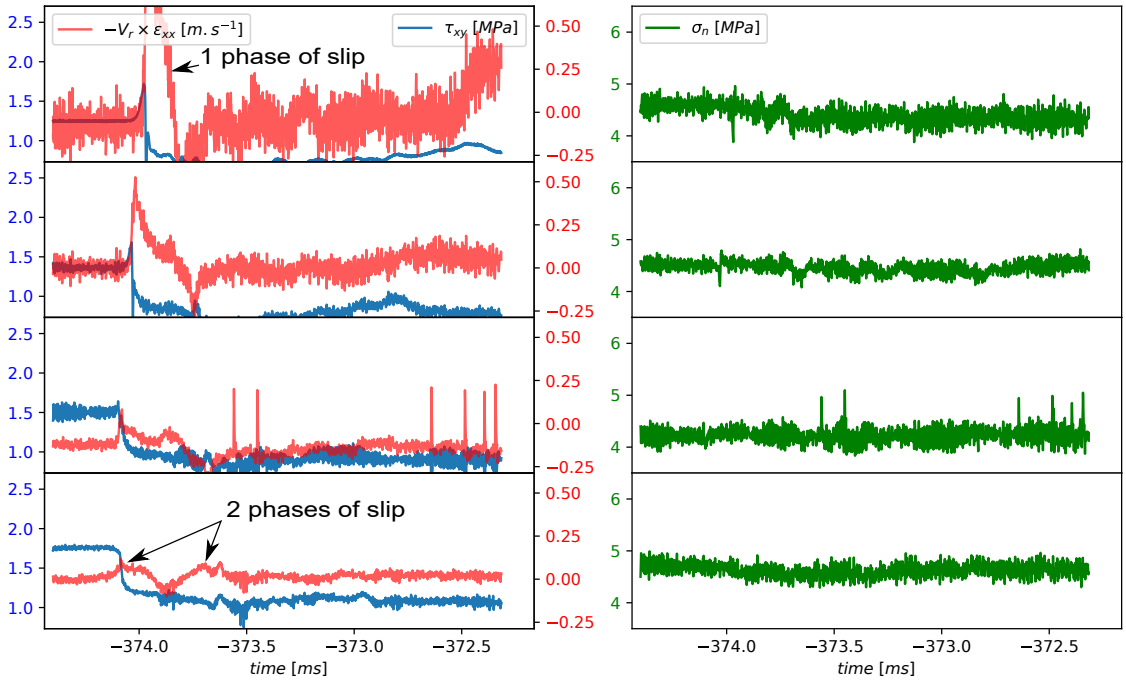

FIGURE B.5: Slip velocity record evidencing a 2 step slip close to the source, as expected when looking at fig. B.4

Appendix C

Github repository for the codes developed during the PhD

Most of the base codes used during this PhD are made available online at: https://github.com/Simongm/codes-dynamic-rupture-and-earthquakes. Here is a list of the codes and their brief description:

- **Main_plotter.py** and **read_function.py** : **Main_plotter.py** calls **read_function.py**, which together enable to read all the datasets from hdf5 files produces by the high-speed acquisition system. Used mainly to process strain-gauge signals.

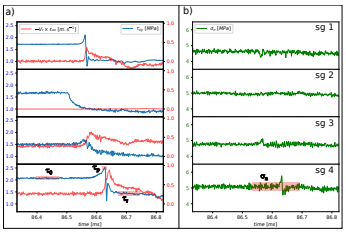

- **Iris_EQ_animation.ipynb**: Python script (jupyter notebook) which finds online earthquake datasets from Iris website, and generates animations of earthquakes sequences for chosen timespans and regions.

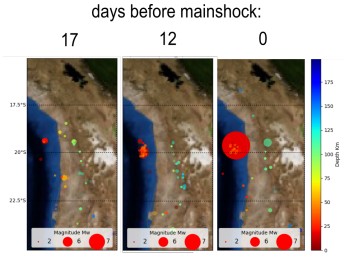

- **dynamic_fd_intro.m**: Matlab script which simulates dynamic inplane ruptures

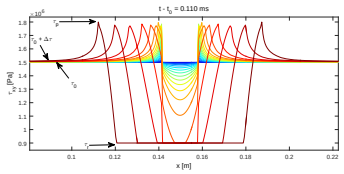

- **dynamic_rupture_snapshot.ipynb**: Python script (jupyter notebook) for the simulation of dynamic inplane ruptures.

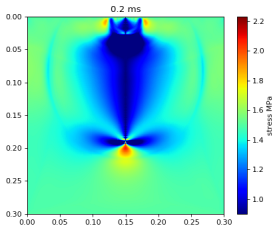

- **DG_version1 static_elasticity_FEM.ipynb**: Python jupyter notebook used for static finite element simulations with simple quadrilateral elements, and possibility to introduce a crack in the domain.

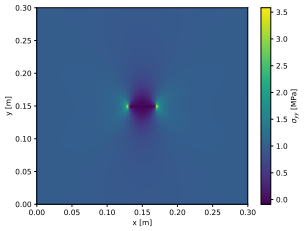

- **FEM2D_models_of_biaxial_loading.ipynb**: Python jupyter notebook used for static finite element simulations , and more specifically for simulation of isochromatics in polycarbonate plates with different loading configurations.

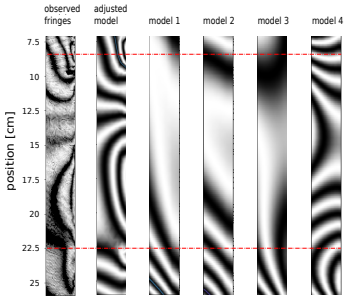

- **loading_triax_crack-forceBC.ipynb**: Python jupyter notebook used for static finite element simulations , and more specifically for simulation loading condition in triaxial apparatus with different materials.

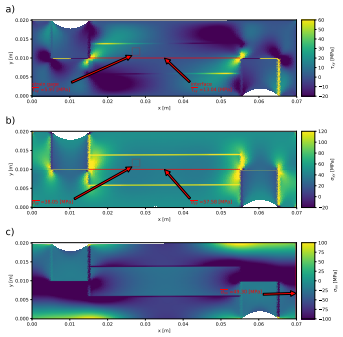

- **DG_version4_(dyn_forces).ipynb**: Python script under development, to simulate dynamic rupture by prescribing tractions at split nodes along an interface.

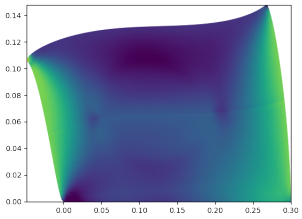

- **processpiv.py**: Python script used to calculate strains in 2D from PIV analysis results (text files such as pivImJ.txt available in the repository) from the PIV plugin of imageJ free software.

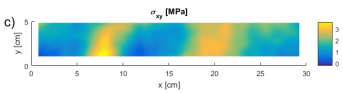

- **inversion-isochromatics-fringes.ipynb**: Python jupyter notebook used to invert isochromatic fringes from photoelastic experiments of dynamic rupture.

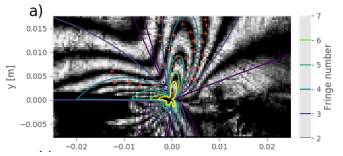

Bibliography

Allmann, Bettina P and Peter M Shearer (2009). "Global variations of stress drop for moderate to large earthquakes". In: *Journal of Geophysical Research: Solid Earth* 114.B1.

Ampuero, Jean-Paul and Allan M. Rubin (2008). "Earthquake nucleation on rate and state faults – Aging and slip laws". In: *Journal of Geophysical Research* 113.B1.

Andrews, DJ (1976). "Rupture velocity of plane strain shear cracks". In: *Journal of Geophysical Research* 81.32, pp. 5679–5687.

Baumberger, T, P Berthoud, and C Caroli (1999). "Physical analysis of the state- and rate-dependent friction law. II. Dynamic friction". In: *Physical Review B* 60.6, p. 3928.

Ben-David, O, G Cohen, and J Fineberg (2010). "Short-time dynamics of frictional strength in dry friction". In: *Tribology letters* 39.3, pp. 235–245.

Ben-Zion, Yehuda (2001). "Dynamic ruptures in recent models of earthquake faults". In: *Journal of the Mechanics and Physics of Solids* 49.9, pp. 2209–2244.

Bhat, Harsha S, Renata Dmowska, Geoffrey CP King, Yann Klinger, and James R Rice (2007). "Off-fault damage patterns due to supershear ruptures with application to the 2001 Mw 8.1 Kokoxili (Kunlun) Tibet earthquake". In: *Journal of Geophysical Research: Solid Earth* 112.B6.

Bhat, HS, CG Sammis, and AJ Rosakis (2011). "The micromechanics of westerley granite at large compressive loads". In: *Pure and Applied Geophysics* 168.12, pp. 2181–2198.

Biegel, Ronald L, Charles G Sammis, and Ares J Rosakis (2008). "An experimental study of the effect of off-fault damage on the velocity of a slip pulse". In: *Journal of Geophysical Research: Solid Earth* 113.B4.

Bird, Robert, Will Coombs, and Stefano Giani (2017). "Fast native-MATLAB stiffness assembly for SIPG linear elasticity". In: *Computers and mathematics with applications* 74.12, pp. 3209–3230.

Bouchon, M., H. Karabulut, M. Aktar, S. Özalaybey, J. Schmittbuhl, and M.-P. Bouin (2011). "Extended Nucleation of the 1999 Mw 7.6 Izmit Earthquake". In: *Science* 331, pp. 877–880.

Broberg, K Bertram (1999). *Cracks and fracture*. Elsevier.

Byerlee, James (1978). "Friction of rocks". In: *Pure and applied geophysics* 116.4-5, pp. 615–626.

Candela, Thibault, François Renard, Yann Klinger, Karen Mair, Jean Schmittbuhl, and Emily E Brodsky (2012). "Roughness of fault surfaces over nine decades of length scales". In: *Journal of Geophysical Research: Solid Earth* 117.B8.

Chester, Frederick M, James P Evans, and Ronald L Biegel (1993). "Internal structure and weakening mechanisms of the San Andreas fault". In: *Journal of Geophysical Research: Solid Earth* 98.B1, pp. 771–786.

Cochard, Alain and Raúl Madariaga (1994). "Dynamic faulting under rate-dependent friction". In: *Pure and Applied Geophysics* 142.3-4, pp. 419–445.

Dally, James W and William F Riley (1965). *Experimental stress analysis*. McGraw-Hill.

Dieterich, James H (1979). "Modeling of rock friction: 1. Experimental results and constitutive equations". In: *Journal of Geophysical Research: Solid Earth* 84.B5, pp. 2161–2168.

Dieterich, James H. (1992). "Earthquake nucleation on faults with rate-and state-dependent strength". In: *Tectonophysics* 211.1-4, pp. 115–134.

Dieterich, James H and Brian D Kilgore (1994). "Direct observation of frictional contacts: New insights for state-dependent properties". In: *Pure and Applied Geophysics* 143.1-3, pp. 283–302.

Dunham, Eric M, Pascal Favreau, and JM Carlson (2003). "A supershear transition mechanism for cracks". In: *Science* 299.5612, pp. 1557–1559.

Ellsworth, W. L. and G. C. Beroza (1995). "Seismic Evidence for an Earthquake Nucleation Phase". In: *Science* 268.5212, pp. 851–855.

Fang, Zijun, James H. Dieterich, and Guanshui Xu (2010). "Effect of initial conditions and loading path on earthquake nucleation". In: *Journal of Geophysical Research* 115.B6.

Fialko, Y (2007). "Fracture and frictional mechanics - theory". In: *Treatise on Geophysics* 4, pp. 83–106.

Frank, William, Baptiste Rousset, Cecile Lasserre, and Michel Campillo (2017). "Revealing the cascade of slow transients behind a large slow slip event". In: *2017 Fall Meeting*.

Frank, William B, Nikolai M Shapiro, Allen L Husker, Vladimir Kostoglodov, Alexander A Gusev, and Michel Campillo (2016). "The evolving interaction of low-frequency earthquakes during transient slip". In: *Science advances* 2.4, e1501616.

Freund, L Ben (1998). *Dynamic fracture mechanics*. Cambridge university press.

Gabuchian, Vahe, Ares J Rosakis, Nadia Lapusta, and David D Oglesby (2014). "Experimental investigation of strong ground motion due to thrust fault earthquakes". In: *Journal of Geophysical Research: Solid Earth* 119.2, pp. 1316–1336.

Griffith, Alan A (1921). "The phenomena of rupture and flow in solids". In: *Philosophical transactions of the royal society of london. Series A, containing papers of a mathematical or physical character* 221, pp. 163–198.

Gu, Ji-Cheng, James James R. Rice, Andy L. Ruina, and Simon T. Tse (1984). "Slip Motion and Stability of a Single Degree of FreFree Elasric System with Rate and State Dependent Friction". In: *J. Mech. Phys. Solids* 32 c, pp. 167–196.

Guerin-Marthe, Simon, Stefan Nielsen, Robert Bird, Stefano Giani, and Giulio Di Toro (2018). "Earthquake Nucleation Size: Evidence of Loading Rate Dependence in Laboratory Faults". In: *Journal of Geophysical Research: Solid Earth*.

Harbord, Christopher (2018). "Earthquake nucleation, rupture and slip on rough laboratory faults". PhD dissertation. Durham University.

Harbord, Christopher WA, Stefan B Nielsen, Nicola De Paola, and Robert E Holdsworth (2017). "Earthquake nucleation on rough faults". In: *Geology* 45.10, pp. 931–934.

Hasegawa, Akira and Keisuke Yoshida (2015). "Preceding seismic activity and slow slip events in the source area of the 2011 Mw 9.0 Tohoku-Oki earthquake: a review". In: *Geoscience Letters* 2.1. ISSN: 2196-4092.

Hatakeyama, Norishige, Naoki Uchida, Toru Matsuzawa, and Wataru Nakamura (2017). "Emergence and disappearance of interplate repeating earthquakes following the 2011 M9. 0 Tohoku-oki earthquake: Slip behavior transition between seismic and aseismic depending on the loading rate". In: *Journal of Geophysical Research: Solid Earth* 122.7, pp. 5160–5180.

Heap, MJ and DR Faulkner (2008). "Quantifying the evolution of static elastic properties as crystalline rock approaches failure". In: *International Journal of Rock Mechanics and Mining Sciences* 45.4, pp. 564–573.

Heaton, Thomas H (1990). "Evidence for and implications of self-healing pulses of slip in earthquake rupture". In: *Physics of the Earth and Planetary Interiors* 64.1, pp. 1–20.

Ida, Yoshiaki (1973). "Stress concentration and unsteady propagation of longitudinal shear cracks". In: *Journal of Geophysical Research* 78.17, pp. 3418–3429.

Ide, Satoshi, Gregory C Beroza, David R Shelly, and Takahiko Uchide (2007). "A scaling law for slow earthquakes". In: *Nature* 447.7140, p. 76.

Im, Kyungjae, Derek Elsworth, Chris Marone, and John Leeman (2017). "The Impact of Frictional Healing on Stick-Slip Recurrence Interval and Stress Drop: Implications for Earthquake Scaling". In: *Journal of Geophysical Research: Solid Earth* 122.12.

Imoto, Masajiro (1991). "Changes in the magnitude—Frequency b-value prior to large (from Mw 6.0) earthquakes in Japan". In: *Tectonophysics* 193.4, pp. 311–325.

Irwin, G. R. (1957). "Analysis of stresses and strains near the end of a crack traversing a plate". In: *J. Appl. Mech.* 24, pp. 361–364.

Kanamori, Hiroo (1977). "Seismic and aseismic slip along subduction zones and their tectonic implications". In: *Island Arcs, Deep Sea Trenches and Back-Arc Basins*, pp. 163–174.

Kanamori, Hiroo and Emily E Brodsky (2004). "The physics of earthquakes". In: *Reports on Progress in Physics* 67.8, p. 1429.

Kaneko, Y and J.-P Ampuero (2011). "A mechanism for preseismic steady rupture fronts observed in laboratory experiments". In: *Geophys. Res. Lett.* 38.21, p. L21307.

Kaneko, Yoshihiro, Stefan B. Nielsen, and Brett M. Carpenter (2016). "The onset of laboratory earthquakes explained by nucleating rupture on a rate-and-state fault". In: *Journal of Geophysical Research: Solid Earth* 121.8, pp. 6071–6091.

Kaneko, Yoshihiro, Brett M. Carpenter, and Stefan B. Nielsen (2017). "Nucleation process of magnitude 2 repeating earthquakes on the San Andreas Fault predicted by rate-and-state fault models with SAFOD drill core data". In: *Geophysical Research Letters* 44.1, pp. 162–173.

Kato, Aitaro, Kazushige Obara, Toshihiro Igarashi, Hiroshi Tsuruoka, Shigeki Nakagawa, and Naoshi Hirata (2012). "Propagation of slow slip leading up to the 2011 Mw 9.0 Tohoku-Oki earthquake". In: *Science* 335.6069, pp. 705–708.

Kato, N. and T. Hirasawa (1996). "Effects of strain rate and strength nonuniformity on the slip nucleation process: A numerical experiment". In: *Tectonophysics* 265.3-4, pp. 299–311.

Kato, Naoyuki, Kiyohiko Yamamoto, Hidekazu Yamamoto, and Tomowo Hirasawa (1992). "Strain-rate effect on frictional strength and the slip nucleation process". In: *Tectonophysics* 211.1-4, pp. 269–282.

Kawamura, Masashi and Kate Huihsuan Chen (2017). "Influences on the location of repeating earthquakes determined from a and b value imaging". In: *Geophysical Research Letters* 44.13, pp. 6675–6682.

Kohlstedt, DL, Brian Evans, and SJ Mackwell (1995). "Strength of the lithosphere: Constraints imposed by laboratory experiments". In: *Journal of Geophysical Research: Solid Earth* 100.B9, pp. 17587–17602.

Latour, S, A Schubnel, S Nielsen, R Madariaga, and S Vinciguerra (2013). "Characterization of nucleation during laboratory earthquakes". In: *Geophysical Research Letters* 40.19, pp. 5064–5069.

Lay, Thorne, Hiroo Kanamori, Charles J Ammon, Keith D Koper, Alexander R Hutko, Lingling Ye, Han Yue, and Teresa M Rushing (2012). "Depth-varying

rupture properties of subduction zone megathrust faults". In: *Journal of Geophysical Research: Solid Earth* 117.B4.

Livne, Ariel, Eran Bouchbinder, and Jay Fineberg (2008). "Breakdown of linear elastic fracture mechanics near the tip of a rapid crack". In: *Physical review letters* 101.26, p. 264301.

Lu, Xiao, Nadia Lapusta, and Ares J Rosakis (2007). "Pulse-like and crack-like ruptures in experiments mimicking crustal earthquakes". In: *Proceedings of the National Academy of Sciences* 104.48, pp. 18931–18936.

— (2010a). "Pulse-like and crack-like dynamic shear ruptures on frictional interfaces: experimental evidence, numerical modeling, and implications". In: *International Journal of Fracture* 163.1-2, pp. 27–39.

Lu, Xiao, Ares J Rosakis, and Nadia Lapusta (2010b). "Rupture modes in laboratory earthquakes: Effect of fault prestress and nucleation conditions". In: *Journal of Geophysical Research: Solid Earth* 115.B12.

Marone, Chris (1998a). "Laboratory-derived friction laws and their application to seismic faulting". In: *Annual Review of Earth and Planetary Sciences* 26.1, pp. 643–696.

— (1998b). "The effect of loading rate on static friction and the rate of fault healing during the earthquake cycle". In: *Nature* 391.6662, p. 69.

Mclaskey, Gregory C. and Futoshi Yamashita (2017). "Slow and fast ruptures on a laboratory fault controlled by loading characteristics". In: *Journal of Geophysical Research: Solid Earth* 122.5, pp. 3719–3738.

Michel Bouchon Virginie Durand, David Marsan Hayrullah Karabulut and Jean Schmittbuhl (2013). "The Long Precursory Phase of Most Large Interplate Earthquakes". In:

Nasseri, MHB, A Schubnel, PM Benson, and RP Young (2009). "Common evolution of mechanical and transport properties in thermally cracked westerly granite at elevated hydrostatic pressure". In: *Rock Physics and Natural Hazards*. Springer, pp. 927–948.

Nielsen, S and R Madariaga (2003). "On the self-healing fracture mode". In: *Bulletin of the Seismological Society of America* 93.6, pp. 2375–2388.

Nielsen, S, J Taddeucci, and S Vinciguerra (2010). "Experimental observation of stick-slip instability fronts". In: *Geophysical Journal International* 180.2, pp. 697–702.

Ohnaka, M. and Y. Kuwahara (1990). "Characteristic features of local breakdown near a crack-tip in the transition zone from nucleation to unstable rupture during stick-slip shear failure". In: *Tectonophysics* 175, pp. 197–220.

Ohnaka, Mitiyasu (1992). "Earthquake source nucleation: A physical model for short-term precursors". In: *Tectonophysics* 211.1-4, pp. 149–178.

— (2003). "A constitutive scaling law and a unified comprehension for frictional slip failure, shear fracture of intact rock, and earthquake rupture". In: *Journal of Geophysical Research: Solid Earth* 108.B2.

— (2013). *The physics of rock failure and earthquakes*. Cambridge University Press.

Olson, Erik L. and Richard M. Allen (2005). "The deterministic nature of earthquake rupture". In: *Nature* 438.7065, pp. 212–215.

Ottosen, Niels Saabye and Hans Petersson (1992). *Introduction to the finite element method*. Prentice-Hall.

Passelègue, François X, Alexandre Schubnel, Stefan Nielsen, Harsha S Bhat, and Raùl Madariaga (2013). "From sub-Rayleigh to supershear ruptures during stick-slip experiments on crustal rocks". In: *Science* 340.6137, pp. 1208–1211.

Peng, Zhigang and Joan Gomberg (2010). "An integrated perspective of the continuum between earthquakes and slow-slip phenomena". In: *Nature Geoscience* 3.9, pp. 599–607.

Radiguet, M, Hugo Perfettini, N Cotte, A Gualandi, Bernard Valette, V Kostoglodov, T Lhomme, A Walpersdorf, E Cabral Cano, and M Campillo (2016). "Triggering of the 2014 M w 7.3 Papanoa earthquake by a slow slip event in Guerrero, Mexico". In: *Nature Geoscience* 9.11, p. 829.

Ray, Sohom and Robert C Viesca (2017). "Earthquake nucleation on faults with heterogeneous frictional properties, normal stress". In: *Journal of Geophysical Research: Solid Earth* 122.10, pp. 8214–8240.

Reid, Harry Fielding (1911). *The elastic-rebound theory of earthquakes*. University Press.

Rice, J. R. (1968). "A path independent integral and the approximate analysis of strain concentration by notches and cracks". In: *Journal of Applied Mechanics* 35, pp. 379–386.

Rice, James R. (1993). "Spatio-temporal complexity of slip on a fault". In: *Journal of Geophysical Research* 98.B6, p. 9885.

Rice, James R (2006). "Heating and weakening of faults during earthquake slip". In: *Journal of Geophysical Research: Solid Earth* 111.B5.

Rice, James R, Charles G Sammis, and Robert Parsons (2005). "Off-fault secondary failure induced by a dynamic slip pulse". In: *Bulletin of the Seismological Society of America* 95.1, pp. 109–134.

Richardson, Eliza and Chris Marone (1999). "Effects of normal stress vibrations on frictional healing". In: *J. geophys. Res* 104.B12, pp. 28859–28878.

Romanet, Pierre, Harsha S Bhat, Romain Jolivet, and Raul Madariaga (2018). "Fast and slow slip events emerge due to fault geometrical complexity". In: *Geophysical Research Letters* 45.10, pp. 4809–4819.

Rosakis, A.J., K. Xia, G. Lykotrafitis, and H. Kanamori (2007). "Dynamic Shear Rupture in Frictional Interfaces: Speeds Directionality, and Modes". In: *Treatise on Geophysics*. Elsevier, pp. 153–192.

Rouet-Leduc, Bertrand, Claudia Hulbert, Nicholas Lubbers, Kipton Barros, Colin J Humphreys, and Paul A Johnson (2017). "Machine learning predicts laboratory earthquakes". In: *Geophysical Research Letters* 44.18, pp. 9276–9282.

Rouet-Leduc, Bertrand, Claudia Hulbert, and Paul A Johnson (2018). "Breaking Cascadia's Silence: Machine Learning Reveals the Constant Chatter of the Megathrust". In: *arXiv preprint arXiv:1805.06689*.

Rousset, Baptiste, Romain Jolivet, Mark Simons, Cécile Lasserre, Bryan Riel, Pietro Milillo, Ziyadin Çakir, and François Renard (2016). "An aseismic slip transient on the North Anatolian Fault". In: *Geophysical Research Letters* 43.7, pp. 3254–3262.

Rousset, Baptiste, Roland Bürgmann, and Michel Campillo (2019). "Slow slip events in the roots of the San Andreas fault". In: *Science advances* 5.2, eaav3274.

Rubin, AM and J-P Ampuero (2005). "Earthquake nucleation on (aging) rate and state faults". In: *Journal of Geophysical Research: Solid Earth* 110.B11.

Rubino, V, AJ Rosakis, and N Lapusta (2017). "Understanding dynamic friction through spontaneously evolving laboratory earthquakes". In: *Nature communications* 8, p. 15991.

Ruina, Andy (1983). "Slip instability and state variable friction laws". In: *Journal of Geophysical Research: Solid Earth* 88.B12, pp. 10359–10370.

Ruiz, S., M. Metois, A. Fuenzalida, J. Ruiz, F. Leyton, R. Grandin, C. Vigny, R. Madariaga, and J. Campos (2014). "Intense foreshocks and a slow slip event preceded the 2014 Iquique Mw 8.1 earthquake". In: *Science* 345.6201, pp. 1165–1169.

Ruiz, S., F. Aden-Antoniow, J. C. Baez, C. Otarola, B. Potin, F. del Campo, P. Poli, C. Flores, C. Satriano, F. Leyton, R. Madariaga, and P. Bernard (2017). "Nucleation Phase and Dynamic Inversion of the Mw 6.9 Valparaíso 2017 Earthquake in Central Chile". In: *Geophysical Research Letters* 44.20, pp. 10,290–10,297.

Scholz, CH, Max Wyss, and SW Smith (1969). "Seismic and aseismic slip on the San Andreas fault". In: *Journal of geophysical research* 74.8, pp. 2049–2069.

Scholz, Christopher H (1998). "Earthquakes and friction laws". In: *Nature* 391.6662, pp. 37–42.

— (2002). *The mechanics of earthquakes and faulting*. Cambridge university press.

Schubnel, Alexandre, Stefan Nielsen, Jacopo Taddeucci, Sergio Vinciguerra, and Sandro Rao (2011). "Photo-acoustic study of subshear and supershear ruptures in the laboratory". In: *Earth and Planetary Science Letters* 308.3, pp. 424–432.

Schwartz, Susan Y and Juliana M Rokosky (2007). "Slow slip events and seismic tremor at circum-Pacific subduction zones". In: *Reviews of Geophysics* 45.3.

Shearer, Peter M (2009). *Introduction to seismology*. Cambridge University Press.

Shlomai, Hadar and Jay Fineberg (2016). "The structure of slip-pulses and supershear ruptures driving slip in bimaterial friction". In: *Nature Communications* 7, p. 11787.

Smith, Ian Moffat, Denwood Vaughan Griffiths, and Lee Margetts (2013). *Programming the finite element method*. John Wiley & Sons.

Socquet, Anne, Jesus Piña Valdes, Jorge Jara, Fabrice Cotton, Andrea Walpersdorf, Nathalie Cotte, Sebastian Specht, Francisco Ortega-Culaciati, Daniel Carrizo,

and Edmundo Norabuena (2017). "An 8 month slow slip event triggers progressive nucleation of the 2014 Chile megathrust". In: *Geophysical Research Letters* 44.9, pp. 4046–4053.

Svetlizky, Ilya and Jay Fineberg (2014). "Classical shear cracks drive the onset of dry frictional motion". In: *Nature* 509.7499, pp. 205–208.

Svetlizky, Ilya, Daniel Pino Muñoz, Mathilde Radiguet, David S Kammer, Jean-François Molinari, and Jay Fineberg (2016). "Properties of the shear stress peak radiated ahead of rapidly accelerating rupture fronts that mediate frictional slip". In: *Proceedings of the National Academy of Sciences* 113.3, pp. 542–547.

Szabo, Barna A and George C Lee (1969). "Derivation of stiffness matrices for problems in plane elasticity by Galerkin's method". In: *International Journal for Numerical Methods in Engineering* 1.3, pp. 301–310.

Tape, Carl, Stephen Holtkamp, Vipul Silwal, Jessica Hawthorne, Yoshihiro Kaneko, Jean Paul Ampuero, Chen Ji, Natalia Ruppert, Kyle Smith, and Michael E West (2018). "Earthquake nucleation and fault slip complexity in the lower crust of central Alaska". In: *Nature Geoscience*, p. 1.

Udías, Agustín, Ral Madariaga, Elisa Buforn, et al. (2014). *Source Mechanisms of Earthquakes: Theory and Practice*. Cambridge University Press.

Uenishi, Koji and James R. Rice (2003). "Universal nucleation length for slip-weakening rupture instability under nonuniform fault loading". In: *Journal of Geophysical Research: Solid Earth* 108.B1.

Ulrich, Thomas, Alice-Agnes Gabriel, Jean-Paul Ampuero, and Wenbin Xu (2019). "Dynamic viability of the 2016 Mw 7.8 Kaikōura earthquake cascade on weak crustal faults". In: *Nature communications* 10.1, p. 1213.

Virieux, Jean and Raul Madariaga (1982). "Dynamic faulting studied by a finite difference method". In: *Bulletin of the Seismological Society of America* 72.2, pp. 345–369.

Wech, Aaron G. and Noel M. Bartlow (2014). "Slip rate and tremor genesis in Cascadia". In: *Geophysical Research Letters* 41.2, pp. 392–398.

Xu, Shiqing, Eiichi Fukuyama, Futoshi Yamashita, Kazuo Mizoguchi, Shigeru Takizawa, and Hironori Kawakata (2017). "Strain rate effect on fault slip and

rupture evolution: Insight from meter-scale rock friction experiments". In: *Tectonophysics*.

Yao, Dongdong, Jacob I. Walter, Xiaofeng Meng, Tiegan E. Hobbs, Zhigang Peng, Andrew V. Newman, Susan Y. Schwartz, and Marino Protti (2017). "Detailed spatiotemporal evolution of microseismicity and repeating earthquakes following the 2012 Mw 7.6 Nicoya earthquake". In: *Journal of Geophysical Research: Solid Earth* 122.1, pp. 524–542.